



City Research Online

City, University of London Institutional Repository

Citation: Cattell, R. (2019). An experimental investigation in to a highly forward swept, low specific speed turbocompressor. (Unpublished Doctoral thesis, City, University of London)

This is the accepted version of the paper.

This version of the publication may differ from the final published version.

Permanent repository link: <https://openaccess.city.ac.uk/id/eprint/25522/>

Link to published version:

Copyright: City Research Online aims to make research outputs of City, University of London available to a wider audience. Copyright and Moral Rights remain with the author(s) and/or copyright holders. URLs from City Research Online may be freely distributed and linked to.

Reuse: Copies of full items can be used for personal research or study, educational, or not-for-profit purposes without prior permission or charge. Provided that the authors, title and full bibliographic details are credited, a hyperlink and/or URL is given for the original metadata page and the content is not changed in any way.



An Experimental Investigation in to a Highly Forward
Swept, Low Specific Speed Turbocompressor

Ruth Cattell

This thesis is submitted to City University of London for fulfilment of the requirements for
the degree of Doctor of Philosophy

School of Mathematics, Computer Science and Engineering

December 2019

Abstract

A novel turbocompressor with ultra high forward sweep has been investigated using optical flow visualisation, Laser Doppler Velocimetry (LDV) and testing to establish the relationship between inlet conditions and compressor geometry, and compressor performance.

This compressor type, now known as TurboClaw[®], exhibits efficiencies comparable to existing positive displacement compressors but below standard radial turbocompressors designed to operate at much higher shaft speed. This work extends the understanding of the compressor by examining the internal flow field with the intention of informing new designs in order to improve performance.

A three times scale model of a commercially available compressor was designed and built. The test rig had optical access allowing flow visualisation of the whole diffuser passage and the rotor. High speed photography with smoke injection was used to image the bulk flow. In addition, LDV was used to determine the flow field to facilitate future CFD studies. These investigations showed the presence of pulsing flow that propagated the full length of the diffuser. However, there was no evidence of flow separation in the LDV results, even though the flow gravitated to the outer wall of the diffuser as it flowed round the bend. The LDV also showed a difference between the direction of the flow exiting the impeller and entering the diffuser implying slip is a significant factor in the compressor's performance.

Investigations on the effect of blade height and the generation of an empirical prediction tool were performed on a second compressor test rig with commercial scale dimensions. A method for comparing various blade height data on a single chart was developed. This showed that there is a positive relation between blade height and pressure ratio. This data was used to develop an empirical performance prediction tool that links impeller diameter, blade height and inlet conditions to the compressor performance. Measurements of the static pressure at the exit of the impeller have shown significant pressure rise showing the reaction of TurboClaw is higher than previously thought.

Acknowledgements

Firstly, tradition dictates I must thank my parents. So, thank you to my mother for providing the brains for me to complete this work and to my father for the procrastination skills that meant I almost didn't.

Academic assistance is probably the most important part of any research degree, from my direct supervisors Prof Pullen and Prof Nouri, to academic staff with no direct link to my work, other than being incredibly helpful, Dr Yan for providing the base of the Matlab code, Dr Lockett for his assistance with the high-speed photography, to the technical staff, Grant, Rob and Jim, who ensured the rigs went together even if it required a hammer and some gentle persuasion. Whilst undertaking experimental work, the equipment used is vital to the success or failure of the investigation. I am eternally grateful to the EPSRC equipment loan pool for coming to the rescue with the LDV equipment for use in this work and Martin Hyde from TSI for his knowledge and guidance on how to get the best out of it.

Without friends the world is a lonely place, I'd like to say they kept me sane, but who am I kidding. To my great friend Zander, without those cider and sushi sessions working out the best way to rebuild Boris, and occasionally talking about lasers, mostly the feasibility of strapping them to a shark's head, the last 8 years would have been a very dull place. Long may our friendship continue! To those I shared an office with, thanks for all the great banter!

To all my friends and colleagues at DBS, you have put up with my long tails of broken lasers and malfunctioning optics without (too much) complaint. Without the design effort and manufacturing resources of DBS the "square box" would never have been built, you may not have liked the shape, but it worked. I only hope some of what has been learnt will be of use. Shahram, you sent me down the rabbit hole of research when you suggested me for this work, thank you for all your help in guiding me back out again. And finally, Niall, the constant cry of "you'll never finish" was the best motivation you could have provided.

Declaration

This thesis describes work undertaken by the author. To the best of the author's knowledge the work is original. Where the work of others has been used, appropriate reference has been made.

Contents

| | |
|---|----|
| Abstract | 2 |
| 1. Introduction | 20 |
| 1.1. Euler turbomachinery equation | 22 |
| 1.2. Slip | 23 |
| 1.3. Reynolds scaling | 23 |
| 1.4. Specific Speed & Flow Coefficient | 24 |
| 1.5. TurboClaw Development | 28 |
| 1.6. Research Aims and Objectives | 32 |
| 1.7. Thesis Overview | 33 |
| 2. Literature Review | 34 |
| 2.1. Research on Low Specific Speed Compressors | 34 |
| 2.2. TurboClaw Research | 36 |
| 2.3. Flow Field Investigative Techniques | 40 |
| 2.3.1. Schlieren Photography | 40 |
| 2.3.2. Laser Doppler Velocimetry, LDV | 40 |
| 2.3.3. Phase Doppler Particle Analysis, PDPA | 41 |
| 2.3.4. Particle Image Velocimetry, PIV | 41 |
| 2.3.5. Planar Laser Induced Fluorescence, PLIF | 42 |
| 3. Methodologies used in this work | 43 |
| 3.1.1. High-Speed Camera Requirements | 43 |
| 3.1.1. High Speed Camera Set Up | 45 |
| 3.1.2. High-Speed Camera Image Processing | 46 |
| 3.1.3. Laser Doppler Velocimetry Theory | 47 |
| 3.1.4. Laser Doppler Velocimetry Set Up | 50 |
| 3.1.5. Errors in LDV Measurements | 57 |

| | | |
|----------|---------------------------------|-----|
| 4. | Optical Access Test Rig | 58 |
| 4.1. | Previous Setup..... | 58 |
| 4.2. | Optical Research Test Rig | 61 |
| 4.2.1. | Optical Access | 61 |
| 4.2.2. | Balancing..... | 62 |
| 4.2.3. | Impeller | 63 |
| 4.2.4. | Bearing Housing | 68 |
| 4.2.4.1. | Bearings | 68 |
| 4.2.4.2. | Seals..... | 73 |
| 4.2.4.3. | Shaft..... | 73 |
| 4.2.4.4. | Housing..... | 75 |
| 4.2.5. | Main support..... | 75 |
| 4.2.6. | Collector | 76 |
| 4.2.7. | Pipe Work..... | 76 |
| 4.2.8. | Motor Connection..... | 77 |
| 4.2.9. | Primary Instrumentation..... | 78 |
| 4.2.10. | Sensor Calibration | 81 |
| 4.3. | Performance Testing | 81 |
| 4.4. | Error Analysis..... | 86 |
| 5. | Flow Visualisation | 97 |
| 5.1. | Block 1 Results..... | 97 |
| 5.1.1. | Pulse Frequency | 103 |
| 5.1.2. | Flow Speed | 103 |
| 5.1.3. | Reynolds Number..... | 103 |
| 5.2. | Results – Block 2 | 104 |
| 5.2.1. | Flow Speed | 105 |

| | | |
|--------|--|-----|
| 5.3. | Results – Block 3 and 4 | 107 |
| 6. | Laser Testing | 109 |
| 6.1. | LDV Results | 109 |
| 6.1.1. | Diffuser Throat | 113 |
| 6.1.1. | Diffuser Vaneless space | 122 |
| 6.1.2. | Diffuser Bend..... | 126 |
| 6.1.3. | Diffuser Exit | 128 |
| 6.2. | Optical Measurement Conclusions | 131 |
| 6.3. | Gas Angles | 132 |
| 6.3.1. | Impeller Inlet..... | 132 |
| 6.3.2. | Impeller Exit | 134 |
| 6.3.3. | Diffuser Inlet..... | 136 |
| 7. | Pressurised Test Rig | 139 |
| 7.1. | Test Aims | 139 |
| 7.2. | Test loop | 148 |
| 7.3. | Data Processing and Error Analysis | 154 |
| 8. | Pressurised Test Rig Results..... | 157 |
| 8.1. | 200% Base Case | 157 |
| 8.2. | Pressure ratio | 158 |
| 8.3. | Map Predictor Tool..... | 166 |
| 8.4. | Pressure tappings and axial force | 175 |
| 8.5. | Efficiency Analysis..... | 180 |
| 8.6. | Error Analysis..... | 187 |
| 9. | Conclusions | 189 |
| 10. | Future work..... | 191 |
| 11. | Appendix: Additional LDV images | 192 |

| | | |
|-------|---|-----|
| 11.1. | Diffuser Bend Individual Images | 192 |
| 11.2. | Diffuser Bend Individual Images | 196 |
| 12. | Appendix: Matlab programmes | 199 |
| 12.1. | Create Mean Image | 199 |
| 12.2. | Background Image Removal | 200 |
| 12.3. | Image Intensity Adjustment | 201 |
| 12.4. | Colour an Image Black or White Depending on Threshold Value | 205 |
| 12.5. | Crop Image to Size | 207 |
| 12.6. | Average LDV Results by Impeller Position | 208 |
| 12.7. | Plot Vector Image from LDV Results..... | 211 |
| 13. | Bibliography | 215 |

List of Figures

| | |
|--|----|
| Figure 1: Piston compressor (Cascade Machinery & Electric, 2014) | 20 |
| Figure 2: Scroll compressor (Tricountypools, 2014) | 20 |
| Figure 3: Screw compressor (Technology, 2018) | 20 |
| Figure 4: Centrifugal compressor (Australia, 2014) | 21 |
| Figure 5: Axial compressor (Turbomachinery, 2014)..... | 21 |
| Figure 6: Regenerative compressor (INC, 2018) | 21 |
| Figure 7: Velocity triangles for centrifugal impeller (Nuclear Power for Everybody, 2019) | 22 |
| Figure 8: The effect of slip on the angle of the gas leaving the impeller | 23 |
| Figure 9: Compressor stage loss vs Reynolds number for centrifugal compressors (Pampreen, 1973) | 24 |
| Figure 10: Impeller geometry variation with changing specific speed (Pumps, 2014) .. | 25 |
| Figure 11: Variation of losses in a compressor with flow coefficient ϕ (Cumpsty, 2004) | 26 |

| | |
|--|----|
| Figure 12: Multistage compressor showing effect of specific speed decreasing with each stage (Kobayashi, et al., 1990) | 27 |
| Figure 13: TurboClaw® Impeller (a) from above and (b) from the side | 29 |
| Figure 14: Conventional centrifugal Impeller (a) from above and (b) from the side | 29 |
| Figure 15: Vine's novel compressor design (Vine, et al., 2003) | 30 |
| Figure 16: Velocity triangles for forward swept compressor | 30 |
| Figure 17: Wedge type impeller proposed by Rusak (Rusak, 1982) | 34 |
| Figure 18: Barske type compressor (Rogers, 1990) | 34 |
| Figure 19: Flow path in a Regenerative Compressor (Song, et al., 2003)..... | 35 |
| Figure 20: Torque meter test rig (Parra, et al., 2015) | 39 |
| Figure 21: LDA schematic (Jensen, 2004)..... | 41 |
| Figure 22: PIV schematic (Jensen, 2004)..... | 42 |
| Figure 23: High speed camera setup..... | 43 |
| Figure 24: Light scattering techniques | 44 |
| Figure 25: Flow Visualisation Areas | 44 |
| Figure 26: High speed camera setup..... | 45 |
| Figure 27: Camera and light source set up – picture captured from behind the high-speed camera looking at the Perspex diffuser lit from behind | 45 |
| Figure 28: Background image – average of 50 photos taken with no smoke injection . | 46 |
| Figure 29: High speed camera image as captured | 46 |
| Figure 30: High speed camera image with background removed | 46 |
| Figure 31: Image used to identify low and high intensity values | 47 |
| Figure 32: Image brightened to highlight the smoke intensity..... | 47 |
| Figure 33: Image with colourmap applied | 47 |
| Figure 34: LDV Schematic..... | 49 |
| Figure 35: Interference bands of crossing laser beam..... | 49 |
| Figure 36: Doppler burst (a) as measured and (b) with DC component removed. | 49 |
| Figure 37: Side view of laser setup | 51 |
| Figure 38: Top view of laser setup | 51 |
| Figure 39: Silicone oil atomiser for LDV seeding..... | 52 |
| Figure 40: Experimental setup for LDV measurements | 52 |
| Figure 41: Laser entering rig during LDV measurements | 53 |

| | |
|--|----|
| Figure 42: Blade leading edge used for "zero" point of LDV measurements | 53 |
| Figure 43: Beam crossing on "zero" point for LDV measurements | 53 |
| Figure 44: Control volume within passage of LDV measurements..... | 54 |
| Figure 45: Silicone oil scattering laser light in passage during LDV measurements..... | 54 |
| Figure 46: Screenshot from the Flowsizer software used to display the results of the LDV testing..... | 55 |
| Figure 47: Cross section drawing of Vine's test rig (Vine, 2005) | 60 |
| Figure 48: Cross section drawing of new rig optimised for optical access..... | 62 |
| Figure 49: Boundary conditions for stress analysis of impeller | 64 |
| Figure 50: Stress in impeller hub at 0 and 20,000 rpm..... | 64 |
| Figure 51: High stress location in impeller hub at 20,000 rpm..... | 65 |
| Figure 52: Stress in bolted impeller shroud at 0 and 20,000 rpm | 65 |
| Figure 53: High stress location in impeller shroud at 20,000 rpm..... | 65 |
| Figure 54: Displacement of impeller at 20,000 rpm | 66 |
| Figure 55: Section view of the impeller displacement at 20,000 rpm, scale x50 | 66 |
| Figure 56: Goodman diagram for the impeller showing an infinite life design..... | 68 |
| Figure 57: Schematic of the force across the impeller due to pressure imbalance when operating..... | 69 |
| Figure 58: Pressure variation with radius across the surface of the impeller | 69 |
| Figure 59: Simplified impeller surface | 69 |
| Figure 60: Diagram of the pressure imbalance across the impeller causing an axial force to be applied to the bearings..... | 70 |
| Figure 61: Names for the areas generating load due to pressure imbalance | 71 |
| Figure 62: Section view of the bearing housing..... | 72 |
| Figure 63: Bearing removal too..... | 73 |
| Figure 64: Thermocouple holes in the bearing housing for measuring bearing temperatures | 73 |
| Figure 65: Vent hole in the bearing housing to protect the bearing grease from being "blown" out by a pressure imbalance | 73 |
| Figure 66: Campbell diagram for compressor shaft showing subcritical operation..... | 74 |
| Figure 67: Main support for rig showing the sculpting required to maintain optical access | 75 |

| | |
|--|-----|
| Figure 68: Compressor downstream pipe layout including measurement and control devices..... | 76 |
| Figure 69: Complete test rig with hose connections between compressor outlet and downstream pipework..... | 77 |
| Figure 70: Labview programme main screen..... | 78 |
| Figure 71: Compressor Map - Pressure Ratio | 84 |
| Figure 72: Maximum measured pressure ratio plotted against shaft speed | 84 |
| Figure 73: Compressor Map - Efficiency | 85 |
| Figure 74: Garrett centrifugal compressor map (GARRETT MOTION INC., 2019) | 85 |
| Figure 75: PR vs mass flow rate with error bars | 91 |
| Figure 76: Efficiency vs mass flow rate with error bars | 91 |
| Figure 77: PR vs mass flow rate comparison with Vine's data | 93 |
| Figure 78: Maximum pressure ratio vs Speed for Vine and Current Work | 93 |
| Figure 79: Inlet geometry of Vine's impeller | 94 |
| Figure 80: Inlet geometry of new impeller | 94 |
| Figure 81: Efficiency vs mass flow rate comparison with Vine's data | 95 |
| Figure 82: Maximum Efficiency vs Speed for Vine and Current Work..... | 96 |
| Figure 83: Areas imaged using high speed photography..... | 97 |
| Figure 84: Flow at 2,000 rpm shown as a brightened image (left) and with a colourmap applied (right)..... | 98 |
| Figure 85: Flow at 2,500 rpm shown as a brightened image (left) and with a colourmap applied (right)..... | 99 |
| Figure 86: Flow at 3,000 rpm shown as a brightened image (left) and with a colourmap applied (right)..... | 100 |
| Figure 87: Flow at 4,000 rpm shown as a brightened image (left) and with a colourmap applied (right)..... | 101 |
| Figure 88: Flow splitting either side of the leading edge of the diffuser blade, 3,000 rpm on the left, 4,000 rpm on the right | 102 |
| Figure 89: Smoke fronts at 2,000 rpm | 103 |
| Figure 90: Smoke fronts at 4,000 rpm | 103 |
| Figure 91: Block 2 imaged at 2,000 rpm | 105 |
| Figure 92: Smoke front in block 2 at 2,000 rpm | 106 |

| | |
|--|-----|
| Figure 93(a-c): Block 3 results | 107 |
| Figure 94: Block 4 results | 107 |
| Figure 95: Positions measured with LDV | 109 |
| Figure 96: Averaging angle effect on velocity results – horizontal direction | 111 |
| Figure 97: Angle definition for x-axis in Figure 98 and Figure 99 below | 111 |
| Figure 98: Averaging angle effect on velocity results – vertical direction..... | 112 |
| Figure 99: Mean velocity vector image of LDV results - 0 degree impeller rotation.... | 113 |
| Figure 100: Mean velocities at diffuser throat, 1 degree increment impeller rotation | 114 |
| Figure 101: The effect of slip on the velocity triangles of a forward swept compressor | 117 |
| Figure 102: Collated image of all images in Figure 100 showing the flow variation as the impeller rotates through 360 degrees, velocities range from 73.4 m/s to 23.7 m/s... | 118 |
| Figure 103: Velocity profile variation with impeller position at the diffuser throat, legend shows the impeller position in degrees | 119 |
| Figure 104: Location for Figure 103 velocity profile, numbers show the passage width | 119 |
| Figure 105: Velocity profile variation with impeller position at the end of the straight diffuser section Figure 104..... | 120 |
| Figure 106: Flow angles at diffuser throat as impeller rotates..... | 121 |
| Figure 107: Flow angles at diffuser bend as impeller rotates | 121 |
| Figure 108: positive and negative angles of flow for Figure 106 and Figure 107..... | 122 |
| Figure 109: Flow angle relative to the tangential in the vaneless space at 6 measurement locations..... | 123 |
| Figure 110: Upstream measurement locations | 124 |
| Figure 111: Flow velocity in the vaneless space at 6 measurement locations..... | 125 |
| Figure 112: Collated image of all position vectors at the diffuser bend, flow velocity ranges from 41.1 m/s to 3.1 m/s | 126 |
| Figure 113: Velocity profile variation with impeller position at the bend | 127 |
| Figure 114: Location for Figure 113 velocity profile | 127 |
| Figure 115: Flow angles at diffuser bend as impeller rotates | 128 |
| Figure 116: Collated image of all position vectors at the diffuser exit, flow velocity ranges from 37.0 m/s to 3.1 m/s | 128 |

| | |
|--|-----|
| Figure 117: Velocity profile variation with impeller position at the exit of the diffuser | 129 |
| Figure 118: Location for Figure 117 velocity profile | 129 |
| Figure 119: Flow angles at diffuser exit as impeller rotates | 130 |
| Figure 120: Sketch of impeller and diffuser passages with station numbers | 132 |
| Figure 121: Impeller geometric inlet angle | 133 |
| Figure 122: Impeller inlet velocity triangle | 133 |
| Figure 123: Impeller exit geometry | 134 |
| Figure 124: Impeller exit velocity triangle | 135 |
| Figure 125: Exit area of half impeller | 136 |
| Figure 126: Diffuser inlet geometry | 137 |
| Figure 127: Diffuser inlet velocity triangle | 137 |
| Figure 128: High pressure test rig – known as the "Square box" rig | 141 |
| Figure 129: Magtrol Torque Meter (Magtrol, 2019) | 142 |
| Figure 130: H125 and H80 test heads | 143 |
| Figure 131: Different blade heights, shown in red, within the same housing | 144 |
| Figure 132: Exploded view of "square box" compressor | 145 |
| Figure 133: Pressure tappings on inlet pipe | 146 |
| Figure 134: 3.64mm blade height (solid) and 9.10 blade height (transparent) | 146 |
| Figure 135: Schematic of pressurised test loop | 151 |
| Figure 136: Sources of loss between torque meter and impeller | 152 |
| Figure 137: Windage data for 1-5 bar absolute in CO ₂ | 153 |
| Figure 138: Residual plot of power correlation | 154 |
| Figure 139: Pressure ratio vs mass flow rate for base case 85x200% in CO ₂ | 158 |
| Figure 140: Water cooling of Torque Tube | 159 |
| Figure 141: Pressure ratio vs mass flow rate for CO ₂ testing | 160 |
| Figure 142: Impeller blade height area shown in green | 162 |
| Figure 143: Impeller blade height area cut line | 162 |
| Figure 144: Pressure ratio vs corrected mass flow for the 85x200% base case CO ₂ at various inlet pressures | 163 |
| Figure 145: Pressure ratio vs corrected mass flow rate for all sizes and pressures | 165 |
| Figure 146: Generic compressor map | 167 |

| | |
|---|-----|
| Figure 147: Speeds lines for 35,000 rpm and 44,000 rpm..... | 168 |
| Figure 148: Surge test data vs calculated data | 171 |
| Figure 149: Choke test data vs calculated data | 171 |
| Figure 150: Residual plot of surge curve fit | 172 |
| Figure 151: Residual plot of choke curve fit | 172 |
| Figure 152: All test data vs calculated data | 174 |
| Figure 153: percentage difference between test data and calculated data | 174 |
| Figure 154: 85x100% front face tappings measurements take as the compressor was near surge, results showing pressure ratio of impeller | 175 |
| Figure 155: 85x100% front face tappings measurements take as the compressor was at choke, results showing pressure ratio of impeller..... | 176 |
| Figure 156: 85x100% front face tappings measurements take as the compressor was near surge, results as a percentage of the total pressure rise | 177 |
| Figure 157: 85x100% front face tappings measurements take as the compressor was at choke, results as a percentage of the total pressure rise..... | 177 |
| Figure 158: 85x100% and 85x250% front face tappings measurements take as the compressor was near surge, results showing pressure ratio of impeller only | 178 |
| Figure 159: 85x100% and 85x250% pressure ratio results..... | 179 |
| Figure 160: Efficiency vs mass flow rate for 85x200% in CO ₂ | 180 |
| Figure 161: Efficiency vs mass flow rate for 85x200% in CO ₂ with losses due to windage and bearings removed. | 181 |
| Figure 162: Windage variance with speed and pressure..... | 182 |
| Figure 163: Magtrol torque coupler used to connect the motor via the torque meter to the compressor (Magtrol)..... | 183 |
| Figure 164: Efficiency vs corrected mass flow rate for all sizes (except 85x250%) and pressures in CO ₂ | 184 |
| Figure 165: Efficiency data for 85x250% compressor..... | 185 |
| Figure 166: Efficiency results at 45,000 rpm in CO ₂ | 186 |
| Figure 167: Error in PR and corrected mass flow rate for the pressurised test rig | 187 |
| Figure 168: Error in efficiency and corrected mass flow rate for the pressurised test rig | 188 |

| | |
|---|-----|
| Figure 169 (a-ad): Mean velocities at diffuser throat, 1 degree increment impeller rotation | 192 |
| Figure 170 (a-ad): Mean velocities at diffuser throat, 1 degree increment impeller rotation | 196 |

List of Tables

| | |
|--|-----|
| Table 1: Compressor specification | 61 |
| Table 2: Fatigue stresses | 66 |
| Table 3: Modifying factors for endurance limit | 67 |
| Table 4: Axial force radii and pressures | 71 |
| Table 5: Loads on impeller areas | 71 |
| Table 6: Sensor list | 79 |
| Table 7: National Instruments Hardware List | 80 |
| Table 8: Performance monitoring sensors with absolute accuracy | 87 |
| Table 9: Measurement errors | 89 |
| Table 10: Data fields recorded by LDV software | 110 |
| Table 11: Impeller inlet velocities | 134 |
| Table 12: Impeller exit velocities | 136 |
| Table 13: Diffuser inlet velocities..... | 137 |
| Table 14: Rig specification | 140 |
| Table 15: blade heights manufactured for each component | 146 |
| Table 16: Possible compressor blade heights available..... | 147 |
| Table 17: Measured impeller blade heights | 147 |
| Table 18: Actual impeller blade heights | 147 |
| Table 19: Performance instrumentation list..... | 149 |
| Table 20: Safety monitoring instrumentation list..... | 150 |
| Table 21: National Instruments modules..... | 150 |
| Table 22: Sensor accuracy..... | 154 |
| Table 23: Tested compressor matrix | 164 |
| Table 24: Constraints and optimised result for constant optimisation | 170 |
| Table 25: Constraints and optimised result for constant optimisation of PR | 173 |
| Table 26: Windage torque at compressor peak pressure ratio | 182 |

Nomenclature

Main Symbols

| | |
|-----------|---|
| a | Cylinder radius (windage calculation) (m) |
| a | Speed of sound (m/s) |
| A | Area (m ²) |
| A | Cross sectional area (m ²) |
| c | Constant (C_p calculation) |
| CAD | Computer aided design |
| CFD | Computational fluid dynamics |
| C_{mc} | Moment coefficient for a cylinder |
| C_p | Specific heat capacity at constant pressure |
| D | Diameter (D) |
| D_H | Hydraulic diameter |
| F | Focal length of transmitting optics (m) |
| f | Frequency (Hz) |
| F | Force (Axial force calculations) (N) |
| f_0 | Frequency shift (Hz) |
| f_D | Measured frequency (Hz) |
| h | Enthalpy (kJ/kg) |
| HP | High pressure |
| I | Current (Error analysis) |
| L | Characteristic length (m) |
| L | Cylinder length (windage calculation) (m) |
| LDV | Laser Doppler Velocimetry |
| LP | Low pressure |
| \dot{m} | Mass flow rate (kg/s) |
| n | Sample size (Error analysis) |
| NI | National Instruments |
| N_s | Specific speed |
| P | Power (windage calculation) |
| P | Pressure (axial force calculation) (Pa) |

| | |
|--|--|
| <i>PDPA</i> | Phase Doppler Particle Analysis |
| <i>PIV</i> | Particle Image Velocimetry |
| <i>PLIF</i> | Planar Laser Induced Fluorescence |
| <i>PM</i> | Permanent magnet |
| <i>PMT</i> | Photomultiplier |
| <i>PR</i> | Pressure ratio |
| <i>q</i> | Computed value (Error analysis) |
| <i>r</i> | Radius (m) |
| <i>R₀</i> | Beam radius for Gaussian distribution (m) |
| <i>Re_φ</i> | Rotational Reynolds number |
| <i>R_{specific}</i> | Specific gas constant for dry air (J/Kg.K) |
| <i>RTD</i> | Resistance temperature detectors |
| <i>s</i> | Entropy (kJ/kg.K) |
| <i>s</i> | Fringe spacing (m) |
| <i>S</i> | Signal (Error analysis) |
| <i>SE_{\bar{x}}</i> | Standard error of the mean |
| <i>U</i> | Tip speed (m/s) |
| <i>v</i> | Velocity (m/s) |
| <i>V</i> | Voltage (Error analysis) |
| \dot{V} | Volume flow rate (m ³ /s) |
| \dot{V} | Volume flow rate (m ³ /s) |
| <i>W</i> | Work |

Greek Symbols

| | |
|-----------|-------------------------------|
| α | Beam crossing angle (degrees) |
| Δ | Change in |
| δ | Control volume length |
| η | Efficiency |
| λ | Wavelength of light (m) |
| μ | Dynamic viscosity (kg/m.s) |
| ρ | Density (kg/m ³) |
| τ | Shaft torque (Nm) |

| | |
|----------|---|
| ν | Kinematic viscosity (m ² /s) |
| ϕ | Flow coefficient |
| ω | Angular velocity (m/s) |
| γ | Ratio of specific heats |
| δ | Small change (Error analysis) |
| δ | Control volume length (LDV) |
| σ | Stress (MPa) |
| σ | Standard deviation (Error analysis) |

Subscripts

| | |
|------------------|------------------------------|
| 0 | Stagnation |
| 1 | Compressor inlet conditions |
| 2 | Impeller outlet conditions |
| 3 | Compressor outlet conditions |
| <i>actual</i> | Actual input to compressor |
| <i>amplitude</i> | Amplitude of value |
| <i>bs1</i> | Inner edge of back seal |
| <i>bs2</i> | Outlet edge of back seal |
| <i>c</i> | Corrected |
| <i>dw</i> | Drum windage |
| <i>fm</i> | Flow meter conditions |
| <i>m</i> | Measured |
| <i>M</i> | Mach number |
| <i>mean</i> | Mean value |
| <i>nom</i> | Nominal conditions |
| <i>s</i> | Constant entropy process |
| <i>sf1</i> | Inner edge of front seal |
| <i>sf2</i> | Outlet edge of front seal |

1. Introduction

Compressed gas is used everywhere from the home to large scale industry. Depending on the type, quantity and process, the gas can either be bought bottled for instance acetylene and oxygen used in welding and cutting, or compressed on site such as in a shop airline. To bottle gas, the most common process is fractional distillation where the gas is cooled progressively until each component liquefies and can be collected. For on-site compression, mechanical compressors are used.

In mechanical gas compression, there are 2 main methods of compressing the gas. The first method, positive displacement, involves trapping a quantity of gas inside a chamber formed by at least two mechanical components such as a piston and cylinder. The volume of this chamber is then reduced by movement of one of the components relative to another compressing the trapped gas.

Common types of positive displacement compressor are piston, scroll and screw machines.



*Figure 1: Piston compressor
(Cascade Machinery & Electric,
2014)*



*Figure 2: Scroll compressor
(Tricountypools, 2014)*

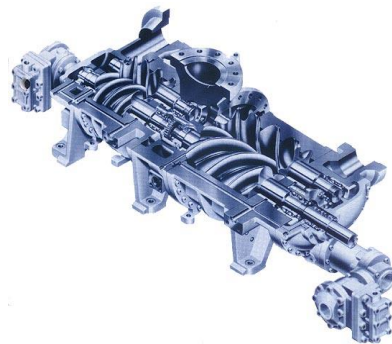


*Figure 3: Screw compressor
(Technology, 2018)*

In oil lubricated positive displacement compressors, oil is used to form a hydraulic seal around the gas pocket, improving compressor efficiency, and to cool the gas, reducing the operating temperature hence increasing the available duty cycle of the compressor. It also lubricates the close tolerance sliding surfaces. However, this oil needs to be removed from the gas after it has exited the compressor necessitating the use of an oil separator.

There are versions of these compressors that can operate either oil-free or oil-less. Oil-free means no oil is used in the compression process and the gas leaving the compressor contains no oil. Oil will be used by the compressor in bearings or the gearbox, but this is sealed so the oil is contained and can't contaminate the gas. Oil-less means no oil is found at all within the compressor. Both of these types of compressor use special coatings, such as polytetrafluoroethylene, PTFE, to lubricate the moving components. These coating wear over time lowering the life of the compressor or necessitating a maintenance cycle that includes recoating. As there is no oil within the compression process, the gas volume lacks the hydraulic seal, relying on the metal to metal seal, which is not nearly as effective, resulting in higher leakage rates and a drop in efficiency of the order of 10 – 20% (USA, 2017).

The second type of compression is known as dynamic compression and uses turbomachinery to compress the gas. This works by having an impeller spinning at high speed adding kinetic energy to the gas, the gas is then decelerated within a stationary component, called a diffuser, generating static pressure. Depending on the compressor design, the impeller generates a percentage of the static pressure rise.



Figure 4: Centrifugal compressor (Australia, 2014)

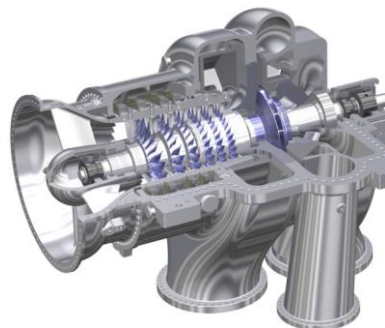


Figure 5: Axial compressor (Turbomachinery, 2014)

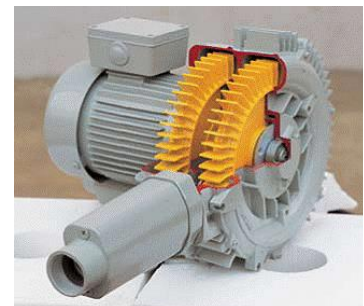


Figure 6: Regenerative compressor (INC, 2018)

Dynamic compressors have the advantage of high throughput for a given size of machine compared to positive displacement compressors. This makes them suitable for high flow applications. Further, due to the nature of the compression process, oil is not required to lubricate the compressor directly. If plain or rolling bearings are used, these would still require oil to lubricate, but that can be minimised. If true oil-less compression is

required, magnetic or air bearings can be used completely removing all oil from the system.

A number of equations can be used to design dynamic compressors, these will be described in the following sections.

1.1. Euler turbomachinery equation

The fundamental equation in turbomachinery design is the Euler turbomachinery equation, Equation 1, and is a result of Newton's second law of mechanics. It states that the change in angular momentum is equal to the sum of the external moments – in the case of turbomachinery the flow at the inlet and outlet and an external torque, τ_{shaft} .

$$\tau_{shaft} = \rho \dot{Q} (r_2 C_{\omega 2} - r_1 C_{\omega 1}) \quad \text{Equation 1}$$

Where r_1 and r_2 are the radii and $C_{\omega 1}$ and $C_{\omega 2}$ are the tangential velocity components at the inlet and outlet to the impeller respectively, ρ is the density and \dot{Q} the volume flow rate at the compressor inlet.

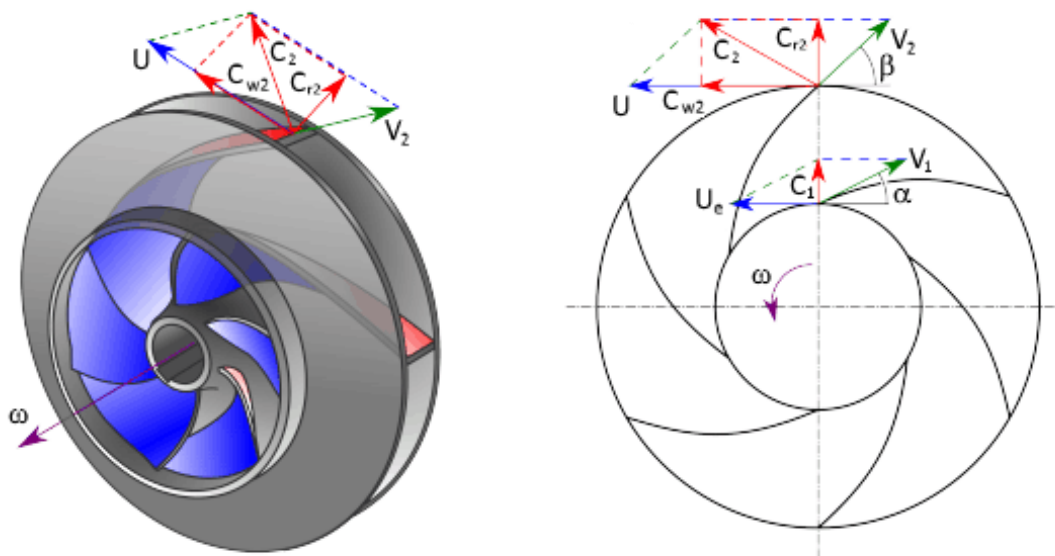


Figure 7: Velocity triangles for centrifugal impeller (Nuclear Power for Everybody, 2019)

This equation is applicable to both compressors and turbines, and is used to calculate the performance of a turbomachine.

1.2. Slip

A feature of dynamic compressors is slip, which can be thought of as the difference between the perfect gas angle and the actual angle that the gas exits the impeller blade. Figure 8 shows the ideal gas angles (black) and the gas angles when affected by slip (blue).

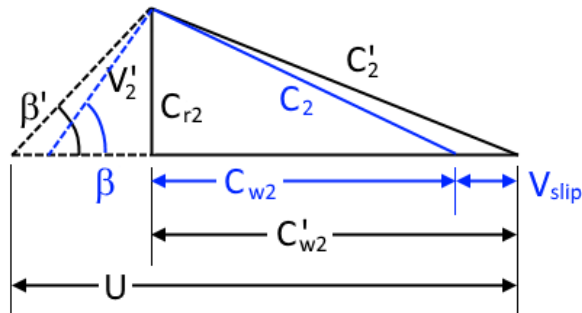


Figure 8: The effect of slip on the angle of the gas leaving the impeller

This difference is caused by a reduction in the force on the flow as the difference in pressure between the pressure and suction surfaces of the blade tend to zero at the trailing edge. If the slip factor is not accounted for in the compressor design, it can lead to a mismatch between the actual gas angle and the diffuser blade angle.

1.3. Reynolds scaling

The Reynolds number is a measure of the ratio of internal forces to viscous forces. As the number is dimensionless it allows experiments with dynamic similarity to be compared.

The Reynolds number is defined as:

$$Re = \frac{\rho v L}{\mu} = \frac{v L}{\nu} \quad \text{Equation 2}$$

Where v is the mean velocity of the fluid relative to the frame of reference, L is the characteristic linear dimension, μ is the dynamic viscosity of the fluid, ν is the kinematic viscosity and ρ is the density of the fluid.

In turbomachinery, the velocity is taken to be the tip speed of the impeller, the characteristic linear dimension as the impeller diameter and the density, dynamic and kinematic viscosities are taken at the inlet to the compressor. Pampreen showed that a straight line with slope of negative 0.164 can be drawn through a plot of compressor

stage loss (1-efficiency) versus Reynolds number (Pampreen, 1973) for a number of different size compressors measured at different inlet conditions. Data for friction in a smooth pipe also shows a negative slope of negative 0.164 for Reynolds numbers greater than 10^5 . Pampreen postulated this shows that losses incurred in centrifugal compressors are a result of turbulent flow.

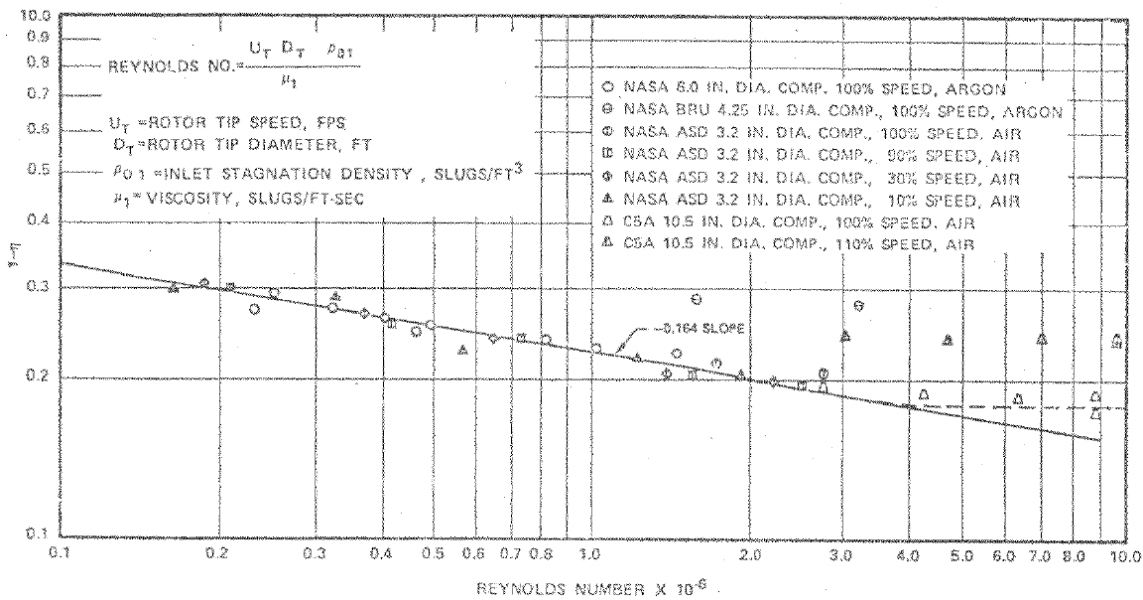


Figure 9: Compressor stage loss vs Reynolds number for centrifugal compressors (Pampreen, 1973)

1.4. Specific Speed & Flow Coefficient

To characterise a given gas compressor, application engineers often use a dimensionless number called the specific speed. This number relates the flow rate to the pressure rise and work input into the gas. The specific speed is defined as:

$$N_s = \frac{\omega \dot{Q}^{1/2}}{\Delta h^{3/4}} \quad \text{Equation 3}$$

Where: \dot{Q} is the volume flow rate; ω is the angular speed of the machine; and Δh is the specific enthalpy change. For a turbocompressors, in general, as the specific speed is lowered the optimal impeller design changes from a high blade height, axial machine; through mixed flow impellers with modest blade height and an axial inlet and radial outlet; to a fully radial design with much smaller blade height, radial exit and higher diameter impeller as shown in Figure 10.

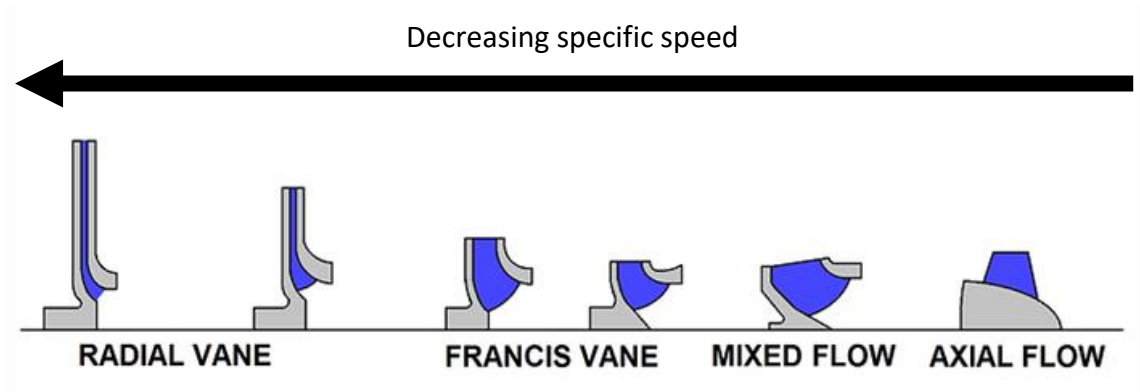


Figure 10: Impeller geometry variation with changing specific speed (Pumps, 2014)

Another useful dimensionless number used to characterise compressors is the flow coefficient defined below in equation 4. High flow coefficient impellers generally have large flow passages relative to their diameter, which allows for more unimpeded flow for a given size of machine.

$$\phi = \frac{\dot{m}}{\rho_{0in} U_2 D_2^2} \quad \text{Equation 4}$$

Where: \dot{m} is the mass flow rate; ρ_{0in} is the inlet density based on total conditions; U_2 is the tip speed of the machine; and D_2 is the impeller diameter. For a given enthalpy change, operating speed and geometry, it can be seen that both the flow coefficient and specific speed are both proportional to the volume flow rate:

As

$$\dot{Q} = \frac{\dot{m}}{\rho_{0in}} \quad \text{Equation 5}$$

Therefore

$$\phi = \frac{\dot{Q}}{U_2 D_2^2} \quad \text{Equation 6}$$

When $U_2 D_2^2$ is a constant

$$\phi \propto \dot{Q} \quad \text{Equation 7}$$

Similarly, for constant ω and Δh

$$N_s \propto \dot{Q}^{1/2} \quad \text{Equation 8}$$

Therefore

$$\phi \propto N_s^2 \quad \text{Equation 9}$$

Figure 11 shows the trend as the design flow coefficient, ϕ , and corresponding specific speed, N_s , is lowered. Disk friction and leakage losses increase progressively due to the rise in blade surface area relative to the blade passage volume.

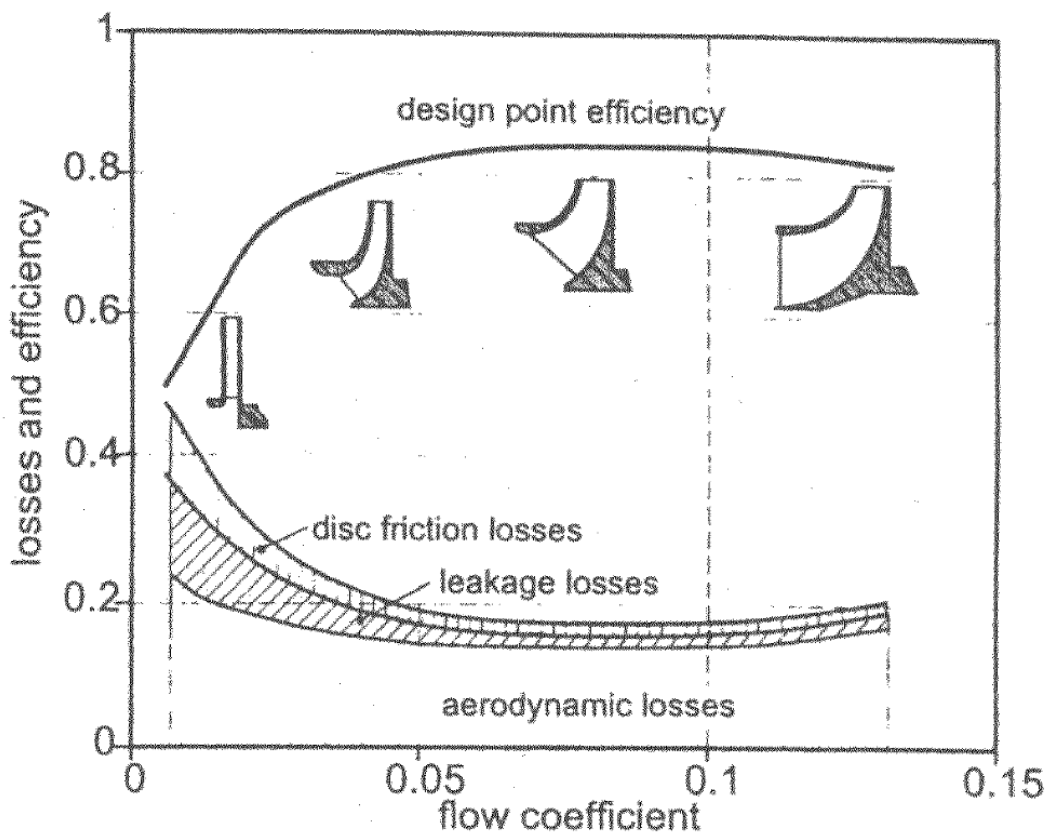


Figure 11: Variation of losses in a compressor with flow coefficient ϕ (Cumpsty, 2004)

When there is a requirement for a single stage, low specific speed compressor, the poor efficiency of a dynamic compressor means it may be a better choice to use a positive displacement machine. In many applications, choosing a positive displacement machines is acceptable as the relatively large size and need for oil lubrication presents no problems.

However, in multistage compression, when multiple stages are on the same shaft, due to the increased pressure and therefore lower volume flow, each additional stage has a

lower specific speed than the last. As can be seen in the example in Figure 12, the first stage has a much larger blade height than the last, also the inlet to the first stage impeller blades is almost axial, where the final stage is almost fully radial, a characteristic trait of a low specific speed stage.

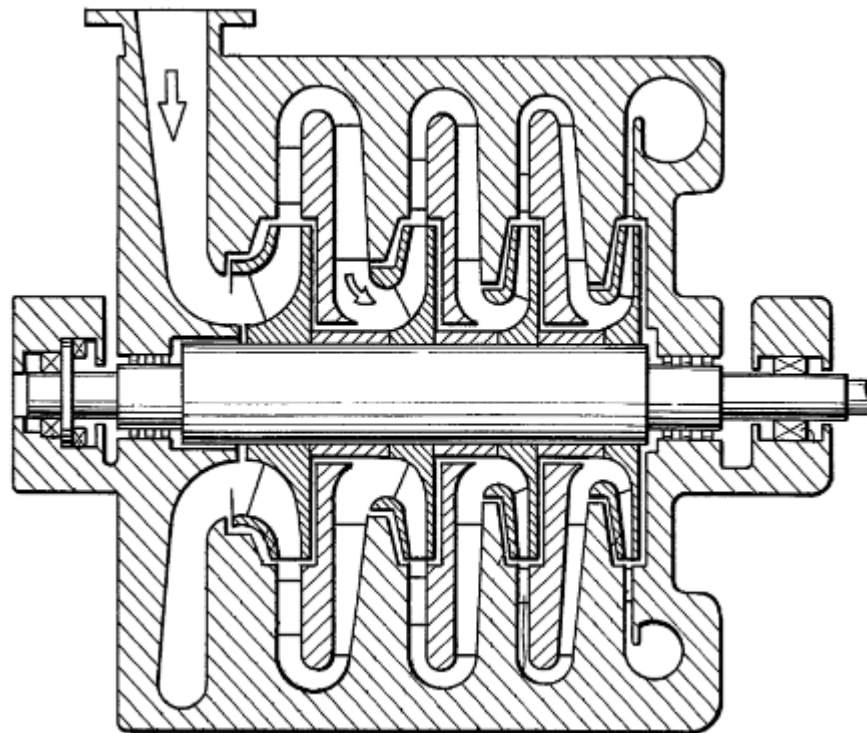


Figure 12: Multistage compressor showing effect of specific speed decreasing with each stage (Kobayashi, et al., 1990)

An application where this is the case is with steam recompression. A large food manufacturer had a large amount of waste steam that was created as a by-product of a frying process. To capture the latent heat contained by the steam to be used by the frying process, it was proposed to use a gas compressor to compress the steam to a higher pressure where it could be sent through a heat exchanger, and that heat used to heat the oil. However, using centrifugal compressors would have required 2 shafts and 21 stages due to the inefficiencies of the low specific speed end stages. If a low specific speed dynamic compressor was available that had similar efficiency to the higher specific speed stages, this could be dropped to a single shaft and 7 stages, massively simplifying the compressor unit, reducing capital costs and improving the payback to a point where it was worth investing in. (DBS, 2014)

The introduction has focused on general principles of turbomachinery and an example application where low specific speed compression is required. The next section will introduce TurboClaw, describe the background to its development and show the differences between it and a conventional centrifugal compressor.

1.5. TurboClaw Development

In 1998, BP had a requirement to compress fuel gas for a micro turbine. The first compressor used was a positive displacement machine but the oil lubrication required for the compressor led to the contamination of the fuel gas which led to higher emissions once the gas/oil mixture had been burnt.

To remove the need for oil lubrication, a turbomachinery solution was sought. Due to the requirement that the compressor was operated at the engine speed, this led to a compressor with a low specific speed. If a conventional centrifugal compressor was used it would be highly inefficient due to the losses described in Figure 11. It was decided to design a new type of dynamic compressor that would be more efficient at low specific speeds than the centrifugal compressor technology available at the time.

A turbocompressor with near tangential forward swept blades and wedge shape diffuser vanes was developed by Vine (Vine, 2005) at Imperial College London. The initial research involved developing the compressor's aerodynamic design, then designing and building a rig to assess the performance of the compressor.

The low specific speed (LSS) compressor developed by Vine was designed to reduce the losses as much as possible, specifically the windage losses were set to be approximately 2.5% of the total work. Using the Euler turbomachinery equation, Equation 1, this led to a design where the tip speed of the rotor was less than the gas velocity as it exited the rotor, resulting in a forward swept design. The design of the TurboClaw® impeller is shown alongside a conventional centrifugal compressor impeller in Figure 13 and Figure 14.

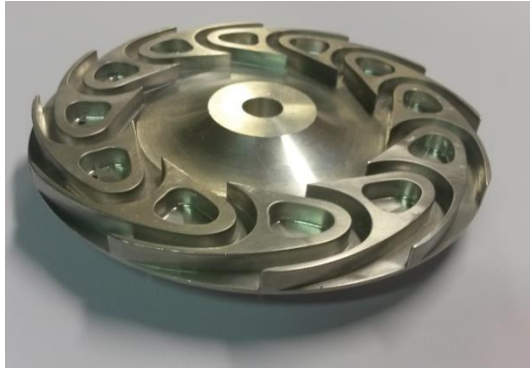


Figure 13: TurboClaw® Impeller (a) from above and (b) from the side

Figure 14: Conventional centrifugal Impeller (a) from above and (b) from the side

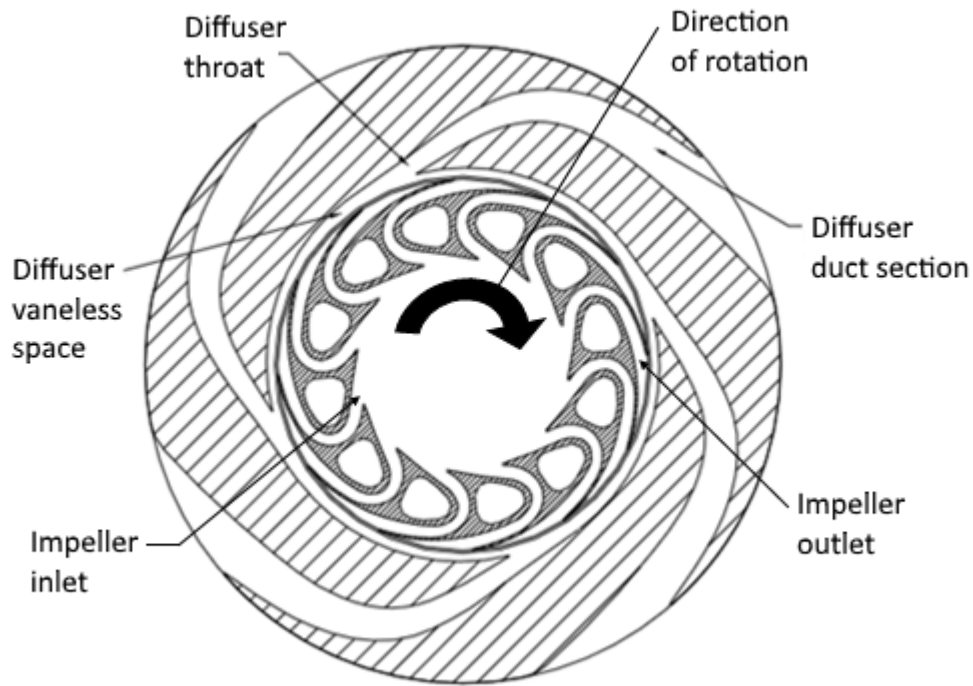


Figure 15: Vine's novel compressor design (Vine, et al., 2003)

The velocity triangles for the forward swept design are shown in Figure 16. The β angle has been reduced to improve the clarity of the diagram, C_2 is expected to be almost tangential to the impeller. This diagram shows the absolute velocity of the gas, C_2 , is greater than the tip speed of the impeller, unlike in a back swept centrifugal compressor where the gas velocity is less than the tip speed, see Figure 7.

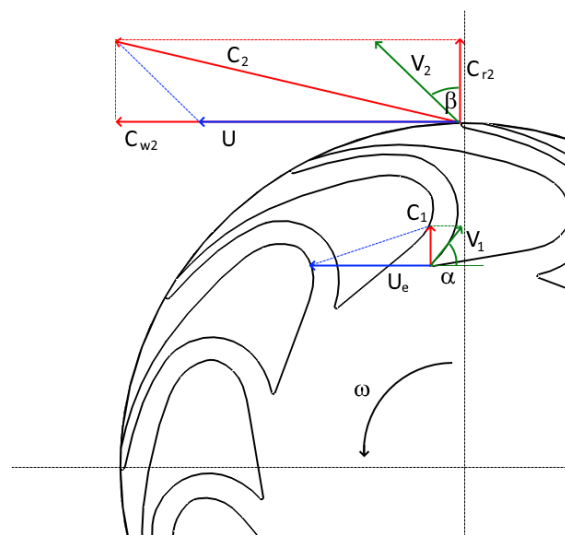


Figure 16: Velocity triangles for forward swept compressor

In conventional centrifugal compressors, the diffuser can be bladed or not depending on the type of performance required – high pressure ratio or wide operating range. Due

to the low flow coefficient and therefore low flow rate in the LSS compressor, a wedge type diffuser was chosen. The gas velocity at the exit of the diffuser was set to have a Mach number of 0.2, the exit pressure and temperature were iterated to find the flow velocity at the exit of the diffuser. From this and the specified mass flow rate, the passage size could be calculated. The inlet to the diffuser was set to have a Mach number of 0.9, from this the passage inlet size could be determined. Vine tested the 4 vane diffuser shown in Figure 15. After testing of the 4 vane diffuser was completed, a 6 vane diffuser was also tested. This design showed an improved efficiency, 54% isentropic efficiency as opposed to 50% for the 4 vane design (Vine, 2005). Therefore the 6 vane design was chosen for this work.

Conventional wisdom surrounding turbomachinery design suggests that machines with forward sweep can be expected to stall easily and have a poor range (Pullen, et al., 2011), it was shown by Vine that this was not the case with the highly forward swept design due to the higher flow speeds inherent in the design.

Vine attempted to use computational fluid dynamic (CFD) simulations to predict the performance and understand the internal workings of the compressor. Due to computational limitations (not enough processor power or memory available), the simulations never converged on a solution. This meant improvements in design could only be developed by a long and expensive cycle of design, build, test and evaluation.

Nevertheless, Vine showed in his research that a highly forward swept compressor could generate the required pressure ratio and mass flow rate at low specific speeds. However, as he was unable to successfully test with a torque sensor all measurements of efficiency were based on the energy balance method which can be unreliable.

As will be shown in the following literature survey, there has been very limited research since Vine and Thornton completed their work on this compressor. Commercially available CFD software has been unsuccessful in modelling the internal flow of the compressor, so it was decided to use experimental methods to investigate the internal flow field of the compressor.

A number of different investigative techniques were identified in the literature survey, but it was decided that two techniques; high speed photography and Laser Doppler

Velocimetry (LDV) were to be used in this research. High speed photography relies on the injection of seed particles that can be “seen” by a visible light camera, into the gas stream. A high-speed camera then records multiple frames at rates in excess of 10,000 frames per second. The movement of the seed particles is then tracked to gain a qualitative understanding of the flow. For these measurements, windows need to be included in the passages being investigated to allow the camera to see the flow and also to provide illumination. Due to the high frame rates, natural light is not enough to illuminate the particles in the flow. High power stage lights can be used to overcome this obstacle.

The second technique, Laser Doppler Velocimetry, LDV, provides quantitative measurements of the flow. By measuring the Doppler frequency shift of laser light that has been scattered by seed particles, the velocity of the seed particle travelling through the control volume can be calculated. When measurements are taken in 3 axes at multiple points within the flow field, a full picture can be described. Also, as the present research investigated a rotating machine, an encoder was included to allow a periodised view of the flow to be seen. This showed the effect of blade position on the flow and any pulsation that would be hidden if a time-averaged scheme was used.

1.6. Research Aims and Objectives

To improve knowledge of the novel forward swept compressor, the objectives of this research were:

- 1) To make flow field measurements of the compressor diffuser to develop a greater understanding of the flow within a novel forward swept dynamic compressor.
- 2) To develop an empirical model of the performance of the forward swept turbocompressor.

During this research several hypothesis’ will be tested:

- 1) The thickness of the blades in the impeller causes the flow to exit with significant pulsation which propagates through the diffuser.
- 2) The bend in the diffuser causes the flow to separate from the inner wall.
- 3) That no static pressure rise occurs within the impeller.

The starting point was to repeat Vine's results using a torque sensor to confirm, or otherwise, his efficiency measurements. Then, building on this, investigate the internal flow field of the compressor using high speed flow visualisation and laser Doppler velocimetry with the aim of producing a comprehensive understanding of the internal flow field of this novel compressor.

1.7. Thesis Overview

This thesis is divided into 10 chapters:

Chapter 2 offers an overview into the current research on TurboClaw and other low specific speed compressors. The work to date and areas which require further investigation are highlighted. The survey also explores the experimental methods available to compressor research.

Chapter 3 describes the methodologies used in the optical measurement techniques chosen. This will lead to a specification for the optical test rig, designed and built specifically for these measurements. The setup of the experimental rig will be described, followed by the methods of processing the data and plotting the results using Matlab.

Chapter 4 shows the development of the large scale test rig. It's concept, design and results from the initial performance testing. The data gathered was subjected to an error analysis, these results were then compared to Vine's results.

Chapter 5 presents the results from the flow visualisation showing analysis of the sections of the diffuser that were studied. Chapter 6 presents the laser Doppler velocimetry results and analysis. Chapter 6 also includes a discussion of results with reference to the research objectives. It discusses some new areas of interest that were discovered during the optical testing – that the flow exiting the impeller is not at the same angle as the geometric angle of the impeller – i.e. that there is slip and was that caused by the degree of reaction of the impeller.

Chapter 7 describes the small, high pressure, test rig that was developed to understand the performance of the compressor. It sets out the specification, aims, test protocol, error analysis and accuracy of measurements.

Chapter 8 shows the test results, analysis and discussion of the small rig. Results for the first geometry will be presented. Here results of varying the blade height and the correlation between blade height and reaction will be shown along with the development of an empirical relationship to allow prediction of compressor performance.

Chapter 9 details the main conclusions of this work and Chapter 10 makes recommendations for future work.

2. Literature Review

The forward swept compressor, TurboClaw, is a unique machine. It was developed during research projects at Imperial College London and subsequently patented [(Vine, et al., 2003), (Thornton, 2013)] which has limited the research. Development and commercial exploitation of the machine after 2006 has been pursued by DBS and as such there is limited research in the public domain on TurboClaw type geometries.

2.1. Research on Low Specific Speed Compressors

During his research, Vine identified 4 low specific speed compressors from the literature. These were Casey (Casey, et al., 1990), Wedge (Rusak, 1982), Barske (Barske, et al., 1960) and Regenerative (Sixsmith, et al., 1977). The geometries of the Wedge, Barske and Regenerative compressors are shown in figures 17 to 19 below. The Casey compressor is not shown as it was a conventional, high backsweep, radial compressor. The Barske Compressor was originally developed as a pump, but the geometry was used by Rogers as a low specific speed natural gas compressor (Rogers, 1990).

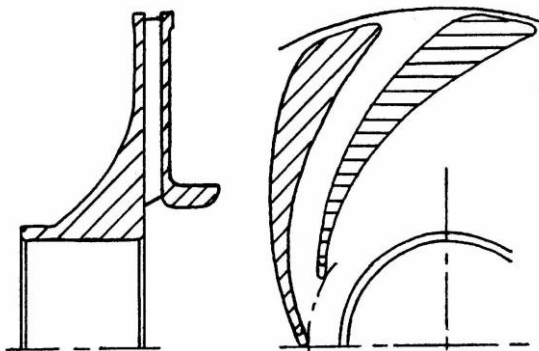


Figure 17: Wedge type impeller proposed by Rusak (Rusak, 1982)

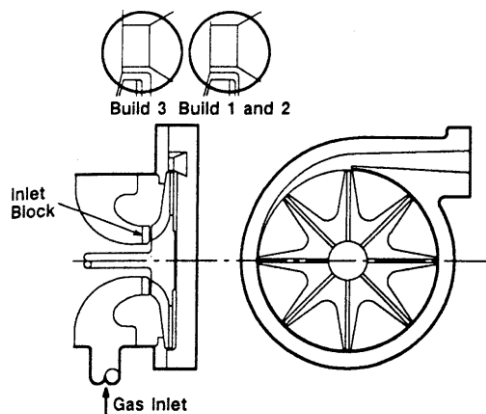


Figure 18: Barske type compressor (Rogers, 1990)

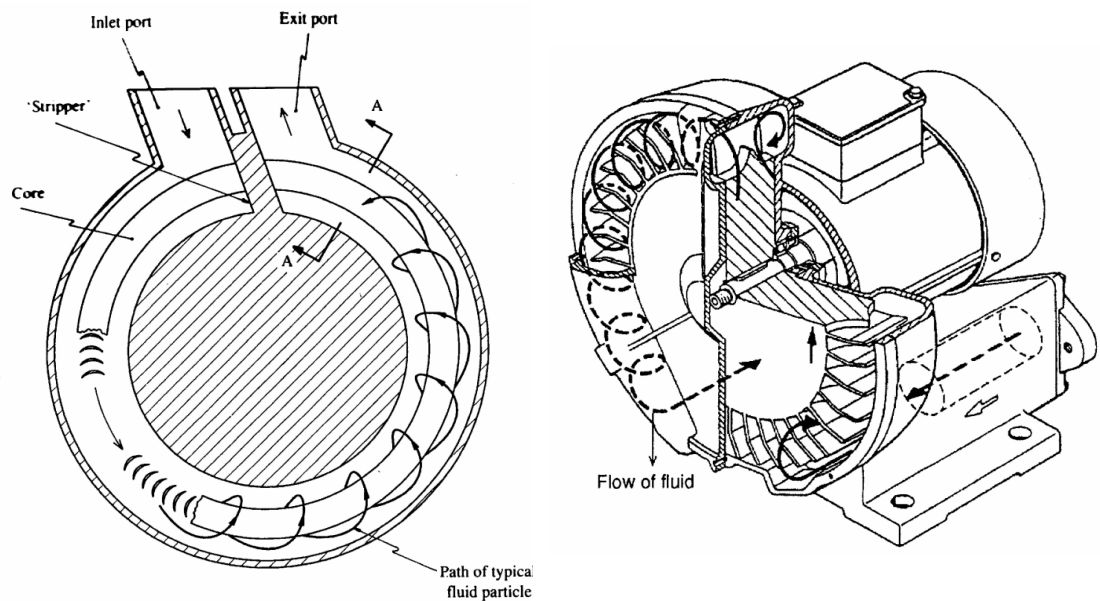


Figure 19: Flow path in a Regenerative Compressor (Song, et al., 2003)

The work on these compressors was experimental performance testing. Since Vine's thesis was published, further work on the wedge type compressor has been published (Tanaka, et al., 2008). An optimisation was performed on the impeller design, CFD simulations were computed and these were compared to experimental measurements. The optimisation resulted in a six percentage point improvement in efficiency and a wider operating map. No data was presented on the internal flow field of the wedge type compressor.

Flow field measurements have been made on the Barske type impeller (Choi, et al., 2006). However, these were made with the impeller being used as a liquid pump rather than a gas compressor. Three optical methods were employed: a two-component LDV measurement system, two-component Particle Image Velocimetry (PIV) and two-dimensional Particle Tracking Velocimetry (PTV). These measurements showed complex secondary flow patterns within the impeller. The measurements also showed a considerable slip factor and that the flow is asymmetric to the impeller axis.

LDV measurements have been conducted on another low specific speed centrifugal pump impeller. The impeller, a two dimensional, backward swept design, is of a type used as an aircraft fuel pump (Abramian, et al., 1994). LDV measurements were taken at design flow rate and 50% design flow rate. The measurements at off-design conditions shows a flow separation at the pressure side of the impeller blades which reattaches by

the exit. Also, under off design conditions, the volute induces periodic unsteadiness at the blade passing frequency.

The regenerative compressor is an example of a commercially available low specific speed compressor. As such, more work has been done trying to understand the flow within the compressor in a quest to improve performance. All this work has focuses on numerical methods rather than direct measurement of the flow, some using commercially available code Quail, et al., 2009, Nejadrajabali, et al., 2016 and Insinna, et al., 2018. Others wrote their own code such as Griffini, et al., 2015 and Song, et al., 2003.

The literature survey has shown that while research has improved the knowledge of low specific speed compressors since Vine's original survey, direct measurement of the flowfield within low specific speed machines has focused on pumps rather than compressors, while CFD has been primarily used on the compressors. The survey has shown how optical measurements can identify areas of flow unsteadiness, recirculation and pulsation within low specific speed compressors. No new designs for low specific speed compressors have been found in the literature. Also, no references to compressors with forward swept blades have been found. The next section will assess the published work on the TurboClaw compressor.

2.2. TurboClaw Research

To date, four patents, seven papers and two PhD theses' have been published. The PhD theses' concern the design, initial testing and computational simulations of the first compressor in a single stage (Vine, 2005) and in a multistage configuration (Thornton, 2005).

Vine's thesis documents the work going into the initial design of the compressor, the initial design constraints such as windage being 2.5% of the total work input and the specification of a pressure ratio of 1.6 at 20,000 rpm. The test rig for the compressor is described along with the performance data and error analysis. The test set up was designed to use a torque sensor to measure the shaft power being transmitted to the compressor. However, the torque sensor chosen proved to be unreliable resulting in no reliable measurements being taken. This resulted in efficiency measurements being calculated using the energy balance method. This method is not nearly as accurate as

direct measurement resulting in calculated efficiency errors of $\pm 3\%$ at 20,000 rpm. Vine himself states in his conclusions that *“The measurement of torque at this speed is considered technically feasible and should be attempted in future with a torque meter from a different manufacturer.”*

Vine also dedicated some time to modelling the compressor using CFD. A steady state model was developed to investigate the internal flow field of the compressor. However, due to limited computer resources at the time, the solution was neither mesh independent and nor did it conserve mass. This completely invalidated any results from the simulation.

Thornton’s thesis (Thornton, 2005) was concerned with multistaging the very low flow rate TurboClaw compressor to produce a machine that could develop a higher overall pressure ratio that could not be managed by a single stage. A computer simulation methodology was developed to predict the performance of the overall machine, taking into account the single stage performance of the compressor as well as windage losses, seal leakage and off-design performance. A test rig was built to validate the computer simulation. However, the single stage pressure ratio was less than predicted leading to mismatched stages and poor performance overall.

Both these works focus on the overall performance of the compressor, either in single or multistage form. Thornton attempted to predict the performance of the compressor with little success, he predicted a single stage pressure ratio of 1.58 but only achieved 1.38, a difference of 34.5%. This was due to poor matching of the stages. The added challenge was the small volume flow rate which meant his first stage had a diameter one third of Vines.

The papers contain two types of information: experimental test data and the use of the compressor in automotive and industrial applications. Vine, et al., 2005 presents data for the single stage compressor developed by Vine for his PhD work (Vine, 2005) and data from the multistage compressor developed by Thornton for his PhD (Thornton, 2005). Limited data is presented for a specific operating point required for the fuel cell application discussed in the paper. Computational Fluid Dynamic, CFD, simulations are said to have been used and validated but no data is presented, or references given to back up this claim.

Pullen, et al., 2009 falls into the latter category, aimed at showing how the compressor can be applied to the fuel cell industry as part of an air management system. While the paper contains some details around specific speed the experimental detail is extremely limited, with only the most basic compressor map included.

Pullen, et al., and Pullen, et al., 2012 both deal with the application of engine downsizing by using an electrically driven supercharger using a Turboclaw compressor. These papers present the same, hardware-in-the-loop test data. Hardware-in-the-loop simulations combine a virtual vehicle with the hardware to be tested, in this case the electrically driven supercharger. All the data presented in these papers only refers to the performance of the compressor within the vehicle and comparisons to normally aspirated or turbocharged vehicles therefore the data cannot be used to understand the compressor in isolation.

Pullen, et al., 2012 does present some experimental data. The majority of the paper is spent explaining industrial applications and the needs for a low specific speed compressor. However, there is detail of tests on a prototype compressor fitted to a direct drive torque meter allowing accurate measurements of efficiency. This paper also describes the test rig built for this research but not the results which were unavailable at the time.

Parra, et al., 2015 builds on the test rig presented in the paper above. Whilst detailing a test rig, Figure 20, used for performance measurements, this paper presents results of these tests at atmospheric conditions showing a peak efficiency of 59.4%. This paper also shows how parasitic losses within the test rig – bearings and diaphragm couplings – have been accounted for to allow measurement of the true compressor efficiency. This paper summarises the experimental work that was carried out at Dynamic Boosting Systems by this author during this research. This work was very helpful in guide the design of the new test rig described in Chapter 7.

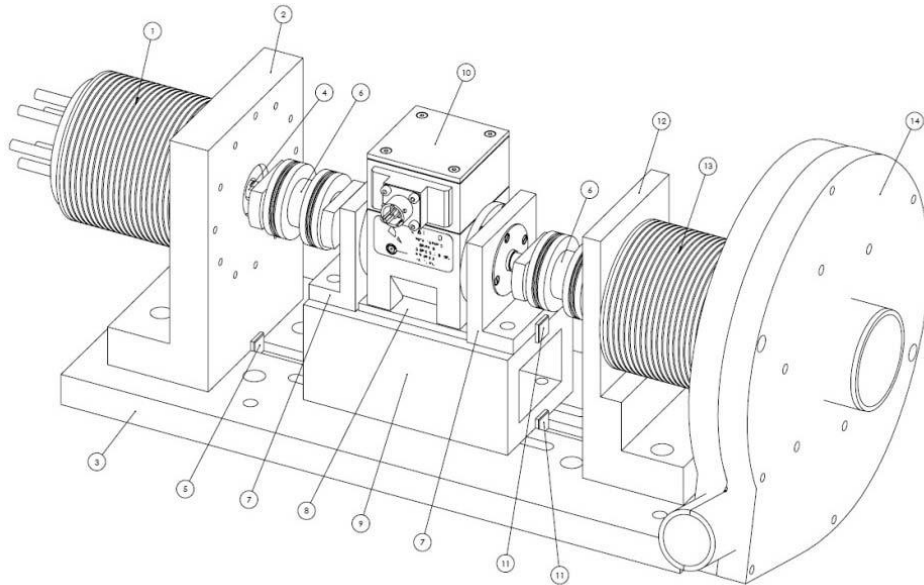


Figure 20: Torque meter test rig (Parra, et al., 2015)

The final paper, Arjeneh, et al., 2013 presents the results of running a TurboClaw compressor as an expander. The testing presented is turbine maps based on energy balance. As this work is specific to a turbine it is not relevant here.

Various CFD based analyses were attempted but the results were of limited value due to the questionable validity. The following gaps in knowledge were identified.

- High quality performance measurements on a number of geometries and inlet conditions. The effect of machine dimensions and gas conditions was known to be important due to changes in Reynolds number and other factors.
- Flow field measurements. No work had been done in this area.
- High quality CFD analysis. Given the difficulty of analysis of a highly transient flow, which later became evident from the experiments, it was decided to leave this line of inquiry to other researchers. The experimental work undertaken in the research is considered essential and a prerequisite to undertaking CFD in any case.

As the papers described above show, only minimal data has been presented on the TurboClaw compressor consisting of experimentally measured compressor maps. The following section will give an overview of the techniques available to qualitatively and quantitatively measure the flow within the diffuser closing this gap in knowledge.

2.3. Flow Field Investigative Techniques

Techniques for measuring flow fields can be split into two categories; invasive and non-invasive measurements. For this work, invasive measurement techniques, such as hot wire anemometry or direct total pressure measurement were discounted as it would be very difficult to separate the disturbances caused by the probes from the natural behaviour of the compressor flow. This is due to the small passage sizes and could only be avoided if a very large diameter machine was produced. From the publications described, experimental performance maps were available for a machine with a 210 mm diameter rotor, with atmospheric inlet conditions but questionable accuracy.

The benefits and limitations of the non-invasive measurement techniques are described below.

2.3.1. Schlieren Photography

This is a process that allows the photographing of fluids of varying density. A collimated light source shines on the target and density gradients in the fluid cause variations in the refractive index which distort the collimated light. Generally, this is a technique used in supersonic compressors where there are large changes in density within the flow field so it was considered inappropriate for this work. [Saito, et al., 1985, Verdonk, 1978, Bell, et al., 1995].

2.3.2. Laser Doppler Velocimetry, LDV

LDV is a technique that can measure the velocity of particles suspended in a flow, at a single point within the flow. The particles must be small enough to follow the flow, but not so small that the LDV equipment cannot measure them. LDV also requires that the medium in which the particles are suspended is transparent, and that transparent windows be present to allow optical access to the flow field.

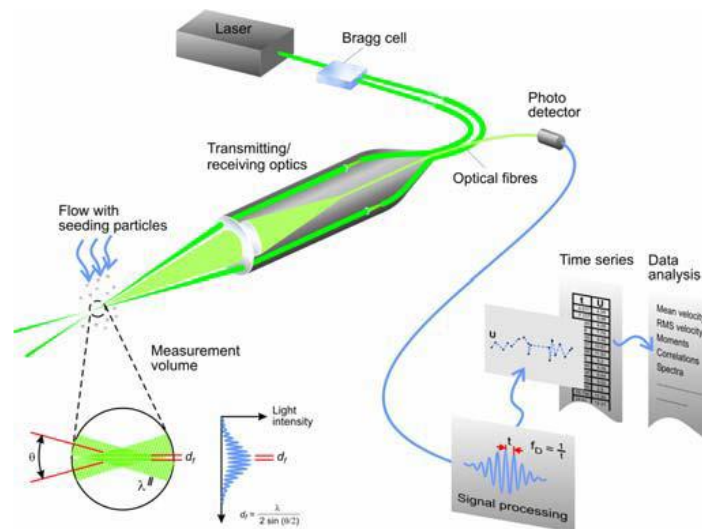


Figure 21: LDA schematic (Jensen, 2004)

LDV systems do not require calibration due to the stability and linearity of optical electromagnetic waves. The optics of a LDV system allow the generation of a small control volume giving good spatial resolution. The fast processing ability of modern electronics gives LDV very good temporal resolution allowing measurement of highly fluctuating flows. If multi-component systems are available, two or three axis of measurement can be made simultaneously (Jensen, 2004). LDV systems have been used extensively to measure the internal flow field of compressors for example Ubaldi, et al., 1997, Ibaraki, 1998, Stahlecker, et al., 1998 and Ibaraki, 2009.

2.3.3. Phase Doppler Particle Analysis, PDPA

PDPA is based upon the same technology as LDV, however, PDPA also includes information on the size of the particles. This information is particularly useful where the “seed” particles are actually part of the normal flow, such as a compressor operating in a wet compression mode (Schnitzler, et al., 2014) but which is not needed in this case.

2.3.4. Particle Image Velocimetry, PIV

Similar to LDV, PIV is a technique that measures velocities within a flow. Unlike LDV, PIV is able to measure an entire flow field simultaneously. A pulsed laser sheet is projected into the flow and a camera takes a picture synchronised to the laser. A brief time later a second picture is taken with a second laser pulse and from these two images velocity can be calculated.

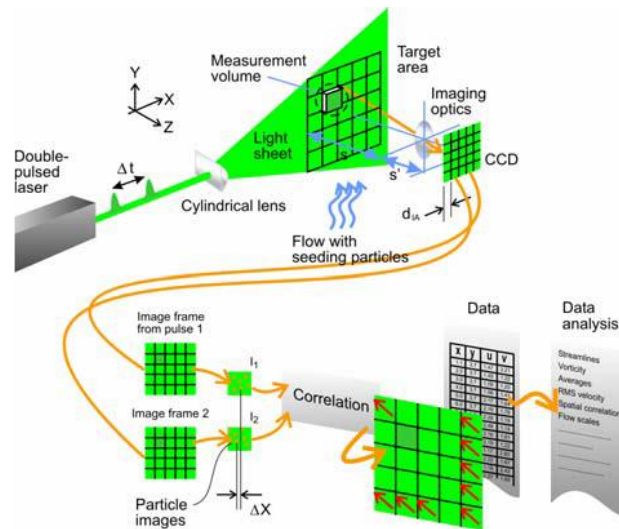


Figure 22: PIV schematic (Jensen, 2004)

PIV requires optical access for the camera and the laser sheet which must run perpendicularly to the camera. Using two cameras allows a technique known as Stereoscopic PIV, making velocity measurement in 3 dimensions possible. PIV has also been used extensively in compressor research for example Cukurel, et al., 2010, Wernet, 1998 and Cukurel, et al., 2008.

2.3.5. Planar Laser Induced Fluorescence, PLIF

PLIF is an extension of PIV, whereby the seed particles fluoresce under the laser light. A dedicated PLIF camera captures the fluorescence which can be converted into scalar properties such as temperature or concentration. PLIF's main applications are combustion, mass and heat flux measurements, contaminant transport and mixing processes. (TSI, 2018).

Due to the added complexity of projecting a laser sheet into the compressor, PIV and PLIF techniques have been rejected. Schlieren photography requires large changes in density which are unlikely in a low specific speed compressor. The technique chosen to gain quantitative measurements of the flow field was LDV. The additional information gained by PDPA on particle size is of no benefit as the particles will not be present during normal operation. LDV and the specifics of the test set up for this work are described in Chapter 3.

3. Methodologies used in this work

It was decided to use two non-invasive methods to investigate the flow field within the diffuser. Firstly using a high-speed camera to obtain a qualitative understanding of the major flow characteristics – such as whether pulsating flow was present, and whether any areas of recirculation could be seen. Then use Laser Doppler Velocimetry, LDV, to obtain quantitative measurements of the flow using the photography to guide the set up.

3.1.1. High-Speed Camera Requirements

City University London were able to provide a Photron Fastcam APX RS high speed camera, a 400W stage light and a DJ smoke machine to obtain the qualitative measurements. To enable the flow to be imaged in either a forward or backscatter arrangement, provision for optical access from both sides is required in the test compressor.

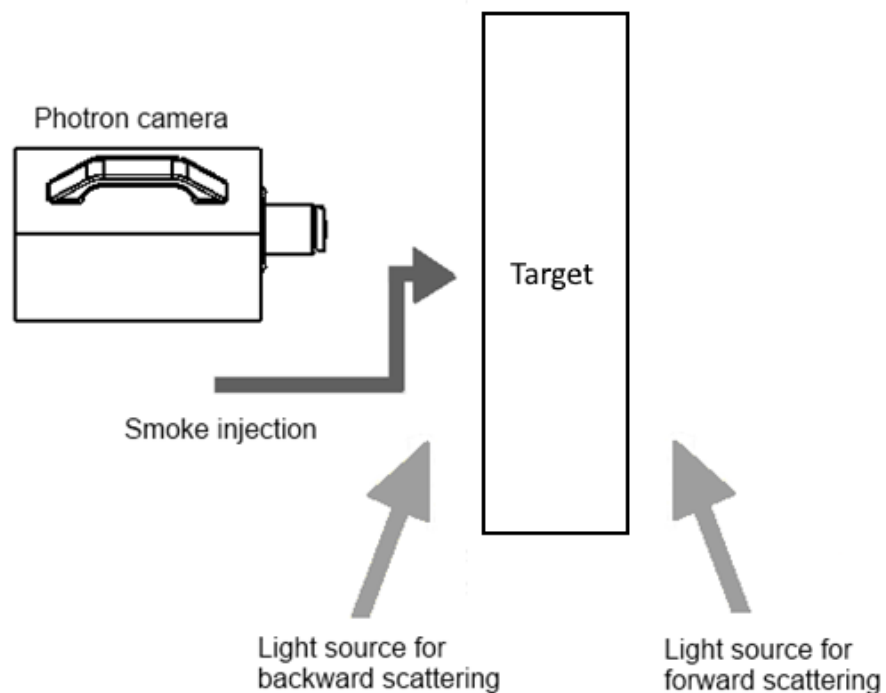


Figure 23: High speed camera setup

In forward scattering the light is diffracted by the smoke particles into the camera's lens, in backscatter the light is reflected as shown in Figure 24.

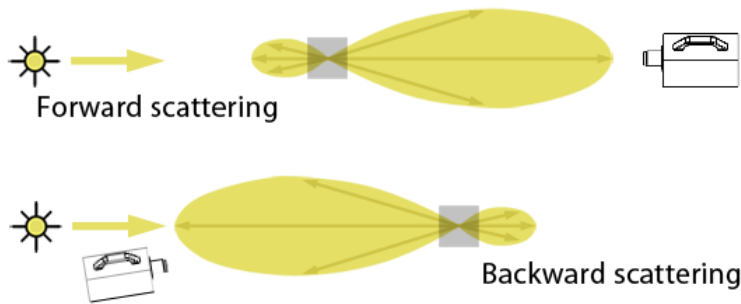


Figure 24: Light scattering techniques

It was decided to focus on 4 specific areas of the diffuser with the high-speed camera as shown in Figure 25. This will require optical access across the whole diffuser, making creating optical access with windows a challenge. A simpler prospect would be to make the whole diffuser out of an optically transparent material.

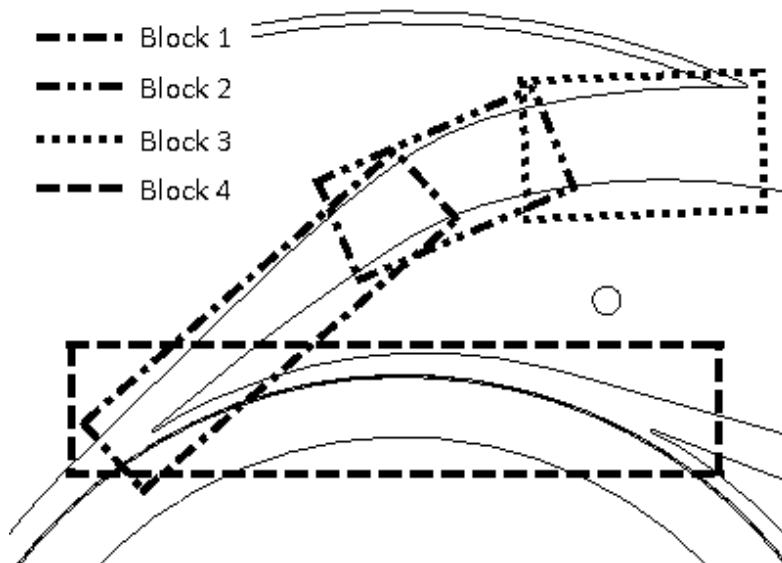


Figure 25: Flow Visualisation Areas

Therefore, the high-speed camera tests required full optical access, both front and back to the diffuser passage. Also, a way to input smoke from the machine into the passage, and space around the compressor to position the camera and light equipment to get the best field of view to take the images.

3.1.1. High Speed Camera Set Up

The arrangement of the camera, light source and smoke injection is shown in Figure 26. The camera was held on a tripod that allowed it to be adjusted in all directions as well as being able to rotate about the lens axis.

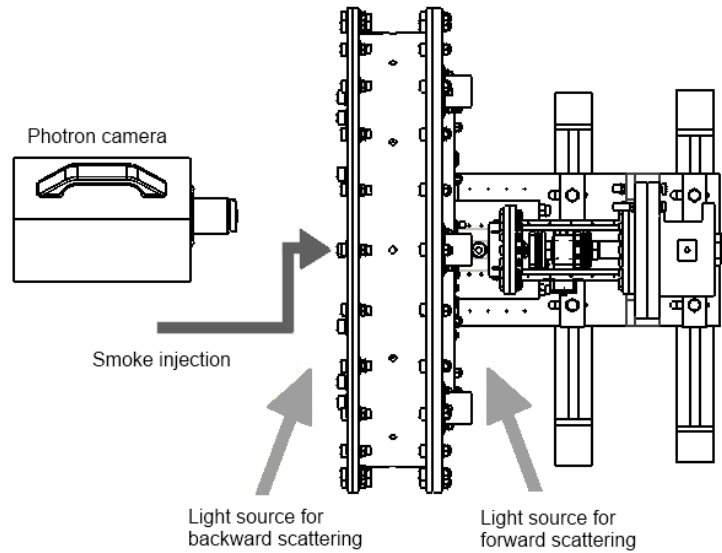


Figure 26: High speed camera setup

The smoke was injected using a 1.5" flexible hose into one portion of the compressor inlet. The smoke couldn't be injected across the whole inlet as the volume produced was too low resulting in too low a density in the area being investigated.

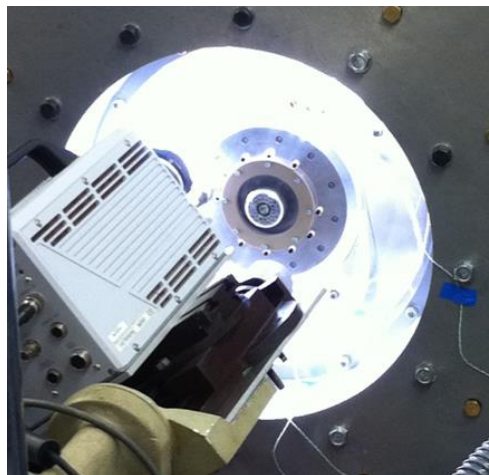


Figure 27: Camera and light source set up – picture captured from behind the high-speed camera looking at the Perspex diffuser lit from behind

3.1.2. High-Speed Camera Image Processing

The images captured by the high-speed camera are difficult to view, therefore several processing steps are required. First, prior to injecting any smoke into the test rig, 50 frames were captured. These images were averaged using Matlab to produce a “background” image. This image was subtracted from all smoke images to remove any areas of brightness in the images that wasn’t from the smoke. Figure 28, Figure 29 and Figure 30 show this process, the red circle highlights the area of brightness at the leading edge of the diffuser.



Figure 28: Background image – average of 50 photos taken with no smoke injection

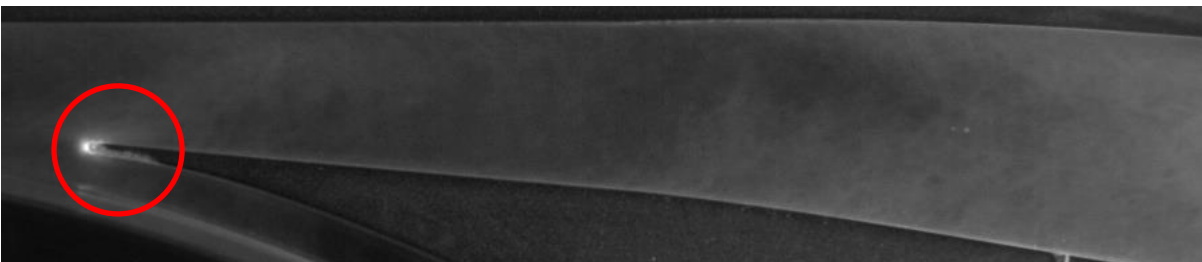


Figure 29: High speed camera image as captured

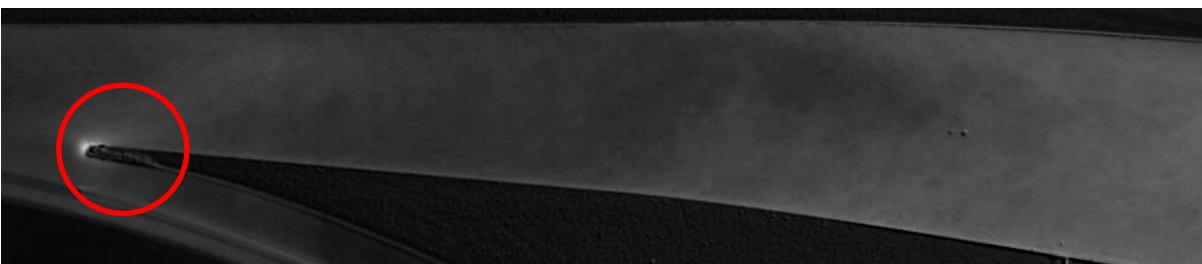


Figure 30: High speed camera image with background removed

The next step was to brighten the images so the detail was more easily seen. One image was chosen and the average intensity at a low and high point were calculated. The image was brightened with a simple multiplication of the intensity to make it easier to identify the high and low areas, Figure 31. These were then set as the low and high bounds for the measured intensity, and a scaling was created to lower the minimum intensity to 0 and increase the maximum to 255. This scaling was then applied to all images.

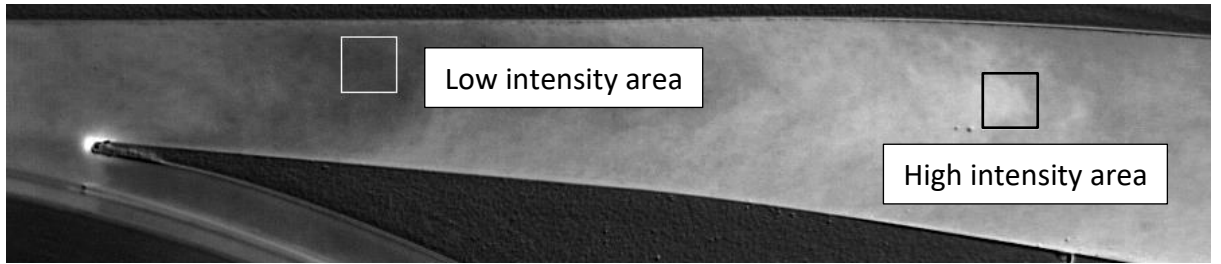


Figure 31: Image used to identify low and high intensity values

The Matlab code used to complete all the image processing is shown in Section 12 Appendix: Matlab programmes.

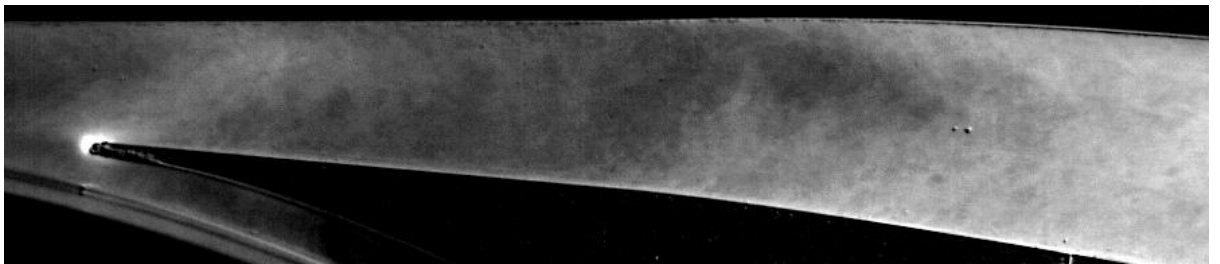


Figure 32: Image brightened to highlight the smoke intensity

Alternately, a colourmap was applied to the image with the background removed. This intensity of the pixel to a colour scale ranging from blue (lowest intensity) to red (highest intensity).

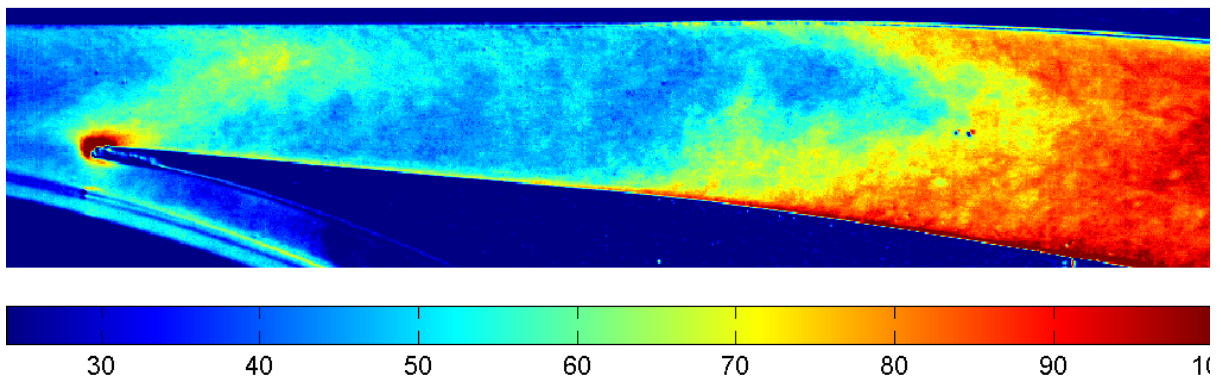


Figure 33: Image with colourmap applied

Chapter 5 shows the results of the high-speed photography.

3.1.3. Laser Doppler Velocimetry Theory

Laser Doppler Velocimetry, LDV, is a technique that allows non-invasive measurements of the flow velocity at a single point. The technique was first demonstrated by Yeh and Cummins in 1964 (Yeh, et al., 1964) in water, followed soon after in gases. It has been used extensively in rotating machinery research for example Ubaldi et al. (Ubaldi, et al.,

1998) used LDV to investigate the interaction between a simplified centrifugal compressor and its vaneless diffuser, Heckaman (Heckaman, 2014) designed optical access within an existing compressor to study the flow within the impeller and diffuser of a low specific speed centrifugal compressor and Arcoumanis et al. (Arcoumanis, et al., 1997) used LDV to quantify the exit flow from two mixed-flow turbines.

The technique works by measuring the Doppler frequency shift of laser light that has been scattered by seed particles, such as smoke, in the flow. In the differential Doppler technique, the laser beam is split into 2 equal intensity beams, both of Gaussian distribution. These are focused so they cross forming a control volume (see Figure 35). Interference fringes form in this control volume which illuminate passing particles. The distance between the fringes can be calculated and consequently the frequency of the pulses of light reflected by particles relates directly to their velocity.

The dimensions of the control volume can be calculated using the following equations:

$$\delta_z = \frac{r_0}{\sin(\alpha/2)} \quad \text{Equation 10}$$

$$\delta_x = \frac{r_0}{\cos(\alpha/2)} \quad \text{Equation 11}$$

$$\delta_y = r_0 \quad \text{Equation 12}$$

$$r_0 = \frac{F\lambda}{\pi R_0} \quad \text{Equation 13}$$

Where F is the focal length of the transmitting optics, λ is the wavelength of the light, for a Gaussian distribution R_0 is the distance from the centre where the intensity is reduced to $1/e^2$ of its maximum value and α is the beam crossing angle. The spacing, s , of the interference fringes is given by Equation 14.

$$s = \frac{\lambda}{2 \sin(\alpha/2)} \quad \text{Equation 14}$$

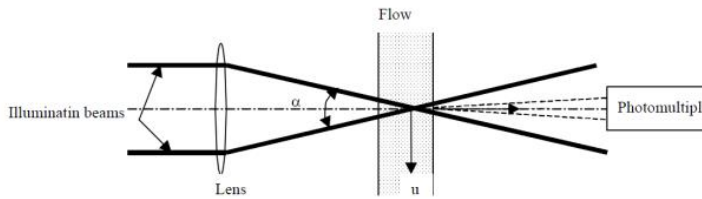


Figure 34: LDV Schematic

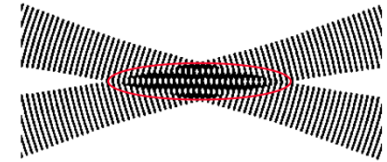


Figure 35: Interference bands of crossing laser beam

When a particle crossed the control volume with velocity v normal to the fringe plane, it will experience a light intensity modulation at a frequency, f , given by Equation 15.

$$f = \left| \frac{2v \sin(\alpha/2)}{\lambda} \right| \quad \text{Equation 15}$$

By measuring the frequency using a photomultiplier, the velocity of the particles normal to the fringes can be calculated. This technique can only measure the absolute velocity, it cannot distinguish between particles travelling in opposite directions at the same speed. For this reason, a frequency shift is applied using a Bragg cell leading to Equation 16.

$$f_D = \left| f_0 + \frac{2v \sin(\alpha/2)}{\lambda} \right| \quad \text{Equation 16}$$

So long as the frequency shift is greater than the largest negative velocity all particle speeds and directions can be measured.

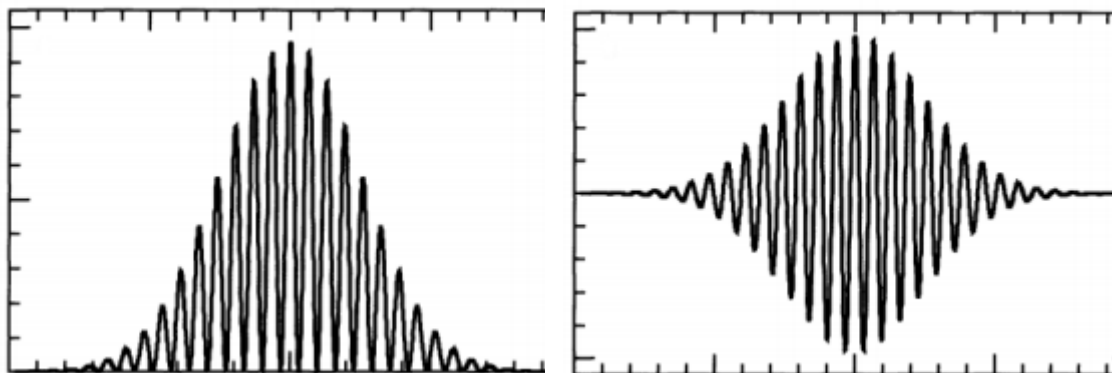


Figure 36: Doppler burst (a) as measured and (b) with DC component removed.

The signal captured by the photomultiplier will be similar to that shown in Figure 36(a). A computer processor removes the DC component of the signal leaving the signal shown in Figure 36(b).

A problem intrinsic to LDV is that larger particles reflect more light than smaller ones. Hence larger particles produce Doppler bursts with higher signal to noise ratio. All LDV signal processors have algorithms designed to reject signals of poor signal to noise ratio. As a result, LDV measurements tend to be biased towards the velocities of larger particles in a flow. This is undesirable if very high speed or highly turbulent flows are being measured as the velocities of large particles are unlikely to match that of the flow (Melling, 1997).

The test compressor requirements for the LDV measurements are very similar to the requirements for the high-speed camera testing. The only major addition is that the optical material used to make either the window or the whole diffuser must have a light transmission of at least 92% and a refractive index of as close to 1 as possible. This is to reduce the aberration caused by the beam passing through the material, altering the focusing point of the beams (Drain, 1980). Depending upon the results from the high-speed photography, if the flow is shown to pulse an encoder will be required to allow measurements to be synchronised to the rotation of the impeller.

3.1.4. Laser Doppler Velocimetry Set Up

LDV testing equipment was supplied by both City University London and the EPSRC equipment pool. A Coherent Innova 90 Argon-ion laser was used, it emitted a beam with a wavelength of 514.5 nm. This was directed through a TSI FB-2 Fibrelight Multicolour Beam Generator which splits the beam into 2 and applied a 40 MHz shift frequency to one of the beams. A fibre optic cable transmitted the 2 beams to a TSI TR260 Transceiver probe. The TR260 was mounted vertically on a traverse with x, y, z movement. Three Mitutoyo Digimatic indicators, with a resolution of 0.01mm, each with 50mm of travel, were used to measure the position of the beam within the diffuser. A 76.2mm diameter Zerodur Laser Line Dielectric Mirror was mounted below using a precision clear edge mirror mount at 45 degrees to direct the beams in to the diffuser.

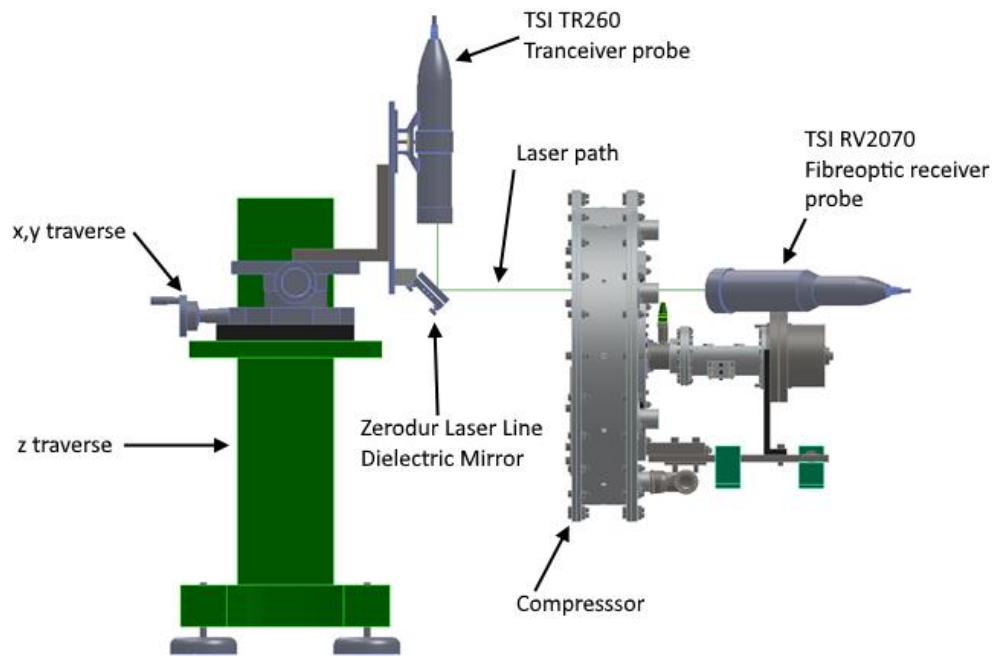


Figure 37: Side view of laser setup

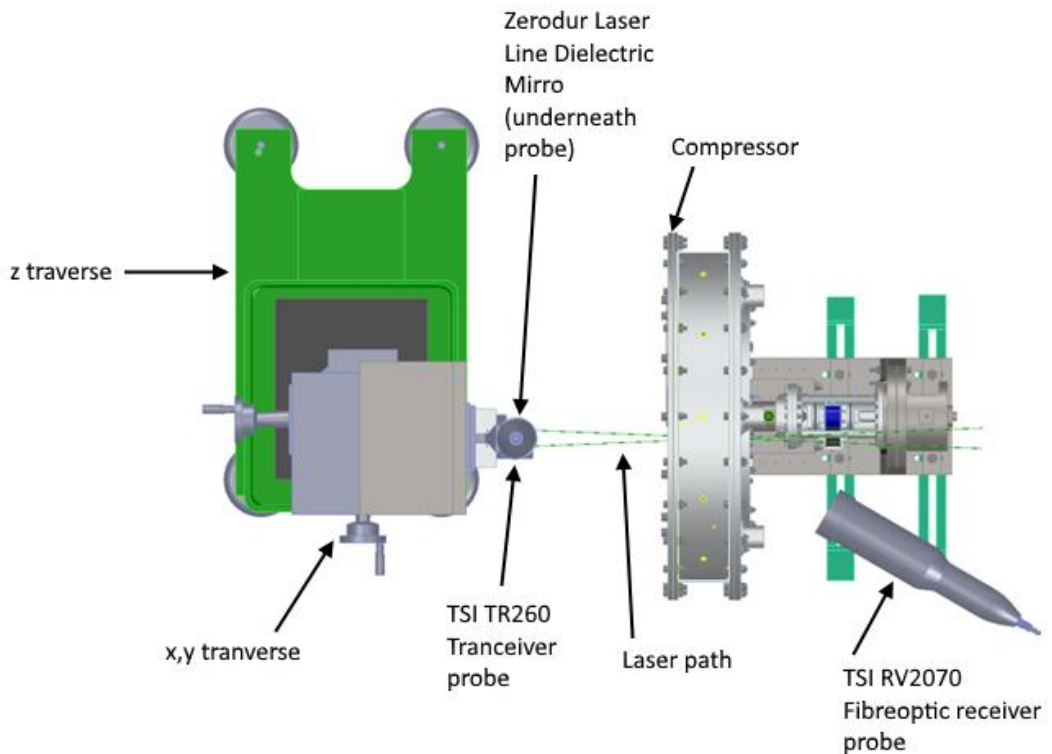


Figure 38: Top view of laser setup

A Norgren 3041-3S Lubricator was used to atomise silicone oil into the flow. A filter silencer ensured that clean air was drawn into the compressor, a pipe cross with one entry blocked was used to mix the clean air and atomised silicone oil before being drawn into the compressor. The typical seed particle diameter is of the order of 3 microns.

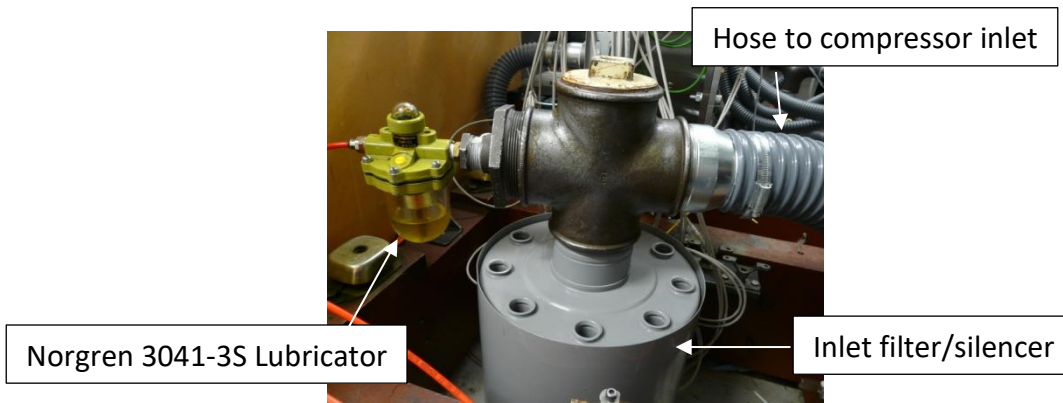


Figure 39: Silicone oil atomiser for LDV seeding

The scattered light was collected by a TSI RV2070 Fibreoptic receiver probe fitted with a 500 mm focal length lens. This was transmitted to a PDM1000 detector module and into a TSI FSA4000-2P signal processor that was fitted with an encoder module. A 1 pulse per revolution signal was sent from the compressor to provide a rotational position for the measurements. The data was analysed using TSI Flowsizer software.

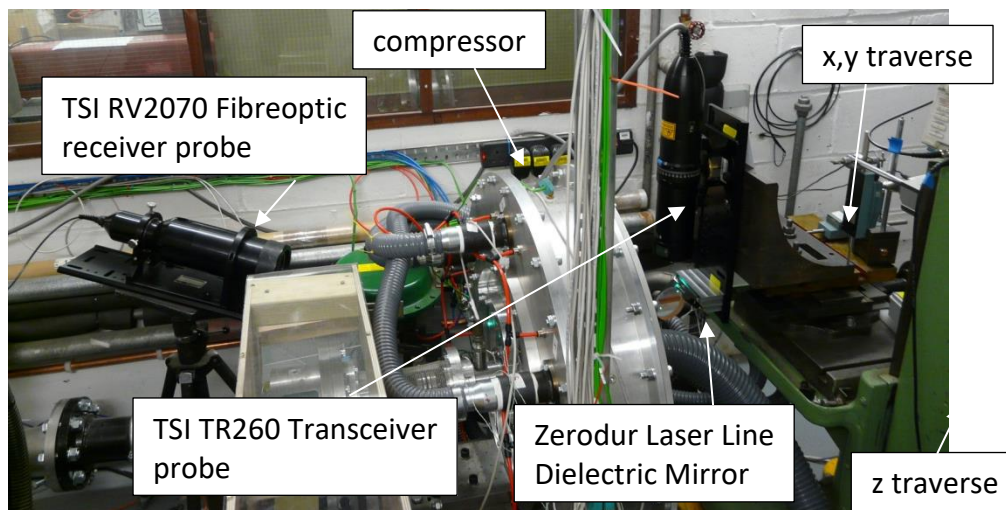


Figure 40: Experimental setup for LDV measurements

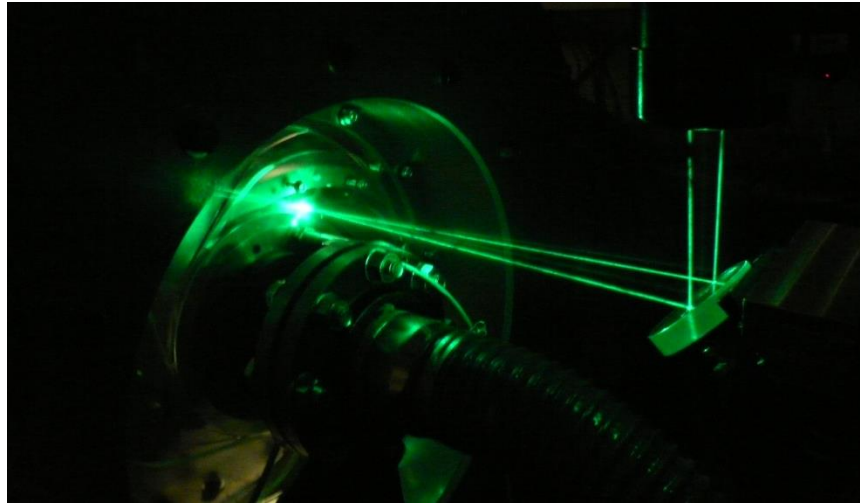


Figure 41: Laser entering rig during LDV measurements

To provide a repeatable and accurate zero point for the measurements, the crossing point of the beams was aligned on the leading edge of the measured diffuser blade, at the surface on the inside of the passage. The digital indicators were zeroed and then the control volume could be positioned for measurement. The beam diameter in these experiments was 2.65 mm with a separation of 50 mm. The focal length of the lens in the transmitting optics was 512.3 mm and the laser emitted light at 514.5 nm (green). This gave a beam waist of 126.6 μm , an angle of 5.59 degrees and fringe spacing of 5.28 μm . The control volume size was 63.3 μm x 67.3 μm x 1.30 mm. A 150 μm pin hole in the receiving optics reduced the size of the control volume to 63.3 x 67.3 x 150 μm .

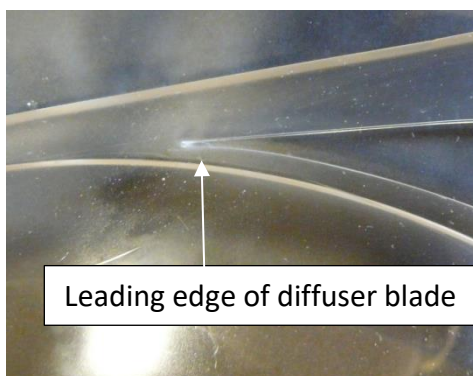


Figure 42: Blade leading edge used for "zero" point of LDV measurements

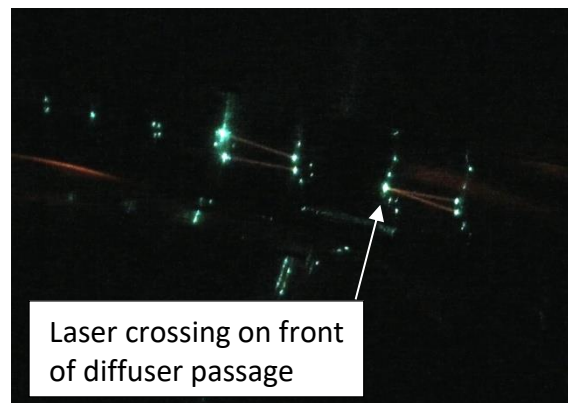


Figure 43: Beam crossing on "zero" point for LDV measurements

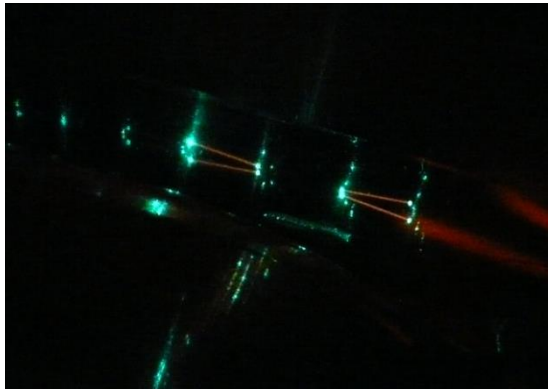


Figure 44: Control volume within passage of LDV measurements

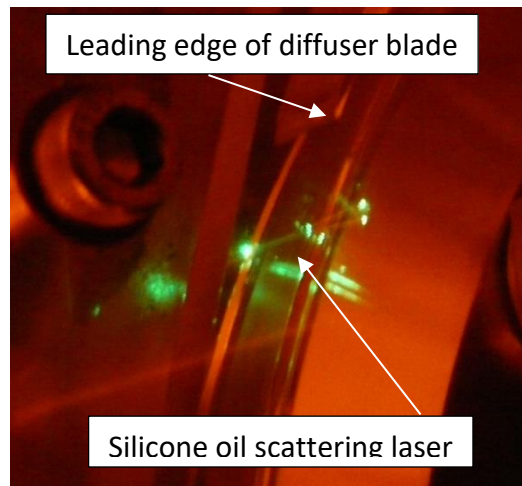


Figure 45: Silicone oil scattering laser light in passage during LDV measurements

The signal processor applies a band pass filter to the collected data to remove the DC component of the signal and high frequency noise. When the flow velocity was greater than 30 m/s, a band pass of 5-30 MHz was chosen, otherwise 2-20 MHz was used. The Bragg cell in the Fibrelight Multicolour Beam Generator causes 40 MHz to be applied to the Doppler frequency of each burst, allowing flow reversals to be measured. Down-mixing removes some of this added frequency to allow the use of the narrowest band pass filter. The down-mix applied was 31 MHz in the vertical direction and 34 MHz in the horizontal. The Photomultiplier (PMT) Voltage parameter sets the voltage that is applied to the PMT. Increasing the voltage increases the gain in the PMT, increasing the signal and the noise. The PMT voltage was set at 550 V for all points measured. The burst threshold is a voltage level that a signal must reach before the processor identifies it as a Doppler burst, this was set at 200 mV for all experiments.

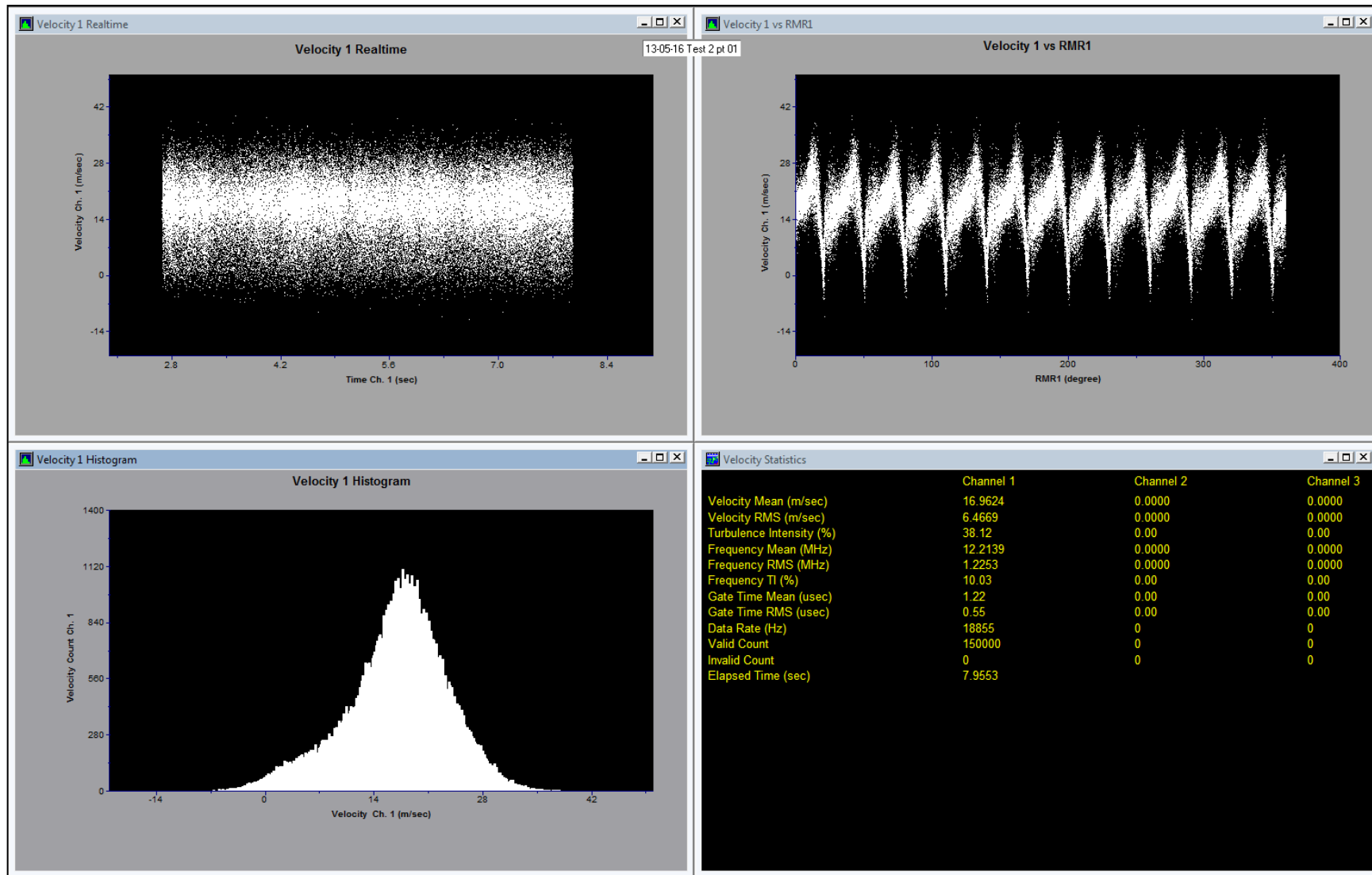


Figure 46: Screenshot from the Flowsizer software used to display the results of the LDV testing

A shaft encoder supplied rotor position information to the signal processor by means of 1 pulse per revolution signal. The signal processor generated 3,600 pulses per revolution and uses the 1 pulse per revolution encoder signal to synchronise. A tolerance can be set to ensure that the shaft speed is stable. For this experiment that was set at 0.3 degrees so for each revolution so long as the processor pulses were between 3,597 and 3,603 per revolution that was considered in tolerance. Any data collected outside of this was marked as out of tolerance by the processor and was discarded. To ensure enough data was collected, 150,000 samples were collected at each measured point. Initial testing showed that approximately 40,000 of the samples would be marked out of tolerance leaving 110,000 valid measurements. If these measurements were averaged over 0.5 degree segments within the axisymmetric part of the impeller (30 degrees) that would give over 1,800 measurements per position per degree, which is more than adequate. Figure 46 shows an example of the output from Flowsizer once a point has been measured.

The top left window of Figure 46, labelled Velocity 1 Realtime, shows the Doppler burst captures against the time they were taken. It can be seen the capture took 7.95 seconds to collect all 150,000 samples. The top right window of Figure 46, labelled Velocity 1 vs RMR1, shows the Doppler burst plotted against the rotor position. This plot clearly shows the pulsing nature of the compressor and confirms what was seen in the flow visualisation. The bottom left window of Figure 46, labelled Velocity 1 Histogram, shows that the data follows a normal distribution which implies that the seed particles are evenly sized and there is minimal biasing in the sample. The bottom right window of Figure 46, labelled Velocity Statistics, gives overall mean velocity and rms, frequency mean and rms, gate time and data rate.

It is noted however that the Perspex diffuser showed very high 12x vibration (blade passing frequency). This limited the speed at which the compressor could operate at for these tests. For the LDV the compressor was spun at 4,000 rpm with a pressure ratio of 1.010 at a mass flow rate of 23.3 g/s. This condition was chosen as it was close enough to surge for the compressor to be generating a pressure ratio, but not so close that and surge induced instability, such as flow reversals, would affect the results.

3.1.5. Errors in LDV Measurements

A number of sources can cause errors in the LDV measurement. These range from optical misalignment, to velocity biasing due to higher velocity particles being sampled more than lower velocity ones. A detailed uncertainty analysis is presented in (Martin, et al., 2000) covering uncertainties due to measurement, calibration, data reduction and sources of frequency bias. These are; Fringe bias, See particle bias, velocity bias and velocity gradient bias. The experiment will be set up to reduce these errors to the minimum possible.

4. Optical Access Test Rig

This chapter will present the design of the large scale optical test rig that will be used to gather data on the forward swept compressor. It will show the reasons for designing a new test rig, the design considerations and the analysis used to engineer the test rig. The instrumentation that will be used to gather the data is described here along with the performance testing of the compressor – pressure ratio, mass flow rate and efficiency measurements, along with the error analysis.

4.1. Previous Setup

In order to undertake the flow visualisation and Laser Doppler Velocimetry experiments detailed in Chapter 3, it was decided that a purpose-built test rig was required. During Vine's research he designed and built a test rig to measure the performance of the compressor, Figure 47. This rig included pressure, temperature and flow measurement sensors. It also included a torque sensor to measure the power transmitted from the motor to the compressor. This test rig was available at the start of this work; however, it was decided not to use for the following reasons:

- Windows would need to be cut in four thick pieces of metal, three in the casing and one in the diffuser, the thickest 22 mm, per viewing area and the diffuser walls replaced with Plexiglas. A minimum of three viewing areas are planned for the flow visualisation and LDV studies requiring nine windows. These windows would need to be aligned precisely on the flow side so as to not disturb the flow which was considered impractical.
- Since Vine's rig has a high thermal mass, requiring a very long time for temperature equalisation to occur, extra time would need to be allocated for all compressor testing.
- The rig was previously connected to a 30 kW, 3,000 rpm electric motor and the belt and pulley system was designed for this configuration. This gave a maximum compressor speed of 20,000 rpm. On the motor available in the City University test cell this speed would be 16,700 rpm restricting the maximum pressure ratio to 1.3.
- The torque sensor purchased during the previous research was found to be defective, it was unable to correctly measure the torque of a rotating shaft. A

new high accuracy torque meter has been procured and this will require a re-design of the housing to fit the new sensor.

- The bearings that support the compressor shaft were visually inspected and found to be worn due to use in the rig. The bearing grease contained dirt and grit from being stored since 2004 therefore new bearings would be required.
- The compressor shaft was measured and found to be bent from either poor manufacturing or handling. This would need to be remade.
- The impeller shroud was poorly manufactured, a hole in the shroud was drilled in the wrong place, meaning the whole shroud would need to be remade.
- Holes would have to be drilled through the diffuser blades to allow smoke to be fed into the passages for flow visualisation with high speed cameras and placed for these holes were limited.

With this number of parts to modify/remake it was decided to redesign the rig to include a number of improved features enhancing test rig robustness and functionality.

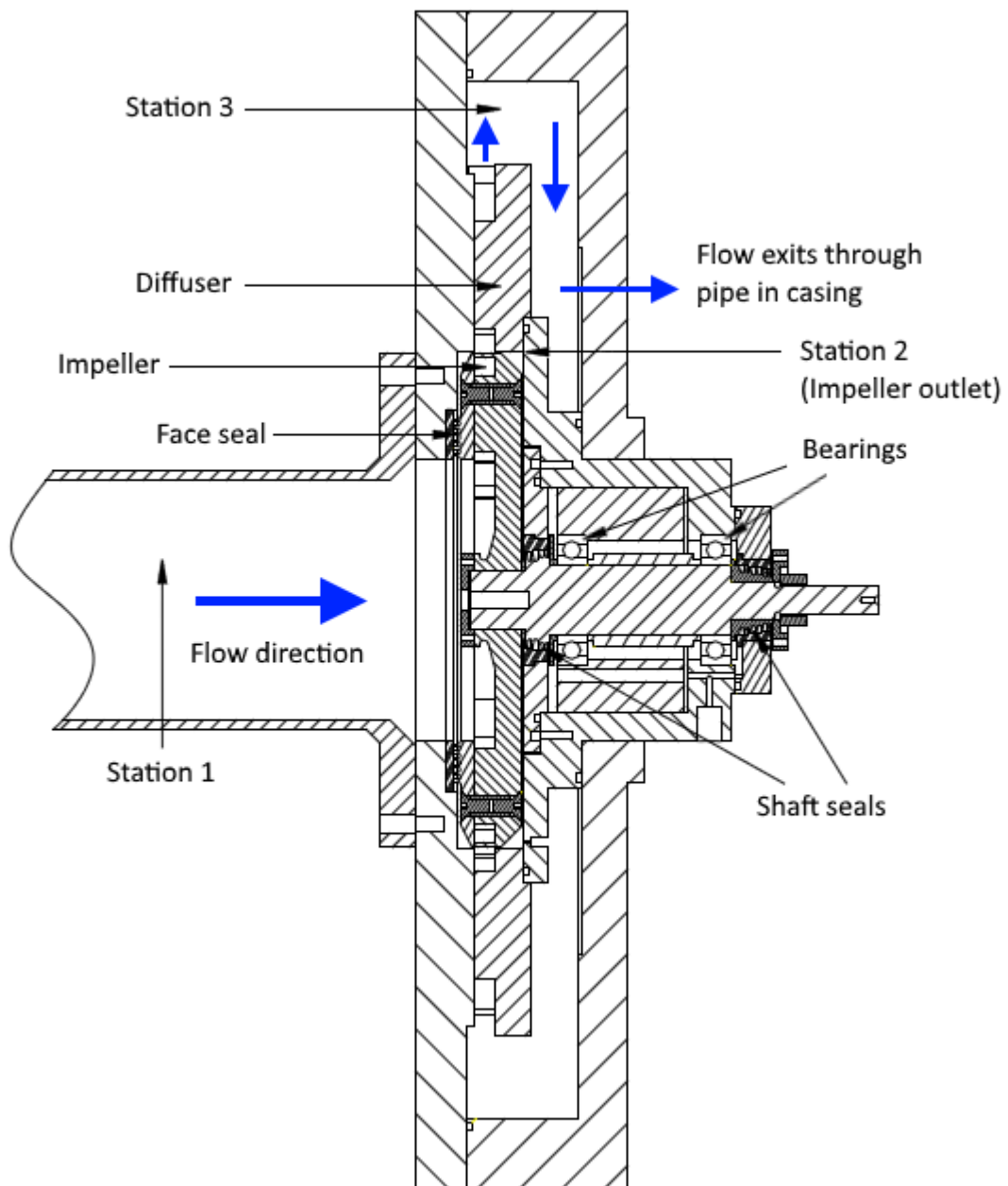


Figure 47: Cross section drawing of Vine's test rig (Vine, 2005)

4.2. Optical Research Test Rig

To ensure the best possible outcomes from this research, a new test rig was designed and built as part of the work. Figure 48 shows a cross section drawing of the new optical test rig. As there was significant uncertainty over the efficiency measurements by Vine, it was decided to use the same impeller and diffuser geometry so the results could be compared. The specification of the compressor is shown in Table 1.

Table 1: Compressor specification

| | |
|---------------------------------------|------------|
| Impeller diameter | 210 mm |
| Impeller blade height | 9 mm |
| Maximum expected pressure ratio | 1.6 |
| Mass flow rate at peak pressure ratio | 90 g/s |
| Maximum speed | 20,000 rpm |

The general layout is similar to Vines rig with a straight inlet pipe leading to the impeller and a large plenum at the outlet of the diffuser. Face seals were used on the front of the impeller and shaft seals behind to reduce leakage from the compressor. The step up belt drive from Vine's rig was used to drive the compressor, once the bearings and belt had been replaced.

The following sections focus on the design details that were considered due to the high speed nature of the test rig.

4.2.1. Optical Access

A primary objective of this testing is to use Laser Doppler Velocimetry and high-speed photography to investigate the flow field within the diffuser. The most common way to gain optical access is to make a small window in the casing of the machine and fill with Plexiglas or quartz. Due to the low pressure nature of this compressor and the geometrically simple design it was decided to not use the window method, but to make the entire diffuser out of clear acrylic with a light transmission of greater than 92%. This would mean no limitations on where measurements could be made.

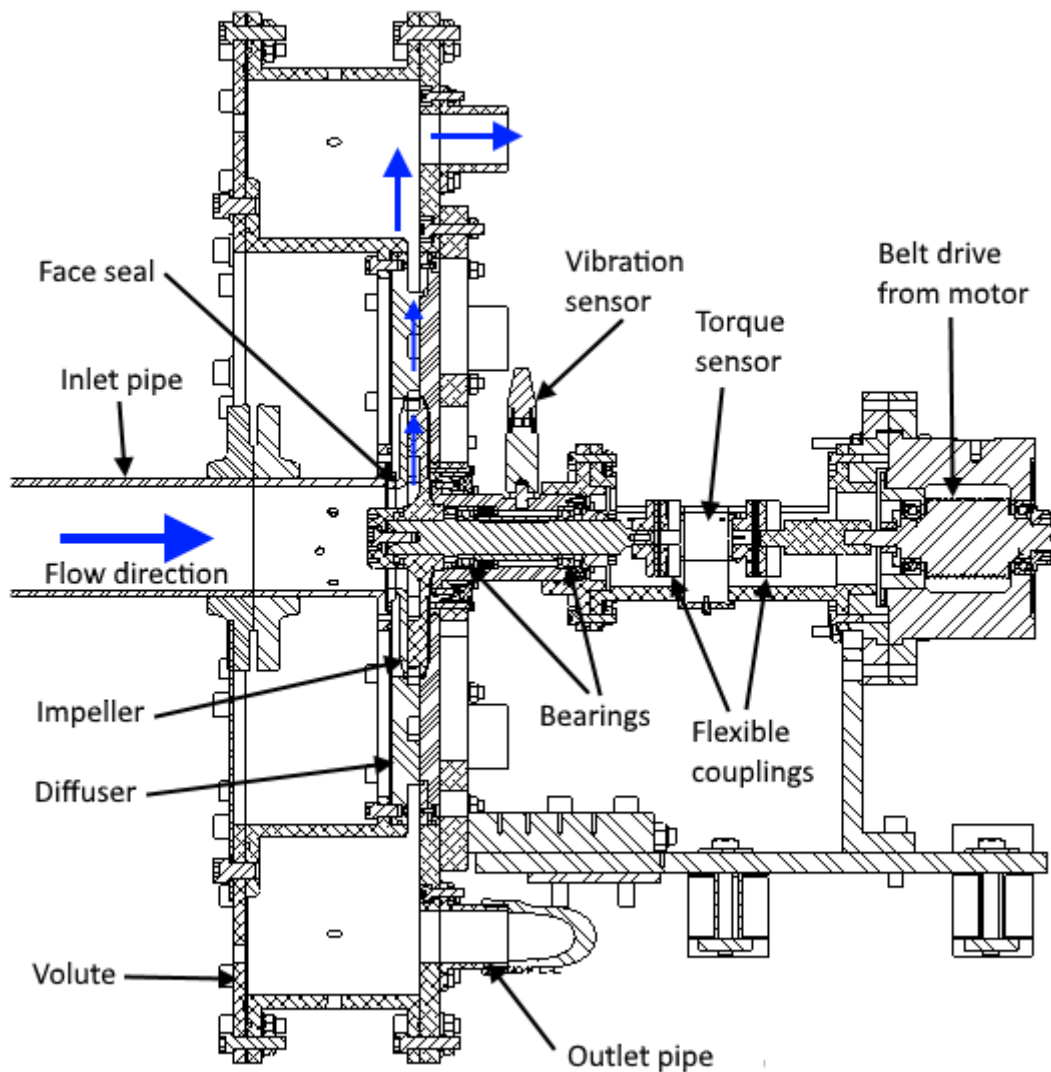


Figure 48: Cross section drawing of new rig optimised for optical access

4.2.2. Balancing

The high speed nature of the compressor required that it was balanced with the shaft, bearings, locking nuts, spacers and balancing rings to reduce the vibrational loads and reduce the risk of exciting shaft natural frequencies. This reduced the likelihood of premature failure of any of the components. City University London has a balancing machine which is suitable for balancing of the rotating components but was limited to an operational weight limit of 5 kg. Hence, it was decided to make the impeller out of aluminium alloy to keep the weight below this limit, Vine's impeller was machined from steel.

To reduce the overall weight, the balancing assembly (all the rotating components plus the bearing housing and preload springs), was designed to be constructed and inserted into the main rig as a single unit. This also allowed the diffuser front and back plates to be changed without rebalancing.

Two rings, the first made of an engineering steel, EN24T, had 20 M3 holes, the second, made from 6082-T6 aluminium had 40 M3 holes. These were used to balance the assembly as well as securing the impeller to the shaft. Weight was added to correct any imbalance by the addition of cap head and grub screws.

4.2.3. Impeller

Due to the high tip speed of the impeller, the centrifugal loading is very likely to cause high stresses at the maximum operating speed of 20,000 rpm. A full stress analysis was undertaken using ANSYS to ensure that failure due to yield or fatigue would not occur and also that any deflection would not cause the impeller to touch the casing.

The boundary conditions for this analysis were cyclic symmetry, only one twelfth of the model was analysed. This is more computationally efficient for an axis-symmetric model. The shaft and clamping bolt were included to fix the model in space and allow the calculation of the bolt applied stresses to the impeller. The cut face of the shaft was fixed in the axial direction, but free to move in both the radial and tangential. Bolt pretensions of 5,500 N and 1,300 N were applied to the impeller to shaft bolt and the hub to shroud bolt respectively. As the shaft to impeller bolt was only 1/12 of the model, only 1/12 of the bolt pretension was applied, 458 N.

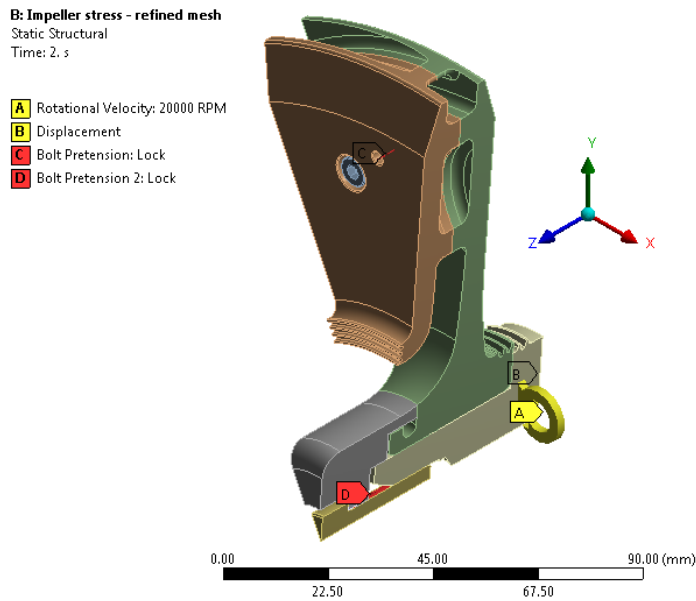


Figure 49: Boundary conditions for stress analysis of impeller

Figure 50 to Figure 55 and Table 2 show the results of these analyses. The maximum stress in the hub is 111 MPa and in the shroud is 186 MPa. These values are well below the yield strength of 7075-T6 aluminium alloy at 503 MPa (Matweb, 2018).

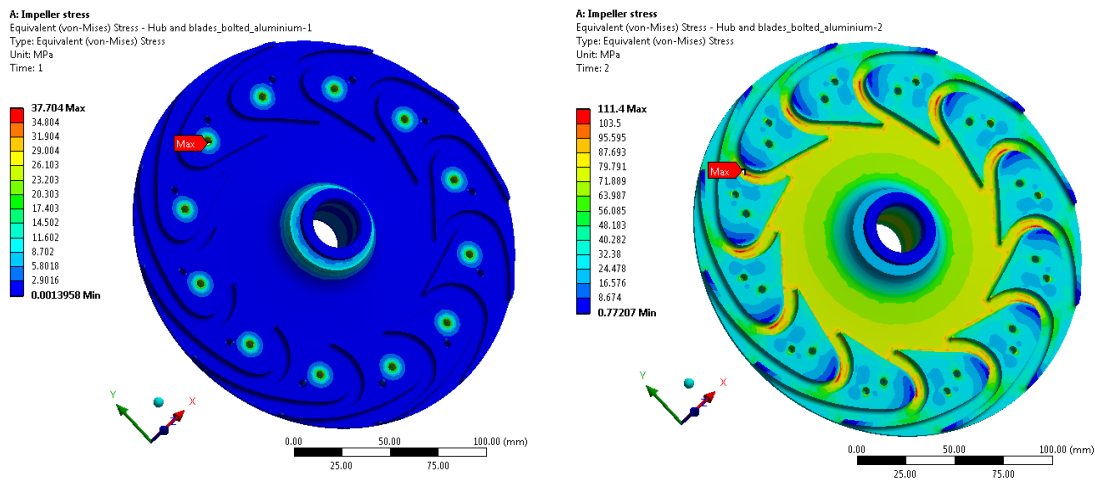


Figure 50: Stress in impeller hub at 0 and 20,000 rpm

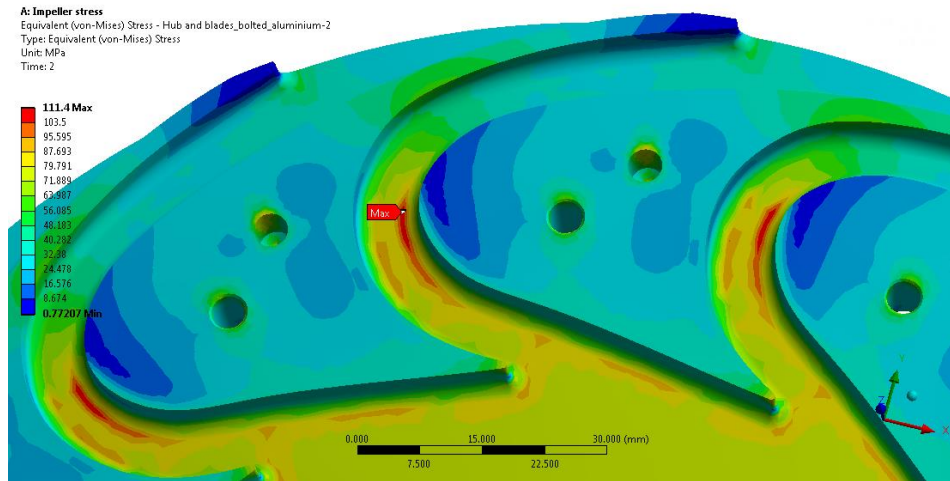


Figure 51: High stress location in impeller hub at 20,000 rpm

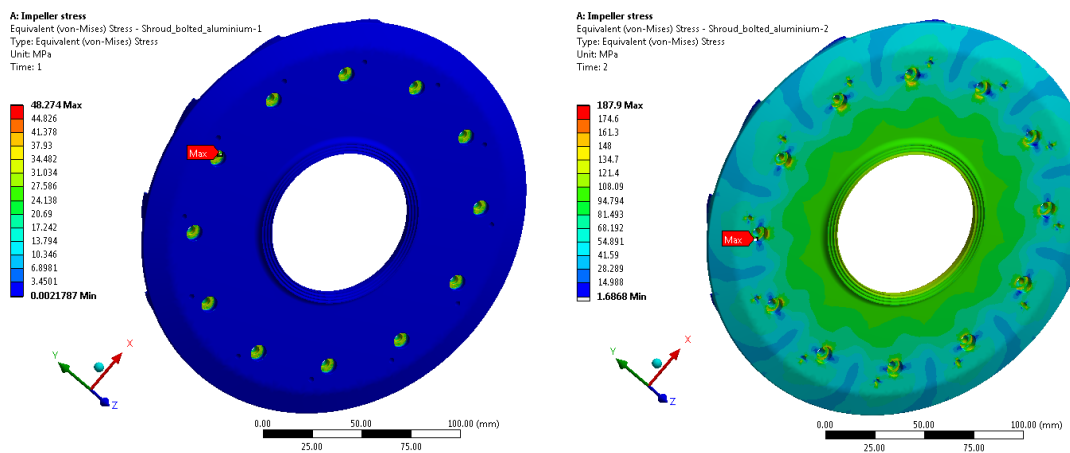


Figure 52: Stress in bolted impeller shroud at 0 and 20,000 rpm

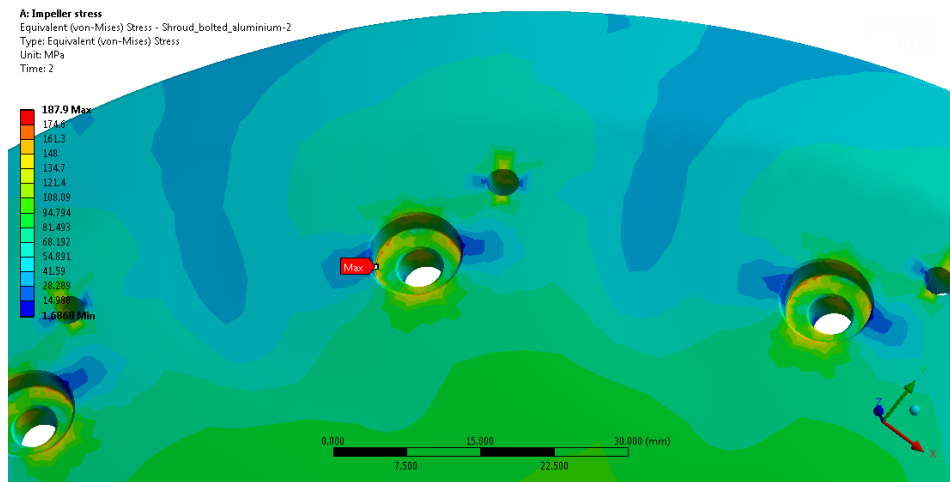


Figure 53: High stress location in impeller shroud at 20,000 rpm

The maximum radial growth of the impeller is 0.08 mm at 20,000 rpm and the maximum axial growth is 0.13 mm. A clearance of 0.5 mm radially and 1 mm axially have been allowed for in the test rig, to avoid impeller touch down. Figure 54 and Figure 55 show

the overall displacement of the impeller at 20,000 rpm. Figure 55 shows an exaggerated section view of the displacement, with a scale of x50.

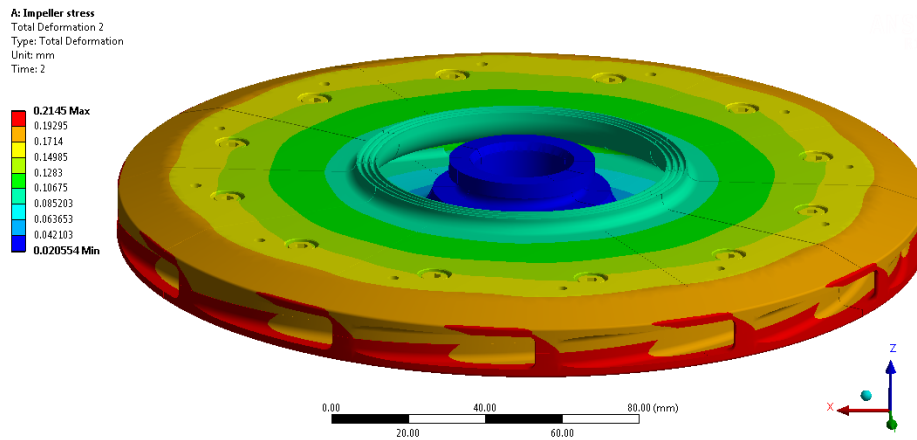


Figure 54: Displacement of impeller at 20,000 rpm

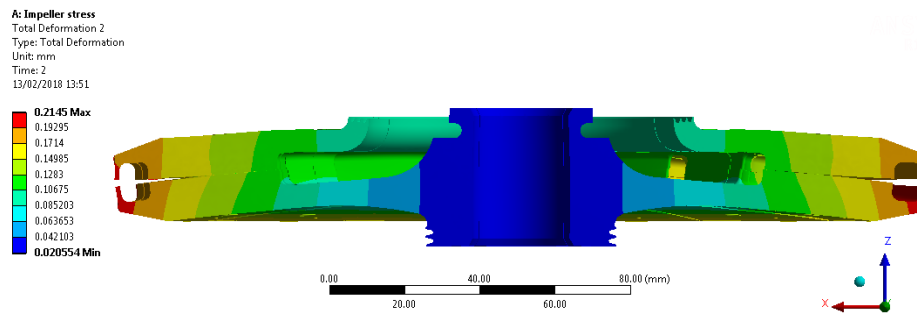


Figure 55: Section view of the impeller displacement at 20,000 rpm, scale x50

Failure modes have also been considered and fatigue failure due to cyclic loading assessed. Fatigue failure is caused by repeated loading and unloading of a structure. In the case of rotating machines, this occurs every time the machine is started and stopped. The unloaded state is the impeller bolted together and assembled onto the shaft, the loaded state is the impeller operating at full speed. The stresses at the unloaded state and loaded state are shown in Table 2 along with the calculated mean stress, σ_{mean} , and the stress amplitude, $\sigma_{amplitude}$.

Table 2: Fatigue stresses

| | Von-Mises maximum | Von-Mises minimum | σ_{mean} | $\sigma_{amplitude}$ |
|-----------------------|-------------------|-------------------|-----------------|----------------------|
| <i>Location</i> | MPa | MPa | MPa | MPa |
| <i>Hub blade root</i> | 111 | 0 | 55.5 | 55.5 |
| <i>Hub bolt hole</i> | 90 | 37 | 63.5 | 26.5 |
| <i>Hub dowel hole</i> | 85 | 0 | 42.5 | 42.5 |

| | Von-Mises maximum | Von-Mises minimum | σ_{mean} | $\sigma_{amplitude}$ |
|--------------------------|-------------------|-------------------|-----------------|----------------------|
| <i>Shroud blade root</i> | 135 | 0 | 67.5 | 67.5 |
| <i>Shroud bolt hole</i> | 186 | 48 | 117 | 69 |
| <i>Shroud dowel hole</i> | 136 | 7 | 71.5 | 64.5 |

The Goodman relation is an equation used to estimate the fatigue life of a component based upon its mean and alternating stresses (Budynas, et al., 2006). Other fatigue failure theories are available, but the Soderberg line, whilst guarding against yield, is biased low. The Gerber failure theory is thought to be most accurate, but as all fatigue failure methods are statistical, it was decided to be conservative and use the Goodman method.

Firstly, a graph of mean stress vs alternating stress is drawn and the results of the stress analysis are plotted for the components. Then a straight line is added connecting the fatigue limit of the material on the y-axis and the ultimate tensile strength on the x-axis. If the plotted points fall below the line, the component will experience infinite life, if they fall above the part could fail in service.

The specimens used in laboratory analysis for determining endurance limits are prepared very carefully. Hence, it is unrealistic to assume that the endurance limit of a component in service will have the exact endurance limit as that in the lab. Modifying factors have been identified and quantified to account for the effects of surface finish, size, loading, temperature and other miscellaneous items. These can be found in (Budynas, et al., 2006). The modifying factors and final endurance limit used in this analysis are shown in Table 3. The endurance limit of 7075-T6 is 159 MPa at 5×10^8 cycles (Matweb, 2018).

Table 3: Modifying factors for endurance limit

| | Surface | Size | Load | Temperature | Miscellaneous |
|--|---------|-------|-------|-------------|---------------|
| | K_a | K_b | K_c | K_d | K_e |
| <i>a</i> | 4.51 | | | | |
| <i>b</i> | -0.265 | | | | |
| | 0.8384 | 1.0 | 1.0 | 1.015 | 1.0 |
| <i>Ultimate tensile strength (MPa)</i> | | | | 572.0 | |
| <i>Endurance limit of the part (MPa)</i> | | | | 135.3 | |

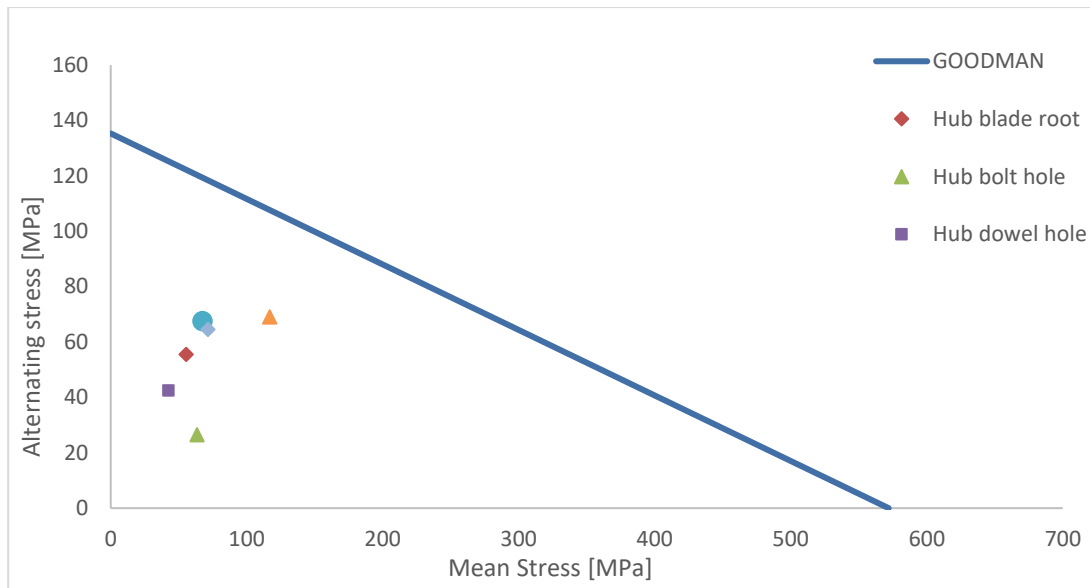


Figure 56: Goodman diagram for the impeller showing an infinite life design

The Goodman diagram shown in Figure 56 shows that the impeller will exhibit sufficient life as all high stress points are below the Goodman Line.

4.2.4. Bearing Housing

4.2.4.1. Bearings

One of the major determinants of bearing life is the axial loading on the bearings. In the case of a compressor, the axial force is generated by pressure acting on different surface areas on either side of the impeller as shown in Figure 57. If there is an imbalance between these forces, the net force, F , is transmitted through the bearings.

In general, the pressure is not constant across the surface. To calculate the magnitude of the force on each surface, an integration must be performed.

$$F = P \times A \quad \text{Equation 17}$$

$$F = \int_{r_1}^{r_2} P \times 2\pi r \, dr \quad \text{Equation 18}$$

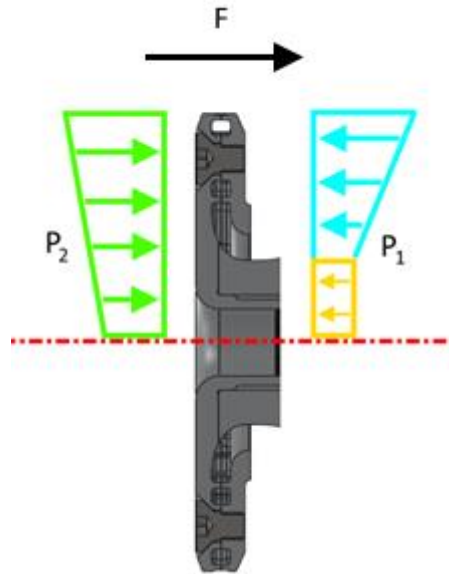


Figure 57: Schematic of the force across the impeller due to pressure imbalance when operating

It is assumed that the pressure varies linearly with radius across the impeller surface as shown in Figure 58 and Figure 59, a typical assumption in made by turbomachinery engineers and it is likely conservative. If the pressure rises parabolically the load will be less.

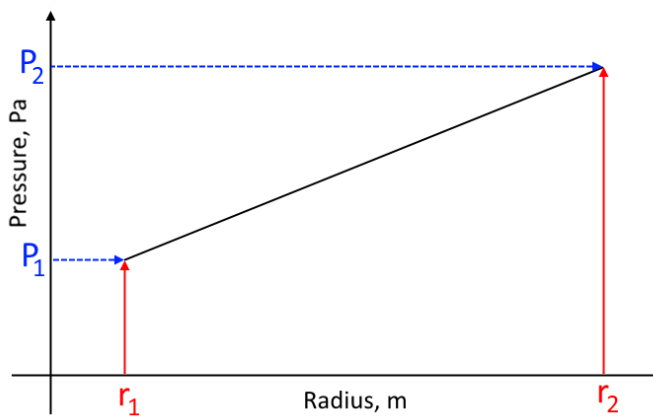


Figure 58: Pressure variation with radius across the surface of the impeller

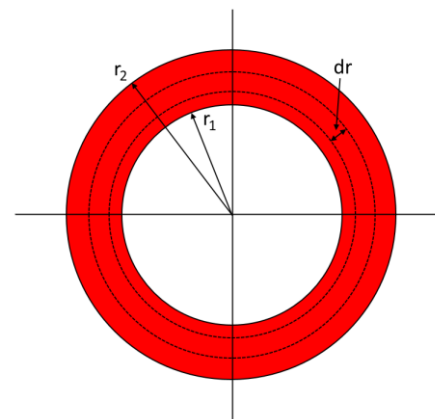


Figure 59: Simplified impeller surface

The pressure distribution can be described as a straight line:

$$P = mr + c \quad \text{Equation 19}$$

Inserting known values of P_1 , P_2 , r_1 and r_2 into Equation 19 allows solving of m and c .

$$m = \frac{P_2 - P_1}{r_2 - r_1} \quad \text{Equation 20}$$

$$c = P_2 - \frac{(P_2 - P_1)r_2}{r_2 - r_1} \quad \text{Equation 21}$$

Inserting Equation 20 and Equation 21 into Equation 18 and solving the integral leads to

$$F = 2\pi \left[\frac{(r_2^3 - r_1^3)m}{3} + \frac{(r_2^2 - r_1^2)c}{2} \right] \quad \text{Equation 22}$$

At the start of this research, the degree of reaction of the impeller was unknown. Also unknown was the effectiveness of the labyrinth seals on the eye and back face of the impeller. As the thrust loading on the bearings has a massive effect on their life, it was decided to take a conservative assumption that 50% of the pressure rise in the compressor was generated within the impeller and that the seals were only partially effective. As the leakage flow rate through the seals was unknown there is no way to calculate the pressure drop across the seal, so it will be assumed that the pressure drop is 50% of the difference between inlet and impeller exit. This allows the calculation of the axial force produced by the impeller when it is operating at full speed and maximum pressure ratio. The positive direction of force was towards the bearings.

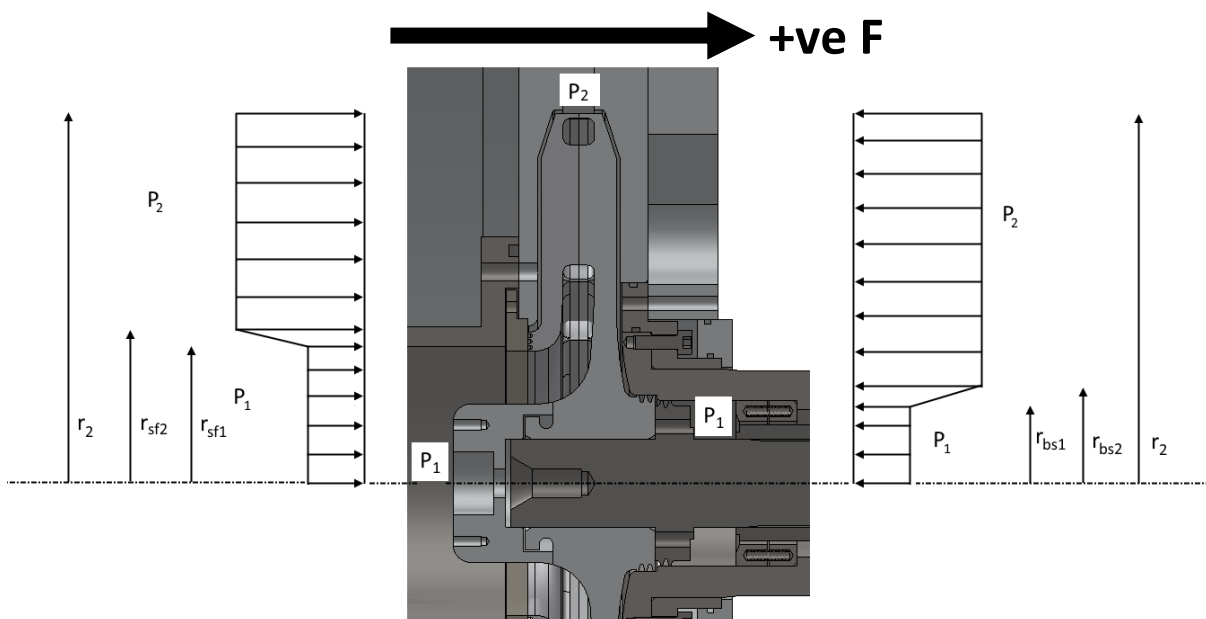


Figure 60: Diagram of the pressure imbalance across the impeller causing an axial force to be applied to the bearings

Table 4: Axial force radii and pressures

| | | |
|--|-----------|------------|
| Inner radius front seal | r_{sf1} | 0.0375 m |
| Outer radius front seal | r_{sf2} | 0.043 m |
| Inner radius back seal | r_{sb1} | 0.0235 m |
| Outer radius back seal | r_{sb2} | 0.025 m |
| Radius of impeller | r_2 | 0.105 m |
| Design pressure ratio | PR | 1.60 |
| Inlet pressure | P_1 | 101,325 Pa |
| Compressor outlet pressure | P_3 | 162,120 Pa |
| Percentage of impeller pressure rise | | 50% |
| Impeller outlet pressure | P_2 | 131,723 Pa |
| Assumed pressure at inner radius of front seal | P_{sf1} | 101,325 Pa |
| Assumed pressure at outer radius of front seal | P_{sf2} | 116,524 Pa |
| Assumed pressure at inner radius of back seal | P_{sb1} | 101,325 Pa |
| Assumed pressure at outer radius of back seal | P_{sb2} | 116,524 Pa |

Using equations Equation 20 - Equation 22, the force on each area can be calculated.

Table 5: Loads on impeller areas

| | |
|----------------------|---------|
| Eye load | 448 N |
| Front seal load | 152 N |
| Shroud load | 3,610 N |
| Bearing housing load | 176 N |
| Back seal Load | 24.9 N |
| Hub load | 4,110 N |

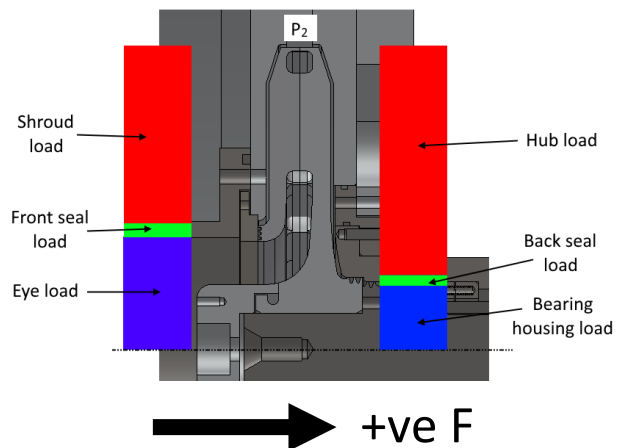


Figure 61: Names for the areas generating load due to pressure imbalance

The axial force generated is then the sum of these force vectors which in this case is 97.4 N away from the bearings. However, the worst case in loading could be as high as 495 N also away from the bearings. This would occur if the front face seal is completely ineffective so the pressure across the front face of the shroud varies from the inlet pressure at the eye to the outlet pressure at the impeller OD whilst at the same time the back face seal is perfect, generating the full pressure drop across it, resulting in the entire back face of the impeller being at the outlet pressure. (If this is reversed the load is only 300 N in the positive direction). This is thought to be an unlikely scenario, but the bearings will be selected such that they can withstand this loading if it should occur.

Due to the magnitude of the axial thrust loading generated by the impeller at the operating point, 2 angular contact bearings, arranged in a back to back configuration were used to support the shaft. The back to back arrangement was chosen as it provides a stiffer bearing arrangement than face to face.

SKF super precision 7005 CD/HCP4A bearings were chosen. These are ceramic balled hybrid bearings, designed to take significant end loads whilst operating at high surface speeds. Using the SKF life calculation, L10, when the bearings are operating at maximum pressure ratio, they have an estimated life of 18,500 hours, or 2.1 years, which is plenty for a test rig. More importantly, the bearings will be grease packed and the grease life will be 3,480 hours, or 4.6 months. This is the life for continuous operation at maximum loading, but a record of operation will be kept so relubrication of the bearings can be done when necessary.

The thrust bearing was fixed rigidly onto the shaft and into the bearing housing. The other bearing had the inner race of the bearing fixed to the shaft while the outer race was allowed to slide. The outer race was located in the bearing housing with the preload springs. The preload was determined to be 82 N from the SKF bearing calculations (SKF, 2005), requiring 8 springs with a spring rate of 2.25 N/mm to be compressed by 4.6 mm. Two end caps were made to contain the springs and ensure that they compress axially without any deformation.

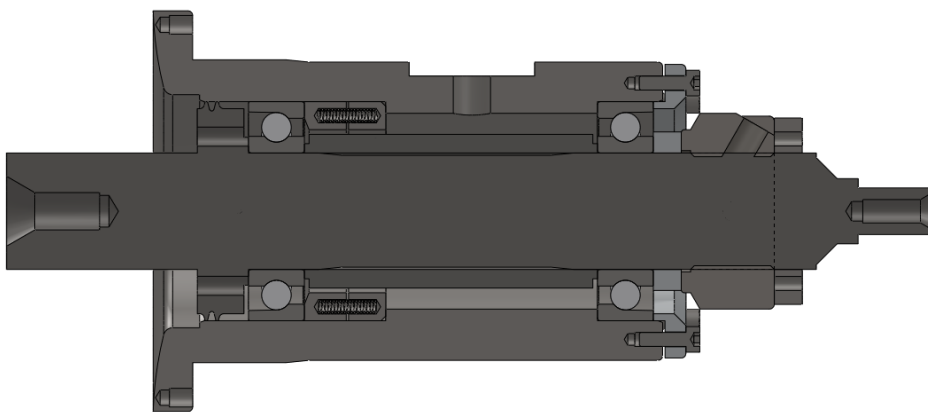


Figure 62: Section view of the bearing housing

The inner races of the bearings were locked in place on the shaft using a SKF locking nut. For the removal of the bearings, 6 holes were drilled in line with the inner race of the

front bearing. The insertion of dowels allowed the bearings and bearing spacer to be pushed off the shaft without damaging the bearings as shown in Figure 63.

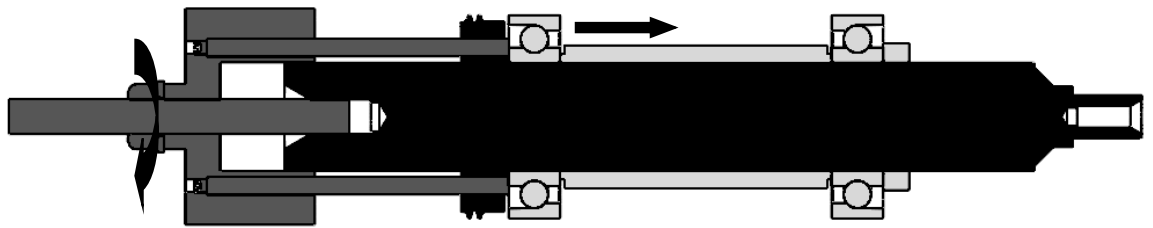


Figure 63: Bearing removal tool

4.2.4.2. Seals

Labyrinth seals on the shaft minimised the flow of high pressure air along the shaft length. The leakage flow was vented to prevent flow through the bearings see Figure 65. If this were to occur, dust could cause damage to the rolling elements and grease could be displaced. There is a labyrinth seal on the back face of the impeller to increase the length of seal.

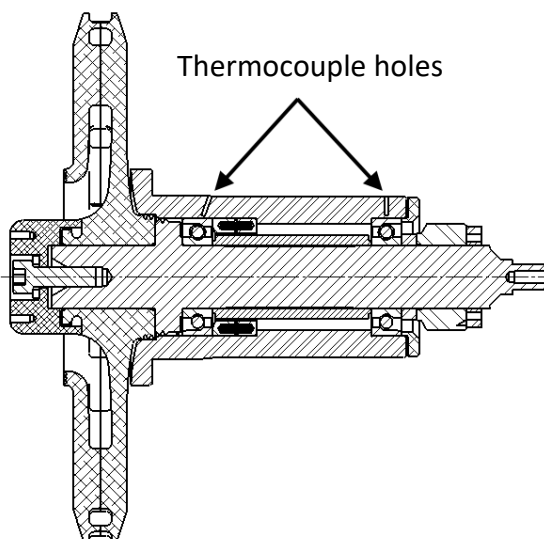


Figure 64: Thermocouple holes in the bearing housing for measuring bearing temperatures

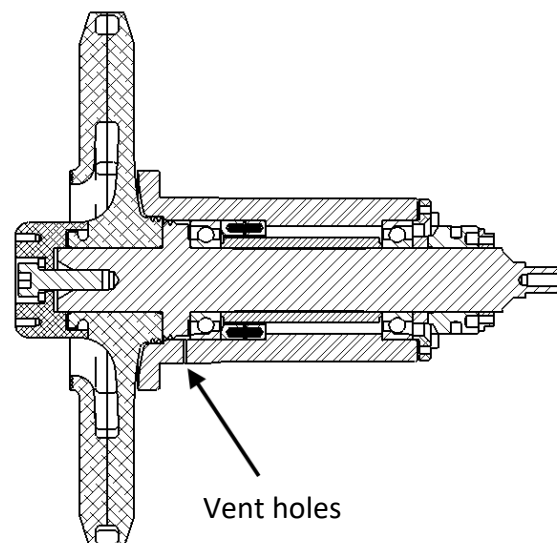


Figure 65: Vent hole in the bearing housing to protect the bearing grease from being "blown" out by a pressure imbalance

4.2.4.3. Shaft

The shaft is 25 mm in diameter which was determined by the bearing and rotordynamic requirements. It has centres at both ends to allow the shaft to be accurately ground to

size. The impeller end of the shaft has an M8 hole for the bolt that clamps the impeller and balancing ring onto the shaft.

To ensure the rotating assembly would be dynamically stable, a full rotordynamic analysis was completed using ANSYS APDL. This produced the Campbell diagram shown in Figure 66. The analysis calculates the rigid body modes, bounces and rocks, and the shaft bend mode. It also shows how the gyroscopic stiffening of the shaft effects the critical speeds of forward and backwards whirls.

The compressor was designed to operate sub-critically, meaning all the critical speeds are above the operating speed of the compressor. The light blue line shows the running speed of the compressor. The Campbell diagram shows that all the modes are above the operating speed of the compressor.

Bearing stiffnesses were supplied by SKF based upon the maximum rotational speed of 20,000 rpm and the axial force calculated above of 97.4 N. This preload value was used as increases in axial force increase the bearing stiffness therefore this is a conservative approach to calculating the modes.

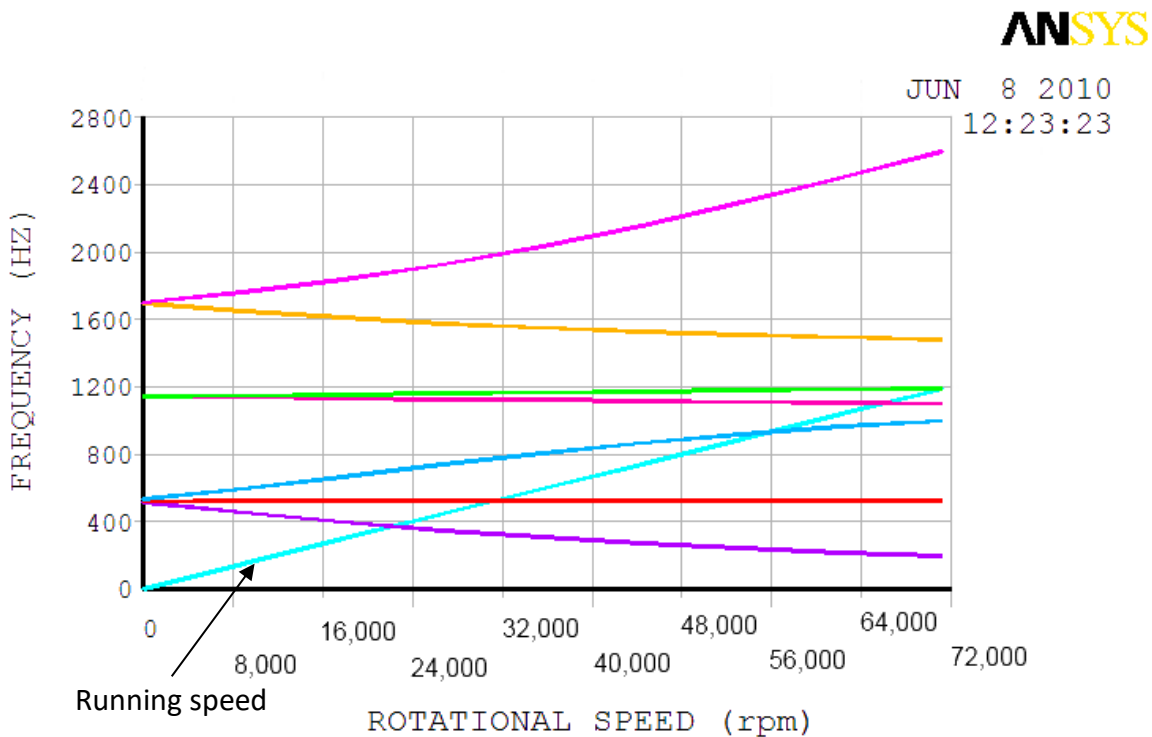


Figure 66: Campbell diagram for compressor shaft showing subcritical operation

4.2.4.4. Housing

The outer diameter of the housing was designed to be supported by a holder in the main rig, allowing the easy removal of the bearing housing with the impeller still attached. Three 1 mm diameter holes were drilled just behind the labyrinth seals to allow any excess pressure to vent to atmosphere, stopping it flowing through the bearings, as shown in Figure 65.

Four 1.5 mm holes were drilled from the outside surface through to where the bearing outer race sits to allow the insertion of thermocouples to monitor the temperature of the bearings as shown in Figure 64.

4.2.5. Main support

The rig was designed such that all components were fixed to a single main support plate, see Figure 67. This part does not provide any alignment. The alignment of the components e.g. the bearing housing, is set by the Bearing Housing Holder. This part is designed to maintain the alignment of any component fixed to the main support when the balancing assembly is removed.

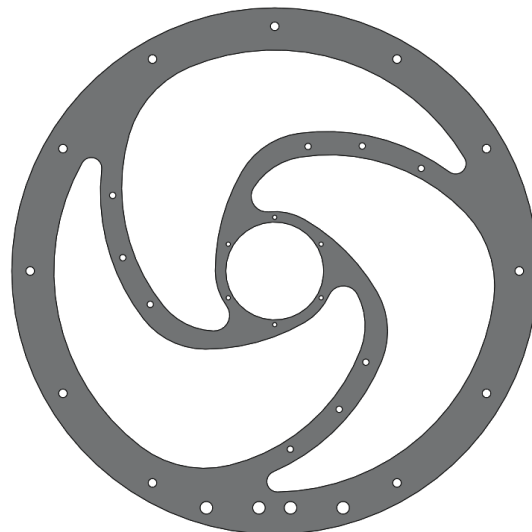


Figure 67: Main support for rig showing the sculpting required to maintain optical access

As laser access is required straight through the rig, the main support was designed as an inner ring to support the bearing housing holder, an outer ring to support the volute and 3 spokes that follow the blade profile of the diffuser, this allowed full access to all the diffuser passages for the laser testing.

4.2.6. Collector

The collector has been sized to allow a variety of designs to be tested such as plenums or volutes. For initial testing, the plenum was designed to eliminate any axisymmetric effects on performance that a volute could create. Tapings were made into the plenum to record pressure and temperature for the evaluation of performance. The collector has six 1.5" outlets, equally spaced around the circumference, which were opened or closed depending on the flow rate being tested.

4.2.7. Pipe Work

The outlets from the collector have six 1.5" diameter pipes with male threads to allow a variety of connections. These are all connected with flexible hoses to a large plenum (8" diameter, 200 mm long) to allow the flows to mix before heading through an actuated valve. This valve provided the restriction to the flow allowing the mass flow and consequently the outlet pressure to be varied.

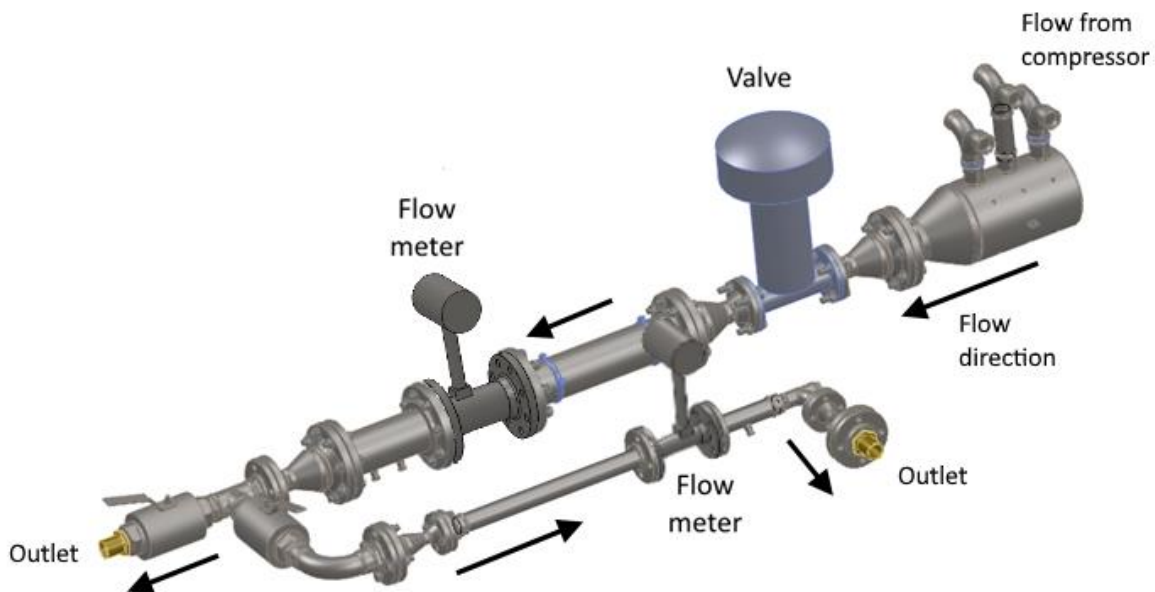


Figure 68: Compressor downstream pipe layout including measurement and control devices

From the valve the flow entered a volume flow meter via a pipe of length of 5 x the diameter of the pipe to allow the flow to settle (as required by ABB, the volume flow meter manufacturer), followed by the flow meter, then the downstream pipe which has a length of 3 x pipe diameter. This is for flow settling and to allow space for a pressure tapping and a temperature probe. These are required to calculate the air density so that

the volume flow reading can be converted to a mass flow. From here a flexible hose took the flow into the exhaust system below the test cell.

On the inlet to the compressor, an adapter was attached to allow a filter/silencer to be fitted. This inlet has tapings for pressure and temperature sensors and allows the inlet conditions to be varied if required.

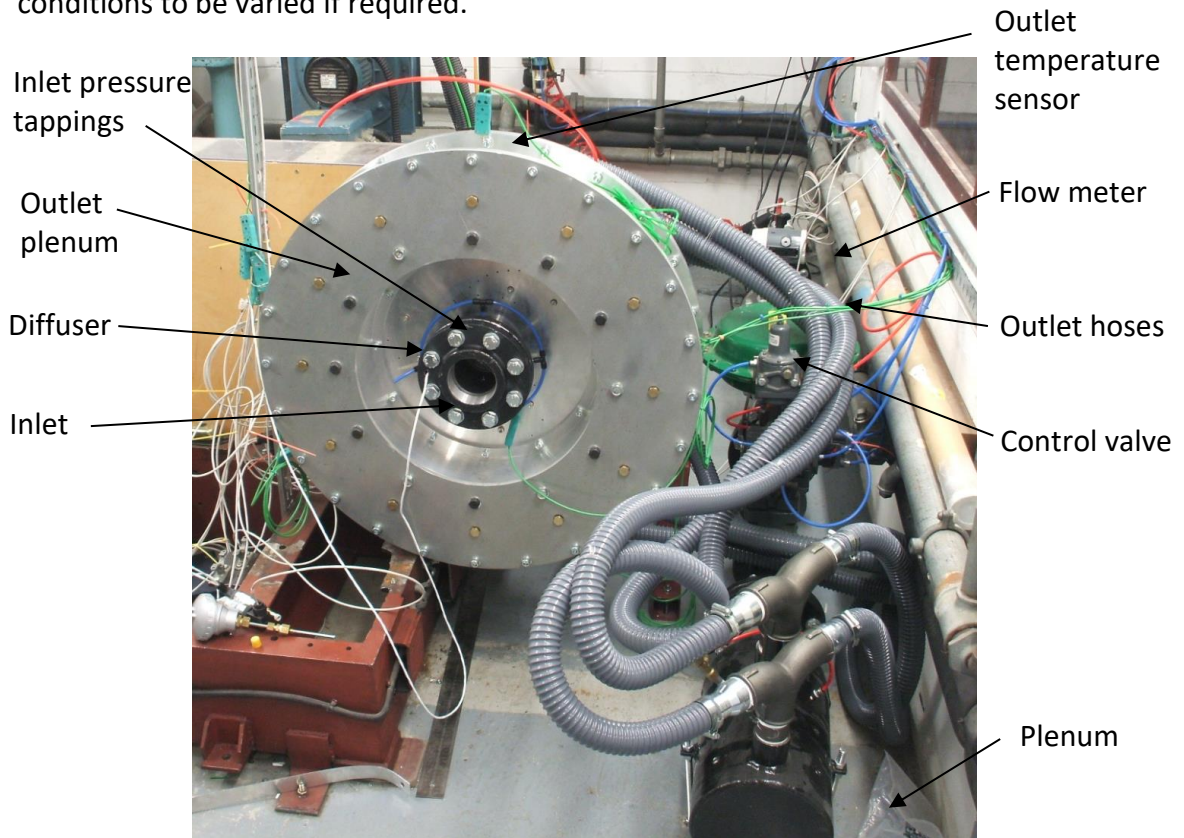


Figure 69: Complete test rig with hose connections between compressor outlet and downstream pipework

4.2.8. Motor Connection

For initial testing, the belt and pulley system from the original test rig was used. At first it was thought that this would limit the compressor to 16,700 rpm as described earlier, however, after inspection it was felt that the motor could be safely operated at 3,000 rpm allowing the compressor to run at 20,000 rpm.

The only alterations to the drive system were the replacement of the belt and the addition of a new torque sensor. This sensor has a maximum speed of 30,000 rpm and a maximum torque of 10 Nm, the maximum torque can be measured independent of speed. The accuracy of the torque sensor is 0.1% of full scale, it will therefore measure

to an accuracy of ± 0.01 Nm. The torque sensor was connected to the high speed pulley and to the impeller shaft with 2 single flex couplings.

4.2.9. Primary Instrumentation

The primary instrumentation for the rig has two functions.

- 1) To monitor the health of the test rig – vibration, bearing temperature etc.
- 2) To measure sufficient quantities to allow the performance of the compressor to be determined – these include inlet/outlet temperature, pressure, torque and speed.

The sensors are all connected to a National Instrument data acquisition system that was controlled using a LabView program. A list of the sensors used is shown in Table 6 and the NI hardware is shown in Table 7. The main screen of the LabView programme is shown in Figure 70.

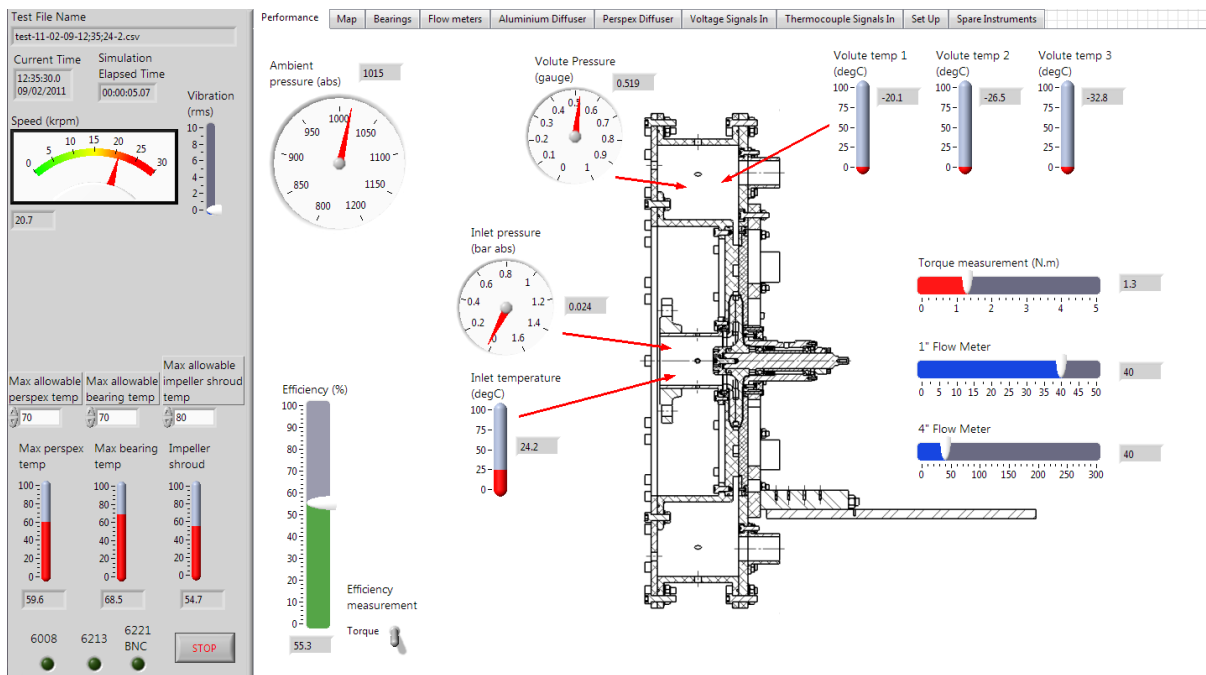


Figure 70: Labview programme main screen

Table 6: Sensor list

| Type | Location | Model | Range | Accuracy |
|-------------|-----------------|---|------------------------------|--|
| Pressure | Test cell | PTX 1400 | 800-1200 mbar absolute | ± 0.15 % |
| Temperature | Test cell | K-type thermocouple, RS Stock No. 397-1539 | -40 °C to +1100 °C | ± 1.5 °C |
| Pressure | Inlet | PTX 1400 | 0 – 1.6 bar absolute | ± 0.15 % |
| Temperature | Inlet | Pt100 Class A (assumed) with mA transmitter | 0 to 150 °C | Pt100 ± (0.15 + 0.002 t) Transmitter ± 0.1 % span |
| Pressure | Outlet | PTX 1400 | -0.5 – 1.0 bar gauge | ± 0.15 % |
| Temperature | Outlet 1 | K-type thermocouple, RS Stock No. 397-1539 | -40 °C to +1100 °C | ± 1.5 °C |
| Temperature | Outlet 2 | K-type thermocouple, RS Stock No. 397-1539 | -40 °C to +1100 °C | ± 1.5 °C |
| Temperature | Outlet 3 | K-type thermocouple, RS Stock No. 397-1539 | -40 °C to +1100 °C | ± 1.5 °C |
| Torque | Shaft | Interface inline torque meter, T11-10Nm | 10 Nm | ± 0.1 % |
| Speed | Shaft | Interface inline torque meter, T11-10Nm | 6 pulse/rev TTL | ± 10 rpm |
| Flow meter | Downstream | ABB Swirl Flow meter, FS4000-ST4 ST401211HDA15A2EX0AAA1 | 65 – 1500 m ³ /hr | ± 0.5 % flow rate |
| Pressure | FS4000 | PTX 1400 | 0 – 1.0 bar gauge | ± 0.15 % |
| Temperature | FS4000 | Pt100 Class A (assumed) with mA transmitter | 0 – 300 °C | Pt100 ± (0.15 + 0.002 t) Transmitter ± 0.1 % span |
| Flow meter | Downstream | ABB Vortex flow meter, FV4000-VT4 VT4012140DA15A2EX0AAA1 | 15-150 m ³ /hr | ± 1.0 % flow rate |
| Pressure | FV4000 | PTX 1400 | -1 – 4.0 bar gauge | ± 0.15 % |
| Temperature | FV4000 | T-type thermocouple with mA transmitter | 0 to 150 °C | T-type ± 1.0 °C or ± 0.75% whichever is greater Transmitter ± 0.2 % span |
| Temperature | Bearing 1 | K-type thermocouple, Welded tip, PTFE cable | -50 °C to +250 °C | ± 1.5 °C |
| Temperature | Bearing 1 | K-type thermocouple, Welded tip, PTFE cable | -50 °C to +250 °C | ± 1.5 °C |
| Temperature | Bearing 2 | K-type thermocouple, Welded tip, PTFE cable | -50 °C to +250 °C | ± 1.5 °C |
| Temperature | Bearing 2 | K-type thermocouple, Welded tip, PTFE cable | -50 °C to +250 °C | ± 1.5 °C |
| Vibration | Bearing housing | Bently Nevada Velomitor, 330500-A02-B00 | 1270 mm/s | 3.94 mV/mm/s ±% |

| Type | Location | Model | Range | Accuracy |
|-------------|--------------------|---|-------------------|--|
| Temperature | Perspex diffuser 1 | K-type thermocouple, Welded tip, PTFE cable | -50 °C to +250 °C | ± 1.5 °C |
| Temperature | Perspex diffuser 2 | K-type thermocouple, Welded tip, PTFE cable | -50 °C to +250 °C | ± 1.5 °C |
| Temperature | Perspex diffuser 3 | K-type thermocouple, Welded tip, PTFE cable | -50 °C to +250 °C | ± 1.5 °C |
| Temperature | Perspex diffuser 4 | K-type thermocouple, Welded tip, PTFE cable | -50 °C to +250 °C | ± 1.5 °C |
| Temperature | Perspex diffuser 5 | K-type thermocouple, Welded tip, PTFE cable | -50 °C to +250 °C | ± 1.5 °C |
| Temperature | Perspex diffuser 6 | K-type thermocouple, Welded tip, PTFE cable | -50 °C to +250 °C | ± 1.5 °C |
| Temperature | Impeller | Infrared probe with k-type output, OS136-1 | -18 to 204 °C | ± 3 % or ± 4.4 °C whichever is greater |

Table 7: National Instruments Hardware List

| NI module | Type | Sampling rate | ADC resolution | Accuracy |
|--------------|---------------------------------------|---------------------------|----------------|------------------------------|
| USB-6221 BNC | 8 differential voltage input channels | 250 kS/s (single channel) | 16 bits | 1.62 mV |
| | 2 general purpose counters | NA | 32 bits | 50 ppm (base clock accuracy) |
| | 24 digital input/output channels | NA | 8 bits | NA |
| USB 6008 | 8 single ended voltage input channels | 10 kS/s (all channels) | 11 bits | 14.7 mV |
| NI USB-9213 | 16 channel thermocouple module | 75 S/s (all channels) | 24 bits | < 0.25 °C |

4.2.10. Sensor Calibration

Prior to testing, all the sensors were calibrated. Using available equipment, pressure was applied to the sensor and a calibrated sensor simultaneously. The reading from the test sensor and calibrated sensor were recorded and a correction factor was applied in the NI software.

The temperature sensors were two-point calibrated using a bath of distilled crushed ice water mixture and a bath of boiling distilled water whilst being compared to an accurate thermometer. The torque sensor was supplied calibrated.

4.3. Performance Testing

Tests were performed to produce the compressor map over its range of operation. Inlet pressure, and temperature as well as volume flow, pressure and temperature downstream of the compressor were measured. Due to the relatively low velocity at the measuring stations, these values can be assumed to be static measurements. I.e. for the maximum mass flow rate recorded during testing, the flow velocity at the inlet was 14.9 m/s which translates to a dynamic pressure of 131 Pa. The static pressure measurement corresponding to this dynamic pressure was 102,684 Pa. This equates to 0.13% of the measured static pressure and therefore can be discounted.

In addition to enable mechanical power input to be calculated, the shaft torque and speed were also measured. For these measurements the air was assumed to be acting as an ideal gas. The static-static Pressure ratio, PR , was calculated from:

$$PR = \frac{P_3}{P_1} \quad \text{Equation 23}$$

Where P_3 is outlet static pressure and P_1 is inlet static pressure.

Mass flow, \dot{m} , was calculated from:

$$\dot{m} = \rho \dot{V} \quad \text{Equation 24}$$

$$\rho = \frac{P_{fm}}{R_{specific} T_{fm}} \quad \text{Equation 25}$$

Where P_{fm} , is the pressure, and T_{fm} , the temperature, downstream of the volume flow meter, $R_{specific}$ is the specific gas constant for dry air (287.058 J/(kg.K)) and \dot{V} , the volume flow rate from flow rate sensor.

Efficiency is a measure of the actual work input to the compressor relative to the ideal work. For an ideal compressor that is adiabatic and reversible, no entropy change occurs within the compressor. Isentropic efficiency is a measure of the work input to this ideal compressor (W_s) compared to the actual compressor.

Isentropic efficiency, η_{isen} , is calculated using:

$$\eta_{isen} = \frac{W_s}{W_{actual}} \quad \text{Equation 26}$$

The actual work input to the compressor is measured using the torque sensor.

$$W_{actual} = \frac{|\tau|\omega}{\dot{m}} \quad \text{Equation 27}$$

Where τ is the measured torque, ω is the angular velocity and \dot{m} is the mass flow rate. However, as the compressor was not insulated, this will not be a true isentropic efficiency. Heat transfer from the compressor will slightly reduce the actual work input compared to a fully insulated compressor. Hence the efficiency will be denoted as η for this compressor.

As this compressor is adiabatic, the work input is equal to the rise in total enthalpy, h_{01} . However, as shown earlier, the dynamic component of the flow is so small that total and static values can be assumed to be equal.

$$h_1 \cong h_{01} \quad \text{Equation 28}$$

The ideal work W_s is equal to the change in enthalpy assuming a constant entropy process.

$$W_s = h_{3s} - h_1 \quad \text{Equation 29}$$

Inserting Equation 27 and Equation 29 into Equation 26 gives:

$$\eta = \frac{\dot{m}(h_{3s} - h_1)}{|\tau|\omega} \quad \text{Equation 30}$$

For an ideal gas, the change in enthalpy can be directly related to the change in temperature of the gas. While the value of C_p , the specific heat capacity at constant pressure, does vary significantly with temperatures, for the temperatures experienced by this compressor, C_p can be assumed constant and based upon the inlet temperature T_1 .

$$\Delta h = Cp\Delta T \quad \text{Equation 31}$$

$$Cp = c_1 + c_2T_1 + c_3T_1^2 + c_4T_1^3 + c_5T_1^4 \quad \text{Equation 32}$$

$$\begin{array}{llll} c_1 & 1.019 & c_4 & 4.240 \times 10^{-10} \\ c_2 & -1.378 \times 10^{-4} & c_5 & -3.763 \times 10^{-13} \\ c_3 & 1.984 \times 10^{-7} & & \end{array}$$

Therefore

$$h_{3s} - h_1 = Cp(T_{3s} - T_1) \quad \text{Equation 33}$$

$$h_{3s} - h_1 = CpT_1 \left(\frac{T_{3s}}{T_1} - 1 \right) \quad \text{Equation 34}$$

For an ideal gas, the isentropic temperature rise can be written as a pressure ratio.

$$\frac{T_{3s}}{T_1} = \left(\frac{p_3}{p_1} \right)^{(\gamma-1)/\gamma} \quad \text{Equation 35}$$

Equation 35 then becomes:

$$h_{3s} - h_1 = CpT_1 \left(\left(\frac{p_3}{p_1} \right)^{(\gamma-1)/\gamma} - 1 \right) \quad \text{Equation 36}$$

Inserting Equation 36 into Equation 30 gives us Equation 37, the equation for efficiency.

$$\eta = \frac{\dot{m}CpT_1}{\omega|\tau|} \left(\left(\frac{P_3}{P_1} \right)^{(\gamma-1)/\gamma} - 1 \right) \quad \text{Equation 37}$$

Where τ is shaft torque, ω angular velocity, Cp is the specific heat capacity at constant pressure and γ is the ratio of specific heats.

Figure 71 and Figure 73 show the results of the testing. Unfortunately, during the performance testing, it was discovered that the components that were re-used from Vine's rig – namely the lay shaft, had manufacturing defects that lead to the lay shaft being dynamically unstable, causing the shaft of the torque meter to touch down damaging it. Data was collected up to 12,000 rpm before this problem was discovered. Testing at speeds higher than this was not possible due to the time and cost associated with remanufacture of the lay shaft components.

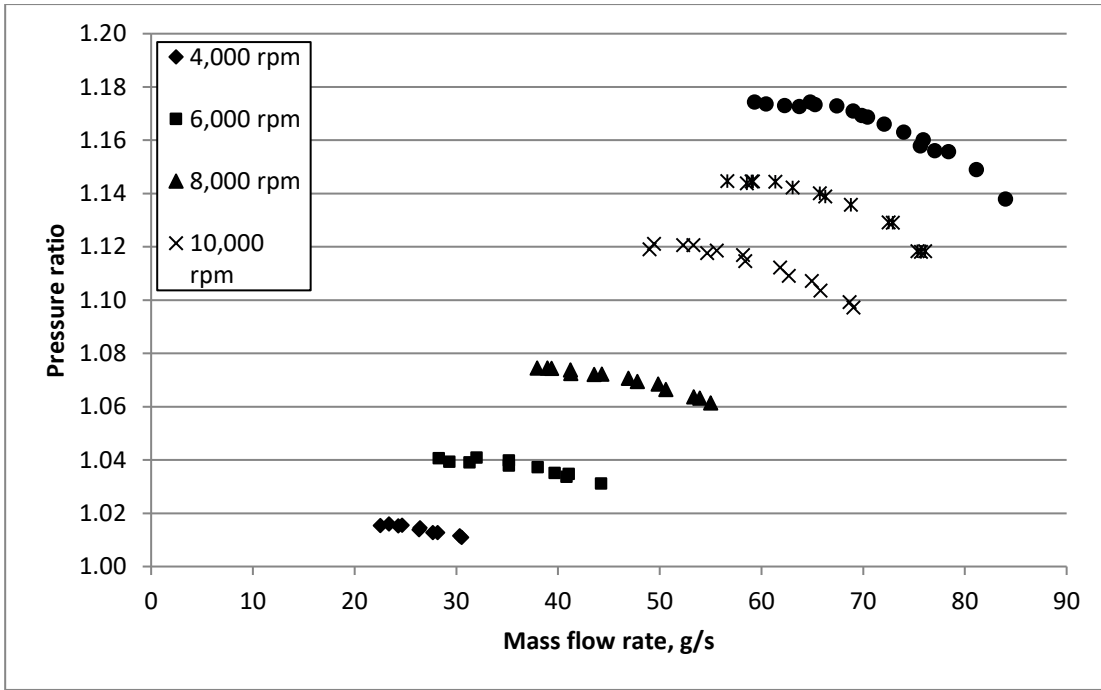


Figure 71: Compressor Map - Pressure Ratio

The maximum pressure ratio for each speed line was plotted against the shaft speed of the compressor. Figure 72 shows that the forward swept compressor shows an x^2 relationship in the same way as a conventional centrifugal compressor. The pressure ratio produced by the compressor is proportional to tip speed squared.

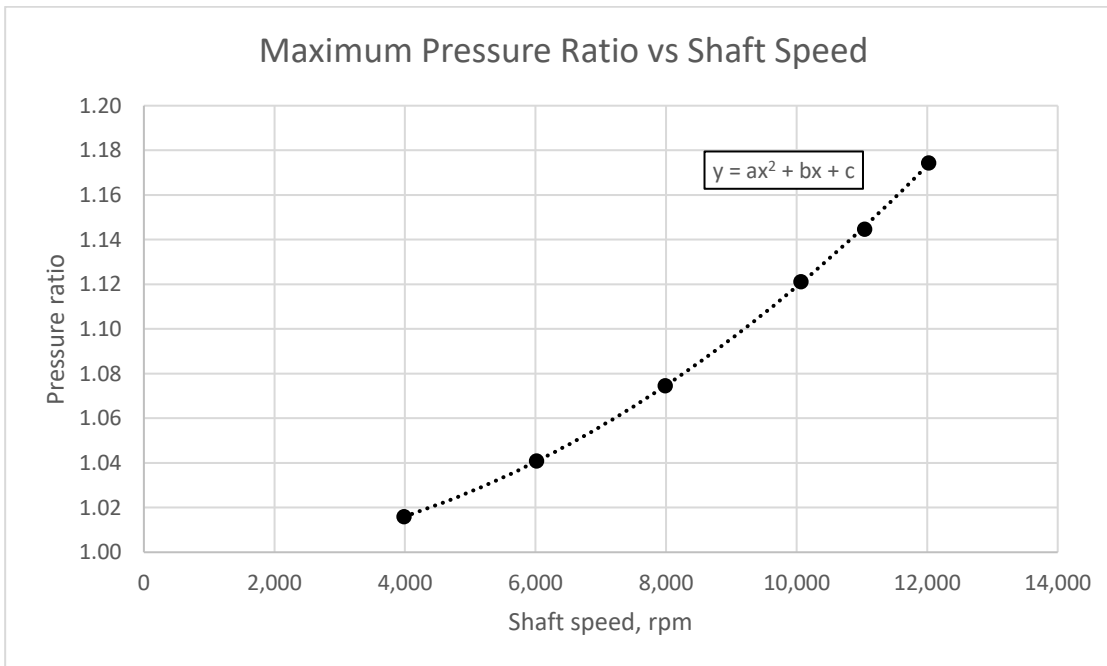


Figure 72: Maximum measured pressure ratio plotted against shaft speed

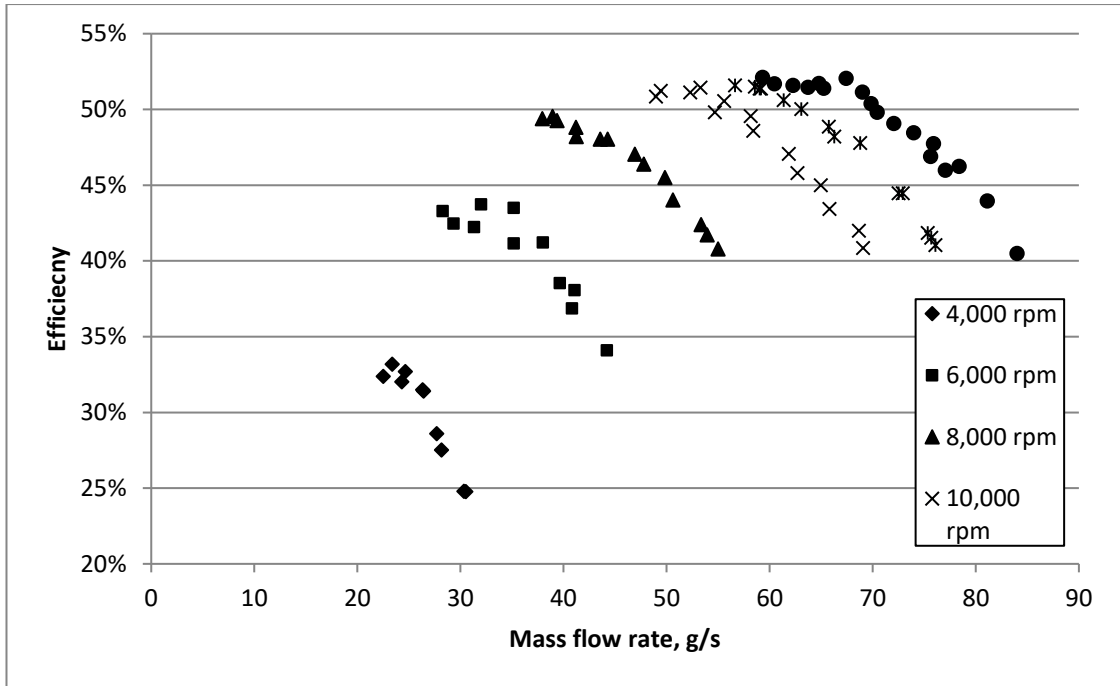


Figure 73: Compressor Map - Efficiency

Figure 73 shows how the efficiency varies with mass flow rate and speed for the highly forward swept compressor. This compressor exhibits peak efficiency at surge unlike conventional centrifugal compressors. These show peak efficiency at higher mass flow rates, with efficiency dropping off towards surge is reached, see Figure 74 below.

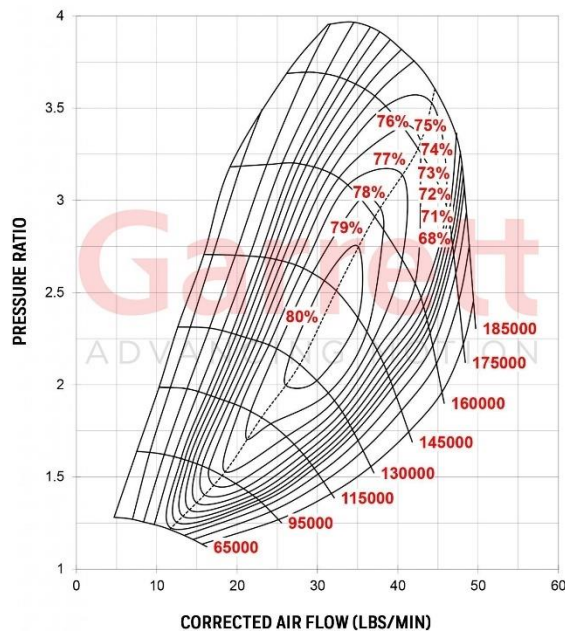


Figure 74: Garrett centrifugal compressor map (GARRETT MOTION INC., 2019)

4.4. Error Analysis

This section will describe the errors in the direct measurements and how those errors propagate through to the calculated values. The results from the experiments along with their errors are compared to the results of Vine to show the similarity in the experimental set up.

The measurement procedure relies upon a sensor converting the property to be measured in to an electrical signal, either current or voltage. This signal is read by the National instruments hardware and processed by a connected computer using a Labview programme shown in Figure 70. When the test rig is in operation, the data acquisition system (DAQ) records all data, both processed and raw, to a comma separated (csv) file every second. When a data point for the map is to be taken, the DAQ measures 10 seconds worth of data and averages it to give the values reported. This sample size was based upon calculating the standard error of the mean (Equation 38) to get a value of the same order as the error in the sensor.

$$SE_{\bar{x}} = \frac{\sigma}{\sqrt{n}} \quad \text{Equation 38}$$

The absolute accuracy of the individual sensors is given in Table 8. The National Instruments, NI, hardware could only record voltage signals, so accurate resistors were used to convert the current output of the sensors in to voltage signals. Current sensors were chosen as they are more immune to electrical interference which was likely due to the large AC motor driving the compressor. These resistors were $249\Omega \pm 0.1\%$ ($\pm 0.2 \Omega$). To calculate the sensor output directly from the voltage readings Equation 39 was used. This method was applicable to the Torque meter as it was the only sensor with a voltage output.

$$S_m = \frac{(S_{max} - S_{min})}{(V_{max} - V_{min})} (V_m - V_{min}) + S_{min} \quad \text{Equation 39}$$

For those sensors that output current (Pressure, converted temperatures and volume flow rate) it was necessary to use Equation 41 which includes a step to convert the voltage reading into current.

Table 8: Performance monitoring sensors with absolute accuracy

| Type | Location | Model | Range | Sensor accuracy |
|-------------|------------|---|-------------------------------|---|
| Pressure | Test cell | PTX 1400 | 0.8 to 1.2 bar absolute | ± 0.0018 bar |
| Pressure | Inlet | PTX 1400 | 0 to 1.6 bar absolute | ± 0.0024 bar |
| Pressure | Outlet | PTX 1400 | -0.5 to 1.0 bar gauge | ± 0.0015 bar |
| Pressure | FS4000 | PTX 1400 | 0 to 1.0 bar gauge | ± 0.0015 bar |
| Pressure | FV4000 | PTX 1400 | -1 to 4.0 bar gauge | ± 0.0060 bar |
| Torque | Shaft | Interface inline torque meter | 10 Nm | ± 0.01 Nm |
| Speed | Shaft | Interface inline torque meter | 6 pulse/rev TTL | ± 10 rpm |
| Flow meter | Downstream | ABB Swirl Flow meter | 65 to 1500 m ³ /hr | ± 7.5 m ³ /hr |
| Flow meter | Downstream | ABB Vortex flow meter | 15 to 150 m ³ /hr | ± 1.5 m ³ /hr |
| Temperature | Inlet | Pt100 with mA transmitter | 0 to 150 °C | Pt100 ± 0.25 °C ¹ Transmitter ± 0.15 °C |
| Temperature | FS4000 | Pt100 with mA transmitter | 0 to 300 °C | Pt100 ± 0.25 °C Transmitter ± 0.30 °C |
| Temperature | FV4000 | T-type thermocouple with mA transmitter | 0 to 150 °C | T-type ± 1.1 °C Transmitter ± 0.3 °C |
| Temperature | Test cell | K-type thermocouple | -40 °C to 1100 °C | ± 1.5 °C |
| Temperature | Outlet 1 | K-type thermocouple | -40 to 1100 °C | ± 1.5 °C |
| Temperature | Outlet 2 | K-type thermocouple | -40 to 1100 °C | ± 1.5 °C |
| Temperature | Outlet 3 | K-type thermocouple | -40 to 1100 °C | ± 1.5 °C |

¹ Pt100 error varies with measured temperature, however, the temperatures measured with these sensors never exceeded 50 °C therefore the author has chosen to take the error value at this temperature as representative for all temperatures to simplify the analysis.

Using Ohm's Law:

$$I = \frac{V}{R} \quad \text{Equation 40}$$

$$S_m = \frac{(S_{max} - S_{min})}{(I_{max} - I_{min})} \left(\frac{V_m}{R} - I_{min} \right) + S_{min} \quad \text{Equation 41}$$

Equation 41 was programmed directly into the Labview programme and all pressures were displayed in real time on screen as well as the pressure and voltage measurements being written to a csv file every second. Thermocouple measurements were converted from mV readings to temperatures directly using the built-in function of the NI 9213 module.

Using the methodology described in (Taylor, 1997) it can be shown that the following uncertainty relations hold true when the errors are independent and random; that the computed value q has an error δq from measured values x, \dots, z and their respective errors $\delta x, \dots, \delta z$:

$$q = f(x \dots z) \quad \text{Equation 42}$$

$$\frac{\delta q}{q} = \sqrt{\left(\frac{\partial x}{\partial q} \delta x\right)^2 + \dots + \left(\frac{\partial z}{\partial q} \delta z\right)^2} \quad \text{Equation 43}$$

Which simplify to Equation 45 and Equation 47.

$$q = x + \dots + z - (u + \dots + w) \quad \text{Equation 44}$$

$$\delta q = \sqrt{(\delta x)^2 + \dots + (\delta z)^2 + (\delta u)^2 + \dots + (\delta w)^2} \quad \text{Equation 45}$$

$$q = \frac{x \times \dots \times z}{u \times \dots \times w} \quad \text{Equation 46}$$

$$\frac{\delta q}{|q|} = \sqrt{\left(\frac{\delta x}{|x|}\right)^2 + \dots + \left(\frac{\delta z}{|z|}\right)^2 + \left(\frac{\delta u}{|u|}\right)^2 + \dots + \left(\frac{\delta w}{|w|}\right)^2} \quad \text{Equation 47}$$

The sources of error in the measurements come from the sensor itself, the resistor in the case of current sensors, the transmitter when a temperature sensor is converted to current at the probe, and the accuracy of the National Instruments hardware in reading the signal.

From Equation 40 and Equation 47, uncertainties in the measurement of current signals can be calculated from:

$$\frac{\delta I_m}{I_m} = \sqrt{\left(\frac{\delta V_m}{V_m}\right)^2 + \left(\frac{\delta R}{R}\right)^2} \quad \text{Equation 48}$$

Where δV is the error in the NI hardware and δR is the error in the resistor. δI_m can be plugged in to Equation 49 to calculate the error in the sensor units.

$$\delta S_m = \frac{(S_{max} - S_{min})}{(V_{max} - V_{min})} \delta V_m \quad \text{Equation 49}$$

The total error can then be calculated by assuming the errors sum and using Equation 45 where δS_m is the error from the measurement of the voltage, δS_A is the error of the sensor and δT_A is the error of the transmitter where one is used.

$$\delta S = \sqrt{(\delta S_m)^2 + (\delta S_A)^2 + (\delta T_A)^2} \quad \text{Equation 50}$$

The total error in measuring pressures, temperatures, volume flow and torque are shown in Table 9.

Table 9: Measurement errors

| Type | Location | Error | Unit |
|-------------|------------|--------|--------------------|
| Pressure | Test cell | 0.0019 | bar |
| Pressure | Inlet | 0.0032 | bar |
| Pressure | Outlet | 0.0025 | bar |
| Pressure | FS4000 | 0.0042 | bar |
| Pressure | FV4000 | 0.020 | bar |
| Torque | Shaft | 0.011 | Nm |
| Speed | Shaft | 10 | rpm |
| Flow meter | Downstream | 9.3 | m ³ /hr |
| Flow meter | Downstream | 1.6 | m ³ /hr |
| Temperature | Inlet | 0.35 | °C |
| Temperature | FS4000 | 1.2 | °C |
| Temperature | FV4000 | 1.3 | °C |
| Temperature | Test cell | 1.8 | °C |
| Temperature | Outlet 1 | 1.8 | °C |
| Temperature | Outlet 2 | 1.8 | °C |
| Temperature | Outlet 3 | 1.8 | °C |

The speed sensor was connected to a counter on the NI hardware. The error in the speed measurement is the sum of the sensor error (10 rpm) and NI error (50 ppm) and is also displayed in Table 9.

The pressure sensors measuring the inlet and outlet pressure were both gauge sensors. These need to be converted to absolute pressure by adding the local atmospheric

pressure to the readings. The error in the absolute measurement can then be found using

$$\delta P_1 = \sqrt{(\delta P_{1sens})^2 + (\delta P_{atm})^2} \quad \text{Equation 51}$$

$$\delta P_3 = \sqrt{(\delta P_{3sens})^2 + (\delta P_{atm})^2} \quad \text{Equation 52}$$

Pressure ratio is calculated using Equation 23, therefore error in this value can be computed from Equation 53.

$$\delta PR = PR \sqrt{\left(\frac{\delta P_1}{P_1}\right)^2 + \left(\frac{\delta P_3}{P_3}\right)^2} \quad \text{Equation 53}$$

Mass flow rate is calculated from Equation 24, therefore the error in density and mass flow are given by Equation 54 and Equation 55.

$$\delta \rho_m = \rho_m \sqrt{\left(\frac{\delta P_m}{P_m}\right)^2 + \left(\frac{\delta T_m}{T_m}\right)^2} \quad \text{Equation 54}$$

$$\delta \dot{m} = \dot{m} \sqrt{\left(\frac{\delta \rho_m}{\rho_m}\right)^2 + \left(\frac{\delta \dot{V}}{\dot{V}}\right)^2} \quad \text{Equation 55}$$

Efficiency is calculated from Equation 37 with PR substituted for P_3/P_1 . For the calculation of error, C_p is assumed to be a constant as the differences in the value are small.

$$\eta = \frac{\dot{m} C_p T_1}{\omega |\tau|} (PR^{(\gamma-1)/\gamma} - 1) \quad \text{Equation 56}$$

$$\delta \eta = \eta \sqrt{\left(\frac{\partial \dot{m}}{\partial \eta} \delta \dot{m}\right)^2 + \left(\frac{\partial T_1}{\partial \eta} \delta T_1\right)^2 + \left(\frac{\partial \omega}{\partial \eta} \delta \omega\right)^2 + \left(\frac{\partial \tau}{\partial \eta} \delta \tau\right)^2 + \left(\frac{\partial PR}{\partial \eta} \delta PR\right)^2} \quad \text{Equation 57}$$

$$\frac{\partial \dot{m}}{\partial \eta} = \frac{C_p T_1}{\omega |\tau|} (PR^{(\gamma-1)/\gamma} - 1) \quad \text{Equation 58}$$

$$\frac{\partial T_1}{\partial \eta} = \frac{\dot{m} C_p}{\omega |\tau|} (PR^{(\gamma-1)/\gamma} - 1) \quad \text{Equation 59}$$

$$\frac{\partial \omega}{\partial \eta} = -\frac{\dot{m} C_p T_1}{\omega^2 |\tau|} (PR^{(\gamma-1)/\gamma} - 1) \quad \text{Equation 60}$$

$$\frac{\partial \tau}{\partial \eta} = -\frac{\dot{m} C_p T_1}{\omega \tau^2} (PR^{(\gamma-1)/\gamma} - 1) \quad \text{Equation 61}$$

$$\frac{\partial PR}{\partial \eta} = \frac{\dot{m} C_p T_1}{\omega |\tau|} \left(\left(\frac{\gamma-1}{\gamma} \right) PR^{((\gamma-1)/\gamma)-1} \right) \quad \text{Equation 62}$$

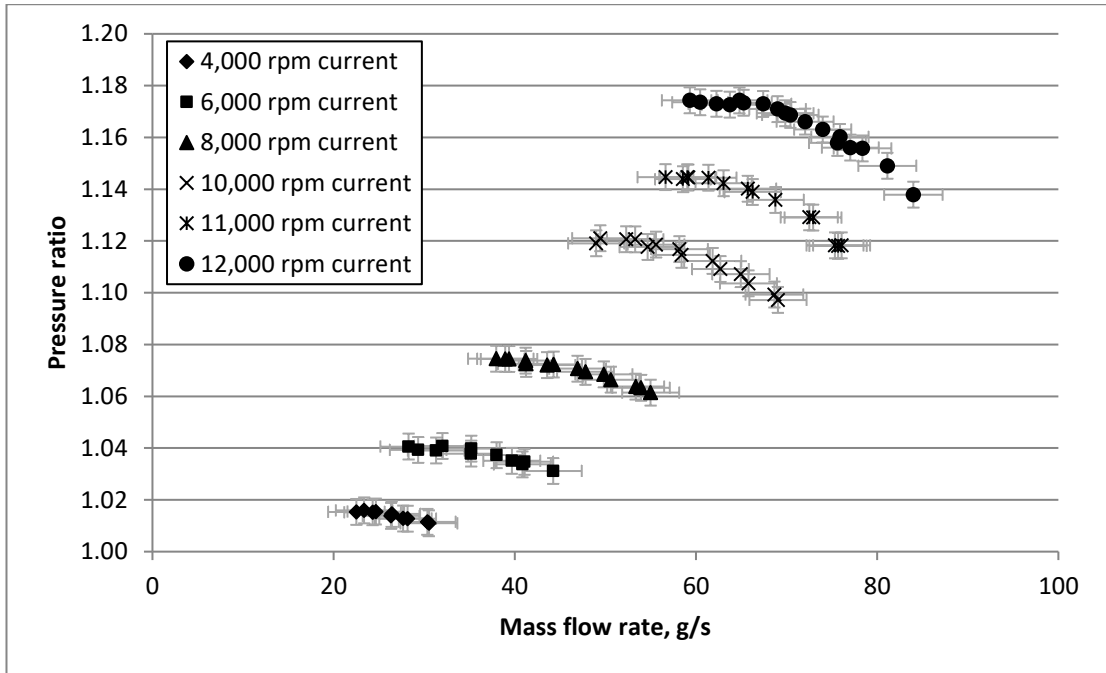


Figure 75: PR vs mass flow rate with error bars

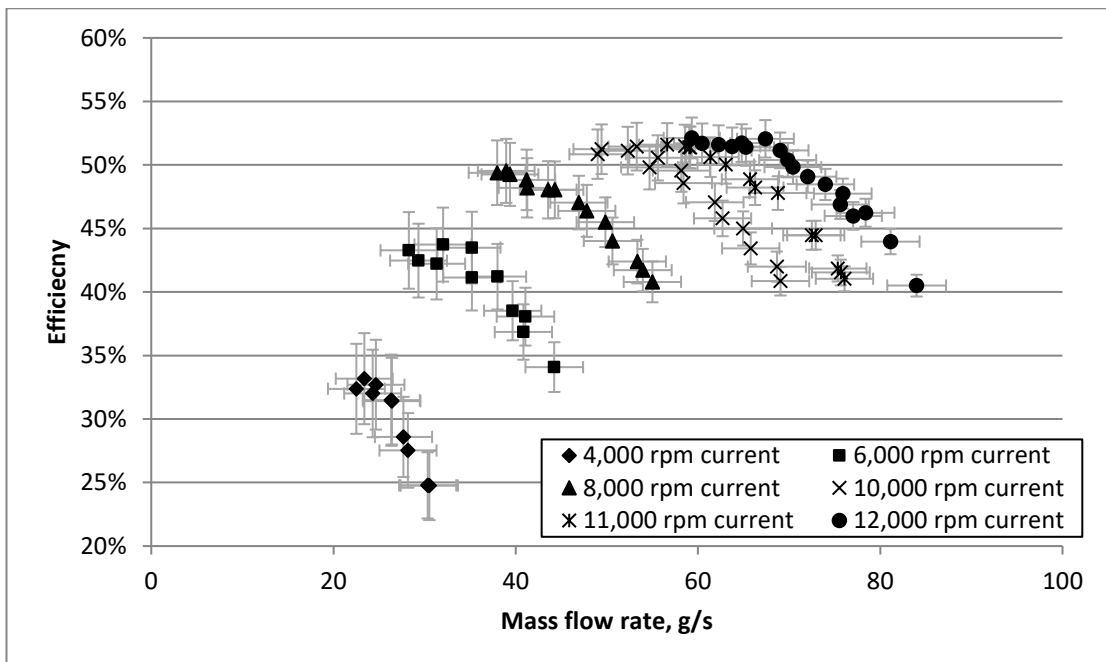


Figure 76: Efficiency vs mass flow rate with error bars

The mass flow rate shows a large error, this is due to three sensors being required to measure this quantity. To improve the error, higher accuracy sensors could be employed such as Pt100 temperature sensors directly connected to the National Instruments hardware. Higher accuracy volume flow rate sensors are also available but for this work their cost was prohibitive.

To allow direct comparison of Vine's data (Vine, 2005) with the data collected during this research, the mass flow and speed have been corrected to a nominal inlet temperature and pressure using an ideal gas based correction method (Cumpsty, 2004). The equations for calculating corrected speed, N_c , and corrected mass flow, \dot{m}_c , are shown in Equation 63 through to Equation 66.

$$\delta = \frac{P_1}{P_{nom}} \quad \text{Equation 63}$$

$$\theta = \frac{T_1}{T_{nom}} \quad \text{Equation 64}$$

$$N_c = \frac{N}{\sqrt{\theta}} \quad \text{Equation 65}$$

$$\dot{m}_c = \frac{\dot{m}_c \sqrt{\theta}}{\delta} \quad \text{Equation 66}$$

The nominal inlet pressure, P_{nom} , and nominal inlet temperature, T_{nom} , were chosen to be 101,325 Pa and 288.15 K respectively. Unfortunately, Vine has not published the full error analysis for the 6 vaned diffuser so only the measurements can be compared.

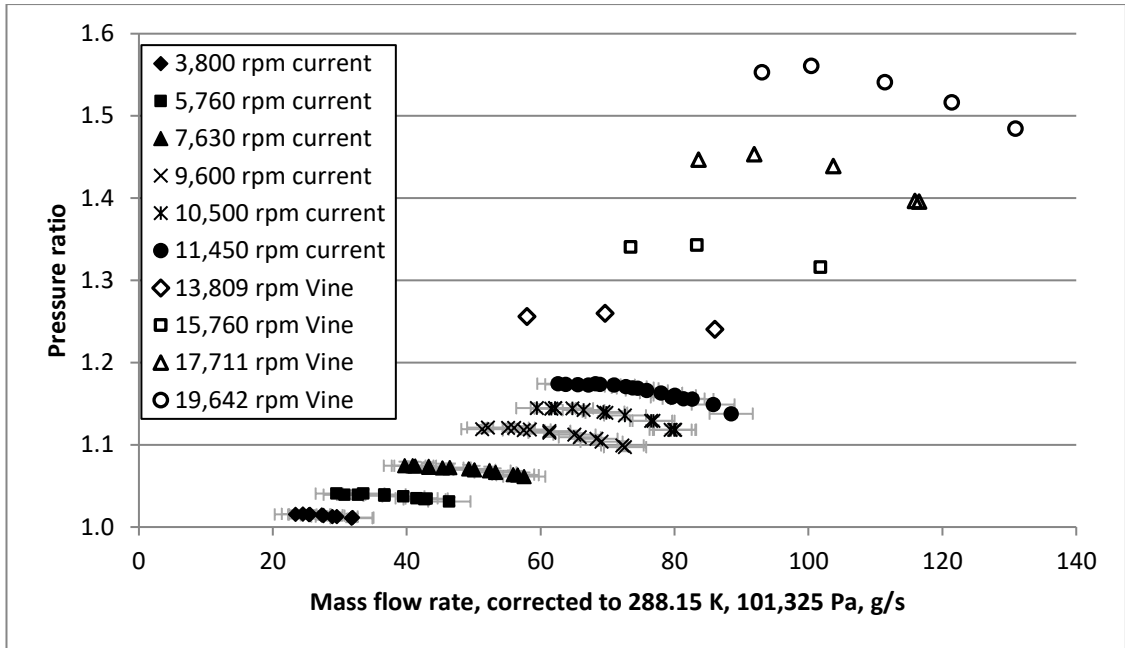


Figure 77: PR vs mass flow rate comparison with Vine's data

Figure 77 shows the data collected by Vine and in this work. As stated earlier, a damaged layshaft caused the failure of the torque sensor resulting in a maximum speed of 12,000 rpm for performance data collected from the new test rig.

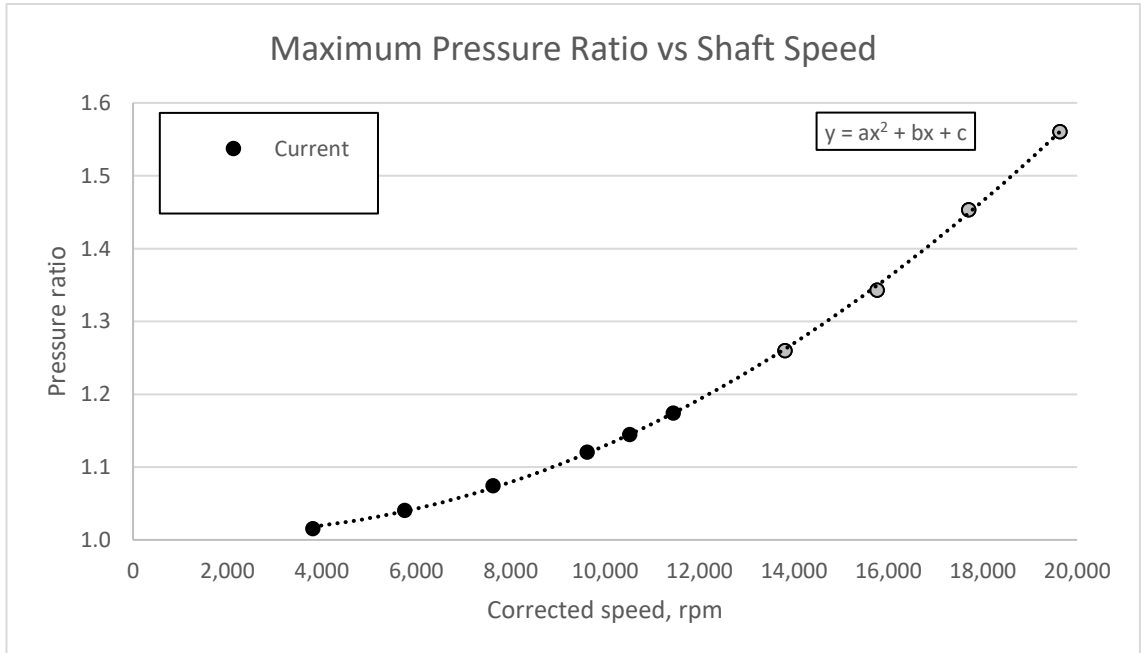


Figure 78: Maximum pressure ratio vs Speed for Vine and Current Work

Although there is no overlap in the data due to the lowest speed measured by Vine and the maximum speed limit of the current data, Figure 78 shows that when the maximum

pressure ratio is plotted against corrected speed the pressure ratio data is consistent between the two test rigs.

The surge and choke lines are not consistent between the test rigs. The mass flow rate of a compressor is dependent upon many things such as upstream pipework, Vine had none, the current rig used a filter/silencer attached to the inlet to reduce the audible noise during testing and protect the rig by filtering and dust/grit in the air. Downstream pipework is also an important factor in compressor measurements. The more blockage there is downstream of the compressor, the more easily the compressor will choke, reducing the width of the map as in Vine's work. Geometric difference also plays a part. Vines impeller had the minimum machinable radius (approx. 0.2 mm) at the root of the blade whereas the new impeller has fillets of 2.0 mm to reduce the stress. Vine's impeller also had a different labyrinth seal arrangement with more teeth on the shroud at a different diameter to those on the new rig. The eye of the new impeller has a smaller area than Vine's see Figure 79 and Figure 80.

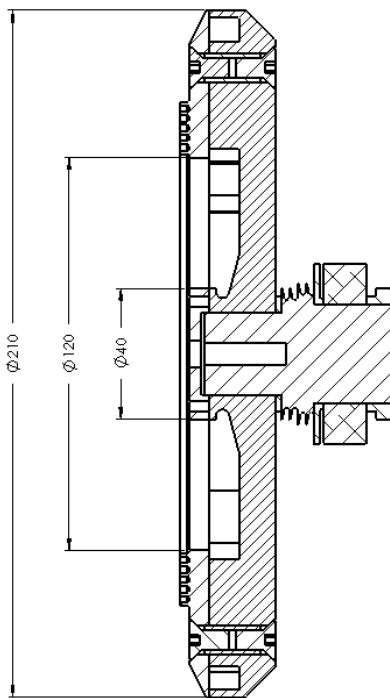


Figure 79: Inlet geometry of Vine's impeller

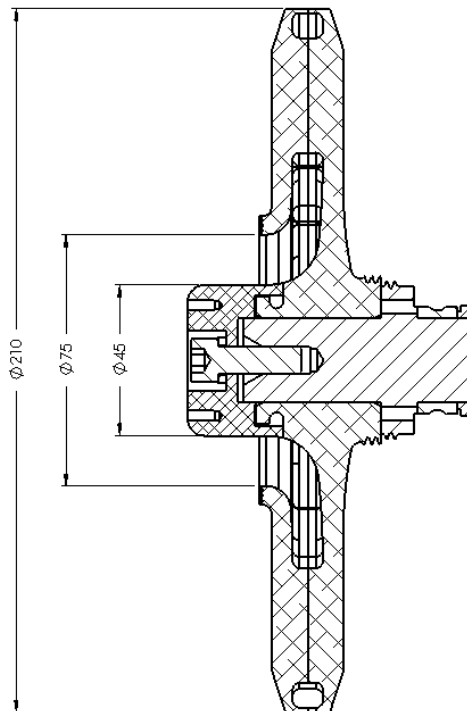


Figure 80: Inlet geometry of new impeller

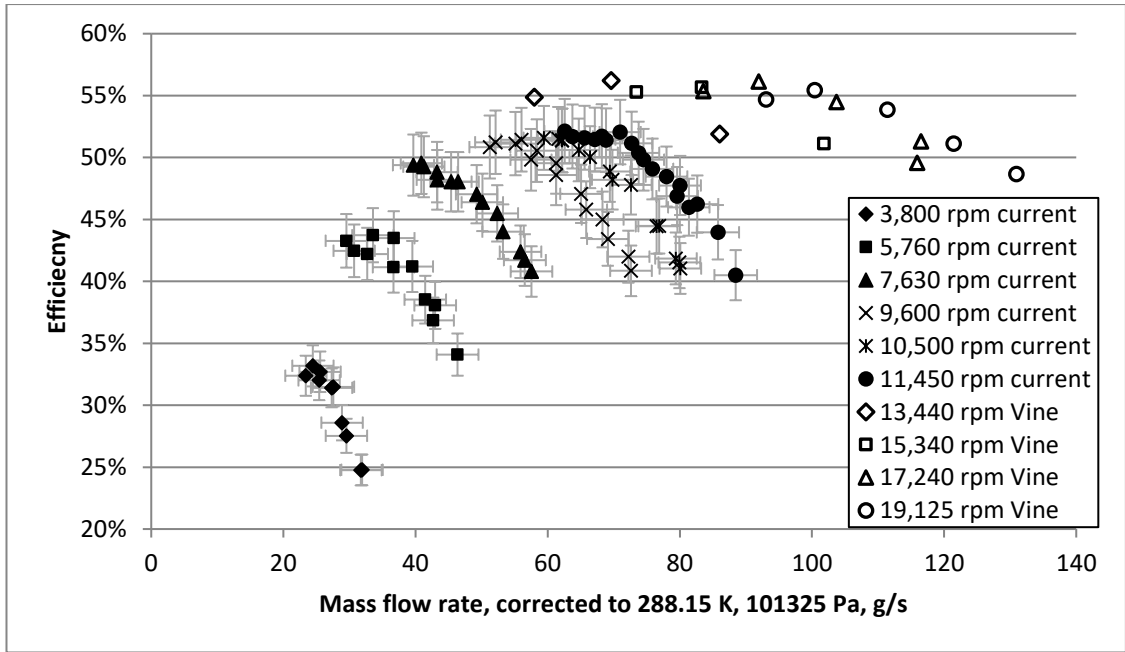


Figure 81: Efficiency vs mass flow rate comparison with Vine's data

Figure 81 and Figure 82 show the comparison between Vine's efficiency data and the current work. Figure 82 shows the maximum efficiency of both rigs for the corrected speeds measured. While the agreement for efficiency is not as strong as for pressure ratio, the trend is consistent. The differences are most likely due to the difference in calculating efficiency. Vine used the energy balance method which tends to give an optimistic measurement due to heat lost from the test rig. A torque meter was used in the new rig to allow direct measurement of the work input giving a higher accuracy result.

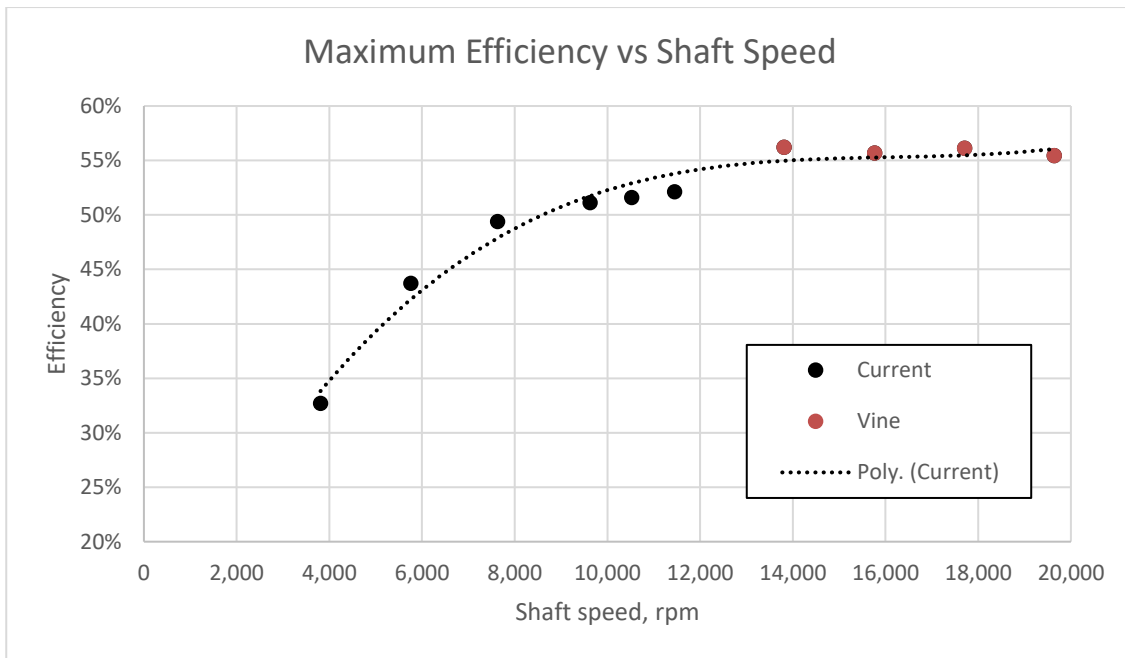


Figure 82: Maximum Efficiency vs Speed for Vine and Current Work

This chapter has presented the design of the optical test rig and the engineering design and analysis that was undertaken to produce it. Performance data – mass flow rate, pressure ratio and efficiency – have been presented and compared to the data from previous research. This comparison has shown that the test rigs produce consistent data even though there is no overlap in measurements due to limitations in the maximum speed of the new test rig. Also in this chapter, error analysis of the measurements has been presented showing the limitations in the measurement accuracy.

5. Flow Visualisation

This chapter presents the results of the flow visualisation using high-speed photography. The experimental set up can be found in section 3.1.1. The aim of this work was to take qualitative measurements of the flow field within the diffuser. This was undertaken to gain an initial understanding that could be used to drive the quantitative Laser Doppler Velocimetry measurements that were subsequently taken.

Figure 83 shows the areas imaged using high speed photography as described in Chapter 3.

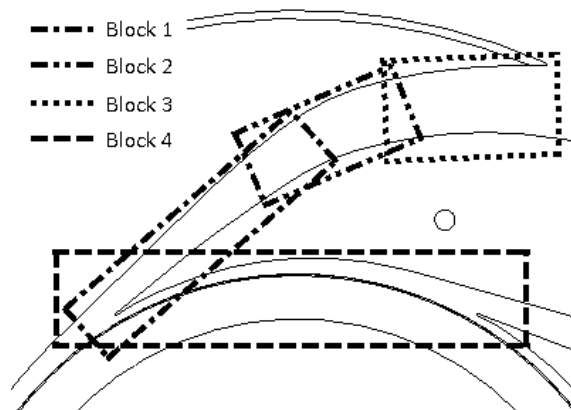


Figure 83: Areas imaged using high speed photography

5.1. Block 1 Results

Block 1 was imaged using the forward scatter method at compressor speeds between 2,000 and 4,000 rpm. Speeds over 4,000 rpm produced high vibration and it was not safe to run at these increased speeds.

Figure 84 to Figure 87 show the smoke pattern at speeds of 2,000, 2,500, 3,000 and 4,000 rpm respectively. All the images were taken at 17,500 with a shutter speed of 1/69,000 sec and an image size of 896 x 192 pixels. The smoke generator used to seed the flow had a fixed output which explains the lower intensities seen in the higher speed images – the higher flow rate diluted the smoke.

These images were recorded 0.34 milliseconds apart (each image is separated by 5 frames) which equates to 4.11° of impeller rotation at 2,000 rpm and 1.34° at 4,000 rpm. One impeller blade passes the diffuser blade every 2.5 milliseconds at 2,000 rpm and 1.25 milliseconds at 4,000 rpm.

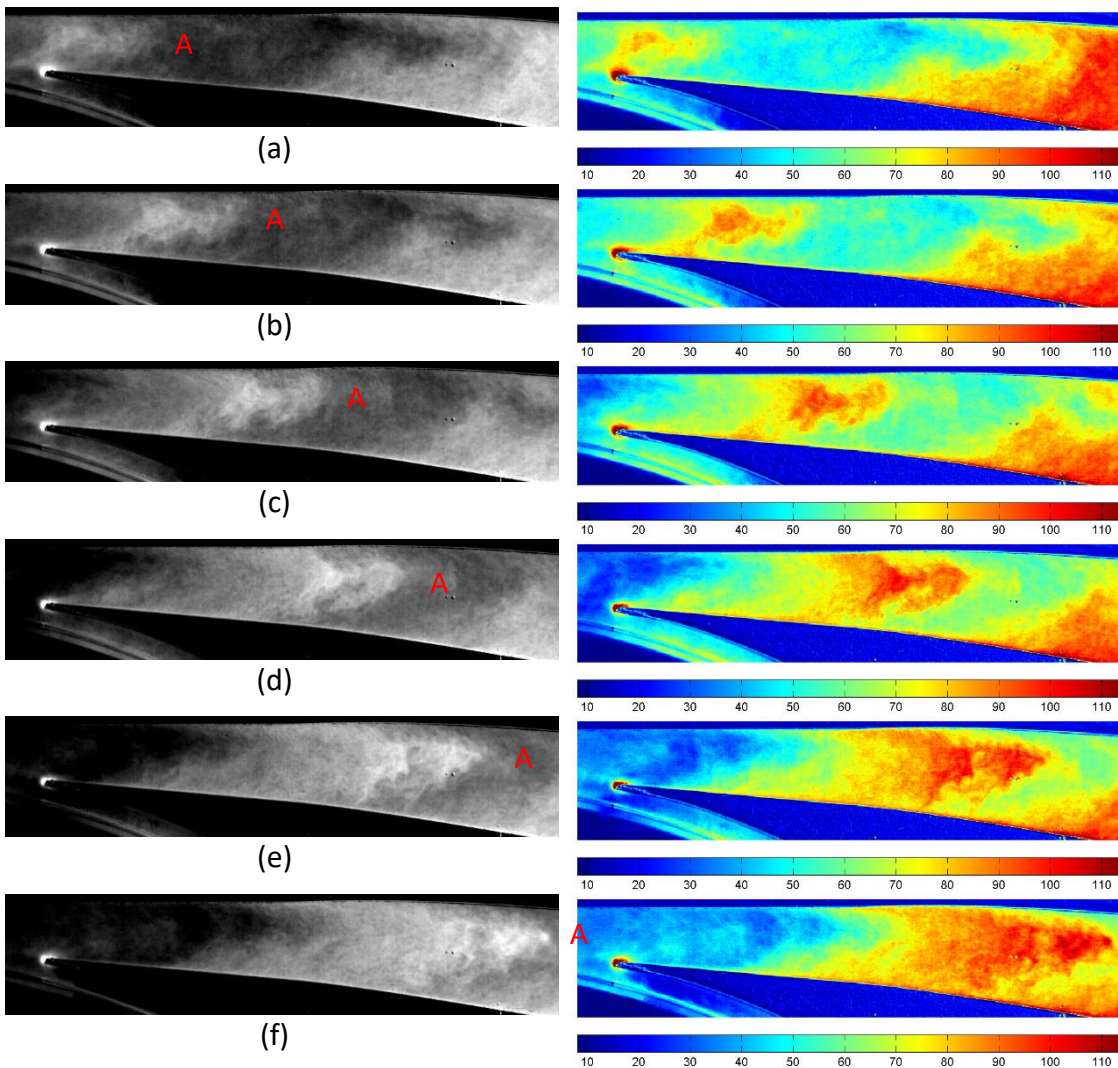


Figure 84: Flow at 2,000 rpm shown as a brightened image (left) and with a colourmap applied (right)

The images on the left show the images with the background removed and brightened. The images on the right show the same frame but with a colourmap applied. The scale is showing the pixel intensity. The letters identify the leading edge of a smoke pulse as it moves through the diffuser passage.

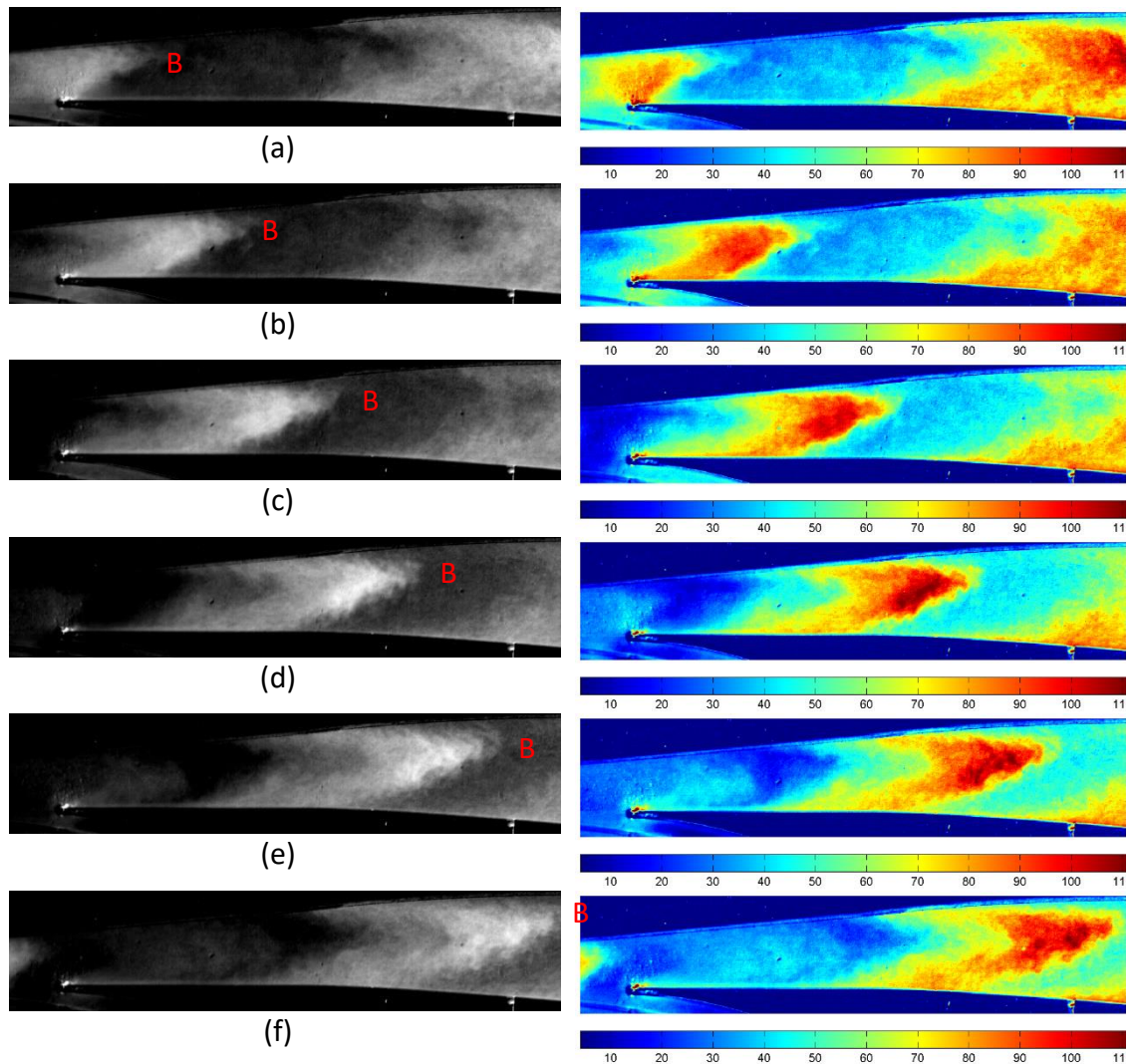


Figure 85: Flow at 2,500 rpm shown as a brightened image (left) and with a colourmap applied (right)

At lower speeds, 2,000 rpm and 2,500 rpm the smoke forms an arrowhead shape, whereas at 3,000 rpm and 4,000 rpm the smoke is closer to a straight line across the passage with rounded corners near the walls. There are also distinct pulses of smoke moving through the diffuser, as identified by the letters on the images. This confirms one hypothesis, that the compressor generates pulsing flow in the diffuser. Whether this is a result of the geometry and if it is necessary for the functioning of the compressor are impossible to determine from these results.

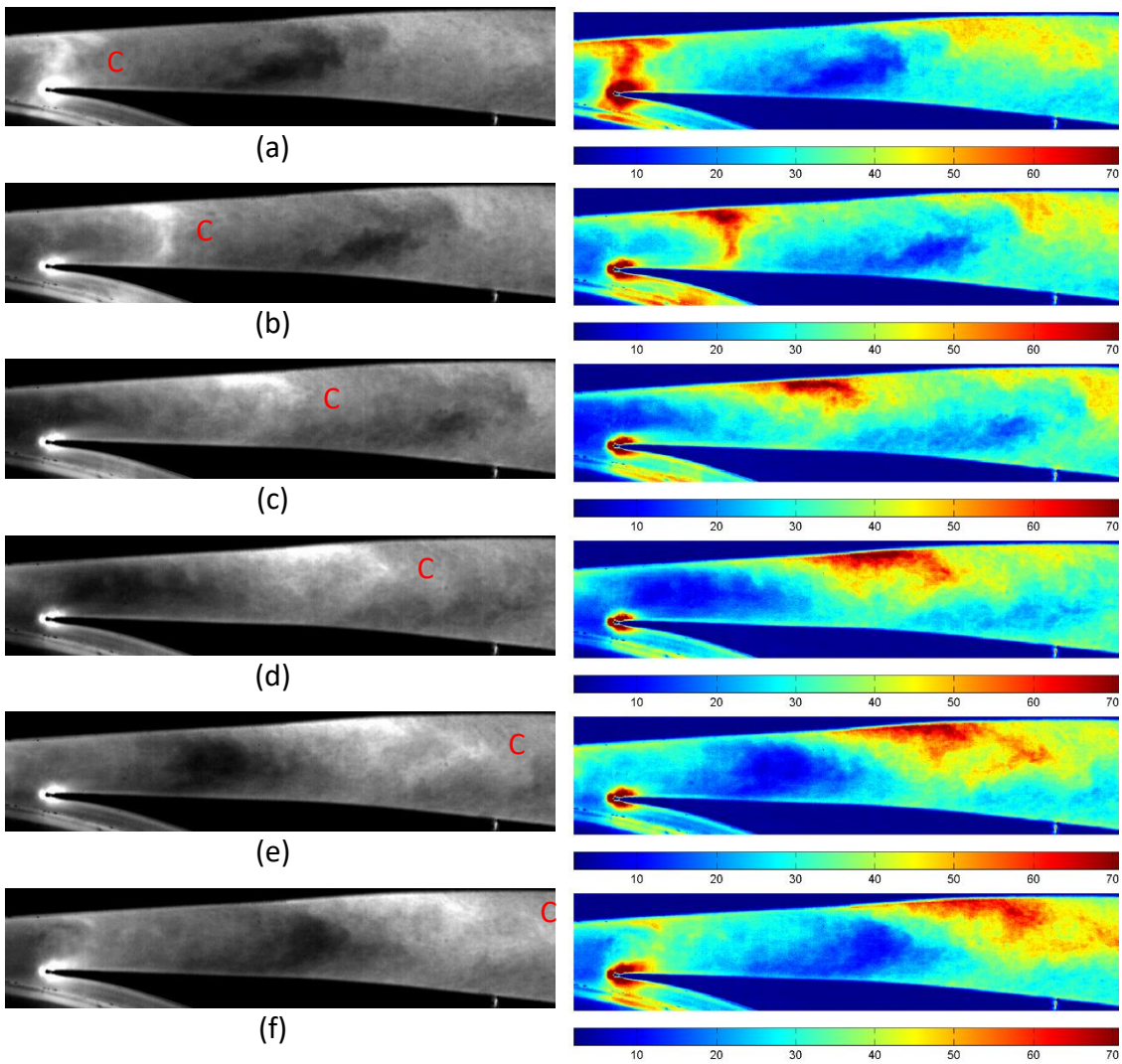


Figure 86: Flow at 3,000 rpm shown as a brightened image (left) and with a colourmap applied (right)

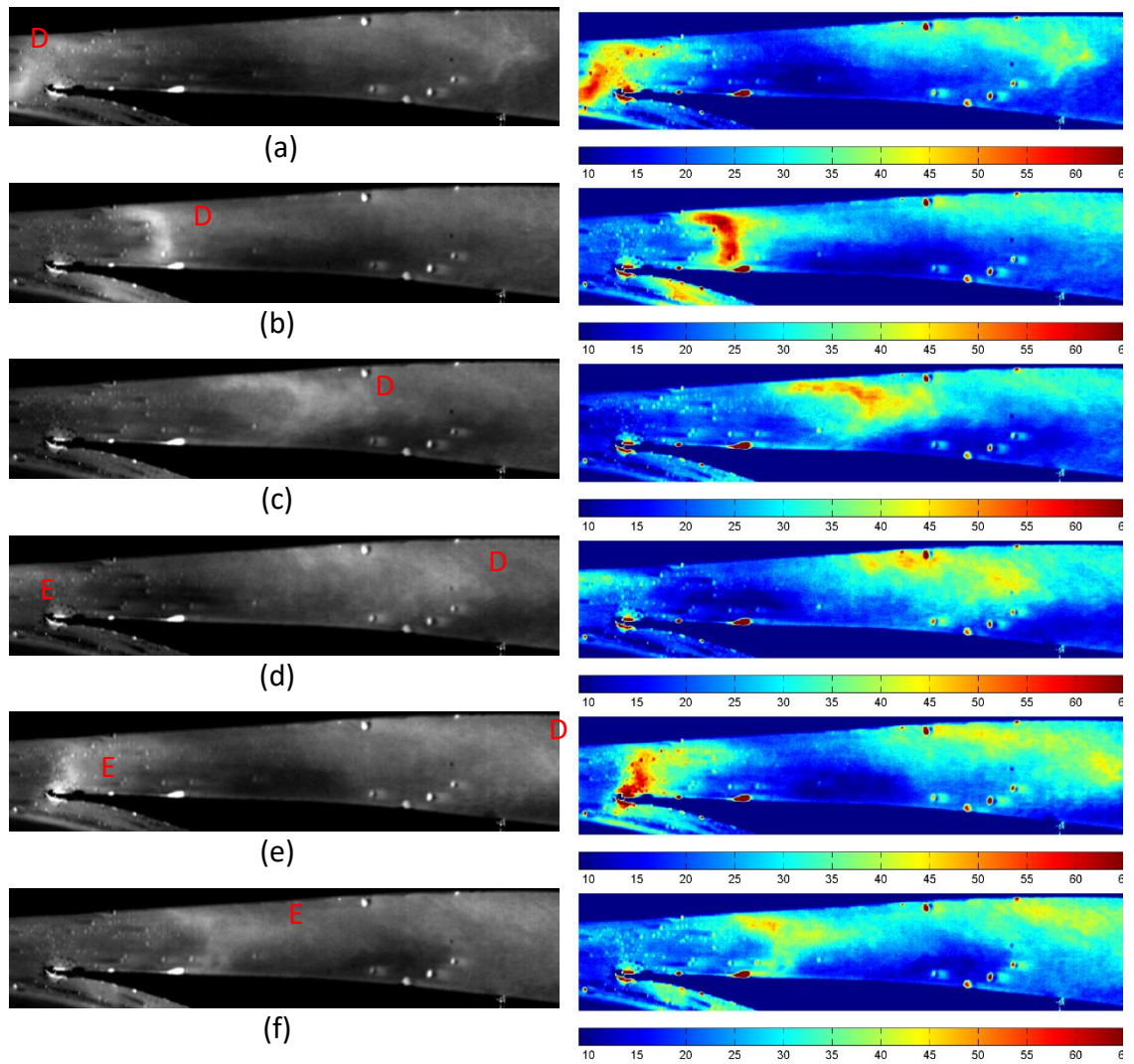


Figure 87: Flow at 4,000 rpm shown as a brightened image (left) and with a colourmap applied (right)

The images at 3,000 and 4,000 rpm both show how the leading edge of the diffuser splits the flow with the majority moving into the main diffuser passage, while the remainder moves into the vaneless space between the impeller and blade. The images in Figure 88 are showing every second frame, and are therefore separated by 0.114 milliseconds.

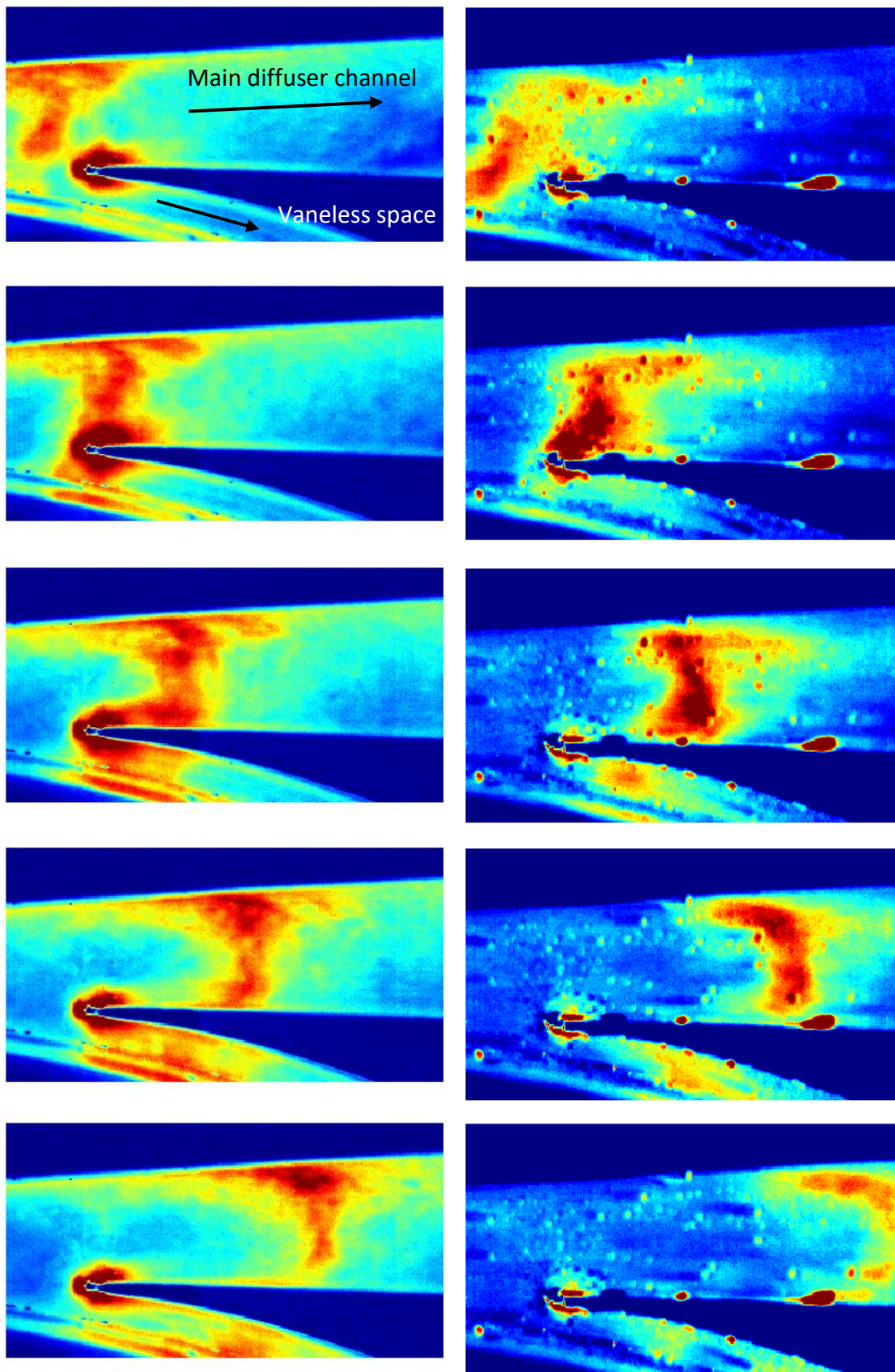


Figure 88: Flow splitting either side of the leading edge of the diffuser blade, 3,000 rpm on the left, 4,000 rpm on the right

5.1.1. Pulse Frequency

The images can be used to calculate the frequency at which the smoke pulses move through the diffuser. By counting the number of frames between consecutive pulses of smoke passing through the throat of the diffuser it was possible to calculate the time between pulses. At 2,000 rpm it was seen that there were 43 frames between pulses, which equates to 2.5 milliseconds. At this rotational speed, this is the time taken for each blade to pass. This relationship between pulses and blade passing frequency was also shown to be true at 2,500, 3,000 and 4,000 rpm. It is unclear as to what the position of the impeller is in relation to the pulses of smoke. The tests would need to be repeated using a shaft encoder to record the impeller position relative to each image.

5.1.2. Flow Speed

The speed of the bulk flow was estimated by measuring how far the smoke front moved over a number of images as shown in Figure 89 and Figure 90. These images were constructed by manually tracing the wave front as it moved through consecutive images. At 2,000 rpm, the smoke travelled 68mm over 40 frames (2.29 milliseconds), giving a speed of 30 m/s. At 4,000 rpm, the smoke travelled 16mm over 6 frames (0.343 milliseconds), giving a speed of 46m/s.

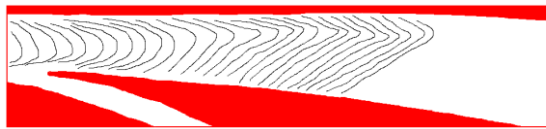


Figure 89: Smoke fronts at 2,000 rpm



Figure 90: Smoke fronts at 4,000 rpm

These speeds agree with the flow speed calculated based on the volume flow rate. The average cross-sectional area of the diffuser passage in block 1 is 125mm². At 4,000 rpm the volume flow rate out of the compressor was 87.0 m³/hr, giving an average flow speed of 43.3 m/s. The flow rate could not be measured at 2,000 rpm as it was below the range of the flow sensor.

5.1.3. Reynolds Number

Reynolds number is a dimensionless number used in all areas of aerodynamics and is introduced in section 1.3. The Reynolds number can be used to assess whether a flow is laminar or turbulent. Reynolds number is a measure of the ratio of internal forces to

viscous forces. As the number is dimensionless it allows experiments with dynamic similarity to be compared.

Laminar flows occur at low Reynolds number, generally less than 2,000 when using the pipe diameter as the characteristic length, where the fluid flow is in parallel layers, with no disruption between the layers. Turbulent flow occurs at higher Reynolds numbers, typically above 3,000, and is characterised by turbulent eddies leading to lateral mixing and a more uniform velocity profile across the pipe.

From the flow speeds detailed in Section 5.1.2 it was calculated that the average Reynolds number of the flow in Block 1 at 4,000 rpm is 28,000. This puts the flow well into the turbulent regime. Turbulent flow is desirable in this case as a turbulent boundary layer tends to be less inclined to separate from the walls than a laminar flow. This in turn enables the diffuser to achieve a higher pressure rise.

5.2. Results – Block 2

Block 2 was imaged at 12,500 fps, at a shutter speed of 1/101,000 seconds and an image size of 768 x 304 pixels.

Figure 91 shows the images from block 2 with the compressor operating at 2,000 rpm. These images show the flow moving around the outside of the bend and show where the flow appears to separate from the inner wall. Images taken at higher rotational speeds did not have enough light to be able to image the flow satisfactorily.

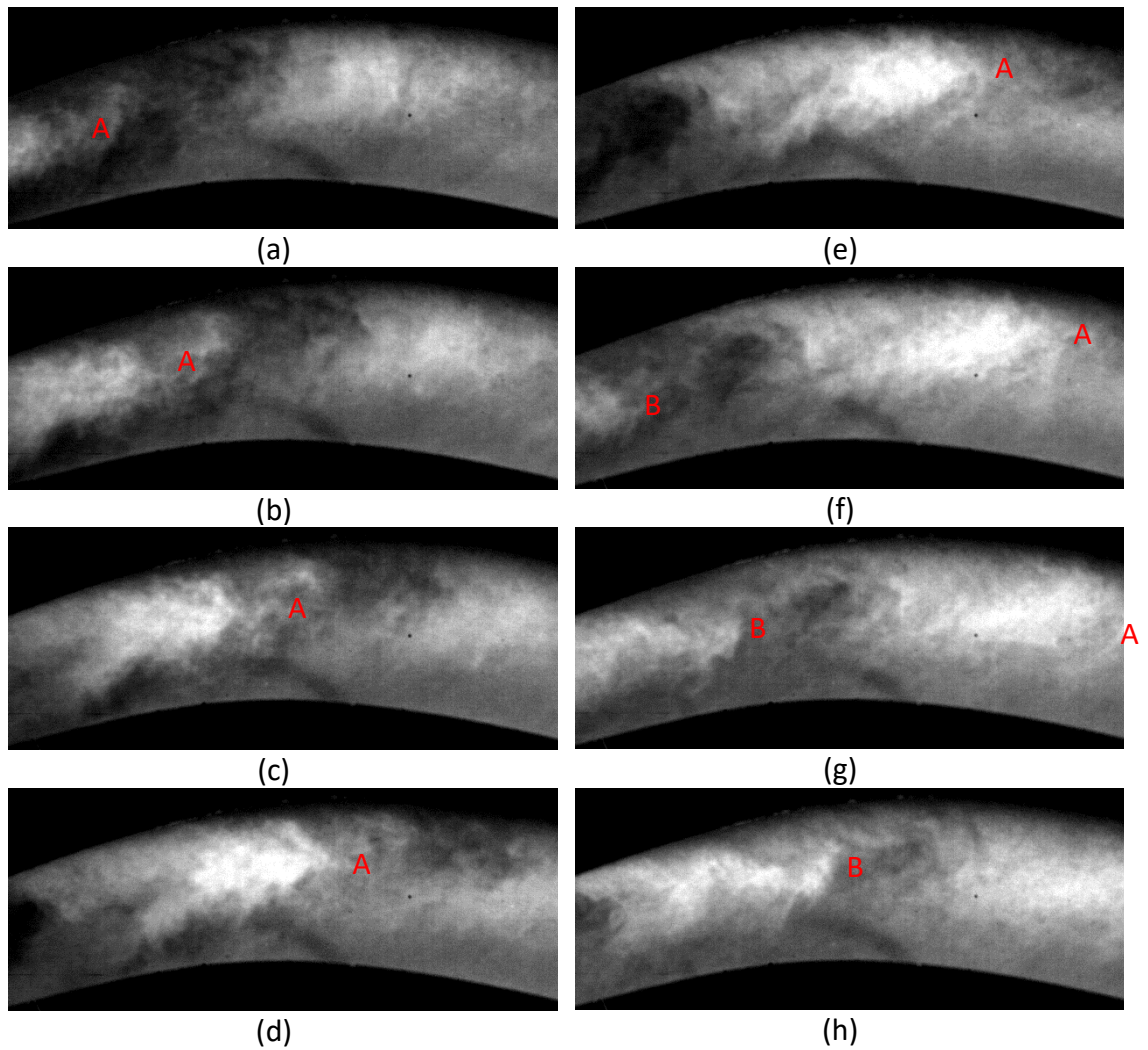


Figure 91: Block 2 imaged at 2,000 rpm

As above, these images provide areas to focus the LDV investigation on, but do not have enough quality to offer any conclusive insights.

5.2.1. Flow Speed

The images in Figure 91 can be used to estimate the speed of the flow giving an indication as to whether the flow is slowing down compared to the speeds calculated in section 5.1.2.

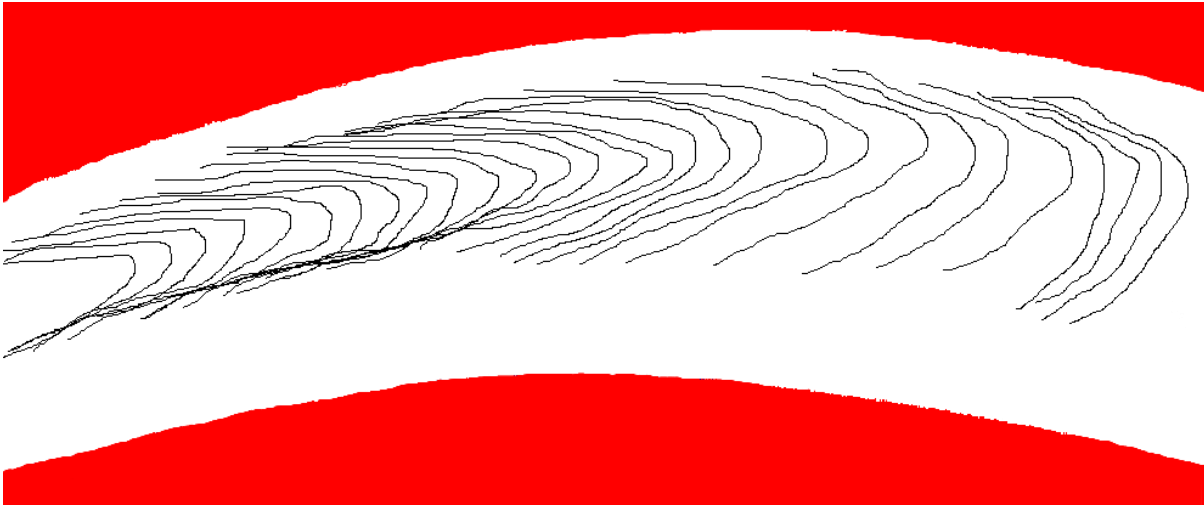


Figure 92: Smoke front in block 2 at 2,000 rpm

At 2,000 rpm, the smoke travelled 56.6mm over 33 frames imaged at 12,500 fps, giving a speed of 21 m/s. This shows the bulk flow speed has dropped considerably, down from 30 m/s in the previous section, which is consistent with the diffuser's function to convert kinetic energy into pressure.

5.3. Results – Block 3 and 4

Due to the limited amount of time that the camera was available and the limited amount of light, the images of blocks 3 and 4 were unsatisfactory.

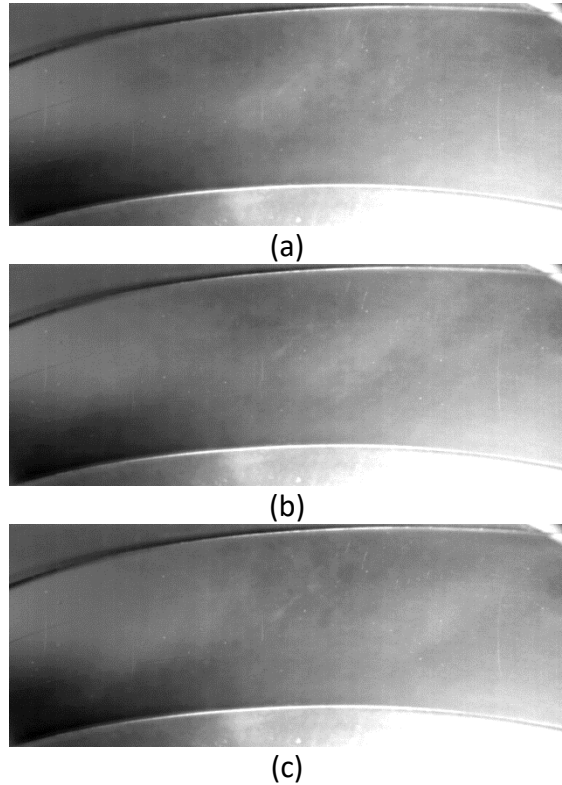


Figure 93(a-c): Block 3 results

Too much shadow was present in the images to draw any conclusions from these results. In any future work, this block would benefit from multiple light sources to remove areas of shadow.

Block 4 would have benefited from having an anodised back plate instead of Perspex, to stop any reflections from surfaces behind the rig while using a backwards scattering technique.

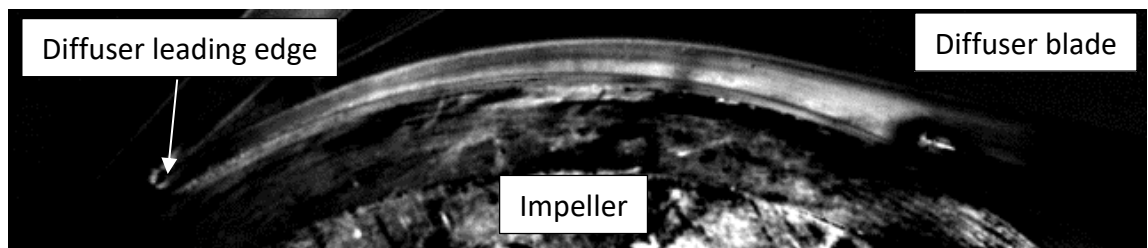


Figure 94: Block 4 results

This chapter presented the results of the high speed photography of the diffuser passage. The aim was to collect qualitative information on the flow field within the diffuser. The diffuser was split into 4 areas of investigation. The first containing the leading edge of the diffuser and straight portion of the diffuser was most informative. Smoke could be seen pulsing through the passage at the frequency of impeller rotation, which supports the hypothesis that the highly forward swept compressor has pulsing flow. An estimate of the velocity of the flow, calculated from the leading edge of the smoke pulses, has shown that the flow in the diffuser is turbulent as the Reynolds number is 28,000 at 4,000 rpm, well in excess of the 3,000 required for turbulent pipe flow.

The second area investigated was at the bend in the diffuser. The hypothesis that the flow separates at the bend could not be proven due to a lack of light causing shadows in the passage. Sections 3 (the bend to the diffuser exit) and 4 (the vaneless space) did not yield any results due to the low quality of the images. In future, anodising the back of the passage and lighting using a back scatter technique would give better results.

6. Laser Testing

This chapter presents the results of the Laser Doppler Velocimetry testing. These test provided a quantitative measure of the flow field within the diffuser and will be used to validate the hypotheses presented in Section 1.6 – that the flow is pulsing and separating near the bend.

6.1. LDV Results

The red dots in Figure 95 show the locations measured during the LDV testing. There are limited points around the exit of the impeller as the oil used to seed the flow tended to stick to the diffuser surfaces, prevent measurements.

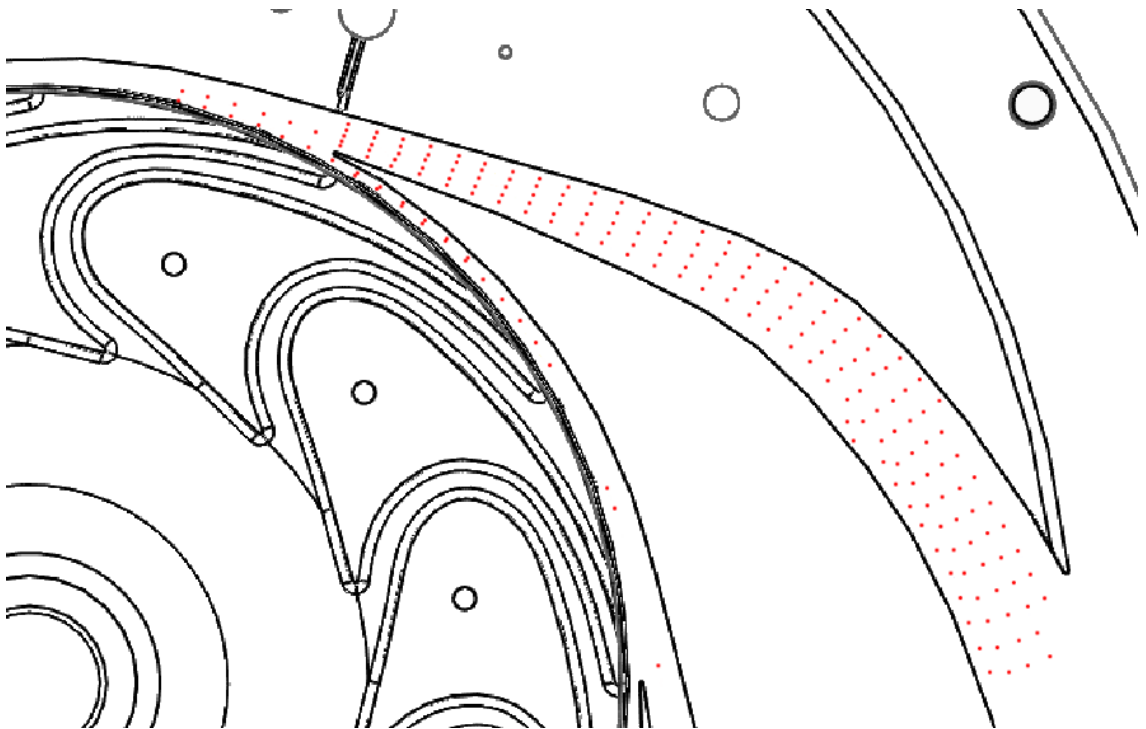


Figure 95: Positions measured with LDV

For each point where data was taken, 2 measurements were made. One in the horizontal direction, and one in the vertical. The LDV set up available did not have the capability to record these measurements concurrently. The processor outputted a comma separated file containing 6 data fields.

Table 10: Data fields recorded by LDV software

| |
|--|
| Time (s) |
| Frequency (MHz) |
| Velocity (m/s) |
| Rotational position (degree) |
| Rotational position out of tolerance (true/false) |
| Gate time (s) |

Frequency is the raw measurement and Velocity is the calculated value based upon test set up, as described in Section 3.1.3 Equation 15. Rotational position and out of tolerance are based upon the encoder and the internal synchronisation giving the rotational position of the impeller when the sample was collected, and whether the current rotation was within tolerance, see Section 3.1.3. The gate time is the time the particle being measured spent within the control volume.

Due to the high speed nature of this compressor, a high accuracy encoder couldn't be found. Instead a one-pulse per revolution encoder was connected to the LDV software. This pulse was used to synchronise a clock within the software. The clock output 3600 ticks between encoder pulse, equating to 0.1 degrees of impeller rotation. If the deviation between the 3600th tick and the encoder pulse was greater than 0.3 degrees (3 ticks) then the data was marked as "out of tolerance".

A Matlab programme was written to remove any samples that were out of tolerance and then average the remaining data over a specified rotational angle, the code is shown in Chapter 12 Appendix: Matlab programmes. Angles were tried from 0.25 degree up to 3 degrees to find the minimum angle that could be averaged without a change in the value, see Figure 96 and Figure 98. Values averaged over 0.25 degrees showed too much variation as there was not enough data to fully resolve to this angle. Whereas 3 degrees has too much smoothing and therefore a loss of detail. One degree was chosen as the best compromise between resolution and accuracy.

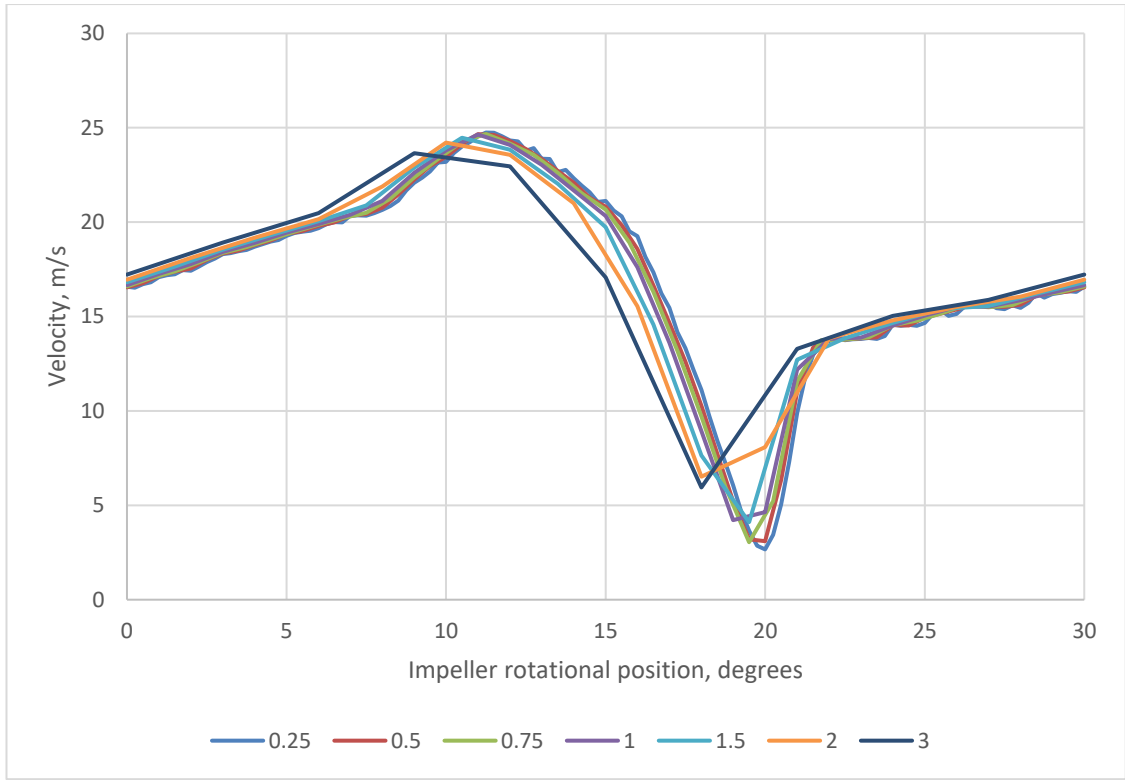


Figure 96: Averaging angle effect on velocity results – horizontal direction

In Figure 96, the legend refers to the angle that the velocity values were average over. The x-axis is the rotational position relative to the diffuser as shown in Figure 97.

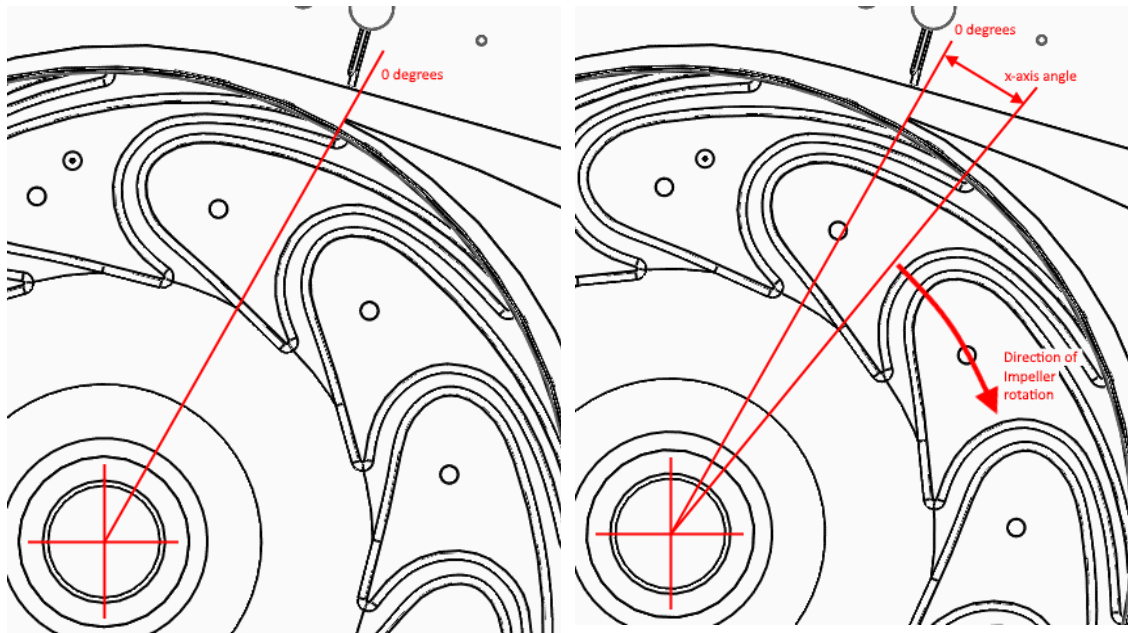


Figure 97: Angle definition for x-axis in Figure 98 and Figure 99 below

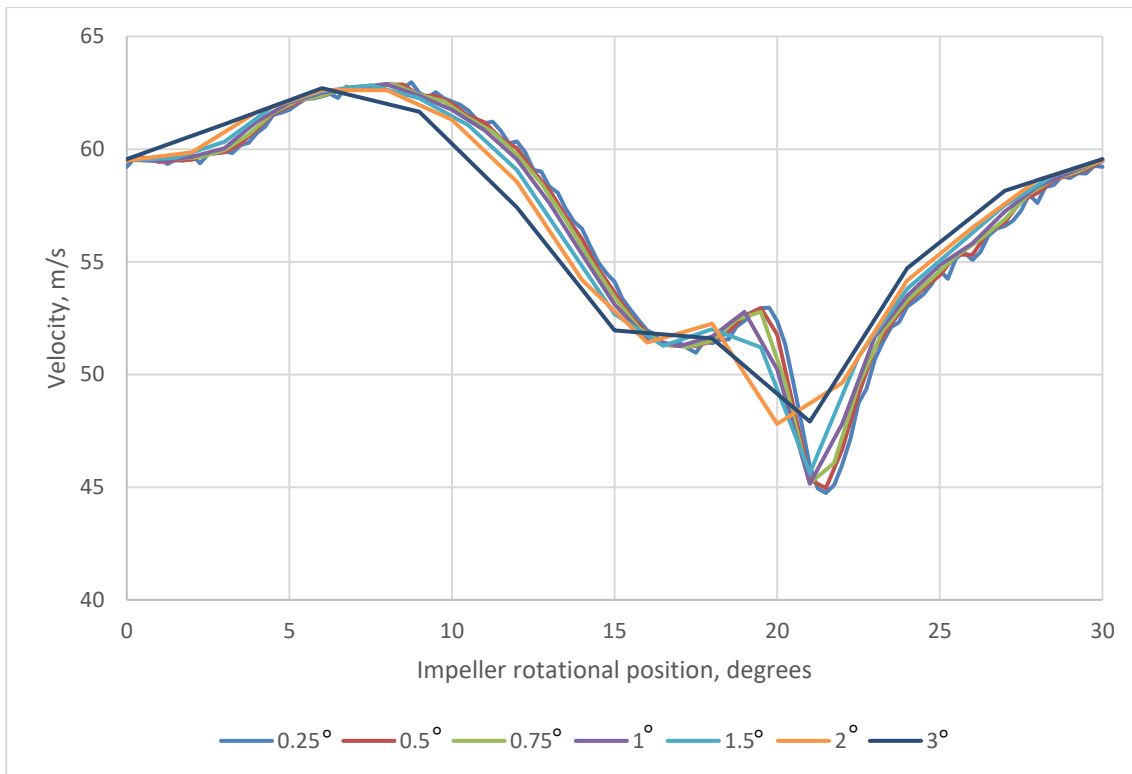


Figure 98: Averaging angle effect on velocity results – vertical direction

For each measurement, 150,000 samples were collected. Of these, on average, 40,000 samples were out of tolerance, leaving 110,000 samples that were in tolerance. Averaging over 1 degree gave 305 points per measurement per degree. However, the impeller is axis-symmetric, so each 1 degree is repeated 12 times per impeller rotation. This meant 3,670 samples were averaged per measurement per degree of rotation. A second Matlab programme was written to calculate the resultant velocity vector for each measurement based upon it's horizontal and vertical components. These were then plotted over a line drawing of the impeller and diffuser as shown in Figure 99.

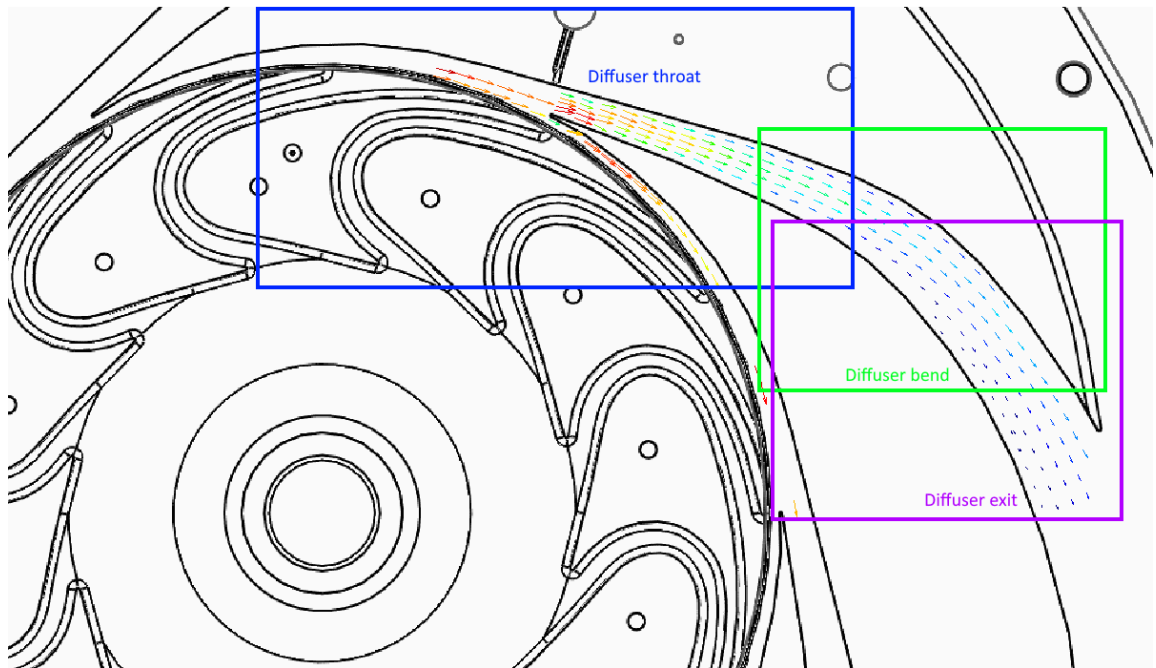


Figure 99: Mean velocity vector image of LDV results - 0 degree impeller rotation

To fully explore these results, the diffuser was broken down into 3 areas; the throat, the bend and the exit as shown in Figure 99.

6.1.1. Diffuser Throat

The velocity vectors in the diffuser throat section are shown in Figure 100. These figures show the variation in flow velocity as the impeller passes the diffuser leading edge.

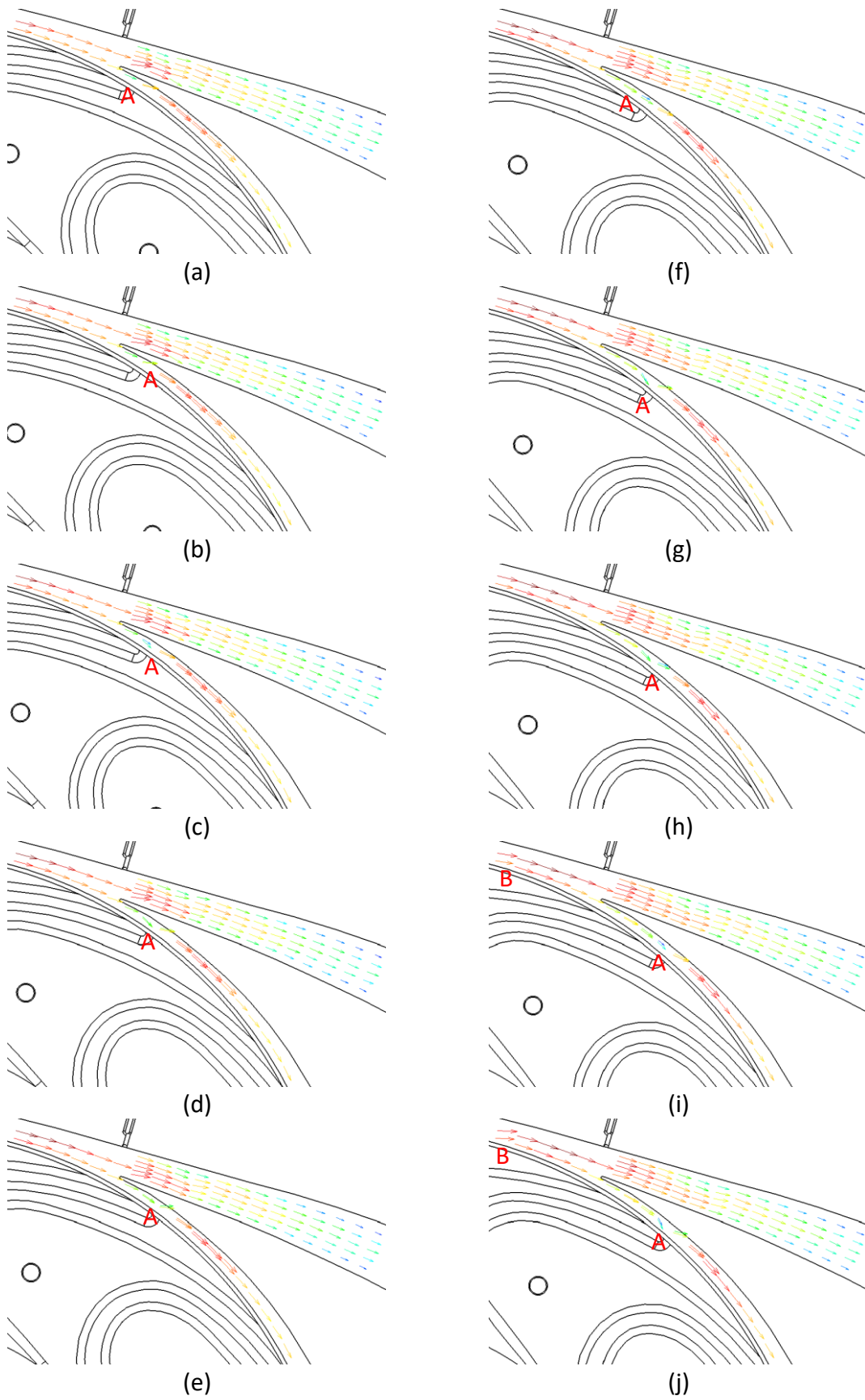


Figure 100: Mean velocities at diffuser throat, 1 degree increment impeller rotation

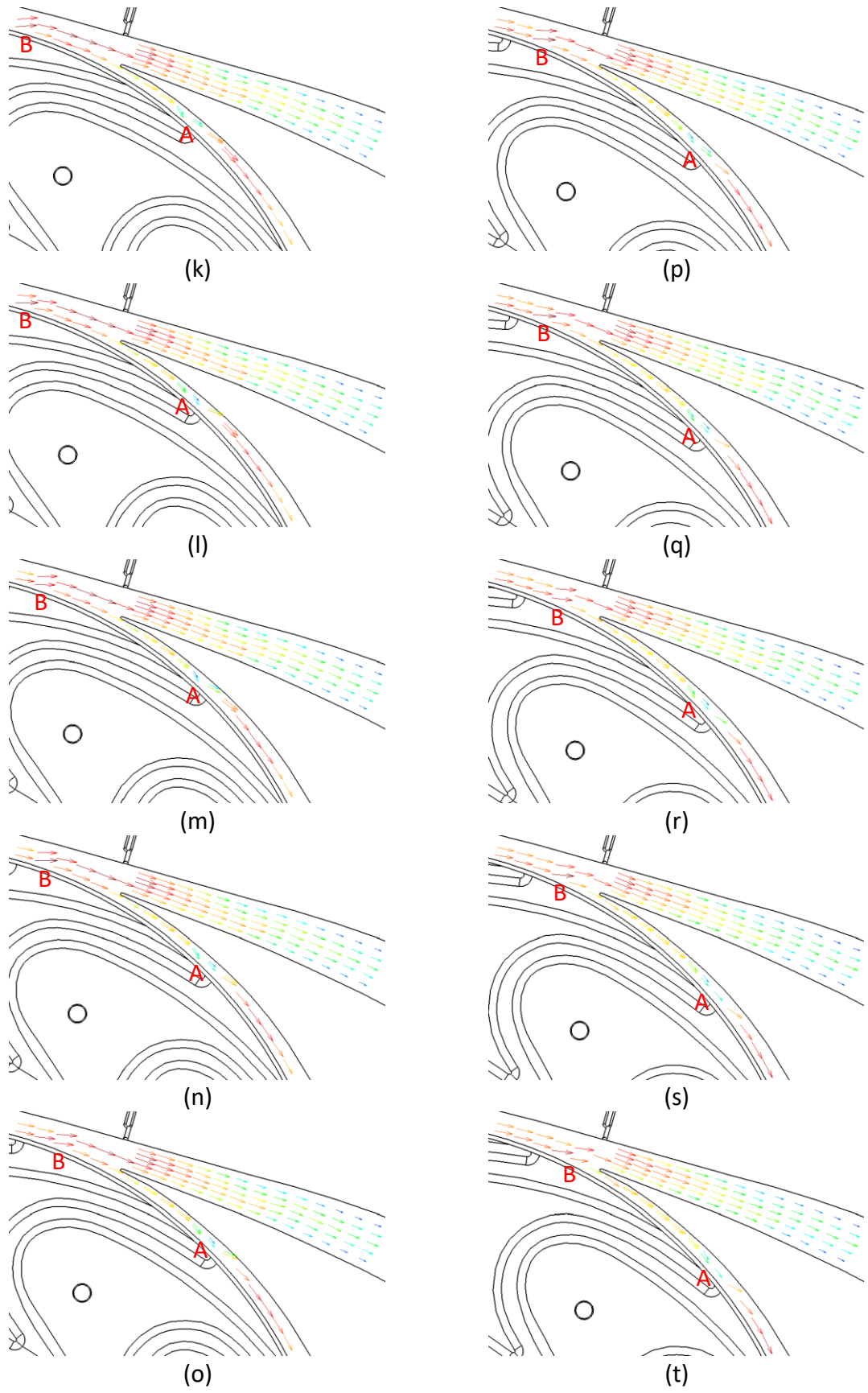


Figure 100 cont.

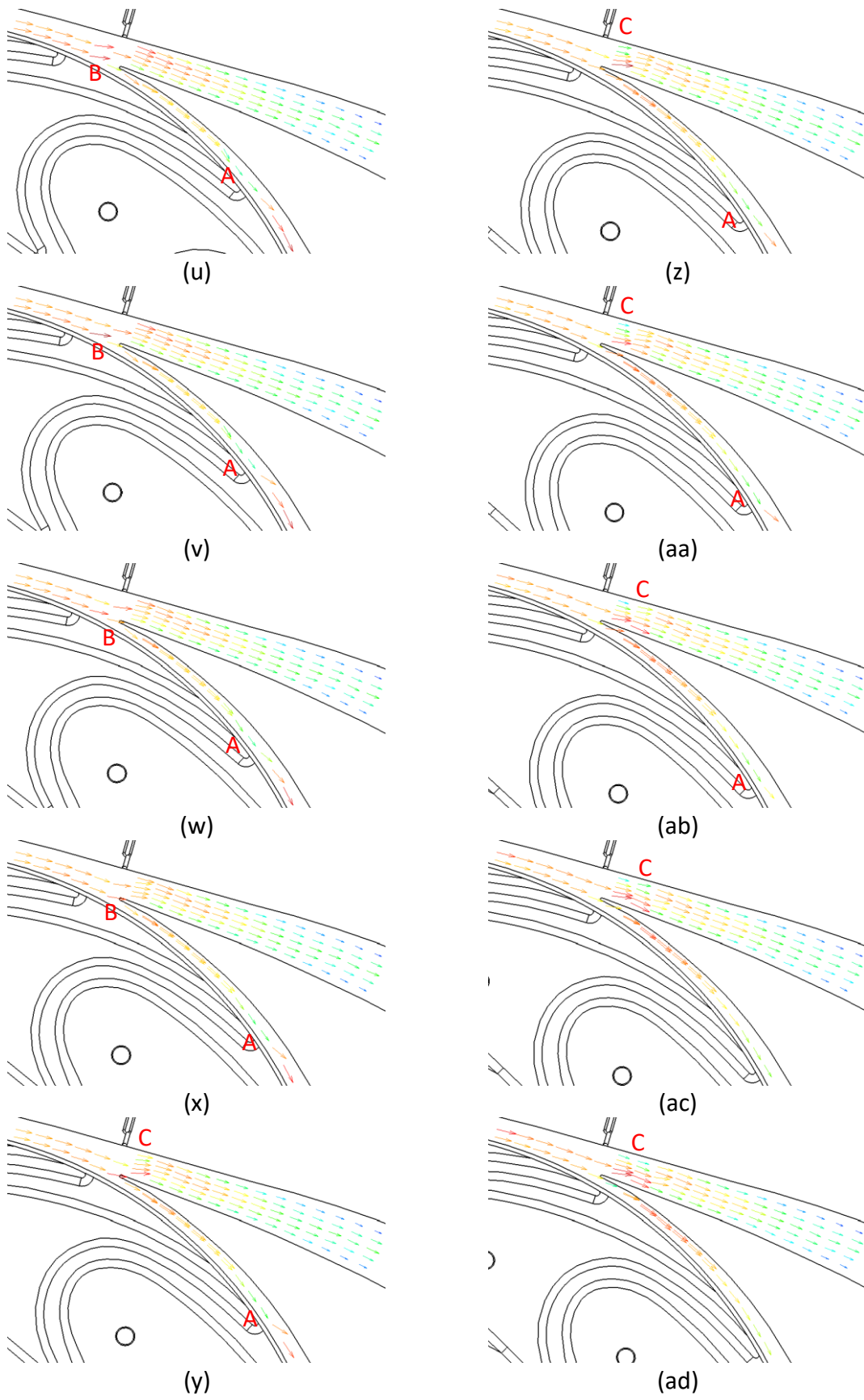


Figure 100 cont.

The data shown in Figure 100 has several interesting features. The label “A” on the images shows an area just behind the impeller trailing edge which shows a large deviation in direction to that of the passage, and a lower velocity than the flow around it.

The label “B” identifies the location where the main jet from the impeller enters the vaneless space of the diffuser. This jet is at a different orientation to the diffuser blade. This is showing there is slip in the compressor. This is what is seen in Figure 100 and schematically in Figure 101, the black triangles showing the ideal velocity triangles and the blue lines showing the effect of slip.

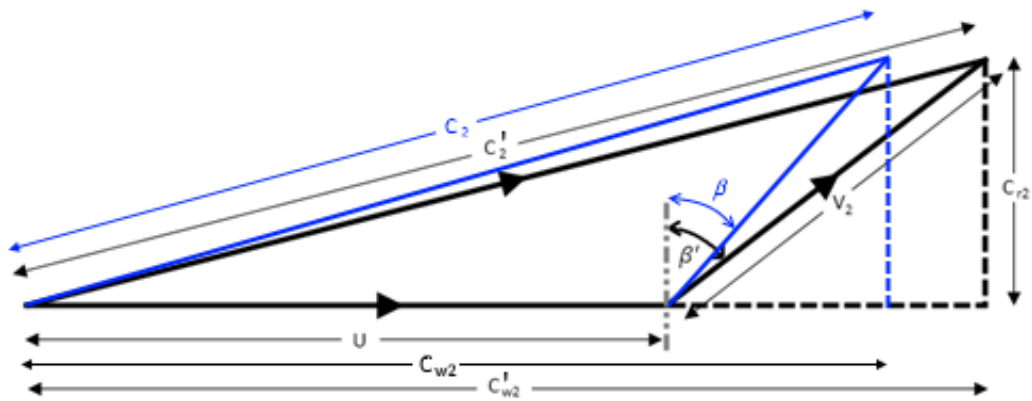


Figure 101: The effect of slip on the velocity triangles of a forward swept compressor

By collating all the images above into a single image, Figure 102, it is possible to see how the pattern of the flow changes as it progresses further along the diffuser. As the flow exits the impeller and enters the “vaneless space” there is variation in the angle and speed of the flow, ranging from almost tangential to rotated towards the radial direction.

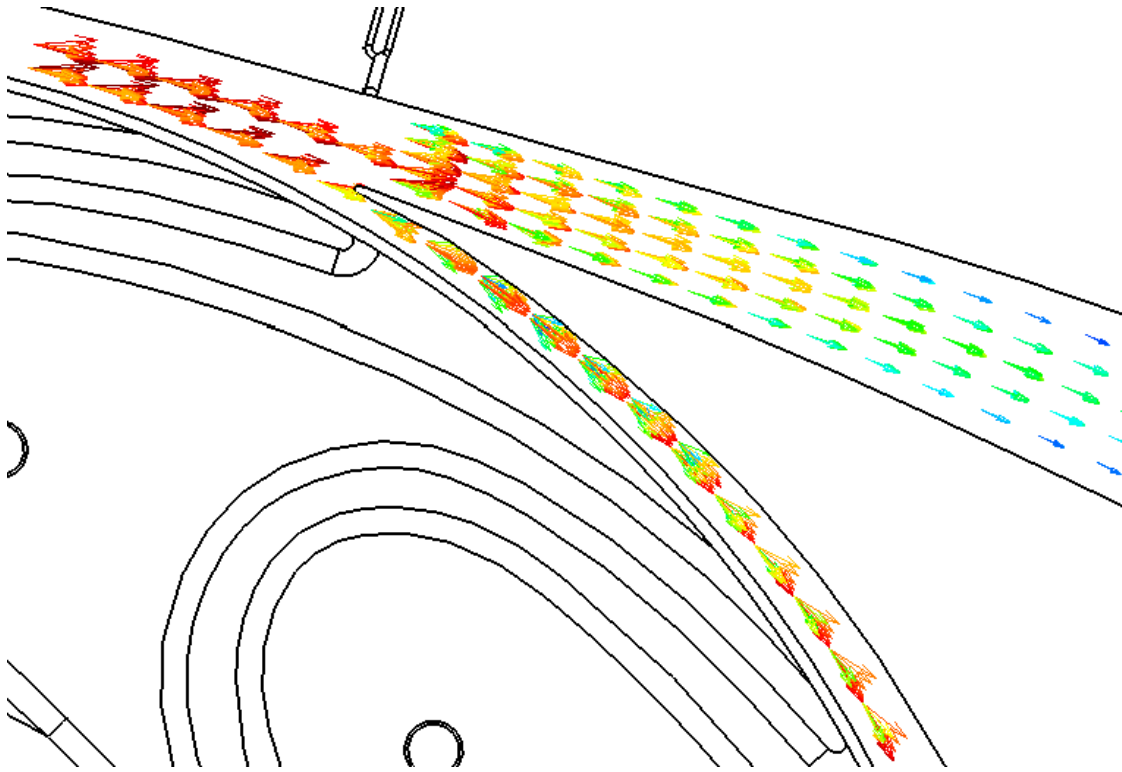


Figure 102: Collated image of all images in Figure 100 showing the flow variation as the impeller rotates through 360 degrees, velocities range from 73.4 m/s to 23.7 m/s

At the throat, shown in Figure 104, the velocities reduce and the flow settles down into a more uniform flow field as it moves further along the diffuser. As the impeller passes the throat of the diffuser there is a large variation in the velocities, at the centre of the passage the flow varies from 46.8 m/s to 66.3 m/s. This ties in with the high-speed photography images shown in section 5.1.2 that showed the flow pulsing in time with the impeller rotation. In Figure 103 each line shows the velocity profile across the passage (from first measurement to last measurement, not the full passage width) as the impeller rotates. The legend shows the impeller rotational angle from 0 degrees to 30 degrees, a full impeller blade pass relative to the diffuser.

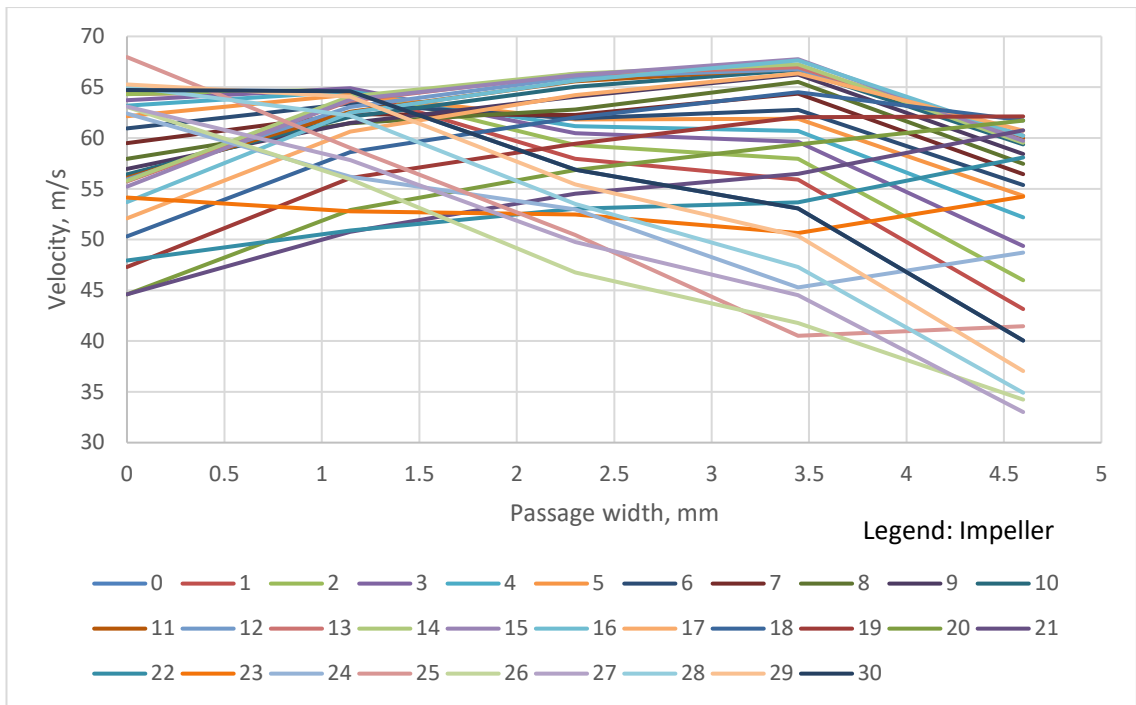


Figure 103: Velocity profile variation with impeller position at the diffuser throat, legend shows the impeller position in degrees

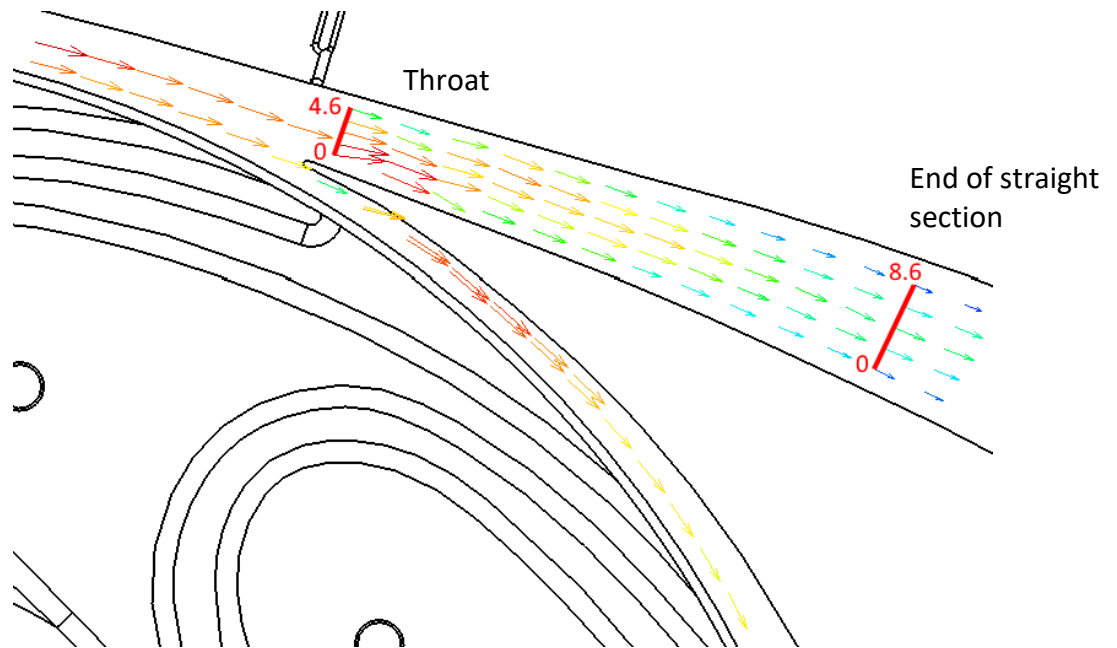


Figure 104: Location for Figure 103 velocity profile, numbers show the passage width

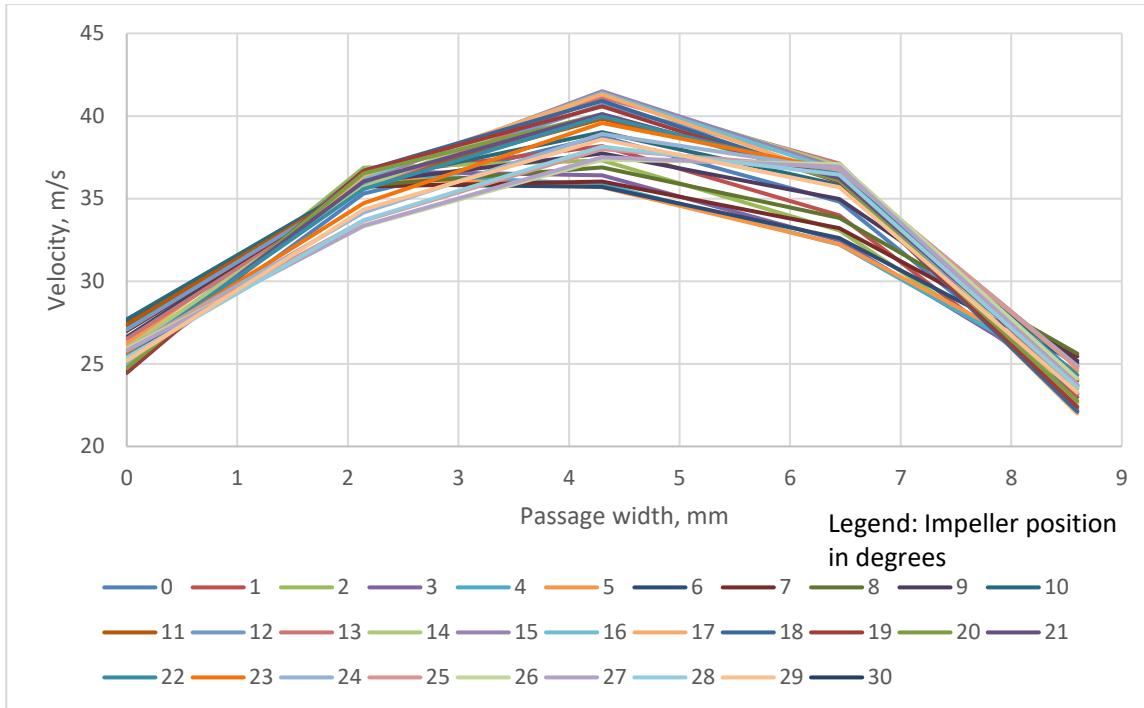


Figure 105: Velocity profile variation with impeller position at the end of the straight diffuser section
 Figure 104

Further along the passage, the flow begins to show a more traditional pipe velocity profile Figure 105. As in Figure 103 each line shows the velocity profile across the passage for a given impeller angle. Depending on the position of the impeller, the profile is either skewed inwards or outwards. When the impeller is rotated 5 degrees from zero, the maximum velocity of 36.3 m/s is at 2.14 mm across the diffuser passage, whereas at 6.44 mm the velocity is only 32.2 m/s. However, at 26 degrees the maximum velocity 37.4 m/s is at the centre, but at 6.44 mm the velocity is 37.1 m/s and at 2.14 mm the velocity is 33.3 m/s, see Figure 105.

Figure 106 shows how the angle of the flow at the diffuser throat varies as the impeller rotates. Figure 107 shows the flow angles end of the straight section of diffuser passage. The legend refers to the location of the measured point across the passage in Figure 104 and the angle is relative to the centre of the passage.

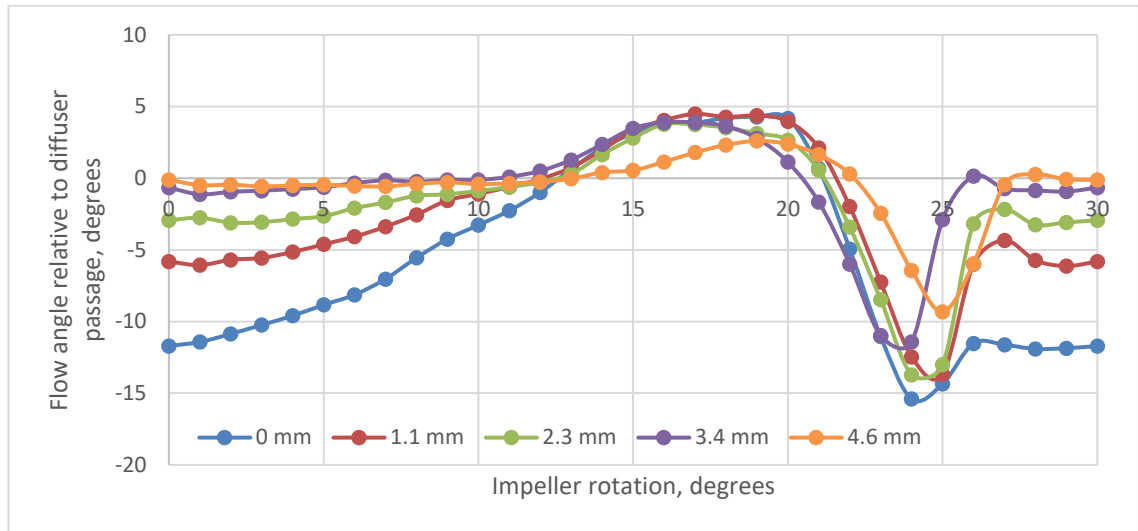


Figure 106: Flow angles at diffuser throat as impeller rotates

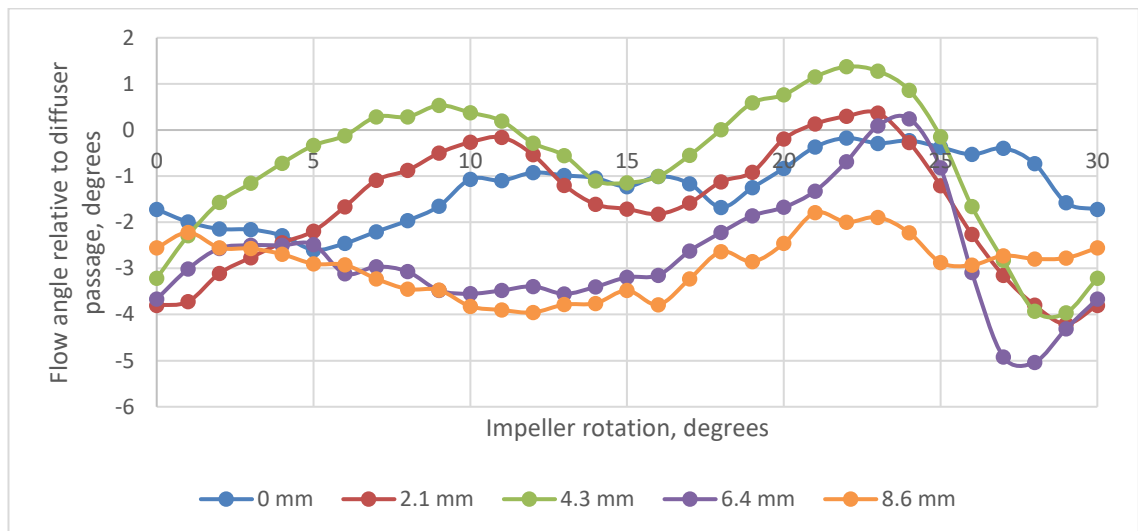


Figure 107: Flow angles at diffuser bend as impeller rotates

It can be seen from Figure 106 that there is large variation in angle at the diffuser throat, from -15.4° up to $+4.49^\circ$. However, as the flow moves down the diffuser, the variation in angle reduces, ranging from -5.04° to 1.37° . The average angle across the passage for a full blade pass also changes, at the throat the average angle is -2.21° , reducing to -1.86° at the end of the straight section of diffuser.

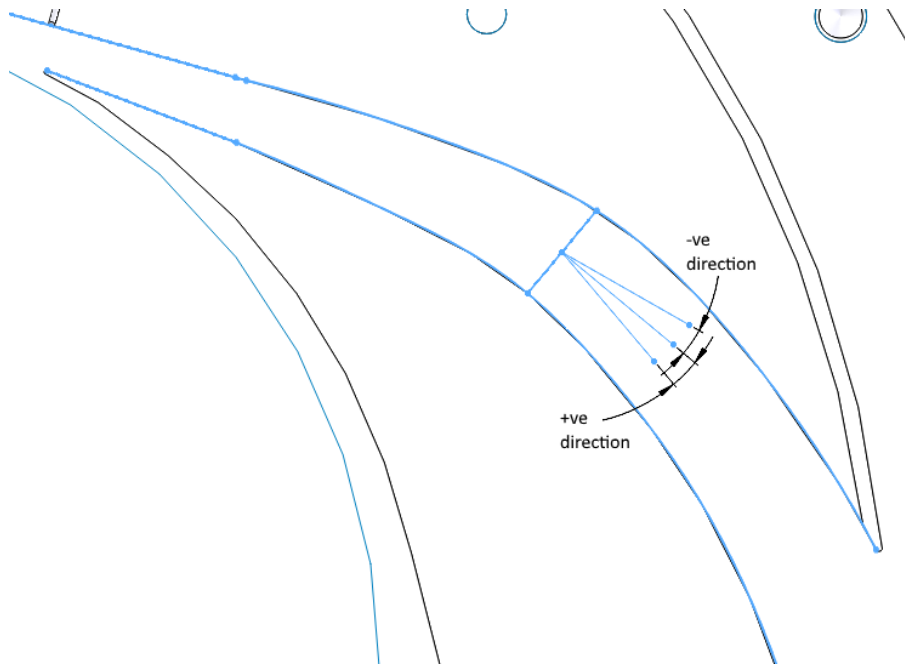


Figure 108: positive and negative angles of flow for Figure 106 and Figure 107

6.1.1. Diffuser Vaneless space

Figure 109 shows how the angle of the flow varies in the vaneless space as the impeller rotates. As the impeller passes the measurement location, there is a sharp increase in the angle of the flow relative to the tangential, followed by an equally sharp return to the almost tangential baseline.

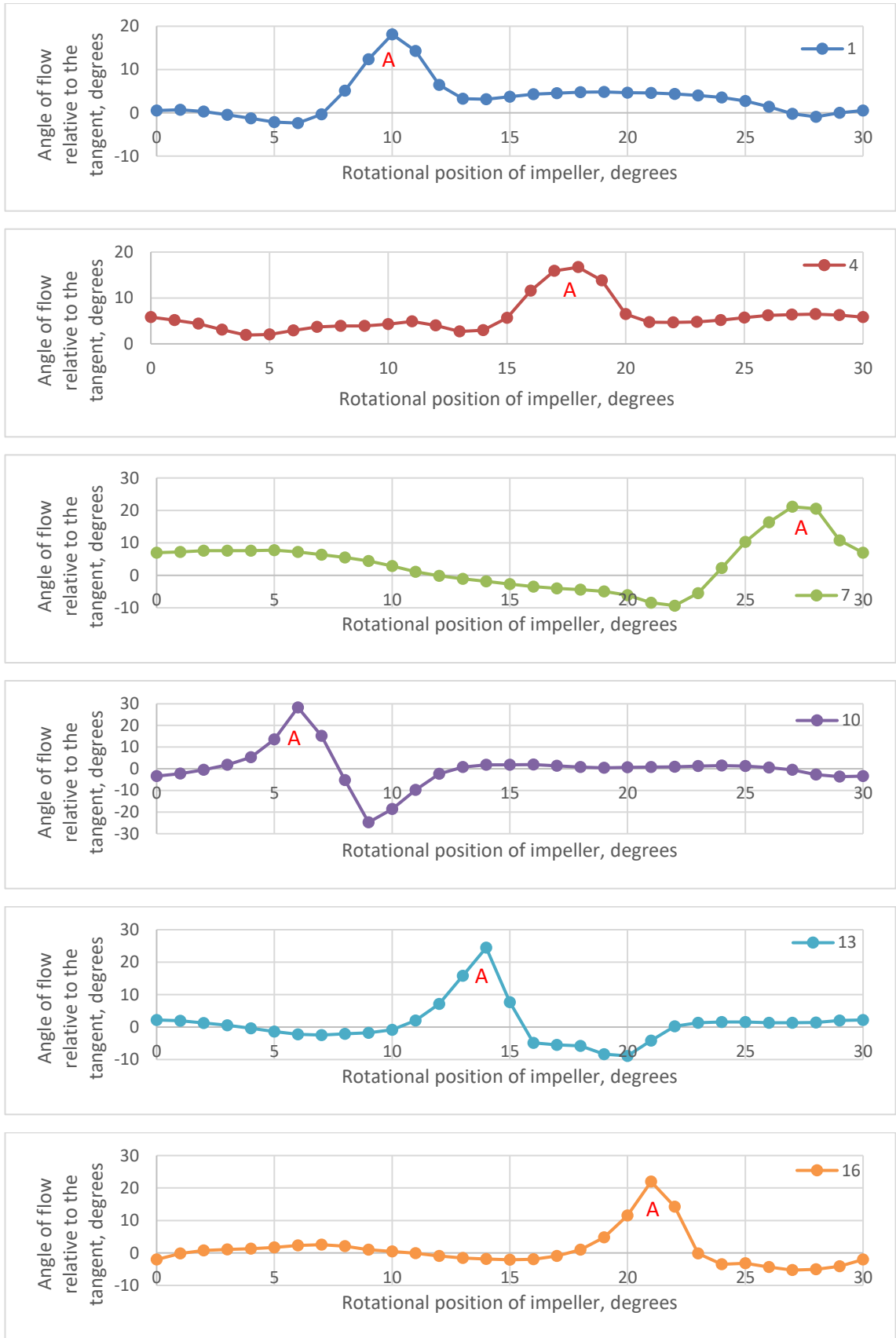


Figure 109: Flow angle relative to the tangential in the vaneless space at 6 measurement locations

The very high changes in angle are from measurements downstream of the leading edge of the diffuser blade, where the diffuser walls are close in. Upstream of the leading edge, the angle changes are less extreme, varying by less than 20 degrees, see Figure 111.

In Figure 109, the legend numbers refer to the measurement location shown in Figure 110.

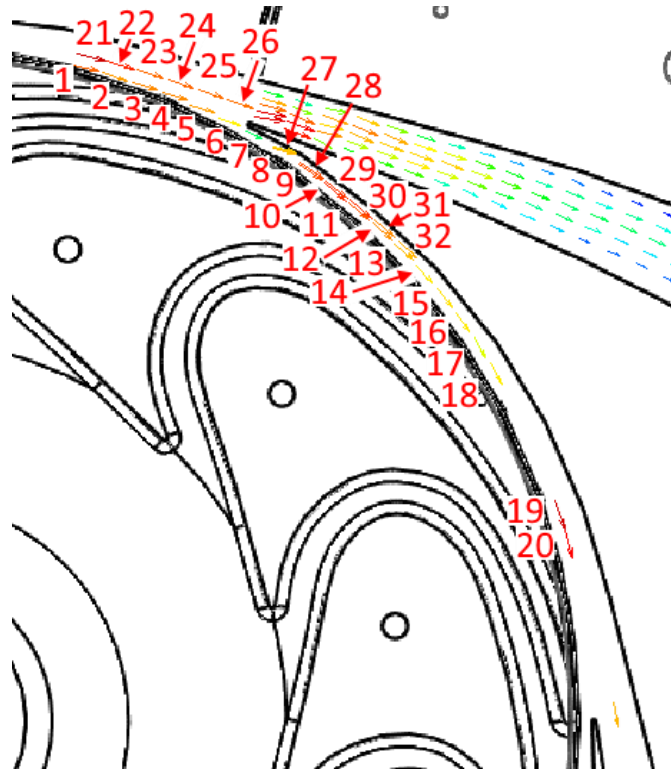


Figure 110: Upstream measurement locations

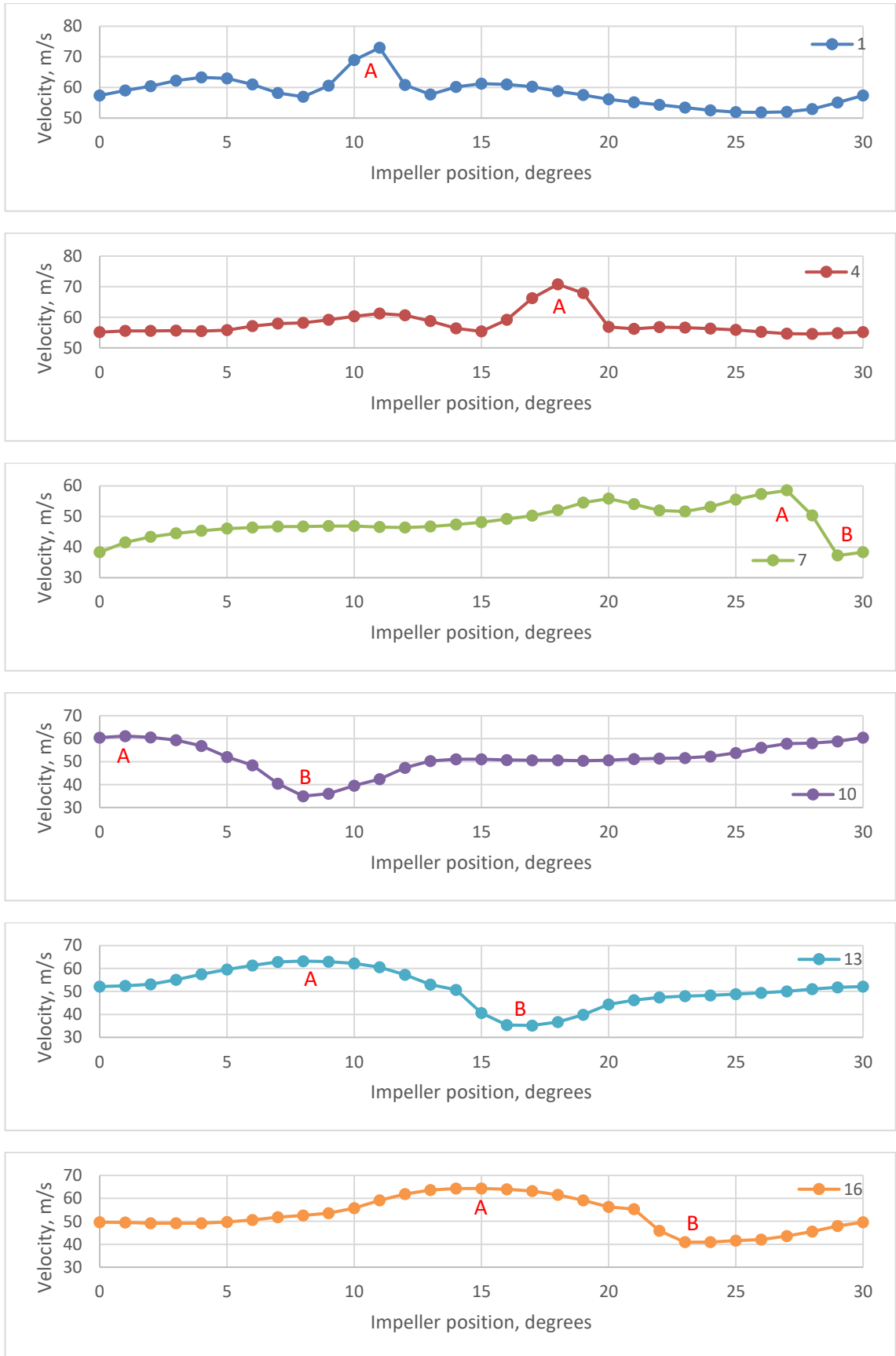


Figure 111: Flow velocity in the vaneless space at 6 measurement locations

Figure 111 shows the velocity at 6 points within the vaneless space. There is a wide range of velocities measured in the vaneless space, ranging from a peak of 73.4 m/s down to a minimum of 22.6 m/s. The average mean velocity within the vaneless space is 54.7 m/s.

All points measured show a velocity peak, labelled as “A” on the charts, where the jet from the impeller occurs. Where the vaneless space is narrower, to the right of the diffuser leading edge, the high velocity peak is followed by a dip, labelled “B”, to a lower velocity before returning to a stable velocity. This dip is up to 15 m/s in magnitude in the case of point 10 and 13.

6.1.2. Diffuser Bend

The diffuser bend has been analysed in a similar way to the throat. Individual images are shown in 11 Appendix: Additional LDV images.

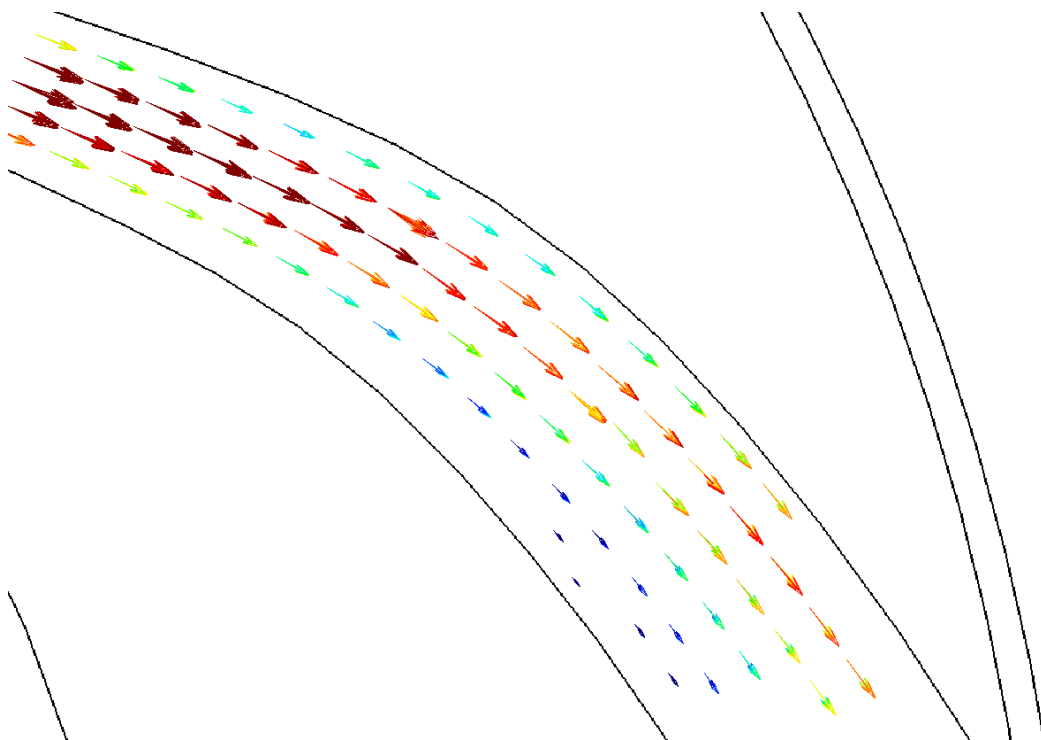


Figure 112: Collated image of all position vectors at the diffuser bend, flow velocity ranges from 41.1 m/s to 3.1 m/s

Figure 112 shows the all the individual images overlaid. This shows that the mean flow is moving in a uniform direction, though the speed varies. Figure 113 shows the velocity profile across the passage for one location at the bend, shown in Figure 114.

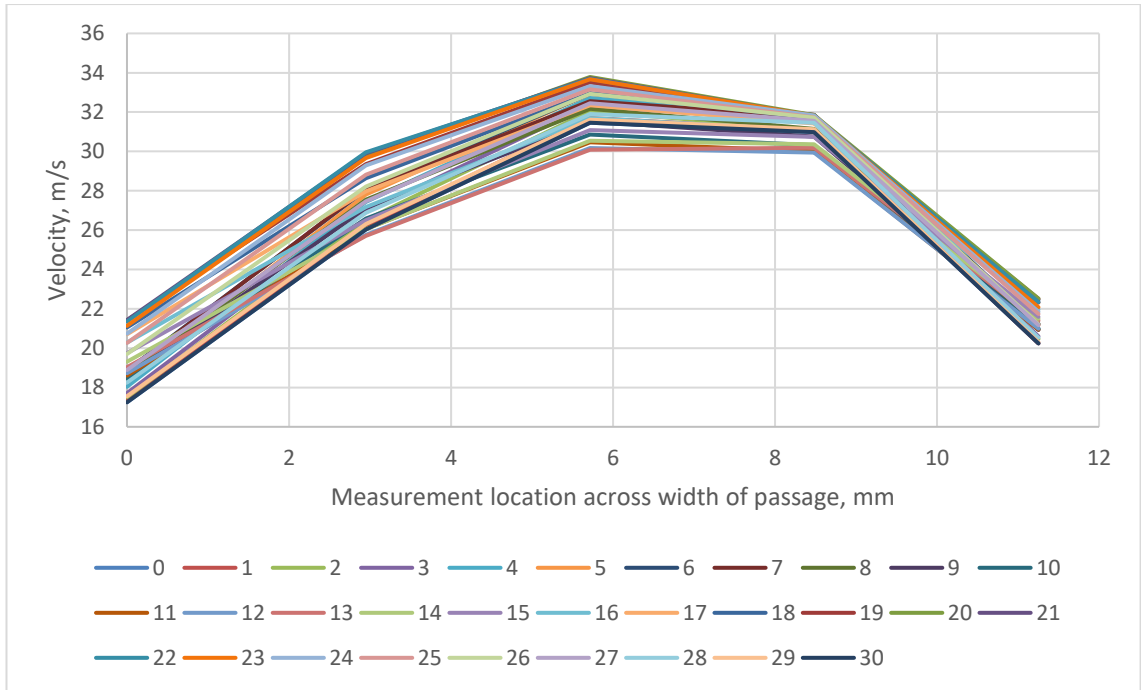


Figure 113: Velocity profile variation with impeller position at the bend

This shows how the flow is still pulsing at the bend, the mean velocity varies from a minimum of 30.1 m/s to a maximum of 33.8 m/s. The figure also shows that the velocity profile is skewed to the outside of the bend.

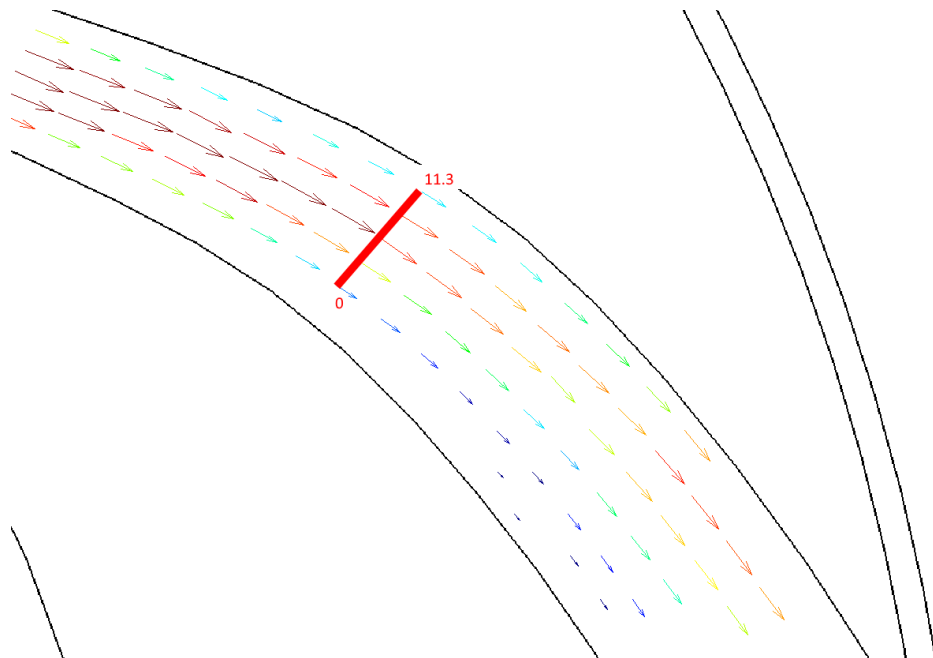


Figure 114: Location for Figure 113 velocity profile

Figure 115 shows the variation in flow angle relative to the diffuser. When compared to the flow at the end of the straight section of the diffuser, Figure 107, there is less

variation in angle but the average angle is more negative. The minimum, maximum and average angles are -8.40° , -2.91° and -6.01° respectively. These negative angles show the flow is migrating towards the outside of the passage. This tallies with the flow visualisation, which also showed the flow migrating outwards.

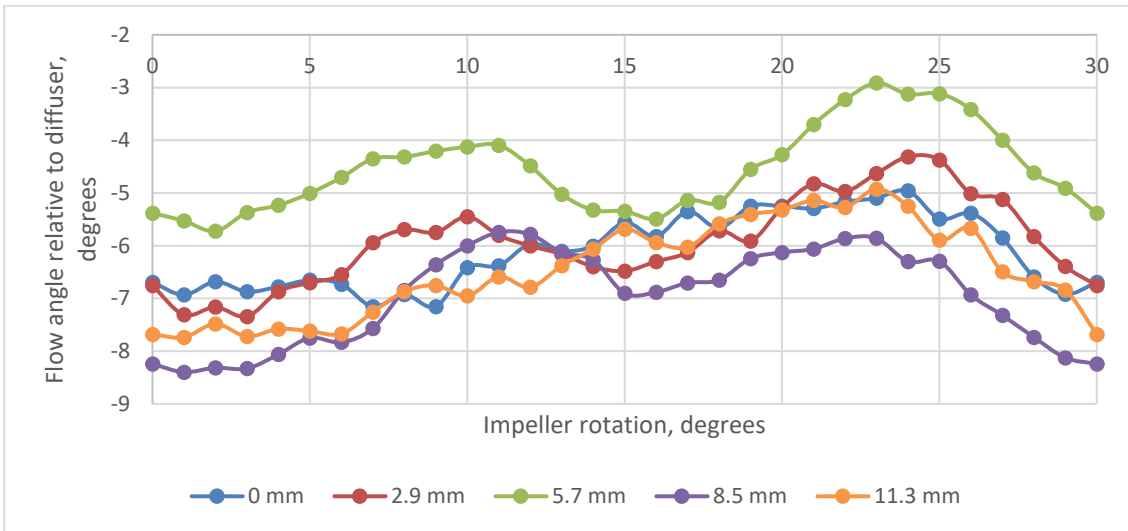


Figure 115: Flow angles at diffuser bend as impeller rotates

6.1.3. Diffuser Exit

The diffuser exit has been analysed in a similar way to the throat and bend.

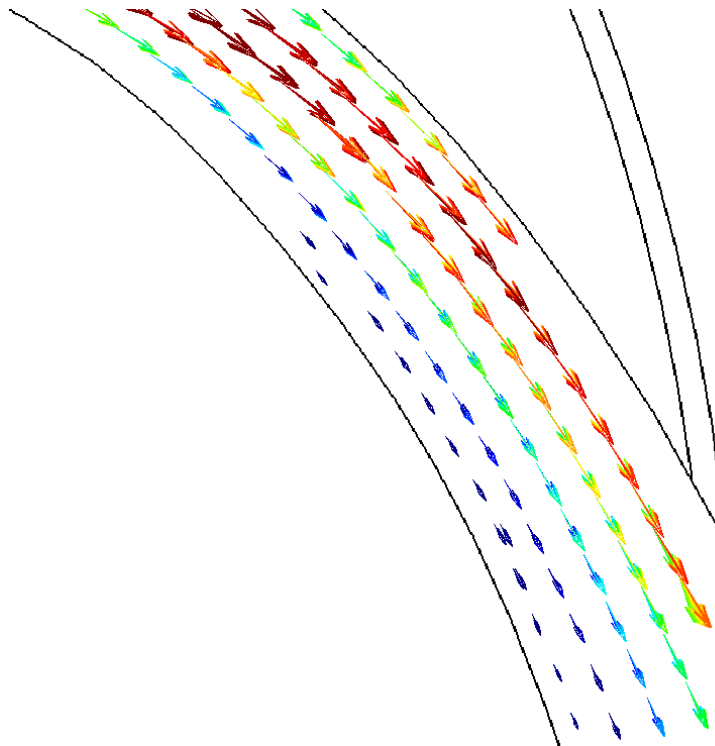


Figure 116: Collated image of all position vectors at the diffuser exit, flow velocity ranges from 37.0 m/s to 3.1 m/s

The diffuser exit is similar to the diffuser bend in that the mean flow direction is uniform. The flow variation at the diffuser exit is greater than at the bend, at the centre of the passage, the maximum mean velocity is 20.7 m/s and the minimum is 13.7 m/s and it shows an increased velocity at the outside of the passage.

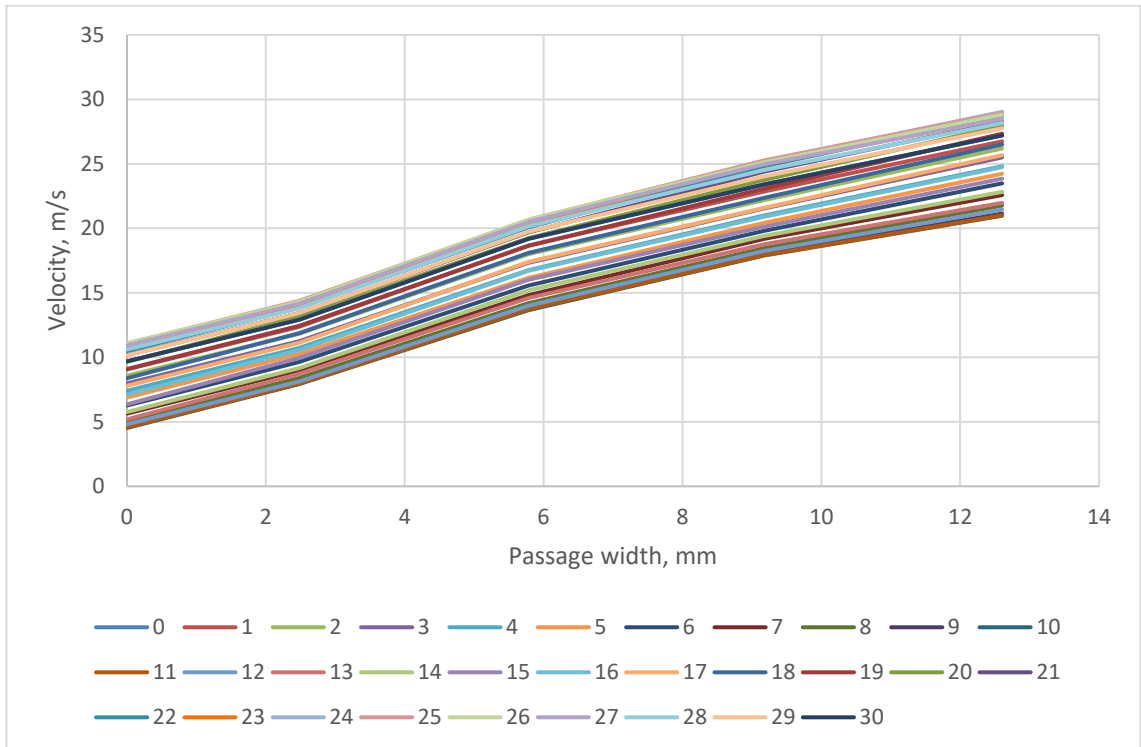


Figure 117: Velocity profile variation with impeller position at the exit of the diffuser

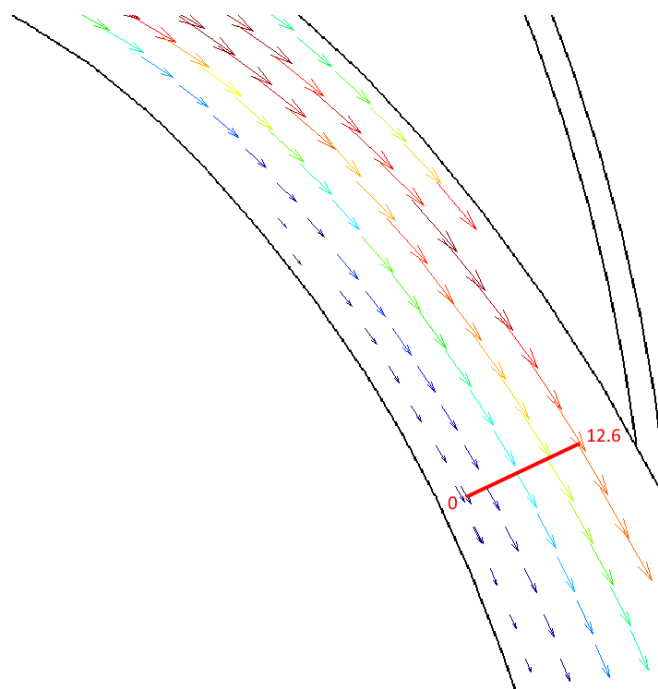


Figure 118: Location for Figure 117 velocity profile

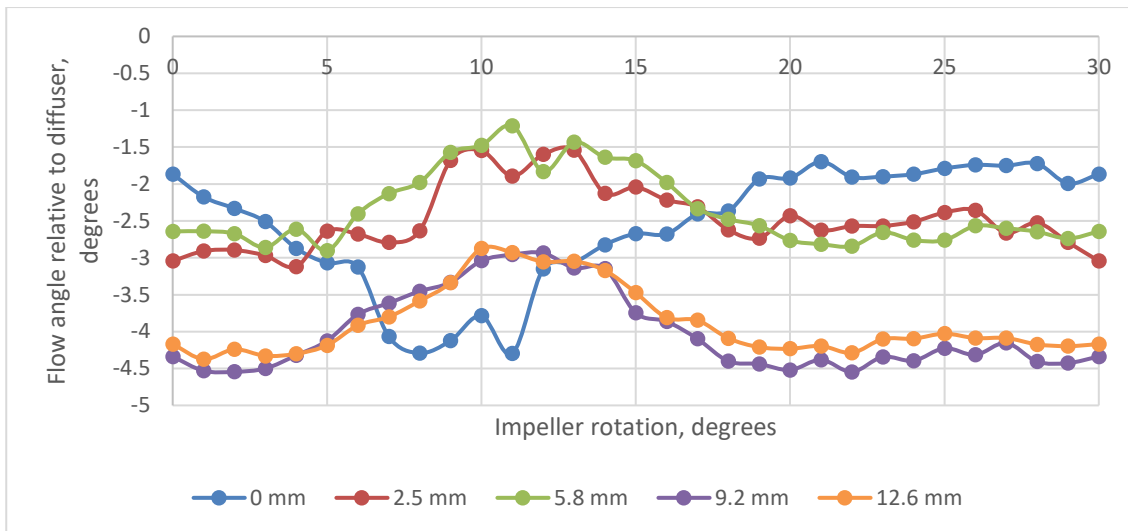


Figure 119: Flow angles at diffuser exit as impeller rotates

At the diffuser exit, Figure 119 shows that the variation in flow has reduced further from the location in the bend. The maximum, minimum and average values are now -1.21° , -4.55° and -3.06° respectively. At the diffuser exit, the angular variation still varies with impeller position showing that the impeller affects the flow down the full length of the diffuser.

Minimum and maximum velocities can't be calculated with the data gathered in this work. This is due to the measurement method being a single direction at a time. Therefore, an instantaneous minimum value in 1 direction could not be tied to its corresponding velocity in the other direction. The only method to measure minimum or maximum velocities would be to repeat this work using a multi-axis LDV set up.

6.2. Optical Measurement Conclusions

High-speed imaging of the diffuser throat showed the flow migrating towards the outside of the passage, Figure 84 to 87. The LDV measurements show the same, Figures 106, 107, 115 and 119 all show that the average flow angles are in the negative direction, i.e. towards the outside of the passage.

This is to be expected in a curved diffuser. The curved surfaces act in the same way as an aerofoil, the concave surface, also known as the pressure surface, and the convex surface, also known as the suction surface, cause the flow to bend. The change in direction causes a pressure gradient to form from the pressure surface towards the suction surface. The pressure differential generates a force across the passage that pushes the flow towards the suction surface. If this force is too great, the flow can separate from the pressure surface and cause an area of recirculation. (Kundu, et al., 2016)

One hypothesis for the diffuser was that there would be separation on the pressure surface. However, no recirculation was observed in the LDV measurements. The mean velocity at all locations remained in the direction of the bulk flow. However, at other conditions such as choke or surge, or at higher operating speeds it is possible that recirculation will occur. Further work is required to establish if that is the case. Ideally a multi-axis LDV set up would be used as it would show if there were any particles recirculating even if the mean flow were not.

The LDV and high-speed imagery from the bend agree even though they were measured at different operating speeds, both show the flow migrating towards the outside of the bend. However, at the diffuser exit and in the vaneless space, the high-speed photography was unsuccessful. The LDV showed, for the operating point measured, that there was no recirculation even though there was a strong tendency for the flow to move to the suction side of the passage. Both the LDV and flow visualisation showed pulsation in the flow, and the LDV showed that these pulsations were still felt at the exit to the diffuser passage.

6.3. Gas Angles

The LDV measurements show the measured gas angles within the diffuser passage. However, using the performance data described in Section 4.3 and a 1 dimensional analysis of the type found in (Cumpsty, 2004), it is possible to calculate the angle that the gas should leave the impeller and then enter the diffuser if a highly forward swept compressor follows standard turbomachinery equations.

Figure 120 shows the station numbering for the following analysis. The LDV measurements were conducted at 4,000 rpm, a pressure ratio of 1.010 and a mass flow rate of 23.3 g/s, with inlet conditions of 1.000 bara at 25.3°C. The reason for the low rotational speed is detailed in section 3.1.4.

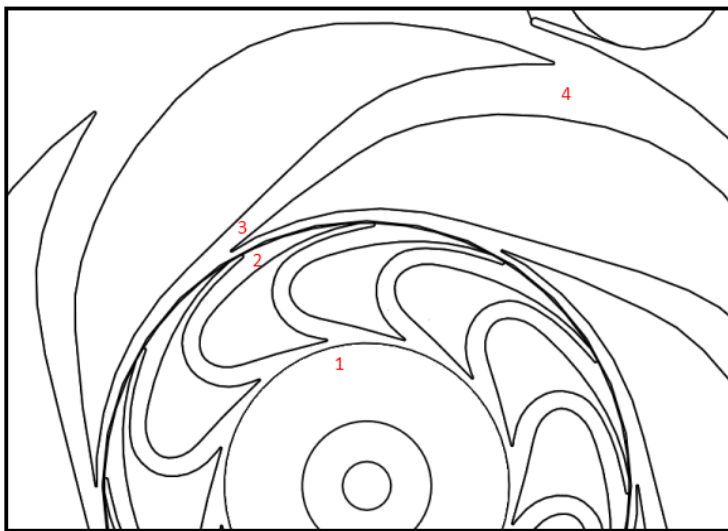


Figure 120: Sketch of impeller and diffuser passages with station numbers

6.3.1. Impeller Inlet

The geometric angle of the impeller inlet is shown in Figure 121, it has an average angle, α , of 23.9°, the inlet diameter is 121.8mm giving a leading edge blade inlet velocity of 25.5 m/s.

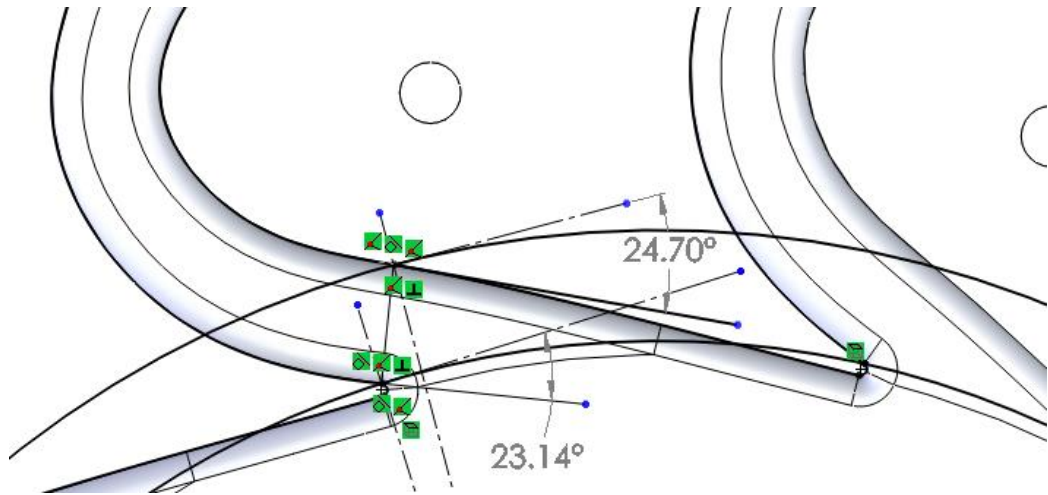


Figure 121: Impeller geometric inlet angle

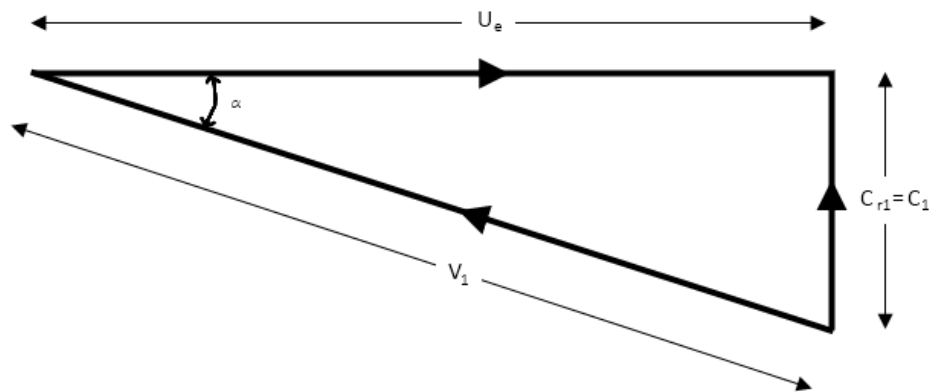


Figure 122: Impeller inlet velocity triangle

Using ideal gas relations, it is possible to calculate the inlet density and volume flow rate. To begin the calculations, the measured temperature T_{01} is assumed to equal T_1 .

$$\rho_1 = \frac{P_1}{RT_1} \quad \text{Equation 67}$$

$$\dot{v}_1 = \frac{\dot{m}}{\rho_1} \quad \text{Equation 68}$$

Assuming that the inlet to the impeller is a continuous cylinder at the eye of the impeller and that the inlet flow is totally radial, $C_{r1} = C_1$.

$$A_1 = \pi d_1 h_b \quad \text{Equation 69}$$

$$C_1 = \frac{\dot{v}_1}{A_1} \quad \text{Equation 70}$$

$$V_1 = \sqrt{(U_e^2 + C_1^2)} \quad \text{Equation 71}$$

The actual value of T_I is then calculated from Equation 72.

$$T_1 = T_{01} - \frac{C_1^2}{2C_p} \quad \text{Equation 72}$$

The whole calculation is iterated until T_I converges, this usually occurs in less than 4 iterations. For the condition described above, the results are show in Table 11.

Table 11: Impeller inlet velocities

| | |
|-----------------|----------|
| $C_I = C_{rI}$ | 9.52 m/s |
| V_I | 79.3 m/s |
| $Ue = C_{wI}$ | 78.7 m/s |
| α_{calc} | 12.8° |

6.3.2. Impeller Exit

The geometric angle of the impeller exit is shown in Figure 123, it has an average angle, β , of 78.7°, the outside diameter is 210.0 mm giving a tip speed, U , of 44.0 m/s.

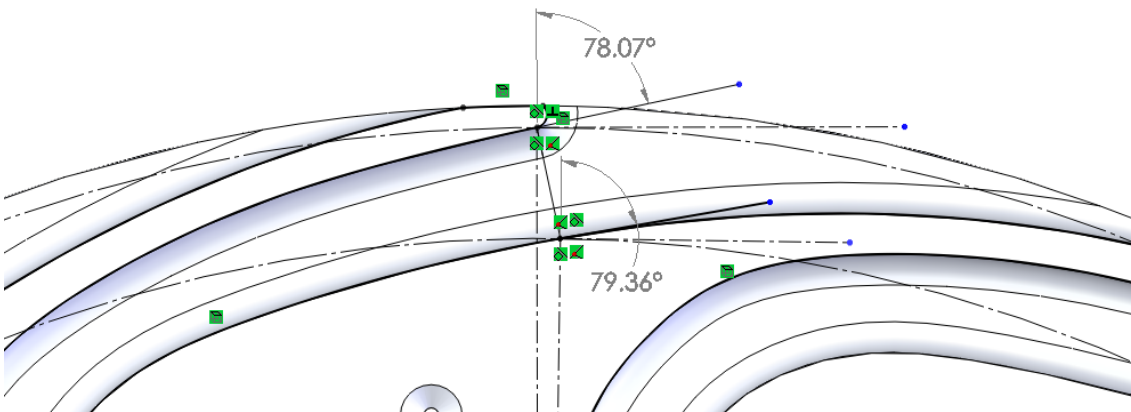


Figure 123: Impeller exit geometry

Figure 124 shows the nomenclature of the exit angle calculation.

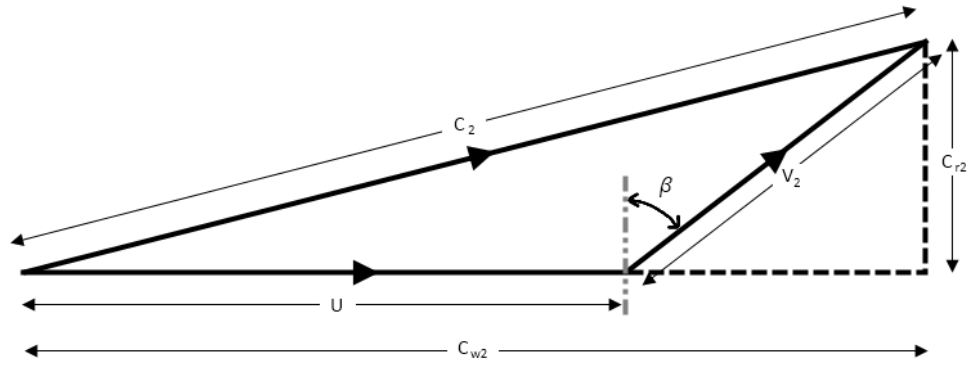


Figure 124: Impeller exit velocity triangle

The power input to the compressor at this condition can be calculated from the torque measurement.

$$P = |\tau|\omega \quad \text{Equation 73}$$

The compressor input power was measured as 92.0 W. The total temperature at the impeller exit can be calculated from Equation 74.

$$T_{02} = T_{01} + \frac{P_E}{\dot{m}C_p} \quad \text{Equation 74}$$

Assuming there is no change in static temperature or static pressure within the impeller allows the calculation of density and volume flow rate at the exit of the impeller.

$$\rho_2 = \frac{P_2}{RT_2} \quad \text{Equation 75}$$

$$\dot{v}_2 = \frac{\dot{m}}{\rho_2} \quad \text{Equation 76}$$

The impeller passage cross sectional area was measured in the computer aided design, CAD, package to be 62.6 mm² for a single passage. There are 12 blades in the impeller, giving a total area of 751 mm². V_2 is the speed of the gas relative to the impeller's speed.

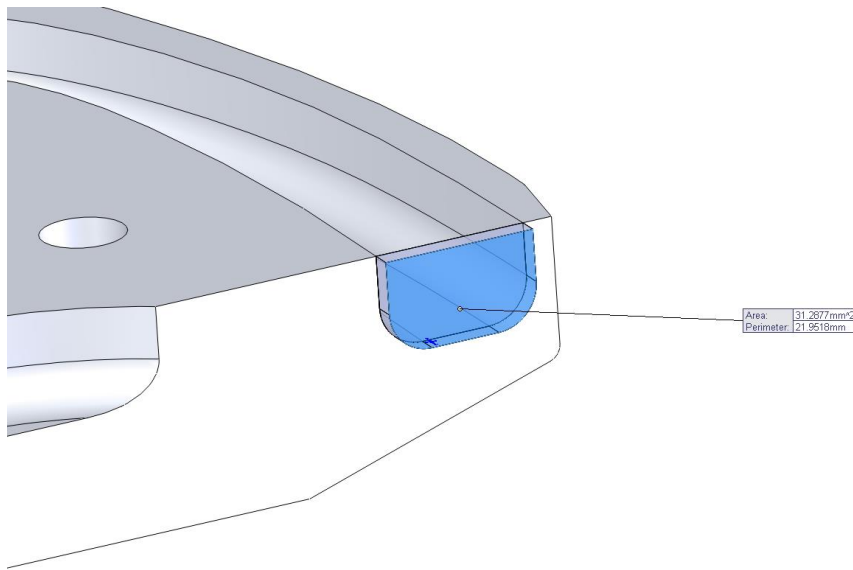


Figure 125: Exit area of half impeller

$$V_2 = \frac{\dot{v}_2}{A_2} \quad \text{Equation 77}$$

Trigonometric relationships allow calculation of the other flow speeds. T_2 is iterated using Equation 78 until its value converges.

$$T_2 = \frac{T_{02}}{\left(1 + \left(\frac{\gamma - 1}{2}\right) M_2^2\right)} \quad \text{Equation 78}$$

$$a_2 = \sqrt{\gamma R T_2} \quad \text{Equation 79}$$

$$M_2 = \frac{C_2}{a_2} \quad \text{Equation 80}$$

For the condition described above, the results are show in Table 12.

Table 12: Impeller exit velocities

| | |
|----------|----------|
| C_2 | 70.4 m/s |
| C_{r2} | 5.23 m/s |
| C_{w2} | 70.2 m/s |
| V_2 | 26.7 m/s |
| U | 44.0 m/s |

6.3.3. Diffuser Inlet

The geometric angle of the diffuser inlet is shown in Figure 123, it has an average angle, ϵ , of 11.4° .

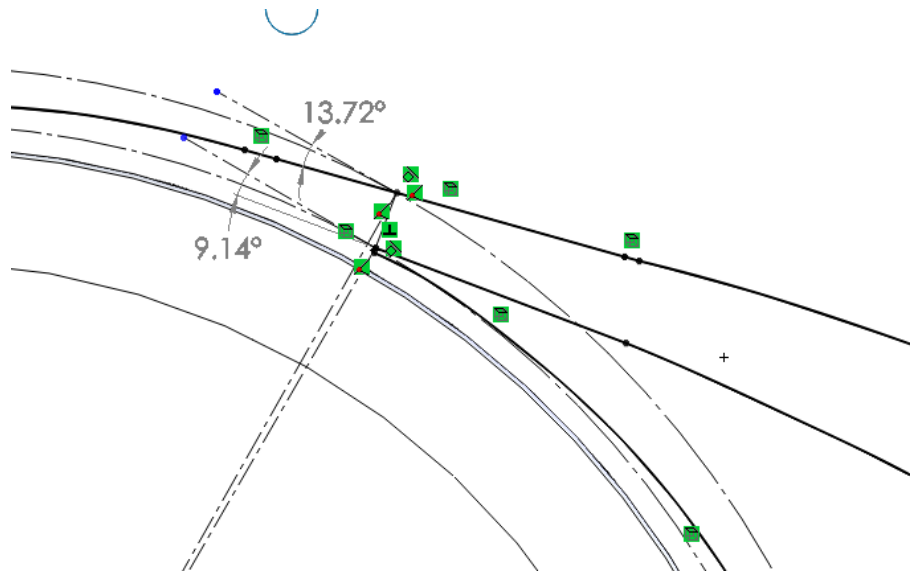


Figure 126: Diffuser inlet geometry

Figure 127 shows the nomenclature of the diffuser inlet angle calculation.

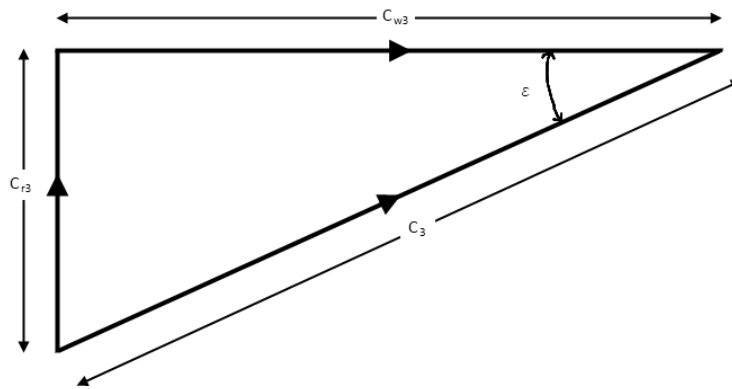


Figure 127: Diffuser inlet velocity triangle

It is assumed that C_2 equals C_3 , i.e. that there are no losses across the boundary between impeller and diffuser and that the circumferential area of the impeller exit is the same as the diffuser vaneless space. Simple trigonometry allows the calculation of the radial velocity component, C_{r3} , and the whirl velocity component, C_{w3} .

Table 13: Diffuser inlet velocities

| | |
|----------|----------|
| C_3 | 70.4 m/s |
| C_{r3} | 13.9 m/s |
| C_{w3} | 69.0 m/s |

The results of the above analysis can be compared to the results from the LDV measurements. The absolute impeller exit velocity was calculated as 70.4 m/s and this was assumed to equal the diffuser inlet velocity. LDV measurements in the vaneless space (the closest location to the impeller exit) mean velocities ranging from 22.6 m/s up to 73.4 m/s with an average of 54.7 m/s.

This shows the calculations do not match the measurements. The assumption with the largest effect on the calculated velocities is the degree of static pressure rise in the impeller. The assumption used above was that there was zero static pressure rise. The fact that the bulk velocity calculation shows a higher velocity than was measured with the LDV gives a good indication that there is a static pressure rise in the diffuser.

The remainder of this work will focus on designing and building a new test rig to evaluate the pressure rise within the impeller along with attempting to find a way to predict the performance of the compressor.

7. Pressurised Test Rig

This chapter presents the design, build and testing of a second experimental rig to test the performance of the compressor under different inlet conditions in various gases. The design, analysis, instrumentation and error analysis of the compressor are described, along with the design of the closed loop pressure system for testing alternate gases. Finally, the methodology for removing the windage loss, associated with the couplings, is described showing how the compressor power can be determined from the torque measurements.

7.1. Test Aims

The first test rig designed and built for this work was developed purely with optical measurements in mind. The addition of a torque meter was to validate previous work, but the majority of the operating time was spent on the high-speed photography and laser Doppler Velocimetry measurements described in previous chapters.

The optical measurements have shed light on many aspects of the TurboClaw compressor performance such as evidence of pulsing flow and a lack of evidence of recirculating flow. However, while these results further the understanding of the flow field within the diffuser and highlight areas for development in the geometry of the compressor, this information is not directly useable to predict the performance of the compressor as is.

For conventional turbomachinery there is a whole suite of equations at hand that have been developed over many years, such as Euler's turbomachinery equation (Cumpsty, 2004), that allow the detailed prediction of the compressors performance. Work by Parra (Parra, 2013) and Thornton (Thornton, 2011) has tried to use some of these equations, such as Reynolds scaling, to predict the behaviour of the forward swept TurboClaw compressor but without success. To address this gap, it was decided to try an empirical method to predict the compressor performance. The prediction would only be focused on the geometry available at the beginning of the work, so would not include any modifications made as a result of the optical testing. However, it would allow for changes in blade height, as the capability to increase the mass flow of a compressor is important to industry. The prediction must be applicable to numerous gases and inlet

pressures/temperatures to make it as broad as possible. A specification was developed for the new test rig and is detailed in Table 14.

Table 14: Rig specification

| | |
|-----------------------|--|
| Impeller diameter | 85 mm |
| Impeller blade height | 2.73 to 15.0 mm |
| Maximum speed | 50,000 rpm |
| Maximum shaft torque | 5 Nm |
| Gas | An inert gas available in a bottle such as CO ₂ |
| Maximum pressure | 16 bar gauge |
| Maximum temperature | 150 °C |
| Diffuser type | 3D |

Based upon this specification, a test rig was developed in collaboration with Dynamic Boosting Systems Ltd, using the new, patented 3D style diffuser, that had been developed after the optical test rig was completed. The blades are geometrically similar to those used in the optical test rig, however, the diffusion now takes place in the axial direction as well as the radial direction. (Thornton, 2013)

To accommodate the large range of blade heights required by the specification, the rig was designed to be expandable. The scroll was machined in two halves, with accurate shims to expand the size of the volute when larger blade height impellers were being tested. As this would result in an oval shaped exit pipe, inserts were designed that could be fitted to the outlet of the pipe to reshape the pipe to being round without disturbing the flow. Furthermore, the relative position of the diffuser to scroll can be investigated as the diffuser can be rotated relative to the scroll for measurements to be taken.

The test rig needed to be fully sealed to allow testing at elevated pressures. A pressure of 16 bar was chosen as PN16 flanges are common and standard steel pipe would be rated to this pressure. The gas loop of the rig was designed to be able to connect to any commercially available bottled gas e.g. CO₂.

The compressor was driven by a permanent magnet (PM) motor supplied by DBS. The M170 motor had a maximum speed of 50,000 rpm and could deliver up to 25 kW. This motor was supplied as semi-hermetic with a rating of 16 bar, adequate for the test rig.

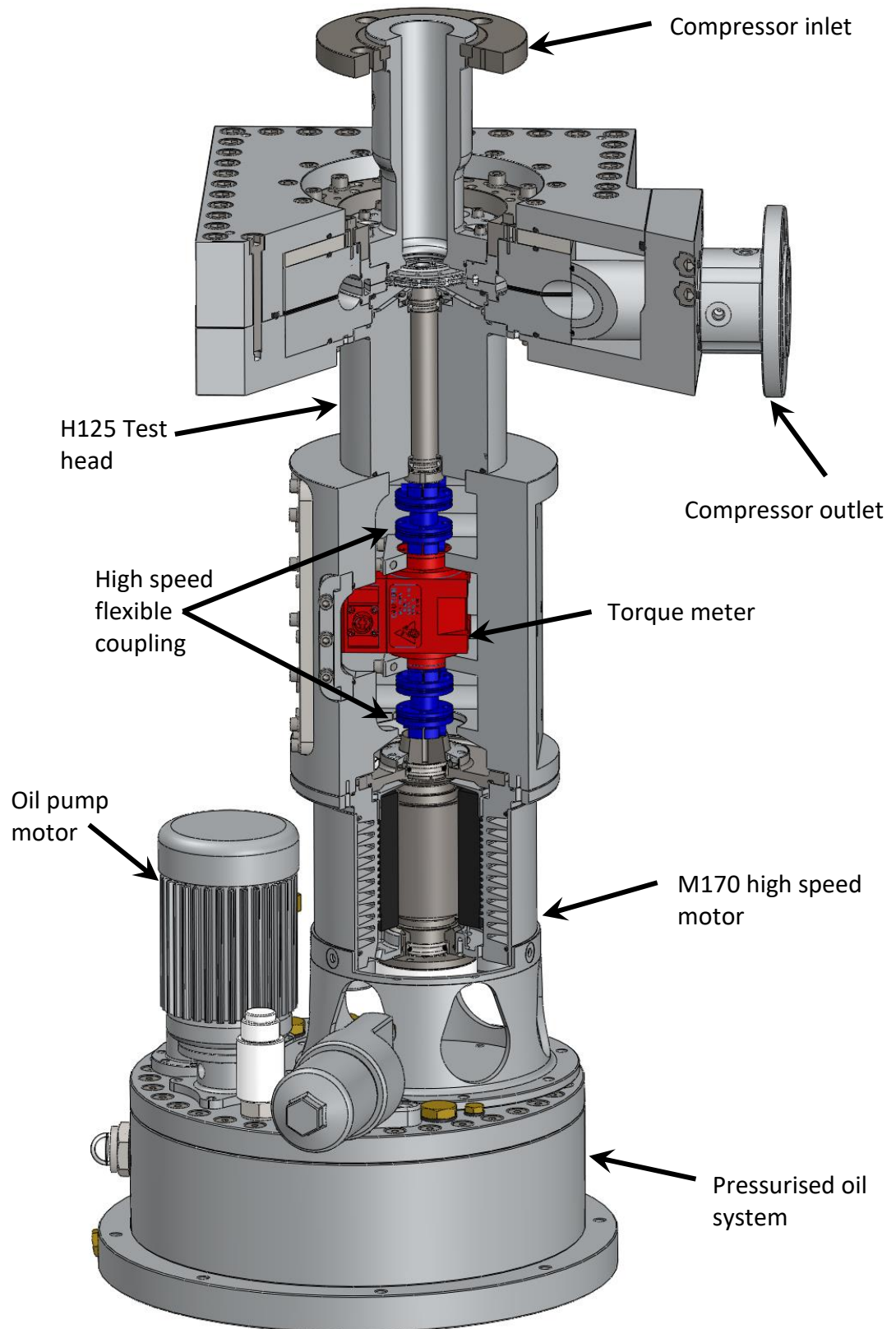


Figure 128: High pressure test rig – known as the "Square box" rig

As in the first test rig, a torque meter was used to measure the shaft power being transmitted to the compressor. In this case, because of the higher speed requirement, a Magtrol torque meter (Magtrol, 2018) was chosen. This torque meter contains four coils, two on the shaft and two on the housing, and two cylinders that rotate with the shaft that have coinciding rows of slots. An alternating current is applied to the primary coil. When no torque is applied, the slots do not overlap. When torque is applied, the deformation zone undergoes an angular deformation and the slots begin to overlap. This leads to a torque proportional EMF being induced in the secondary coil. This EMF is converted into a $\pm 10\text{V}$ signal which is read by the National Instruments hardware.

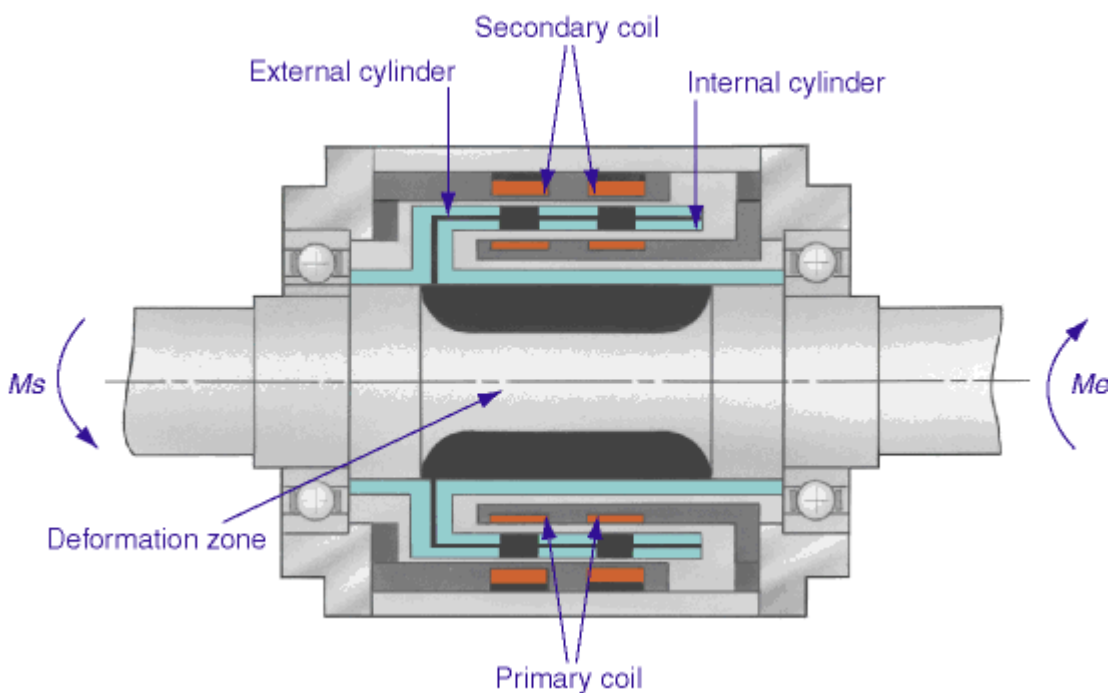


Figure 129: Magtrol Torque Meter (Magtrol, 2019)

Even so, this restricted the test rig to a maximum speed of 50,000 rpm. Two torque sensors were available with ranges of 1 Nm and 5 Nm both accurate to $\pm 0.1\%$.

Figure 128 shows a partial section view of the test rig. As can be seen, the test rig is made up of 4 main elements: the motor, torque tube, test head and compressor. The torque tube houses the torque meter and provides access to the couplings that connect the motor and head shafts to the torque meter shaft. It also supports the hermetic feed through connector that allows the signals from the torque meter to pass through the pressure vessel without introducing a leak path.

The test head's function is to transfer the torque from the motor and support the impeller. The head is interchangeable so if a smaller compressor were to be tested, a suitably smaller head could be used.

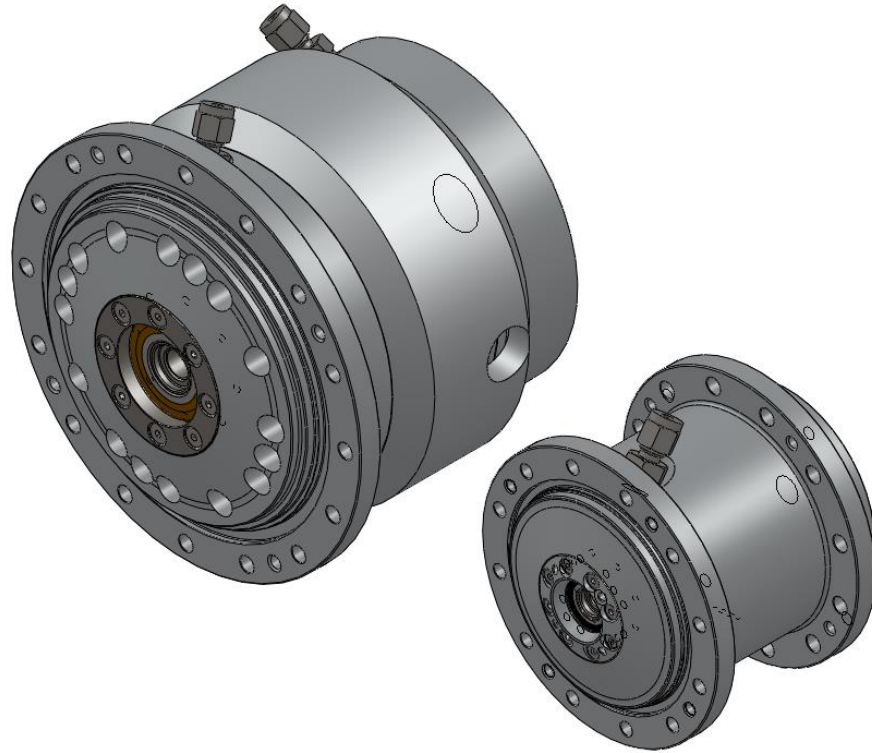


Figure 130: H125 and H80 test heads

The compressor section, also known as the “square box”, is shown as an exploded view in Figure 132. This shows how the compressor is built up in 2 halves, with shims stacked between the scroll halves to accommodate the increase in blade height. Figure 132 shows a section view through the compressor, on the left half is a low blade height configuration, on the right a tall blade height. The height of the inlet flange does change with a change in blade height. However, the pipework in the rest of the test rig flexes enough to accommodate this change.

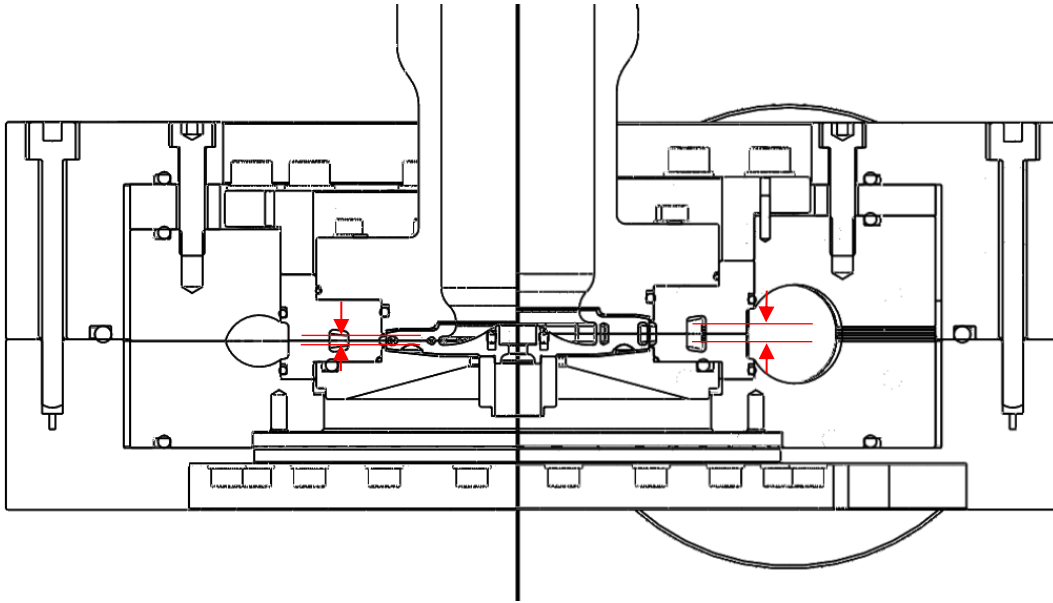


Figure 131: Different blade heights, shown in red, within the same housing

There was a requirement to map the pressure across the front face of the impeller, to find the distribution, but also to measure the degree of reaction of the compressor. As stated in section 4.2.4.1, when calculating the axial force, an assumption of 50% was used to be conservative. However, there was also an assumption that no pressure rise occurred in the impeller as there is no change in area within the impeller passages that would imply a diffusion process. To confirm, tappings were included in the inlet pipe so the pressure across the front face of the impeller could be mapped. One tapping was positioned at the exit of the impeller to allow direct measurement of the static pressure rise within the impeller. Each tapping was 0.5 mm diameter to reduce the likelihood of measuring total rather than static pressure rise.

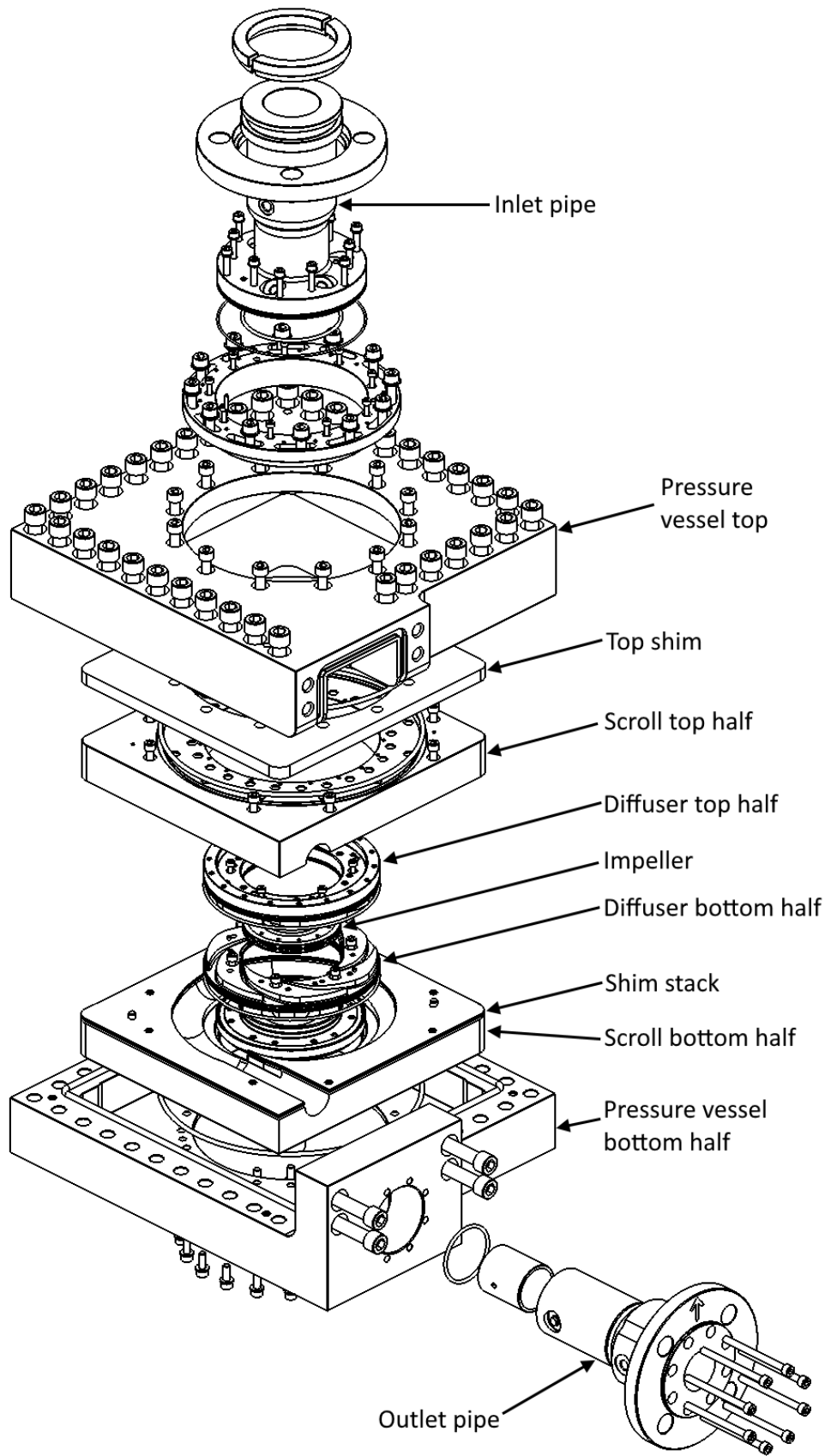


Figure 132: Exploded view of "square box" compressor

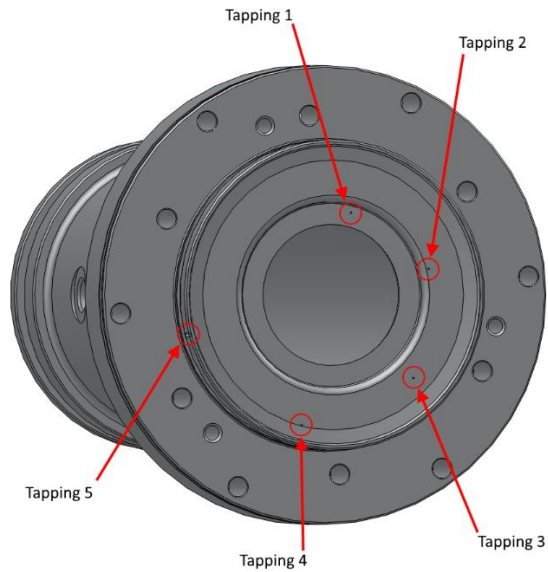


Figure 133: Pressure tapings on inlet pipe

For the first series of tests, the impeller and diffuser half blade heights that were manufactured are shown in Table 15 and the combinations that could be tested are shown in Table 16.

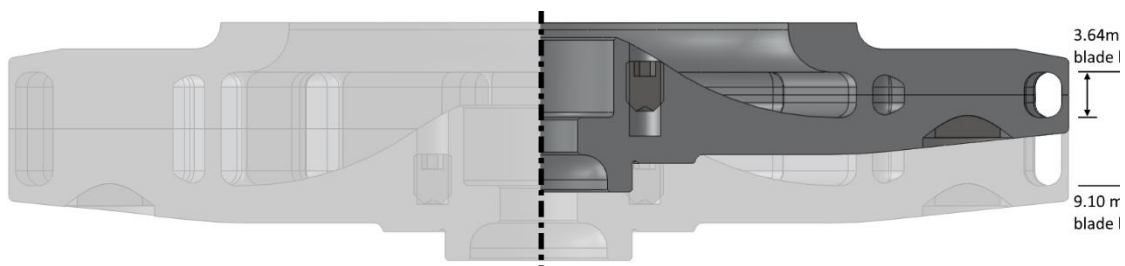


Figure 134: 3.64mm blade height (solid) and 9.10 blade height (transparent)

These tables shown how only 4 complete impellers were manufactured, 7 different blade heights can be tested by mixing and matching the halves. Figure 131 shows the effect of the blade height change on the test rig and Figure 134 on the impeller.

Table 15: blade heights manufactured for each component

| | |
|-------------------|------|
| Blade height (mm) | 1.82 |
| | 2.73 |
| | 3.64 |
| | 4.55 |

Table 16: Possible compressor blade heights available

| Total Blade height (mm) | Top half | | | | |
|-------------------------|-------------|-------------|-------------|-------------|------|
| | 1.82 | 2.73 | 3.64 | 4.55 | |
| Bottom half | 1.82 | 3.64 | 4.55 | | |
| | 2.73 | 4.55 | 5.46 | 6.37 | |
| | 3.64 | | 6.37 | 7.28 | 8.19 |
| | 4.55 | | | 8.19 | 9.10 |

When the impellers were delivered from the manufacturer, they were measured using an optical depth gauge which is accurate to 0.0001 inch. This showed many of the impeller halves were manufactured out of tolerance. Table 17 shows the measured blade heights for the impeller halves and Table 18 shows how this affects the overall impeller blade height.

Table 17: Measured impeller blade heights

| | | | | |
|--------------------|-------|-------|-------|-------|
| Blade height % | 100% | 150% | 200% | 250% |
| Nominal size | 1.820 | 2.730 | 3.640 | 4.550 |
| Hub actual size | 1.889 | 2.784 | 3.653 | 4.555 |
| Shroud actual size | 1.781 | 2.752 | 3.597 | 4.599 |

Table 18: Actual impeller blade heights

| Total Blade height (mm) | Top half | | | | |
|-------------------------|-------------|-------------|-------------|-------------|-------|
| | 1.78 | 2.75 | 3.60 | 4.60 | |
| Bottom half | 1.89 | 3.670 | 4.640 | | |
| | 2.78 | 4.565 | 5.535 | 6.380 | |
| | 3.65 | | 6.405 | 7.250 | 8.252 |
| | 4.56 | | | 8.151 | 9.153 |

A full series of calculations and stress analyses were conducted on the compressor parts checking for an infinite life design, the same as those described in Chapter 4. All the impeller and diffuser parts were machined from 7075-T6 aluminium. The rest of the components were machined from 6082-T6 aluminium. The exceptions being the impeller spool, diffuser clamp, flanges and c-rings which were all machined from EN24T steel. The top shim was water jet cut from mild steel, and the thin shims were laser cut from 304 stainless steel.

7.2. Test loop

As this test rig has a requirement to operate at elevated pressures in gases other than air, a closed gas loop was constructed around the test rig. The loop contained all the instrumentation required to map the compressor. The instrumentation list is given in Table 19 along with sensor accuracies. The National Instruments hardware used for this test rig were one CompactRIO (NI, 2018 p. a) and one CompactDAQ (NI, 2018 p. b) chassis, each with 8 slots for C series I/O module. The list of modules used is shown in Table 21 along with their input/outputs and accuracies. To improve the accuracy of these measurements, all sensor signals are read in the form transmitted, so current sensors are read by current channels, Pt100's are read by RTD channels, no converters were used on performance sensors. The output of the Magtrol torque meters were used on performance sensors. The output of the Magtrol torque meters were found to vary more than the Interface sensor used previously. Using the standard error of the mean calculation, it was found that 200 samples per point were required to be averaged to get a true mean value.

A schematic of the test loop is shown in Figure 135. Gas is fed into the loop from the bottle, through a regulator that keeps the inlet pressure constant. The regulator is set using one of the analogue output channels on the NI system, allowing it to be changed during a test. During a test, pressure and temperatures were measured upstream and downstream of the compressor, and also downstream of the flowmeter. This is to allow calculation of density to convert volume flow as measured to mass flow rate. Between the compressor and the flow meter is a section of parallel pipe with an electrically actuated valve in each leg. The first is a 2" linear ball valve, this allows a large amount of gas to pass through so the compressor can be fully choked. The second valve, a 1" globe valve allows more precise control over the flow rate. Together these valves allow the compressor to be mapped by altering the flow rate over a speed line. As this is a closed loop, a heat exchanger is required to keep the inlet temperature of the gas constant. This uses a flow of cooling oil, whose temperature can be externally controlled, to reduce (or increase) the gas temperature as required. As no test rig can ever be entirely leak free, the gas bottle remains connected during the test so the regulator can top-up the loop as the pressure falls. A pressure relief valve was fitted to prevent over pressure if there was a failure of the top-up regulator.

Table 19: Performance instrumentation list

| Type | Location | Model | Range | Accuracy |
|-------------|-------------|---------------------------------|-----------------------------|--|
| Pressure | Test cell | PTX 7511 | 800-1200 mbar absolute | ± 0.1 % |
| Pressure | Inlet (LP) | PTX 7511 | 0 to 1.6 bar absolute | ± 0.1 % |
| Pressure | Outlet (LP) | PTX 7511 | 0 to 2.0 bar gauge | ± 0.1 % |
| Pressure | FS4000 (LP) | PTX 7511 | 0 to 2.0 bar gauge | ± 0.1 % |
| Pressure | Inlet (HP) | PTX 1400 | 0 to 7.5 bar gauge | ± 0.15 % |
| Pressure | Outlet (HP) | PTX 5072 | 0 to 16.0 bar gauge | ± 0.04 % |
| Pressure | FS4000 (HP) | PTX 640 | 0 to 10.0 bar absolute | ± 0.05 % |
| Pressure | Tapping | PTX 640 | 0 to 10.0 bar absolute | ± 0.05 % |
| Pressure | Torque tube | PTX 1400 | 0 to 4.0 bar gauge | ± 0.15 % |
| Temperature | Test cell | Pt100 Class A | -75 to 250 °C | ± (0.15 + 0.002 t) |
| Temperature | Inlet | Pt100 Class A | -75 to 250 °C | ± (0.15 + 0.002 t) |
| Temperature | Outlet 1 | Pt100 Class A | -75 to 250 °C | ± (0.15 + 0.002 t) |
| Temperature | FS4000 | Pt100 Class A | -75 to 250 °C | ± (0.15 + 0.002 t) |
| Temperature | Torque tube | T-type thermocouple | -50 °C to +250 °C | ± 1.0 °C |
| Torque | Shaft | Magtrol TMHS-304 | 1 Nm | ± 0.1 % |
| Torque | Shaft | Magtrol TMHS-306 | 5 Nm | ± 0.1 % |
| Speed | Shaft | Either TMHS-304 or 306 | 60 pulse/rev TTL | ± 1 rpm |
| Flow meter | Downstream | ABB Swirl Flow meter FS4000-ST4 | 12 – 200 m ³ /hr | ± 0.5 % flow rate |
| O2 sensor | Gas loop | Servomex 756 Oxygen Analyser | 25% to 0.1 vpm in 6 scales | ± 2.0 % full scale deflection ± 1.0 vpm within selected range |

Table 20: Safety monitoring instrumentation list

| Type | Location | Model | Range | Accuracy |
|-------------|---------------------|-----------------------------|-------------------|------------------------|
| Temperature | Motor Bearing 1 | Pt100 Class B | -50 °C to +200 °C | ± (0.3 + 0.005 t) |
| Temperature | Motor Bearing 2 | Pt100 Class B | -50 °C to +200 °C | ± (0.3 + 0.005 t) |
| Temperature | Motor Stator | Pt100 Class B | -50 °C to +200 °C | ± (0.3 + 0.005 t) |
| Temperature | Motor Oil Tank | Pt100 Class B | -50 °C to +150 °C | ± (0.3 + 0.005 t) |
| Temperature | Test Head Bearing 1 | T-type thermocouple | -50 °C to +250 °C | ± 1.0 °C |
| Temperature | Test Head Bearing 1 | T-type thermocouple | -50 °C to +250 °C | ± 1.0 °C |
| Vibration | Motor | Dytran accelerometer 3056B2 | 50 g (100 mV/g) | ±5.0% |
| Vibration | Test head | Dytran accelerometer 3056B2 | 50 g (100 mV/g) | ±5.0% |

Table 21: National Instruments modules

| Module | Type | Qty | Total Channels | DAC resolution | Accuracy |
|---------|--|-----|----------------|----------------|---|
| NI-9217 | 4 channel RTD input | 3 | 12 | 24-bit | ±0.20 °C 3 wire configuration |
| NI-9213 | 16 channel thermocouple input | 2 | 32 | 24-bit | High-resolution mode <0.02°C J,K,T,E,N type High-speed mode <0.25°C J,K,T,E type |
| NI-9203 | 8 channel current input | 2 | 16 | 16-bit | ±0.02% of range (calibrated) |
| NI-9207 | 16 channel (8 current and 8 voltage) inputs | 1 | 16 | 24-bit | Voltage: ±0.04% of range Current: ±0.05% of range |
| NI-9206 | 16 channel voltage inputs | 1 | 16 | 16-bit | ±6,230 µV for ±10 V range ±3,230 µV for ±5 V range |
| NI-9264 | 16 channel voltage outputs | 1 | 16 | 16-bit | ±0.05% of range (calibrated) |
| NI-9375 | 32 channel (16 input, 16 output) digital signals | 1 | 32 | | 7 µs read, 500 µs write delay |
| NI-9234 | 4 channel IEPE accelerometer input | 2 | 8 | 24-bit | 50 ppm |
| NI-9402 | 4 channel DIO LVTTTL | 1 | 4 | | 18 ns typical propagation delay |

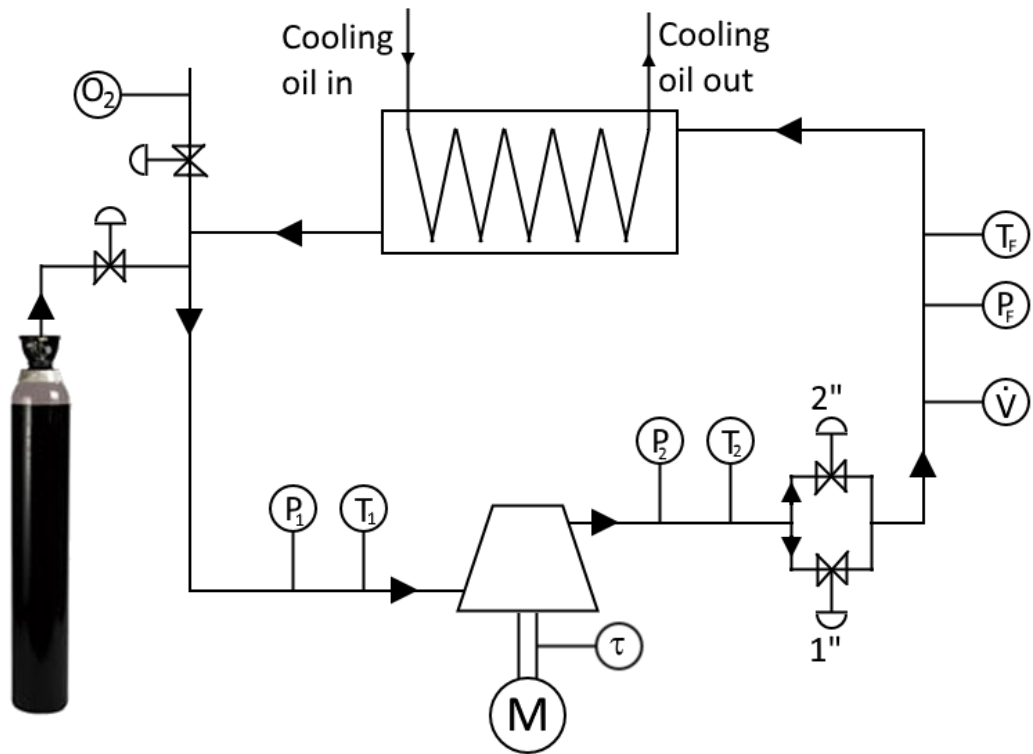


Figure 135: Schematic of pressurised test loop

If the testing is to be completed using a gas that is not air, steps were taken to ensure the gas in the loop was pure. Prior to each set of measurements being taken, the loop is purged multiple times. This involves filling the loop with gas to a high pressure, approximately 5 bar, then venting back to atmospheric pressure. A small bleed of gas from the loop is fed through an oxygen analyser. When the concentration of oxygen drops below 200 ppv, the loop is deemed to be air free and the testing can start.

The procedure for mapping the compressor, once the gas in the loop is pure, is to set the motor speed and inlet pressure, before allowing the rig to settle for 20 mins to let temperatures stabilise. The first data point can then be collected. Once the 200 samples are recorded, the valve (either the 2" or 1") is closed a little to move along the speed line. This will result in either a change in pressure ratio (when near choke) or a change in both pressure ratio and mass flow. The change in valve position was judged to keep the movement along the speed line such that approximately 10 points could be collected between choke and surge.

In order to determine the efficiency of a compressor, there needs to be a way to measure the power being used to compress the gas. For this test rig, a shaft power meter

with an accurate speed sensor were used. However, between the torque meter and the compressor were a large coupling, 2 bearings and a shaft, see Figure 136.

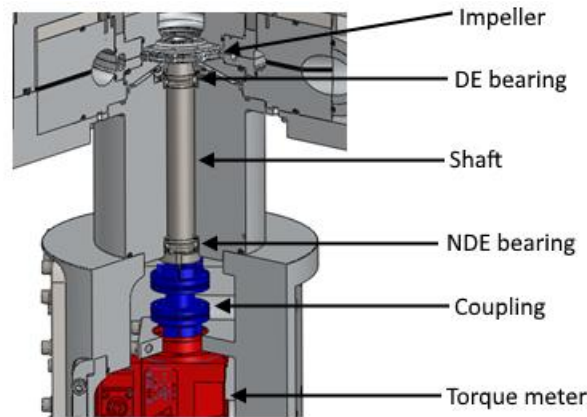


Figure 136: Sources of loss between torque meter and impeller

All these create losses in the system due to friction – either direct metal-to-ceramic contact in the case of the bearings, or as windage losses in the case of the shaft and coupling. These losses will increase as a function of speed and density of the surrounding gas. If these losses were not accounted for it would lead to an overestimation of the power used by the compressor, and a corresponding reduction in the measured efficiency.

To account for these losses, a series of experiments were conducted to measure the losses at all speeds and inlet pressures the rig would operate at. As windage was the dominant loss mechanism, it was decided to correlate the power loss against a windage model to produce a curve that could be used to estimate the losses in future experiments. Using methodologies described in ESDU07004 (ESDU, 2007): Flow in rotating components - discs, cylinders and cavities for windage around rotating cylinders the power required to rotate the coupling was calculated.

$$P_{DW} = \frac{1}{2} \pi \rho \omega^3 a^4 L C_{mc} \quad \text{Equation 81}$$

$$C_{mc} = \left(\frac{1}{-0.8572 + 1.250 \ln(Re_{\phi} \sqrt{C_{mc}})} \right)^2 \quad \text{Equation 82}$$

$$Re_{\phi} = \frac{\rho \omega (2a)^2}{\mu} \quad \text{Equation 83}$$

Where P_{DW} is the drum windage power, a is the cylinder radius, L the length and ω the angular velocity. Re_{ϕ} is the rotational Reynolds number, C_{mc} is the moment coefficient

for a cylinder. ρ is the density and μ the dynamic viscosity of the surrounding gas. As the correlation will be specific to this test rig, the constants and lengths have been removed to simplify the calculation.

$$P_{DW} = \rho\omega^3 C_{mc} \quad \text{Equation 84}$$

$$C_{mc} = \left(\frac{1}{-0.8572 + 1.250 \ln \left((\rho\omega/\mu)\sqrt{C_{mc}} \right)} \right)^2 \quad \text{Equation 85}$$

$$\log_{10} P_m = \log_{10} \tau\omega \quad \text{Equation 86}$$

C_{mc} is found by iterating Equation 85, using an initial guess of 0.02. $\log_{10} P_{DW}$ against $\log_{10} P_m$ is shown in Figure 137 where P_m is the measured Power from the windage test.

As this work was done in collaboration with industry, and that industry has a requirement to compress CO₂, the testing of the compressor in this high-pressure test rig was completed with bottled CO₂.

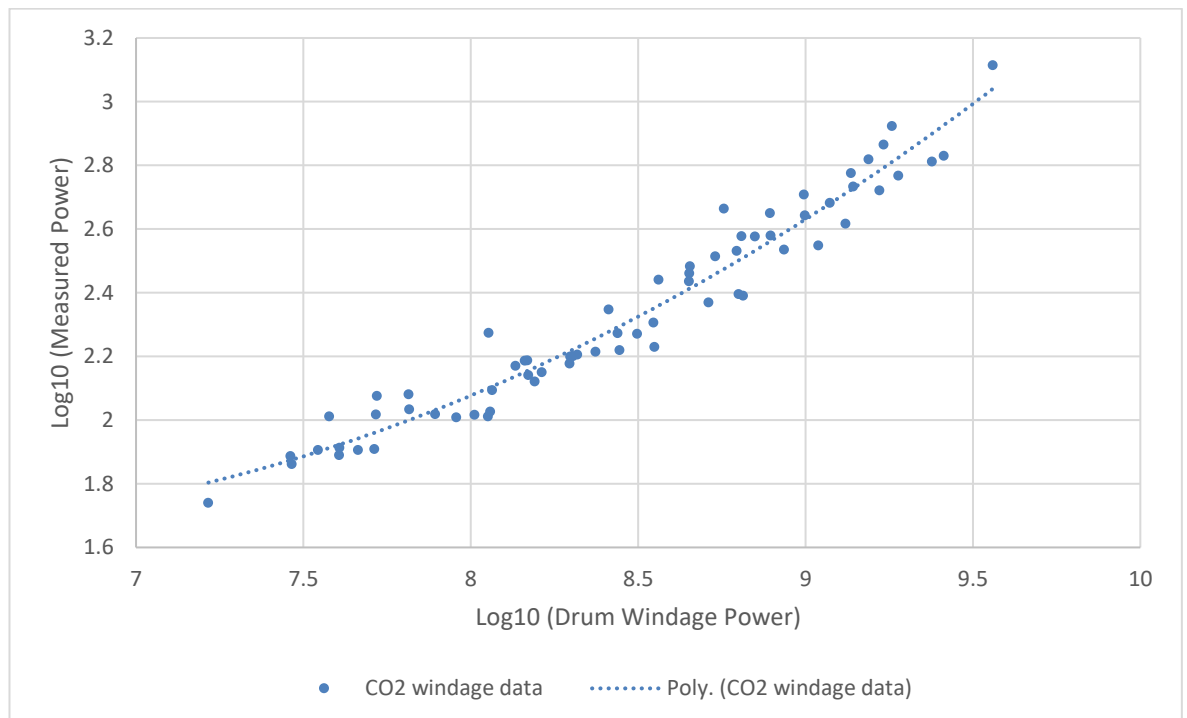


Figure 137: Windage data for 1-5 bar absolute in CO₂

Equation 87 shows the equation used to correlate the measured power with the predicted drum windage power in CO₂. The residual plot in Figure 138 shows a random distribution, and the R² value is high, 0.947, which implies a good fit to the data.

$$\log_{10} P_m = 0.107(\log_{10} P_{DW})^2 - 1.19 \log_{10} P_{DW} + 4.98 \quad \text{Equation 87}$$

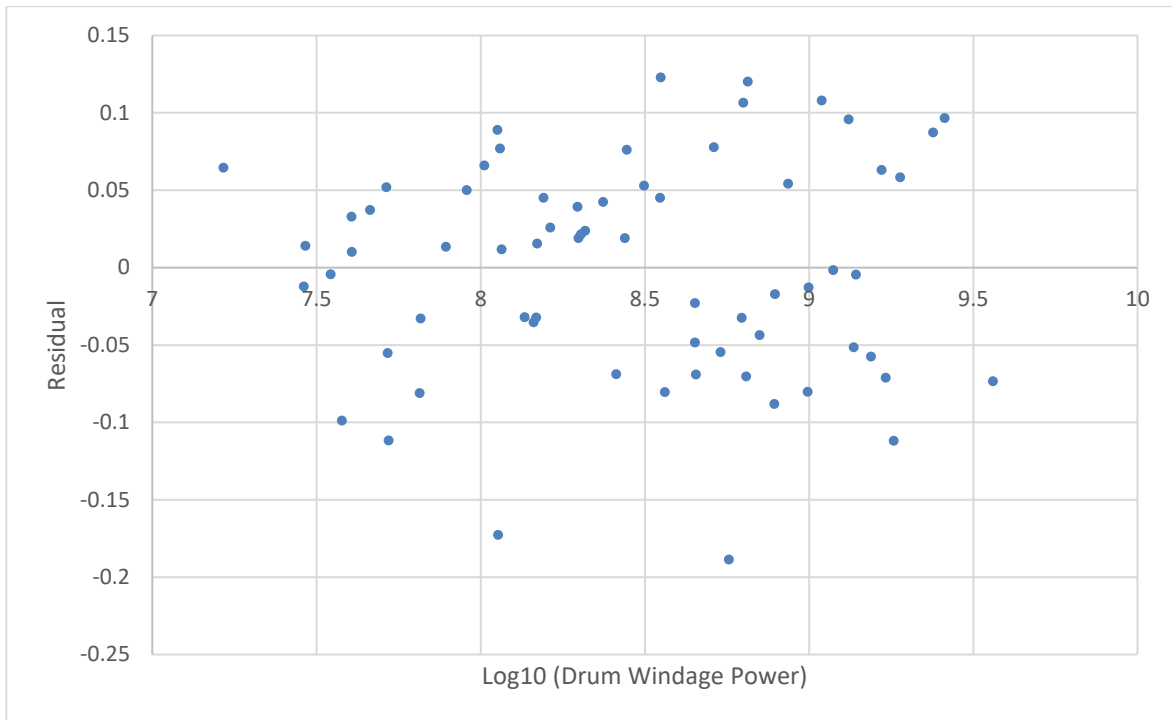


Figure 138: Residual plot of power correlation

7.3. Data Processing and Error Analysis

As in the large scale test rig, see section 4.4, an error analysis has been completed to assess the error associated with all the measurements, and also the error in calculated values. The procedure is the same as that in section 4.4, Table 22 summarises the error for each sensor taking a measurement and the value being recorded.

Table 22: Sensor accuracy

| Type | Location | Model | Range | Sensor accuracy |
|------------|-------------|----------|------------------------------|--------------------------|
| Pressure | Test cell | PTX 7511 | 0.8 to 1.2 bar absolute | ± 0.0012 bar |
| Pressure | Inlet (LP) | PTX 7511 | 0 to 1.6 bar absolute | ± 0.0016 bar |
| Pressure | Outlet (LP) | PTX 7511 | 0 to 2.0 bar gauge | ± 0.0020 bar |
| Pressure | FS4000 (LP) | PTX 7511 | 0 to 2.0 bar gauge | ± 0.0020 bar |
| Pressure | Inlet (HP) | PTX 1400 | 0 to 7.5 bar gauge | ± 0.011 bar |
| Pressure | Outlet (HP) | PTX 5072 | 0 to 16.0 bar gauge | ± 0.007 bar |
| Pressure | FS4000 (HP) | PTX 640 | 0 to 10 bar absolute | ± 0.005 bar |
| Pressure | Tapping | PTX 640 | 0 to 10 bar absolute | ± 0.005 bar |
| Pressure | Torque tube | PTX 1400 | 0 to 4.0 bar gauge | ± 0.006 bar |
| Torque | Shaft | TMHS-304 | ± 1 Nm | ± 0.0012 Nm |
| Torque | Shaft | TMHS-306 | ± 5 Nm | ± 0.006 Nm |
| Flow meter | Downstream | FS4000 | 12 to 200 m ³ /hr | ± 1.0 m ³ /hr |

| Type | Location | Model | Range | Sensor accuracy |
|-------------|-------------|---------------------|---------------|-----------------|
| Temperature | Test cell | Pt100 Class A | -75 to 250 °C | ± 0.3 °C |
| Temperature | Inlet | Pt100 Class A | -75 to 250 °C | ± 0.3 °C |
| Temperature | Outlet 1 | Pt100 Class A | -75 to 250 °C | ± 0.3 °C |
| Temperature | FS4000 | Pt100 Class A | -75 to 250 °C | ± 0.3 °C |
| Temperature | Torque Tube | T-type thermocouple | -50 to 250 °C | ± 1.0 °C |

From these sensor errors, the error in all calculations can be computed. For measurements of the square box, it was decided not to use an ideal gas assumption to calculate efficiency as various gases were to be compared. This led to the use of NIST REPROP programme (database 23, version 9.1) based upon equations of state developed by Lemmon (Lemmon, et al., 2000), to calculate density, enthalpy and entropy. To calculate the ideal enthalpy rise, it is assumed that for an ideal compression, the entropy remains constant. The outlet entropy and outlet pressure can be used to calculate the ideal outlet enthalpy.

$$h_1 = f(P_1, T_1) \quad \text{Equation 88}$$

$$s_1 = f(P_1, T_1) = s_{3s} \quad \text{Equation 89}$$

$$h_{3s} = f(s_{3s}, P_3) \quad \text{Equation 90}$$

$$\eta = \frac{W_s}{W_{actual}} \quad \text{Equation 91}$$

$$W_s = (h_{3s} - h_1) \quad \text{Equation 92}$$

$$W_{actual} = \frac{\tau\omega}{\dot{m}} \quad \text{Equation 93}$$

$$\eta = \left(\frac{1000 \times \dot{m}}{\tau\omega} \right) (h_{3s} - h_1) \quad \text{Equation 94}$$

Where τ is shaft torque, ω angular velocity, h_1 and h_{3s} are enthalpies calculated using NIST. However, as the differences between the mass flow rate and efficiency calculated using REPROP will be small compared to the ideal gas calculations, the ideal form of the equation will be used to calculate the error as described in section 4.4.

Prior to calculating the efficiency, the windage torque is calculated and subtracted from the measured value, leaving the torque that is used by the compressor, allowing a true measurement of compressor efficiency. The windage calculation has an associated error, however, it is small relative to the power associated with the windage loss, which

in itself is small relative to the total power consumed by the compressor. For this reason, the error associated with the windage calculation has not been included.

This chapter has presented the design, analysis and instrumentation of the second test rig built during this work. Also shown is the error analysis and the methodology for removing the windage loss from the torque measurement to get a compressor power measurement for use in the efficiency calculation.

8. Pressurised Test Rig Results

This chapter presents the results from the pressurised test rig with data from air and CO₂ tests. It presents the methodology for normalising the test data so data from different compressors, inlet conditions and gases can be compared. A methodology is presented to predict the performance of the compressor to aid industry in commercialising the technology. Results from pressure measurements around the impeller are presented, this will show how much static pressure rise is generated by the impeller. Finally, the efficiency data will be presented along with any limitations to the measurements.

8.1. 200% Base Case

The base case for the square box testing was the 200% blade height TurboClaw compressor impeller with a diameter of 85 mm. The impeller blade heights were defined as a percentage of the original blade height used by Vine, his impeller was a 210 mm diameter impeller with a blade height of 9 mm. For an 85mm impeller, 100% blade height is 3.64 mm. Therefore, the base case for this testing has a nominal blade height of 7.28 mm.

Initially testing was completed in atmospheric air, to test the rig and de-bug it's operation before testing in high pressure CO₂. Figure 139 shows the Pressure ratio vs mass flow rate for speeds from 20,000 rpm up to the maximum speed of 50,000 rpm.

Pressure ratio analysis is presented first, followed by the efficiency analysis. This is due to the added complexity of the loss estimation of the efficiency calculations.

8.2. Pressure ratio

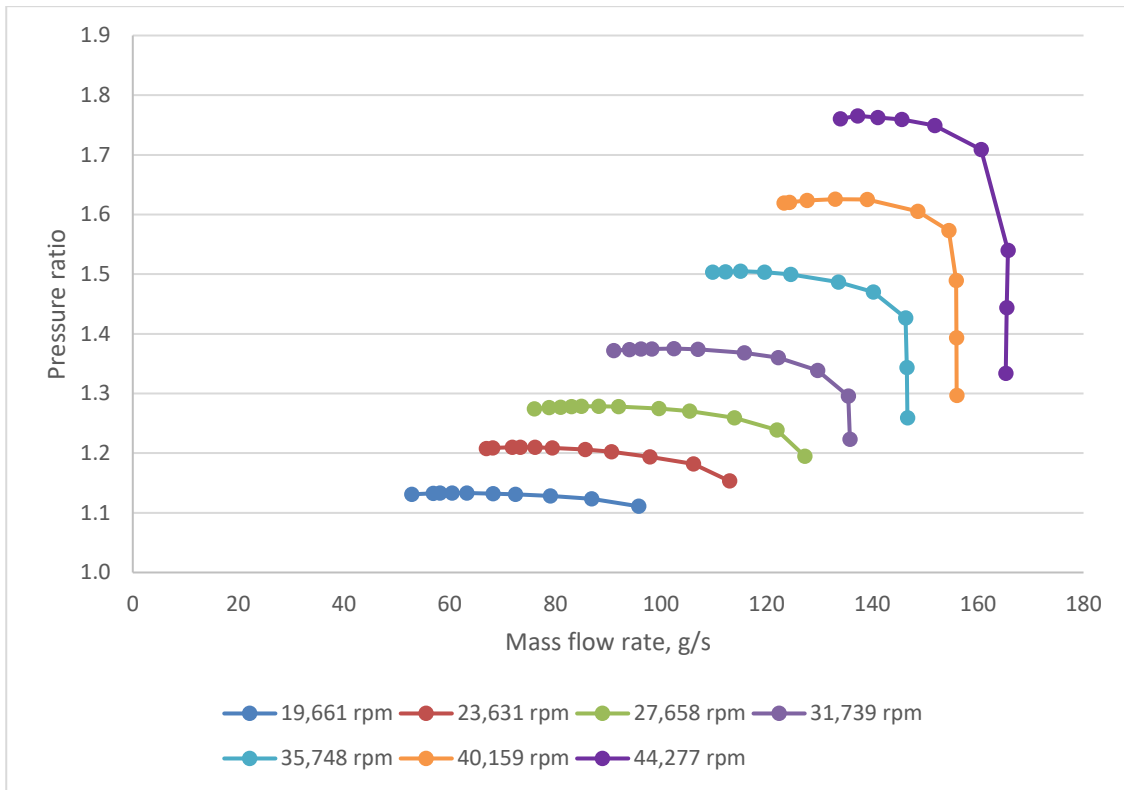


Figure 139: Pressure ratio vs mass flow rate for base case 85x200% in CO₂

Figure 141 shows the results of the initial CO₂ testing of the 85x200% compressor. The majority of the testing was completed at 3 bar absolute. However, due to the excessive power dissipated by the couplings, the temperature within the torque tube exceeded the limit set by the manufacturer. Following the testing of the 200% compressor, water cooling was added to the torque tube so the excess heat could be removed allowing testing at higher speeds and pressures on other blade height compressors.

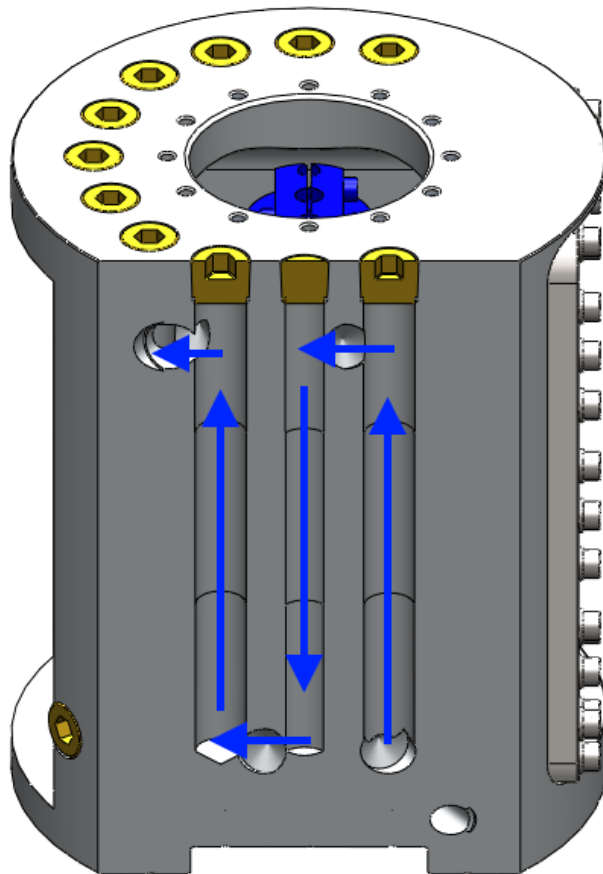


Figure 140: Water cooling of Torque Tube

As can be seen from Figure 141, the increase in pressure from 1 to 5 bar abs has a large effect on the mass flow produced by the compressor. To allow a direct comparison from different inlet pressures and temperatures, and also different gases, it was necessary to non-dimensionalise the map.

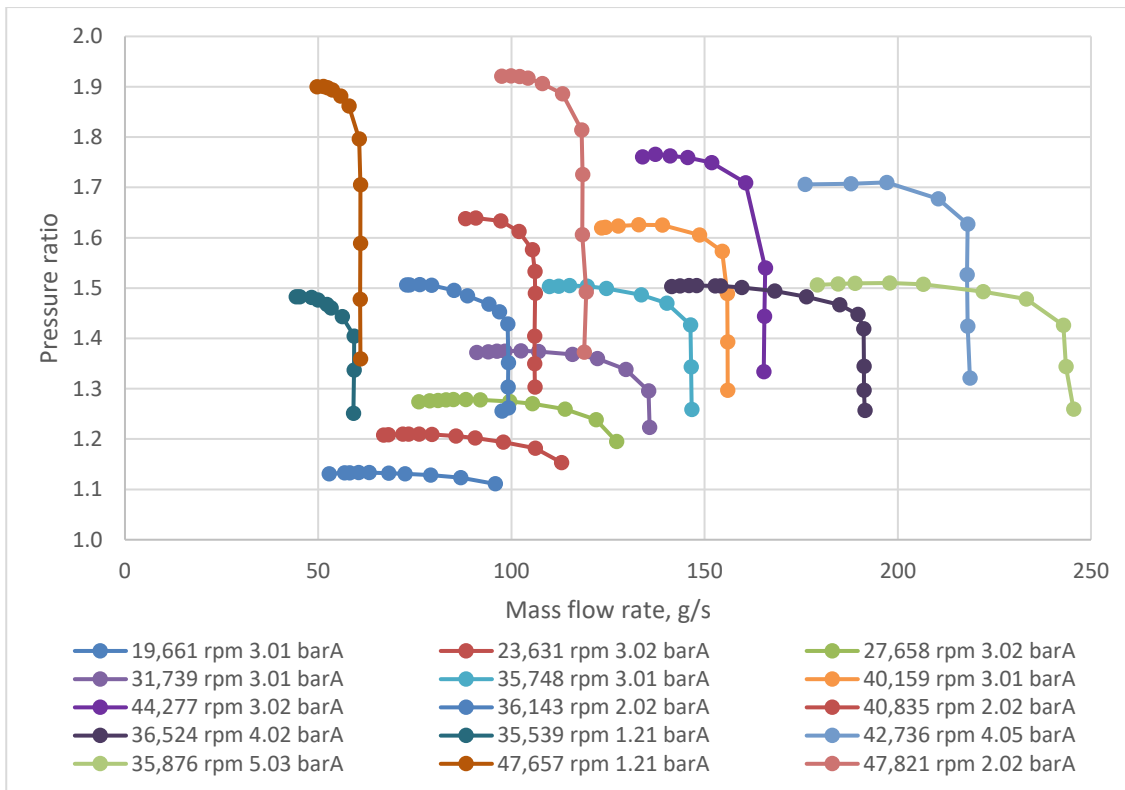


Figure 141: Pressure ratio vs mass flow rate for CO2 testing

However, the map has been re-dimensionalised to have mass flow units of grams per second and speed units of rpm as this makes it more meaningful and easier to understand for the lay person. The equations used to correct the map are shown below. Pressure ratio remains as measured as it is already non-dimensional.

From Compressor Aerodynamics (Cumpsty, 2004) we know that the pressure ratio and mass flow rate of a compressor depend on the compressor speed. The following equations have been derived to allow compressors of different diameter, compressing different gases to be compared. For this reason, the ideal gas assumptions commonly used in aerodynamic scaling equations have been dispensed with in favour of actual gas properties.

The tip speed of a compressor can be found from Equation 95.

$$U = \frac{\pi ND}{60} \quad \text{Equation 95}$$

The simplest way to non-dimensionalise the tip speed is to convert it to a Mach number, similarly with a reference tip Mach number. As the tip Mach number is non-dimensional, the compressor will behave the same for the same value. Therefore, the real tip Mach

number can be set equal to the reference tip Mach number leading to Equation 100 which will “correct” the compressor speed to a set reference condition.

$$U_M = \frac{U}{a} \quad \text{Equation 96}$$

$$U_M = \frac{\pi ND}{60a} \quad \text{Equation 97}$$

$$U_{Mref} = \frac{\pi N_{ref} D_{ref}}{60 a_{ref}} \quad \text{Equation 98}$$

$$\frac{\pi ND}{60a} = \frac{\pi N_{ref} D_{ref}}{60 a_{ref}} \quad \text{Equation 99}$$

$$N_c = N \frac{D/D_{ref}}{a/a_{ref}} \quad \text{Equation 100}$$

Similarly, for the mass flow rate the volume flow rate is the crucial measure. Therefore, the density should be included along with an area that defines the compressor geometry. Equation 101 gives the equation for correcting the mass flow rate.

$$\dot{m}_c = \frac{\dot{m}}{(\rho/\rho_{ref}) (b_{ha}/b_{ha_{ref}}) (a/a_{ref})} \quad \text{Equation 101}$$

Where N is the rotational speed, D is the impeller diameter, a is the speed of sound, \dot{m} is the mass flow rate, ρ is the density, b_r is the blade fillet radius, b_w is the blade width b_h is the blade height. b_{ha} is blade height area measured at the impeller leading edge, see Figure 143. The blade height area is measured across a line perpendicular to the blade leading edge, see Figure 143. The blade width has a linear relationship with the impeller diameter so can be calculated rather than needing to be measured each time. Equation 102 and Equation 103 relate the blade width and blade height area to the diameter, blade height and root radius for geometrically similar impellers.

$$b_w = 0.0378D + 2.60 \times 10^{-10} \quad \text{Equation 102}$$

$$b_{ha} = \pi b_r^2 + 2b_r(b_w - 2b_r) + b_w(b_h - 2b_r) \quad \text{Equation 103}$$

Subscripts c and ref refer to corrected and reference quantities respectively. Reference conditions were chosen as $T_{ref}=288.15$ K, $P_{ref}=1$ bar, $D_{ref}=0.085$ m and $a_{ref}=264.5$ m/s.

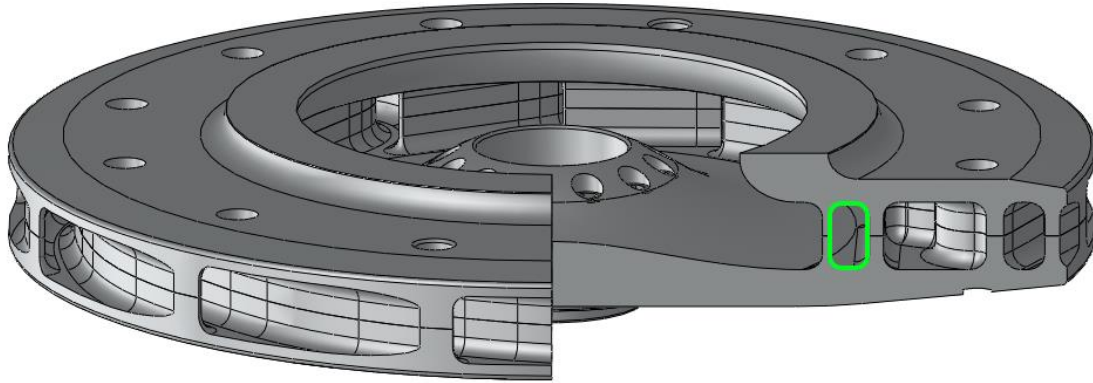


Figure 142: Impeller blade height area shown in green

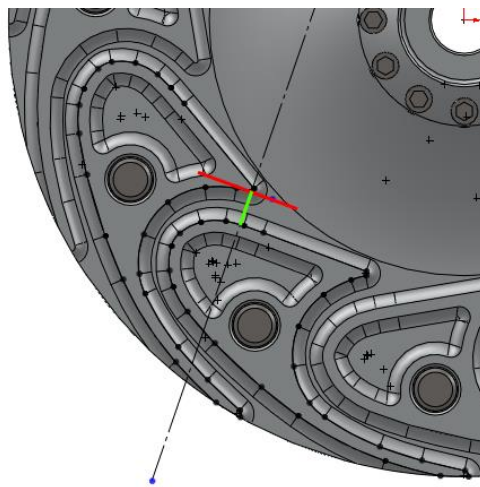


Figure 143: Impeller blade height area cut line

Figure 144 shows the corrected results from the CO₂ tests of the 85x200% compressor. The legend shows shaft speed and inlet pressure for each line.

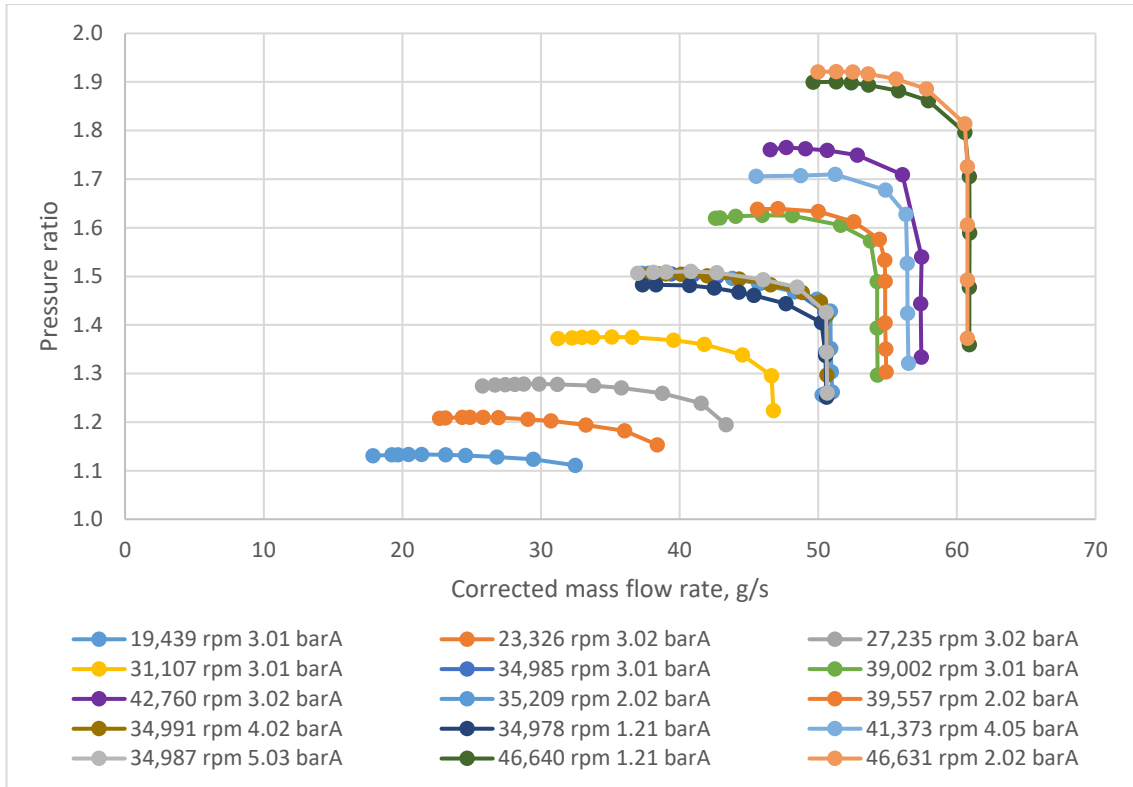


Figure 144: Pressure ratio vs corrected mass flow for the 85x200% base case CO₂ at various inlet pressures

Figure 144 shows how the non-dimensionalising the map has brought speed lines, measured at different inlet pressures, together. This map can be used to predict the pressure ratio for any given corrected speed and mass flow within the range of tested data.

Table 23 shows a matrix of all the tests completed on the square box rig. The higher-pressure testing was limited to the low blade height compressor due to motor power limitations. The maximum speed was limited by the temperature within the torque tube, even with the water cooling it was still prone to overheating.

Table 23: Tested compressor matrix

| | Air 1.0 bar | CO ₂ 1.2 bar | CO ₂ 1.5 bar | CO ₂ 2 bar | CO ₂ 3 bar | CO ₂ 4 bar | CO ₂ 5 bar | CO ₂ 6 bar | CO ₂ 8 bar | CO ₂ 9 bar |
|------------|-------------------|-------------------------------|-------------------------------|--------------------------|--------------------------|--------------------------|--------------------------|--------------------------|--------------------------|--------------------------|
| 15,000 rpm | ④ | | | | | | | | | |
| 20,000 rpm | ④ | | | | ④ ⑤ | | | ① | | ① |
| 25,000 rpm | ③ ④ | | | | ④ | | | | | |
| 30,000 rpm | ④ | | | | ④ ⑤ | | | ① | | ① |
| 35,000 rpm | ③ ④ | ④ | ① ② | ④ | ① ② ④ | ④ | ① ④ | | | |
| 40,000 rpm | ④ | | | ④ | ④ ⑤ | ④ | | ① | | ① |
| 42,500 rpm | | | | | ④ | | | | | |
| 45,000 rpm | | ④ | ① ② | ④ | ① ② | | | | | ① |
| 47,500 rpm | | | | | ⑤ | | | ① | ① | |
| 50,000 rpm | | | | | | | | | | |

Where ① 85x100%, ② 85x125%, ③ 85x150%, ④ 85x175%, ⑤ 85x200%, ⑥ 85x250%.

Figure 145 and Figure 164 show all the data plotted on corrected maps.

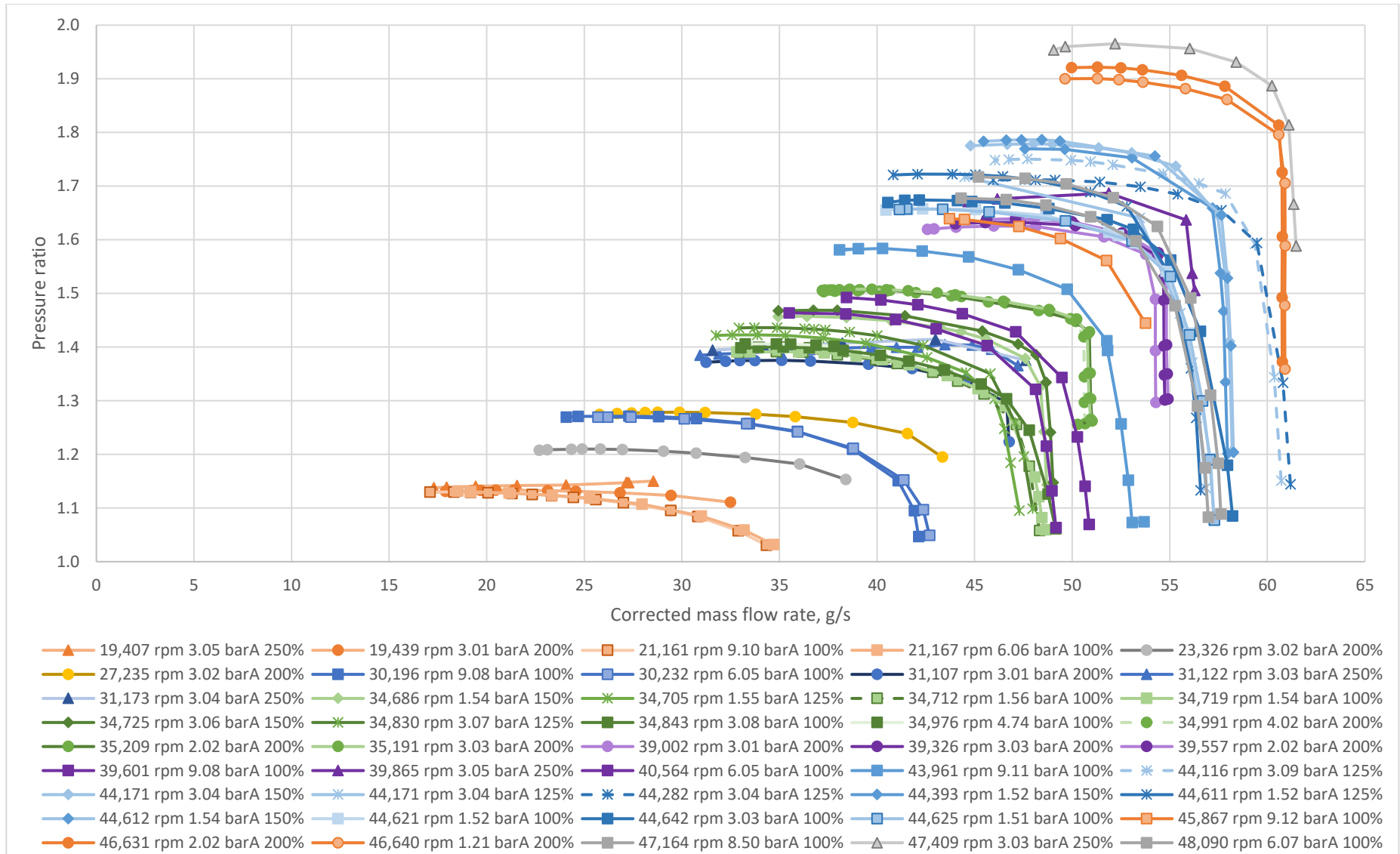


Figure 145: Pressure ratio vs corrected mass flow rate for all sizes and pressures

8.3. Map Predictor Tool

Previous attempts to design a tool that can predict the performance of the forward swept TurboClaw compressor have been based upon Reynolds scaling, these have all proven to be unsuccessful.

The Reynolds number, as well as being used to predict the onset of turbulent flow, can also be used to determine dynamic similitude in fluid dynamic problems. As introduced in Section 1.3, Pampreen showed for centrifugal compressor that if the Reynolds number was plotted against 1-efficiency on log(10) axes, a straight line with a slope of -0.164 fit the majority of points. This shows that for centrifugal compressors the loss in efficiency is a result of turbulent flow. (Pampreen, 1973) If a slope could be found for TurboClaw it could be used to predict performance of the compressor by extrapolating test data.

Thornton's model (Thornton, 2005) was based upon the Reynolds scaling premise. It was initially constructed for single stage compressors, then applied to multistage scaling. It was developed before Vine (Vine, 2005) had carried out preliminary compressor testing which affected its accuracy, this is described in more detail in Chapter 2. Parra (Parra, 2013) also attempted to build a model to describe the operation of the compressor by breaking down the loss mechanisms such as skin friction and blockage within the compressor. He tried to build a physical equation-based model to describe the performance of the compressor but was also unsuccessful and the model was never completed.

For the model presented below, it was decided to approach it in an empirical way. Although some physical properties are used in the equation, the model is primarily a curve fit to the gathered data. In this way, as further data is collected the model can be updated and refined. Because it is a curve fit, the model can only be used to predict performance within the bounds of data collected, it can't be used to extrapolate performance into regions that haven't been tested.

The basic premise of the prediction tool is that with geometric inputs of compressor diameter and blade height, and flow inputs of gas type (Air, CO₂, etc), pressure and temperature a map can be produced showing the performance of a new compressor.

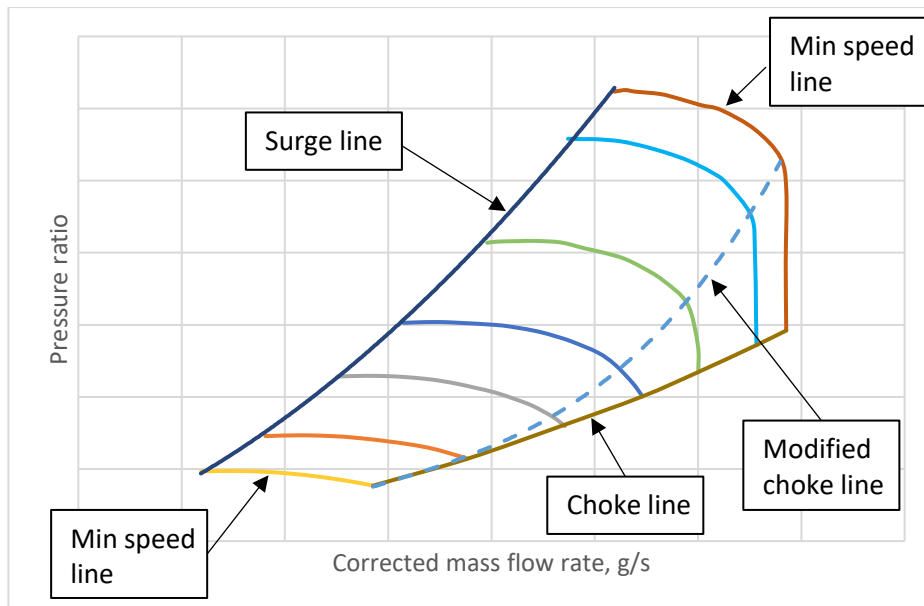


Figure 146: Generic compressor map

Figure 146 shows the generic shape of a compressor map. It is bounded by the minimum and maximum speed lines, the surge line and the choke line. Within the operating envelope, lines of constant speed show how the pressure ratio varies with mass flow.

The speed lines, especially at higher speeds, show a flat section where changes to the mass flow rate hardly affect the pressure ratio. Then a drop off to a section where for very small changes in mass flow rate, there is a large change in pressure ratio. Due to the difficulty in generating a curve that can describe a vertical line transitioning into a horizontal line, a modified choke line has been drawn (dashed line on the chart) and the map will terminate here. In the future either single curve fit that can describe the whole map, or 2 curves to describe each portion of the map need to be developed.

To mathematically describe the map above, 3 equations are required. The first to predict the pressure ratio from a given corrected speed and corrected mass flow, the second and third to describe the surge and modified choke lines so the bounds of the map can be found.

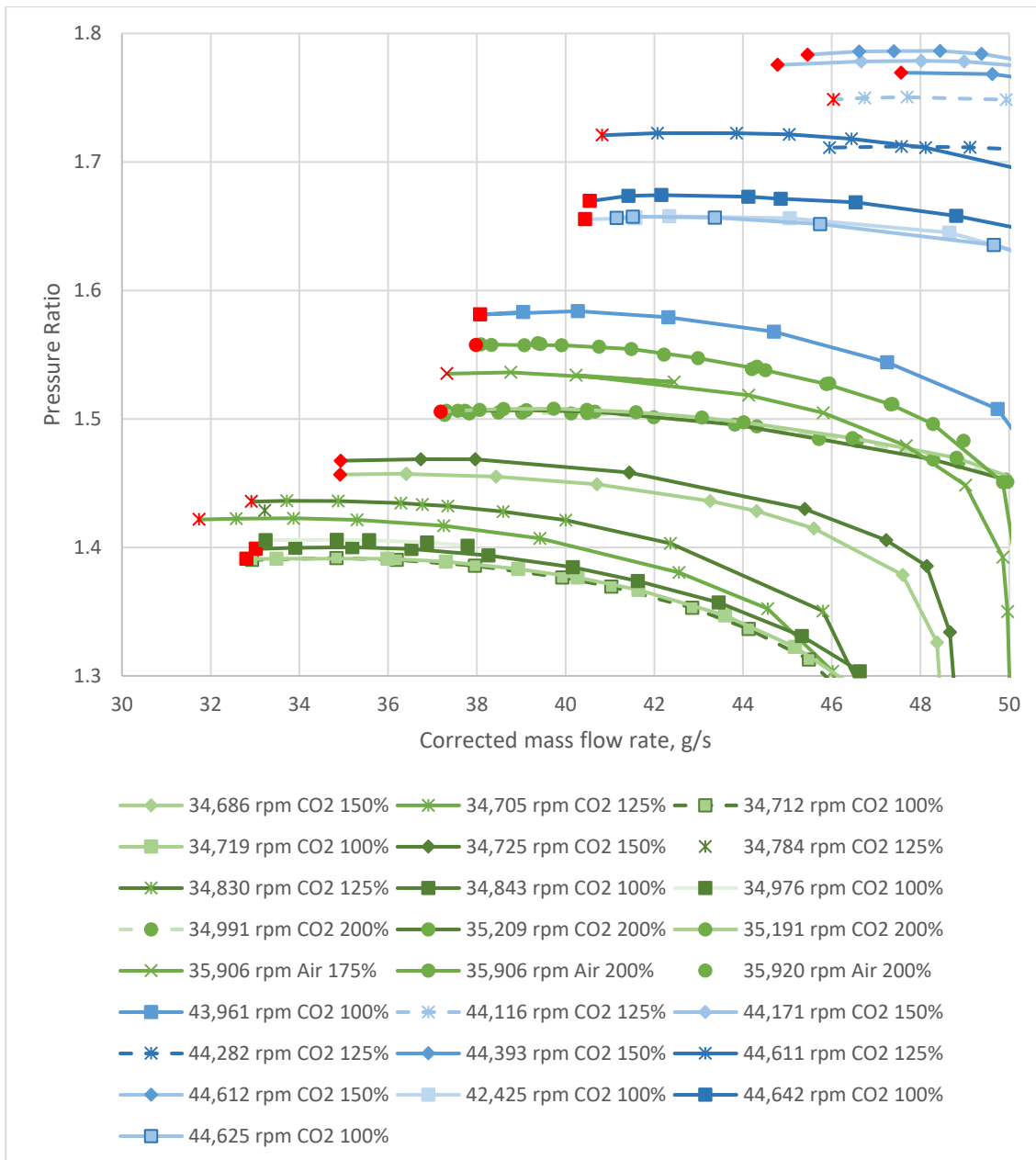


Figure 147: Speeds lines for 35,000 rpm and 44,000 rpm

Beginning with surge, Figure 147 shows how the position of surge changes depending on the blade height and gas. A simple polynomial curve will not accurately describe surge. A more complex base equation was used with the form shown in Equation 104. Similarly, choke is described with Equation 105.

$$\dot{m}_{su} = t + D^s \times \sum_{i=1}^n m_i \times N_c^{n_i} \times a^{p_i} \times \rho^{q_i} \times b_h^{r_i} \quad \text{Equation 104}$$

$$\dot{m}_{ch} = g + D^f \times \sum_{i=1}^n h_i \times N_c^{b_i} \times a^{c_i} \times \rho^{d_i} \times b_h^{e_i} \quad \text{Equation 105}$$

Where \dot{m}_{su} is the corrected surge mass flow rate, \dot{m}_{ch} corrected choke mass flow rate, D is the impeller diameter, N_c is the corrected speed, and b_h the blade height, ρ the density and a is the speed of sound. $b-h$, $m-t$ are constants. To calculate the values of the constants, an optimisation was set up using gPROMS, a process modelling software. Surge and choke lines were calculated separately. Data for corrected speed, mass flow rate, speed of sound, density, blade height and diameter were loaded from test data along with an initial guess for each value of the constants. Historical data supplied by DBS gave mass flow rate and pressure ratio data for a 60x150% and 75x100% compressor, allowing the optimisation to take diameter into account. A weighting, W , was applied to the historical data to lower its effect on the optimisation as the data was not collected in the most rigorous fashion. The program used these values to estimate a “calculated surge mass flow rate”, \dot{m}_{su} , from Equation 104. An objective function, \dot{m}_o , was calculated from Equation 106 where l is the number of data points in the optimisation. The optimisation programme changed the values of the constants to minimise \dot{m}_o .

$$\dot{m}_o = \sqrt{\sum_{j=1}^l \frac{(\dot{m}_{su} - \dot{m}_c/W)^2}{l}} \quad \text{Equation 106}$$

The constants were constrained between maximum and minimum values to avoid overfitting the curve, these are shown in Table 24. It was found through trial and error that an n value of 4 was sufficient to describe the choke and surge lines. Table 24 also shows the values for the constants as optimised by gPROMS.

Table 24: Constraints and optimised result for constant optimisation

| Surge | | | | Choke | | | |
|-------|---------|---------|-----------------|-------|---------|---------|-----------------|
| | Maximum | Minimum | Optimised value | | Maximum | Minimum | Optimised value |
| m_1 | -10 | 10 | -8.50E-05 | h_1 | -10 | 10 | 4.33E-14 |
| m_2 | -10 | 10 | 0.004285 | h_2 | -10 | 10 | 0.416502 |
| m_3 | -10 | 10 | -0.27057 | h_3 | -10 | 10 | 10 |
| m_4 | -10 | 10 | -0.15411 | h_4 | -10 | 10 | 3.996074 |
| n_1 | -4 | 4 | 3.167625 | b_1 | -4 | 4 | 0.950963 |
| n_2 | -4 | 4 | 0.949991 | b_2 | -4 | 4 | -4 |
| n_3 | -4 | 4 | 1.140951 | b_3 | -4 | 4 | 0.550993 |
| n_4 | -4 | 4 | 0.41207 | b_4 | -4 | 4 | -3.89312 |
| p_1 | -4 | 4 | -0.57773 | c_1 | -4 | 4 | 3.455097 |
| p_2 | -4 | 4 | 0.595048 | c_2 | -4 | 4 | -2.32779 |
| p_3 | -4 | 4 | -0.77509 | c_3 | -4 | 4 | -0.72451 |
| p_4 | -4 | 4 | 0.785693 | c_4 | -4 | 4 | 1.185126 |
| q_1 | -4 | 4 | 0.279292 | d_1 | -4 | 4 | -0.40185 |
| q_2 | -4 | 4 | 0.099191 | d_2 | -4 | 4 | -4 |
| q_3 | -4 | 4 | -0.23298 | d_3 | -4 | 4 | 0.022701 |
| q_4 | -4 | 4 | 0.143858 | d_4 | -4 | 4 | 2.954116 |
| r_1 | -4 | 4 | 4 | e_1 | -4 | 4 | -0.52069 |
| r_2 | -4 | 4 | 0.570847 | e_2 | -4 | 4 | 4 |
| r_3 | -4 | 4 | 0.518826 | e_3 | -4 | 4 | 0.15136 |
| r_4 | -4 | 4 | 0.403782 | e_4 | -4 | 4 | -4 |
| s | -4 | 4 | 0.075796 | f | -4 | 4 | -0.29961 |
| t | -100 | 100 | 52.3768 | g | -10 | 10 | -10 |

Figure 148 and Figure 149 show graphically the difference between the measured and calculated values for surge and choke respectively. Figure 150 and Figure 151 show the residual plots. These show the residuals have random scatter, implying the choice of base equation is suitable.

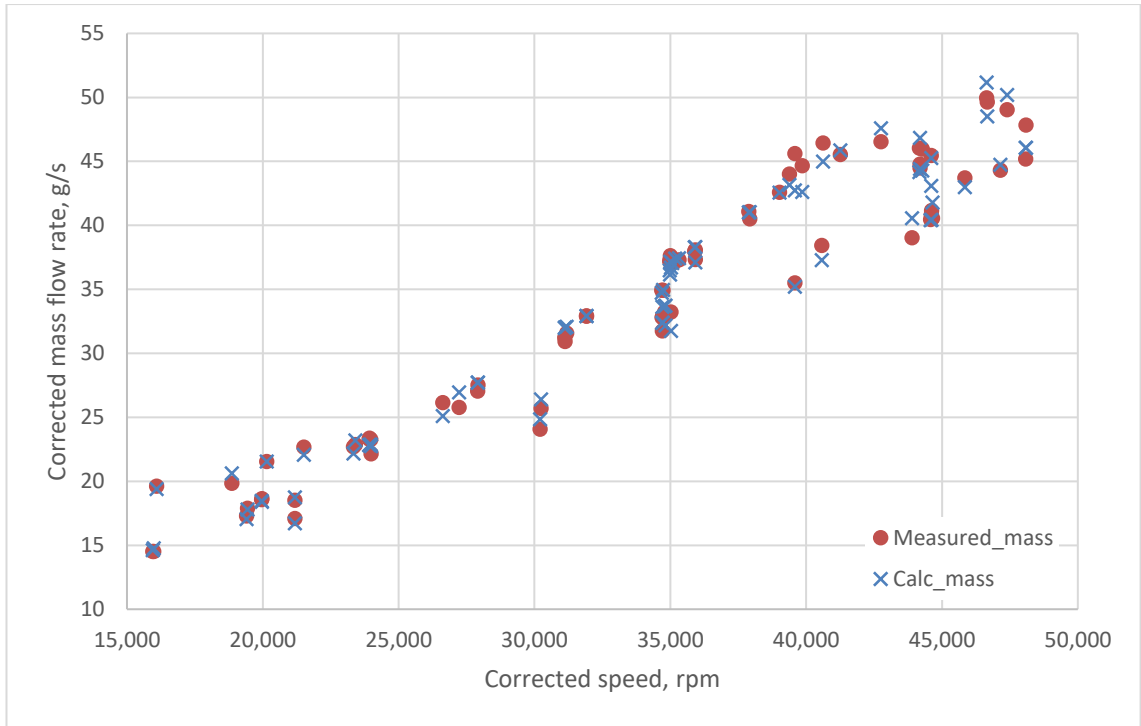


Figure 148: Surge test data vs calculated data

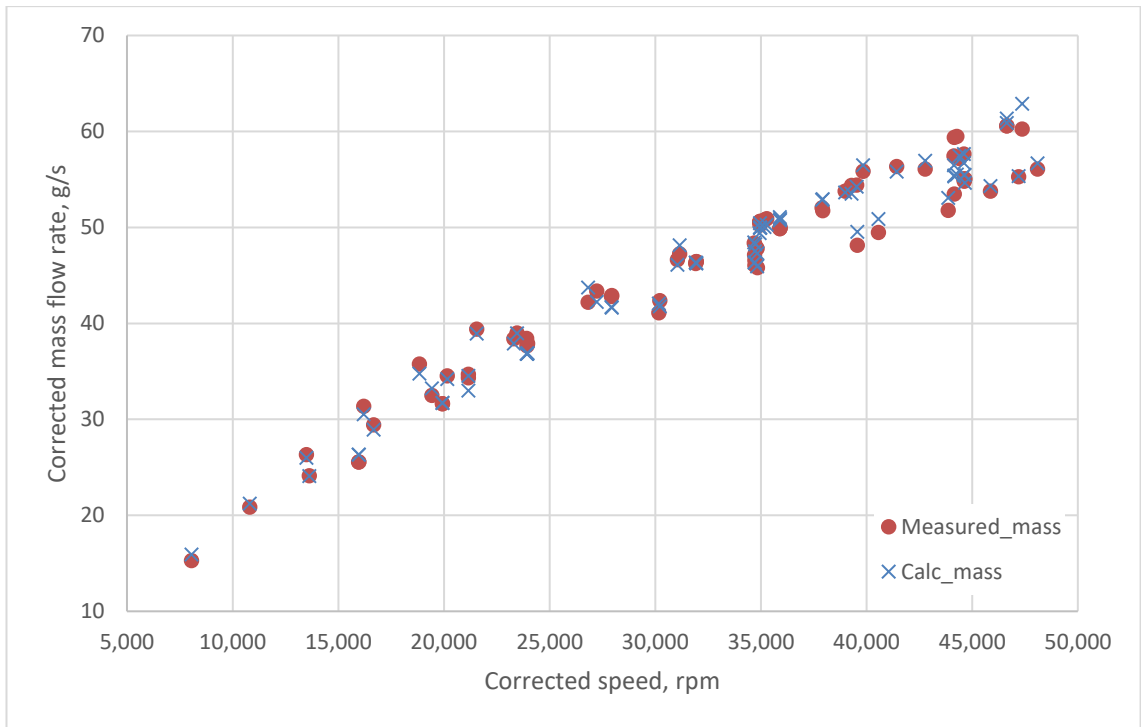


Figure 149: Choke test data vs calculated data

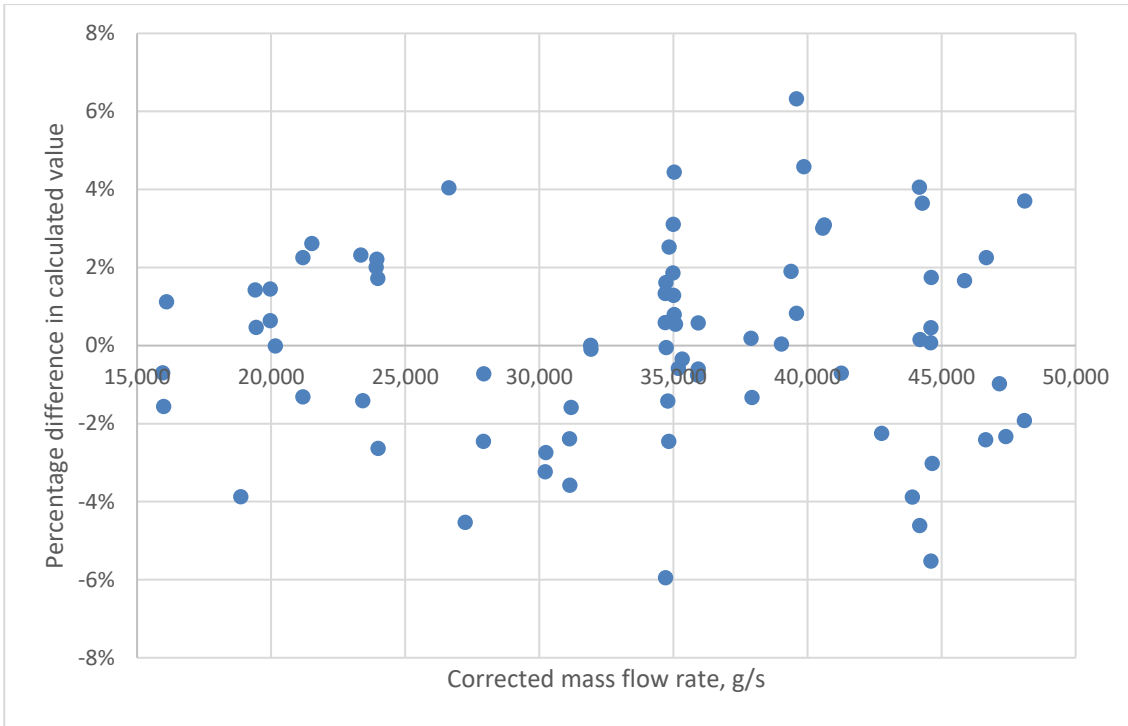


Figure 150: Residual plot of surge curve fit

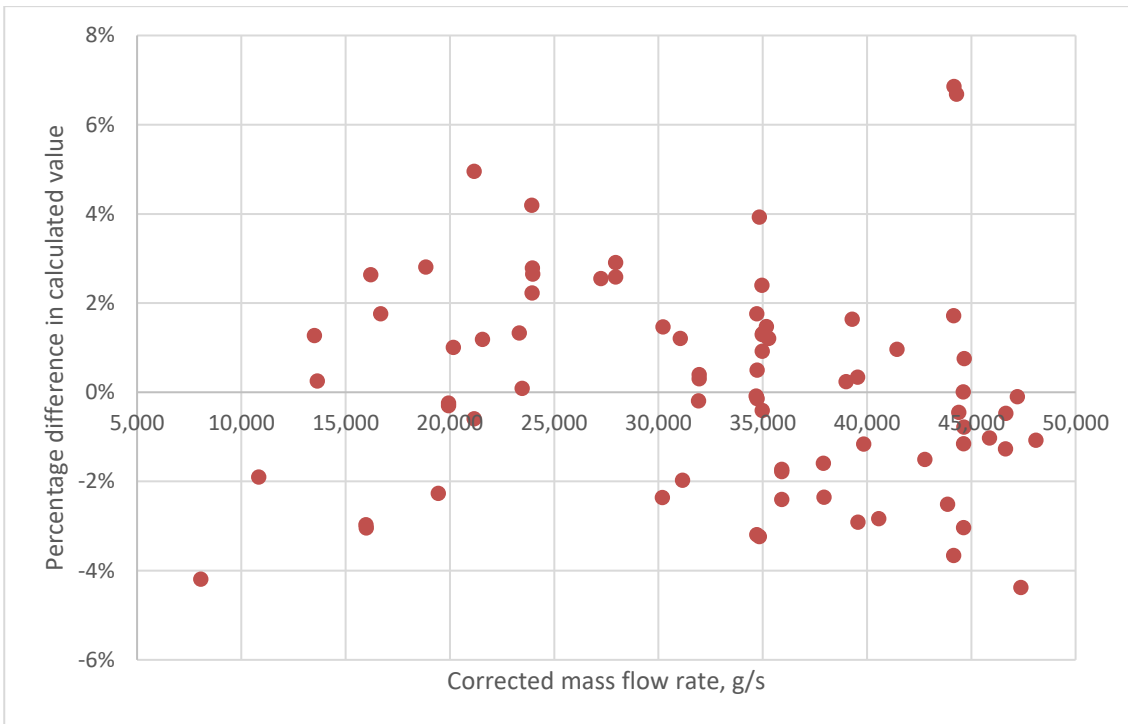


Figure 151: Residual plot of choke curve fit

To curve fit the speed lines, an equation of the form shown in Equation 107 was used. An n value of 5 was chosen as this gave the best fit to the data. Table 25 shows the constraints used for the optimisation along with the optimised values.

$$PR = y + d^x \times \sum_{i=1}^n f_i \times N_c^{g_i} \times \dot{m}_c^{h_i} \times a^{j_i} \times \rho^{k_i} \times b_h^{l_i}$$

Equation 107

Table 25: Constraints and optimised result for constant optimisation of PR

| | | | |
|-------|-----|----|-----------|
| f_1 | -10 | 10 | -4.71E-04 |
| f_2 | -10 | 10 | 3.01E-05 |
| f_3 | -10 | 10 | -0.0063 |
| f_4 | -10 | 10 | -1.78E-06 |
| f_5 | -10 | 10 | 0.002007 |
| g_1 | -4 | 4 | 0.596096 |
| g_2 | -4 | 4 | 0.695002 |
| g_3 | -4 | 4 | 0.590904 |
| g_4 | -4 | 4 | -0.05571 |
| g_5 | -10 | 10 | 0.599308 |
| h_1 | -4 | 4 | 2.19623 |
| h_2 | -4 | 4 | 1.903661 |
| h_3 | -4 | 4 | 2.051982 |
| h_4 | -4 | 4 | 2.686003 |
| h_5 | -10 | 10 | 2.193423 |
| j_1 | -4 | 4 | 0.19866 |
| j_2 | -4 | 4 | -0.12957 |
| j_3 | -4 | 4 | -1.21637 |
| j_4 | -4 | 4 | 1.031707 |
| j_5 | -10 | 10 | -0.04719 |
| k_1 | -4 | 4 | 1.288626 |
| k_2 | -4 | 4 | 0.141112 |
| k_3 | -4 | 4 | 0.180902 |
| k_4 | -4 | 4 | -0.2857 |
| k_5 | -10 | 10 | 1.343251 |
| l_1 | -4 | 4 | 1.087208 |
| l_2 | -4 | 4 | -0.1637 |
| l_3 | -4 | 4 | -0.32242 |
| l_4 | -4 | 4 | -0.14897 |
| l_5 | -10 | 10 | 1.140342 |
| x | -4 | 4 | 1.151516 |
| y | -4 | 4 | 1.02073 |

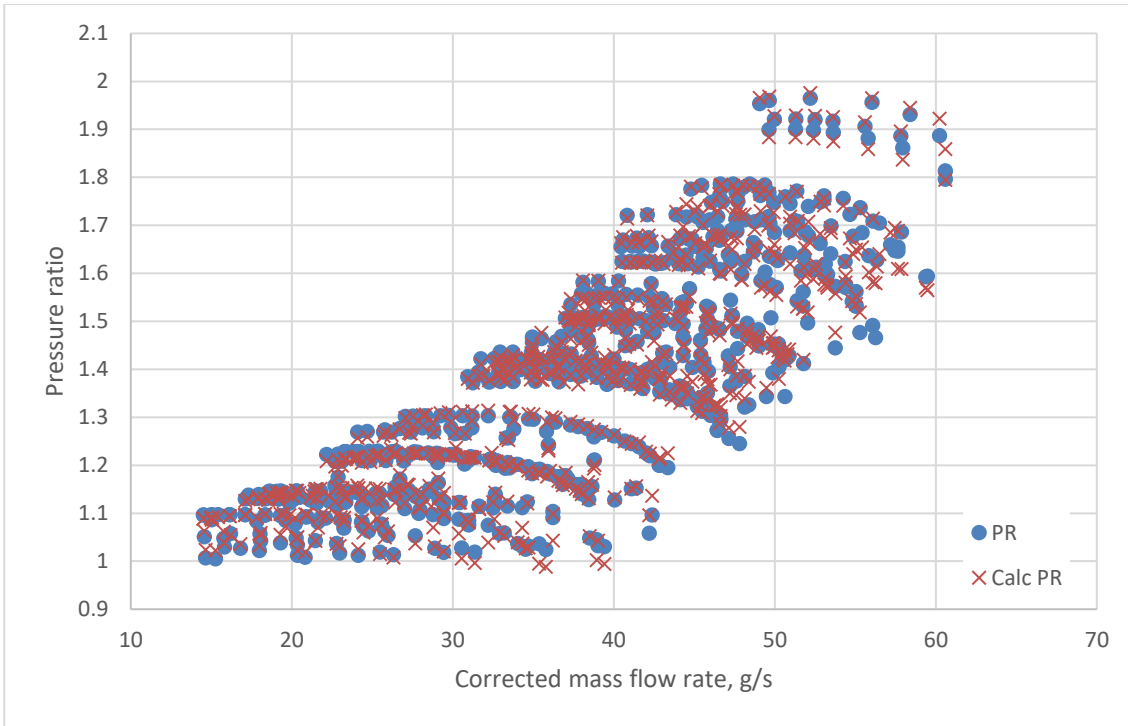


Figure 152: All test data vs calculated data

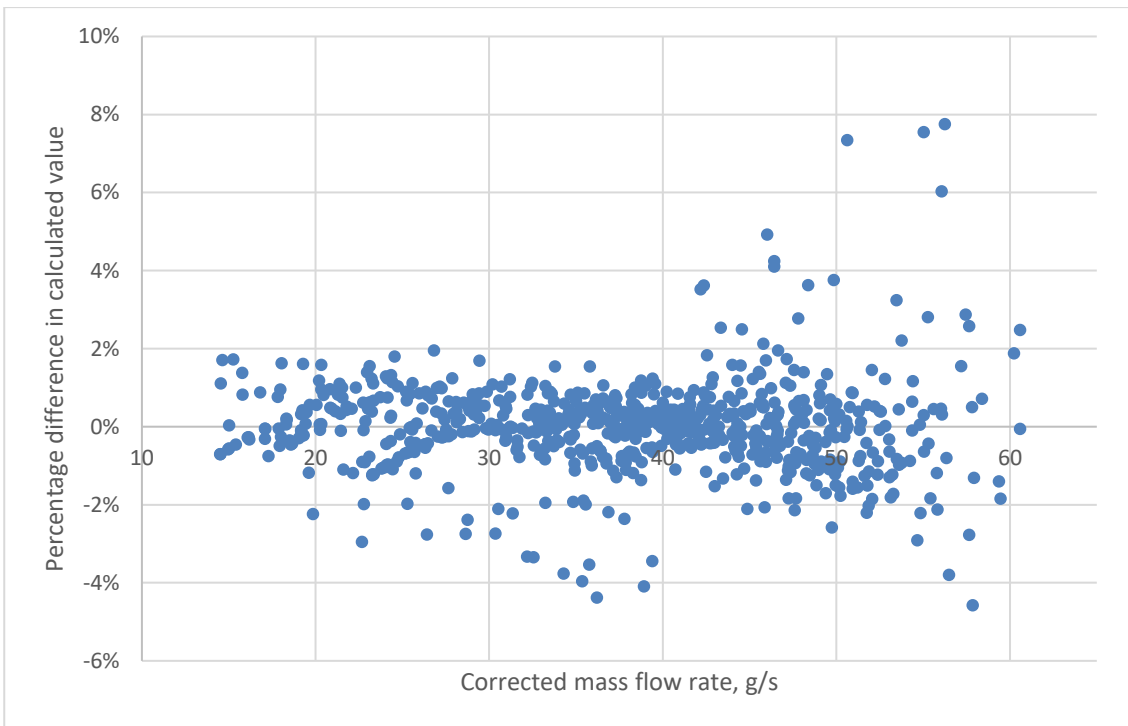


Figure 153: percentage difference between test data and calculated data

These equations now allow the prediction of pressure ratio based upon compressor geometry, inlet conditions, mass flow rate and shaft speed.

8.4. Pressure tapings and axial force

As described in Chapter 7, pressure tapings were added to the inlet pipe to allow measurements of the pressure in the windage gap between the housing and shroud. These measurements also allow an accurate measurement of the degree of reaction of the compressor, so far assumed to be 0%, and also an improved estimation of the axial force transmitted to the bearings during compressor operation.

For the 85x100% case, 5 pressure sensors were connected to the tapings so simultaneous measurements could be taken. Measurements were taken when the compressor was at the surge and choke ends of the map.

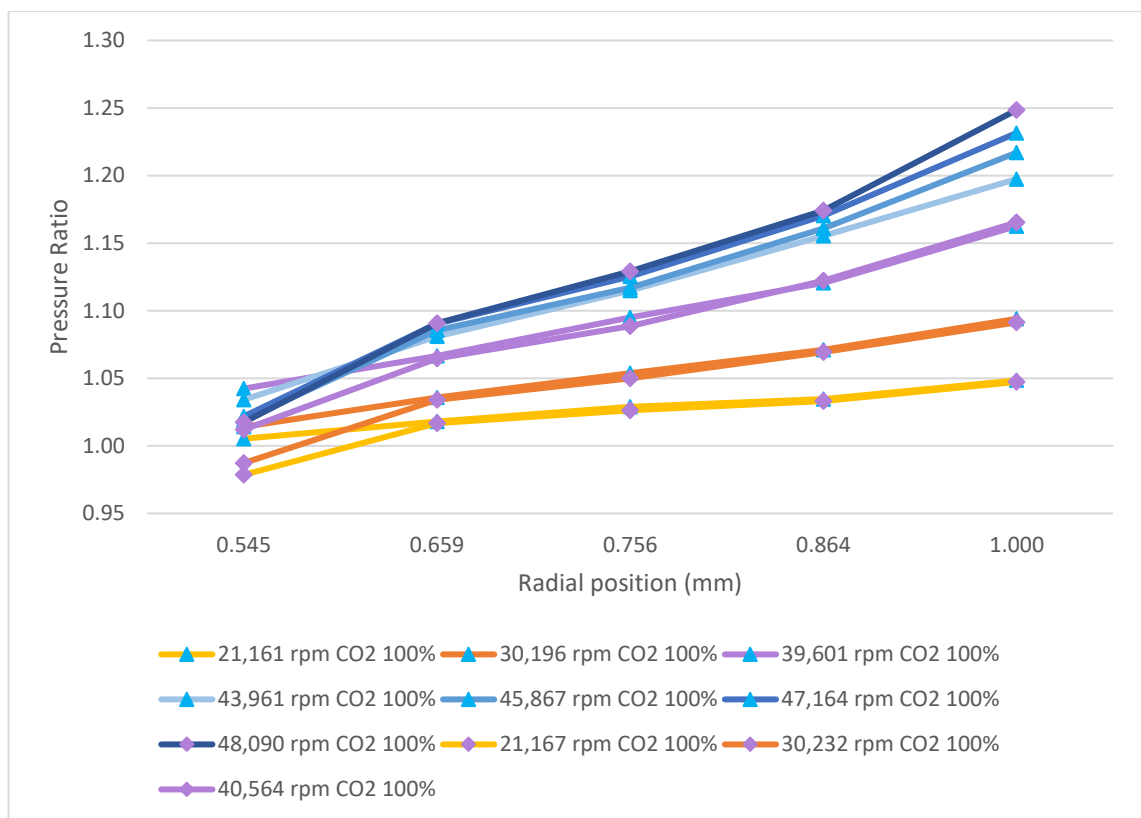


Figure 154: 85x100% front face tapings measurements take as the compressor was near surge, results showing pressure ratio of impeller

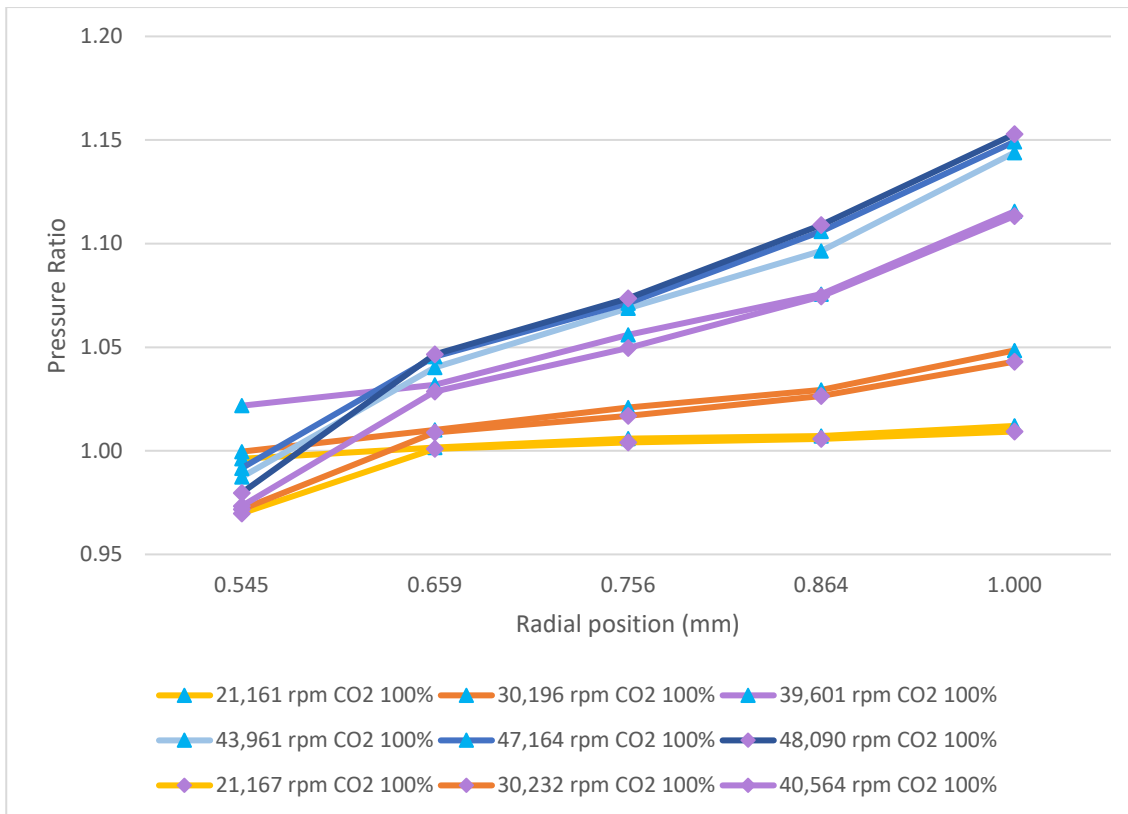


Figure 155: 85x100% front face tappings measurements take as the compressor was at choke, results showing pressure ratio of impeller

Figure 154 and Figure 155 show that the impeller is generating a significant amount of static pressure rise. When the pressure measured at the tapping is plotted as a percentage of the total compressor pressure rise just before surge, it can be seen in Figure 156 that between 33% and 37% of the compressor static pressure rise is generated in the impeller. Whereas at choke, as shown in Figure 157, the impeller is still producing static pressure rise, but the diffuser is so poorly matched, all the pressure rise is lost. This implies that to improve the range of the compressor, a diffuser that is more widely matched would be a benefit. This could be achieved by variable geometry diffuser vanes though there would be cost and complexity implications.

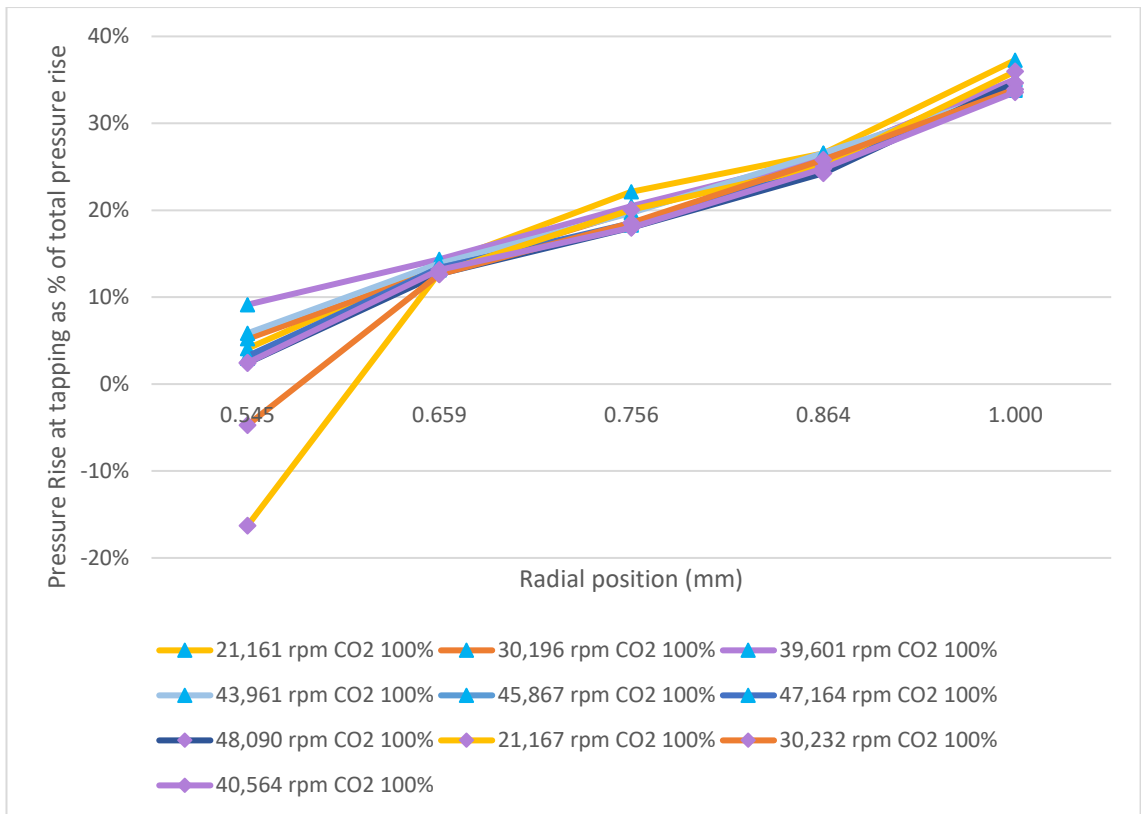


Figure 156: 85x100% front face tappings measurements take as the compressor was near surge, results as a percentage of the total pressure rise

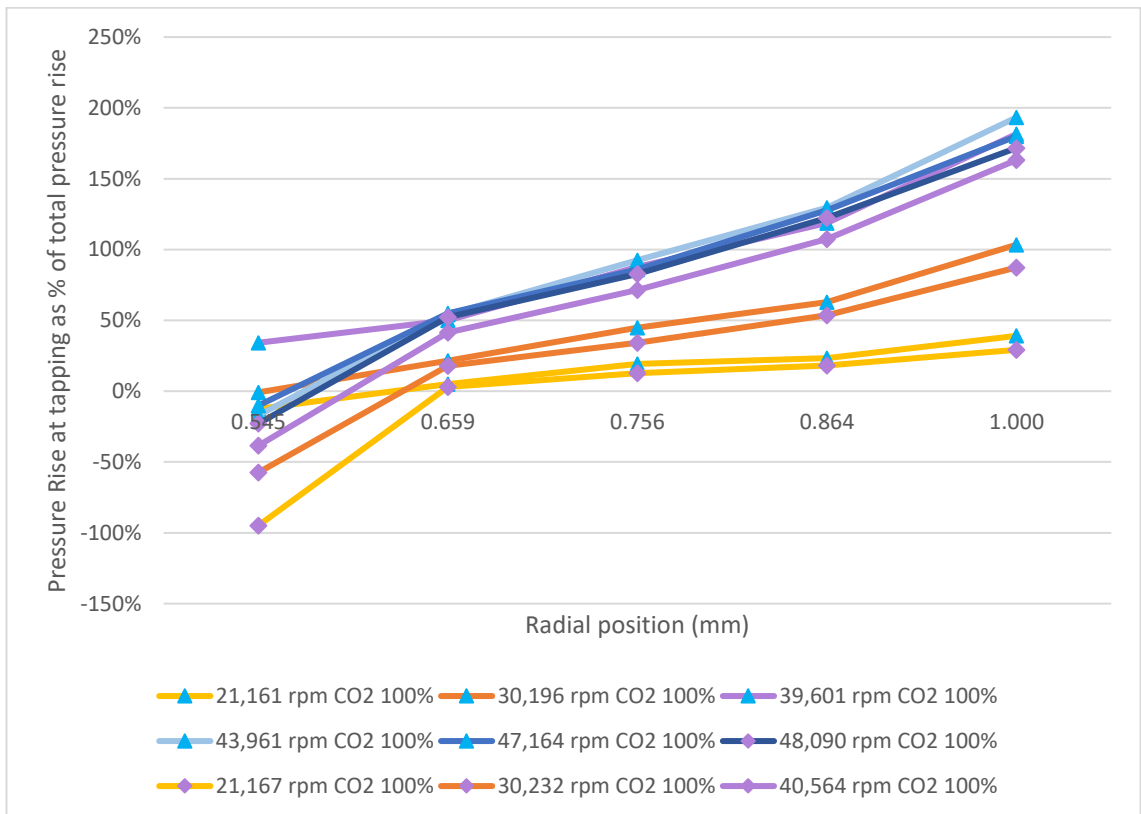


Figure 157: 85x100% front face tappings measurements take as the compressor was at choke, results as a percentage of the total pressure rise

Pressure measurements were also taken on the 85x250% compressor. Figure 158 shows that the 85x100% impeller generated more static pressure rise for a given corrected speed than the 85x250% impeller. This is even though the 85x250% compressor generates more pressure ratio than the 85x100%, see Figure 159.

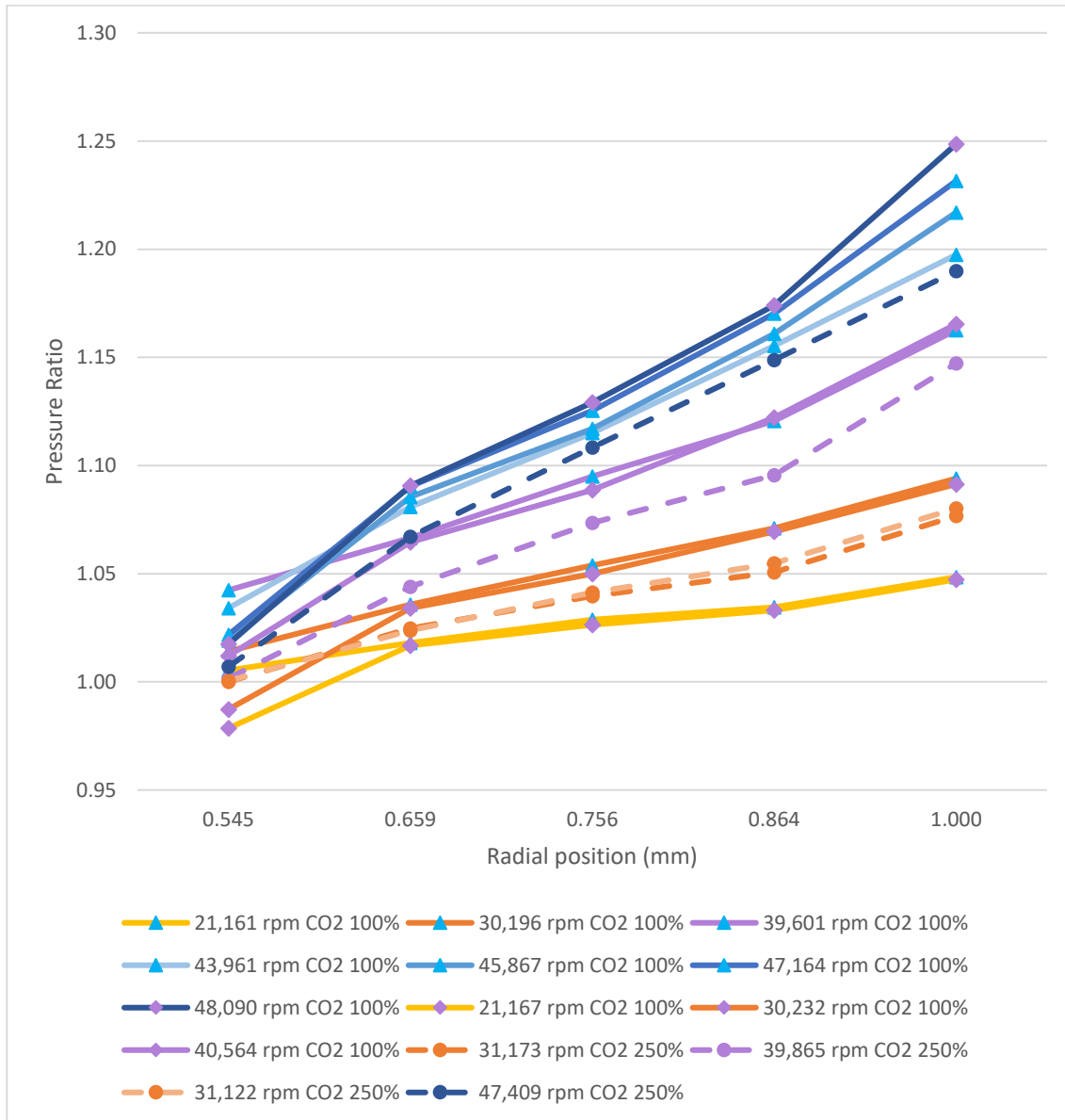


Figure 158: 85x100% and 85x250% front face tappings measurements take as the compressor was near surge, results showing pressure ratio of impeller only

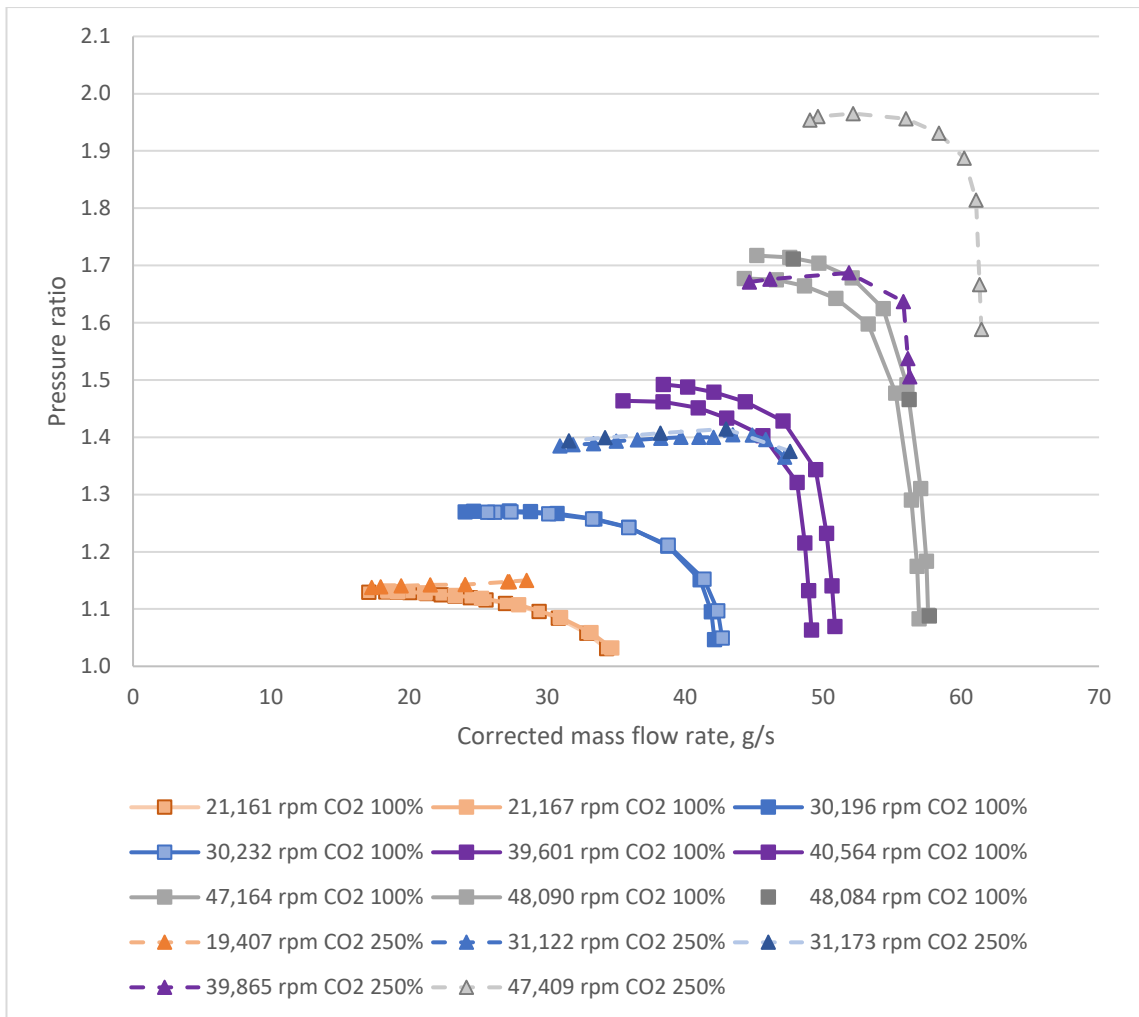


Figure 159: 85x100% and 85x250% pressure ratio results

More work is required to establish the relationship between impeller blade height and static pressure rise. Further, if the reason the 85x100% impeller generated more static pressure rise than the 85x250% impeller can be found, it could be a way to improve the pressure ratio of all compressor sizes.

This result also has implications on the efficiency calculations to follow. To calculate the compressor efficiency, it is necessary to remove all losses from the torque measurement that come from the bearings and windage. To do this, the test rig was spun without an impeller to get a windage torque measurement. These could then be removed from the compressor torque measurement isolating the torque required by the compressor. However, the above result shows that the bearing losses are likely to vary considerably with inlet pressure and operating point.

8.5. Efficiency Analysis

Using the torque meter data, efficiency of the compressor can be calculated using the analysis presented in section 7.3. Figure 160 shows the efficiency of the compressor taking the measured torque data and Figure 161 shows the same data with the windage and bearing losses removed. The bearing losses were calculated using the method described in the SKF super precision catalogue (SKF, 2013) for calculating the total friction moment of the bearings.

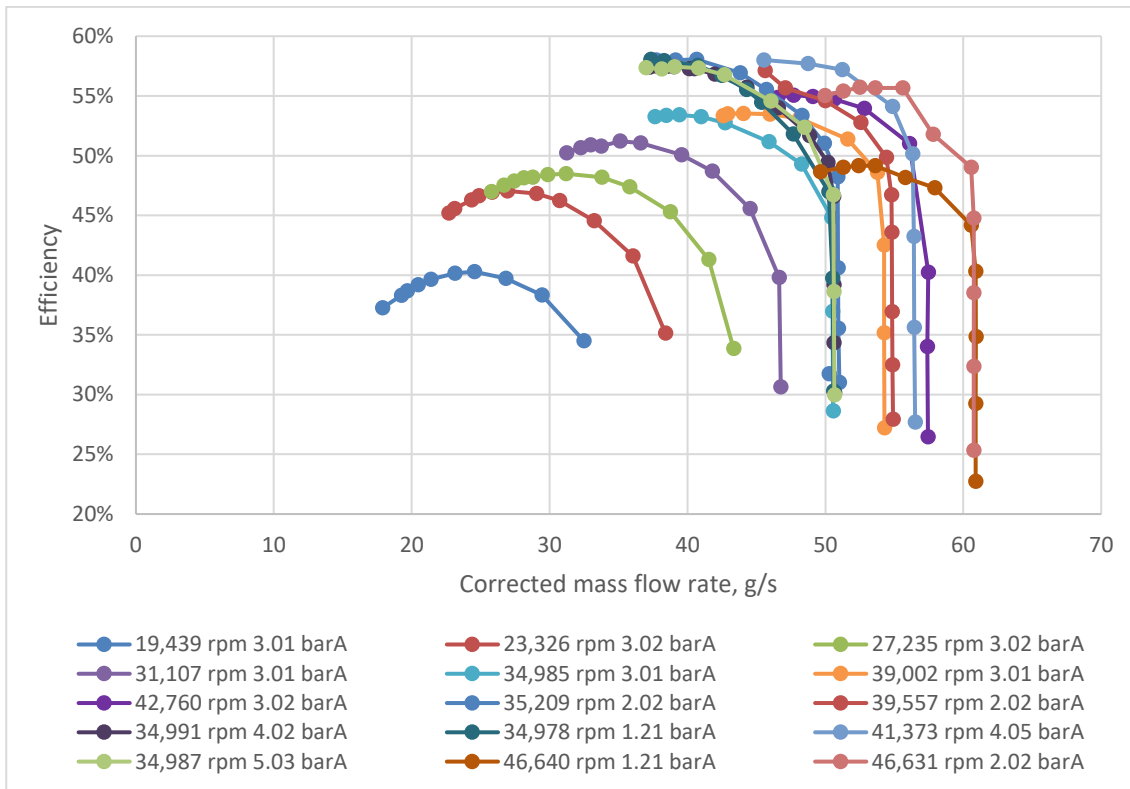


Figure 160: Efficiency vs mass flow rate for 85x200% in CO₂

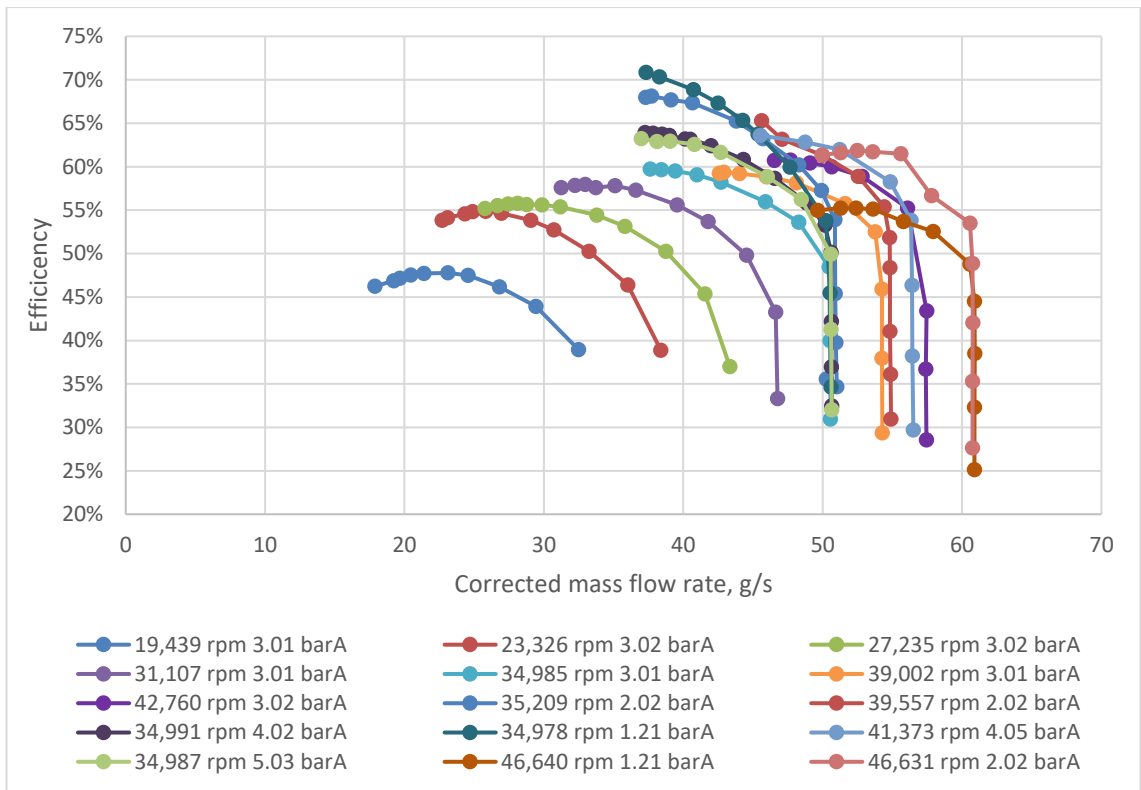


Figure 161: Efficiency vs mass flow rate for 85x200% in CO₂ with losses due to windage and bearings removed.

The majority of the difference in efficiency is due to the windage loss. The windage calculated from the correlation accounts for up to 20% of the measured torque at low speeds. As the speed and pressure increase, the power used by the compressor increases at a higher rate than the windage power, therefore it becomes a smaller percentage of the total power. This can be seen in both Table 26 and Figure 162.

Table 26: Windage torque at compressor peak pressure ratio

| Speed | Inlet pressure | % windage torque |
|--------|----------------|------------------|
| 35,539 | 1.22 | 17.9% |
| 47,663 | 1.22 | 11.0% |
| 36,235 | 2.02 | 14.4% |
| 40,836 | 2.02 | 11.9% |
| 47,873 | 2.02 | 10.0% |
| 19,661 | 3.02 | 17.2% |
| 23,631 | 3.02 | 14.7% |
| 27,658 | 3.03 | 13.1% |
| 31,707 | 3.00 | 11.5% |
| 35,685 | 3.01 | 10.3% |
| 40,145 | 3.01 | 9.14% |
| 41,128 | 3.02 | 9.18% |
| 44,193 | 3.01 | 9.38% |
| 36,524 | 4.02 | 9.93% |
| 42,101 | 4.05 | 8.36% |
| 42,798 | 4.03 | 7.77% |
| 35,827 | 5.04 | 8.47% |
| 35,828 | 5.41 | 8.26% |

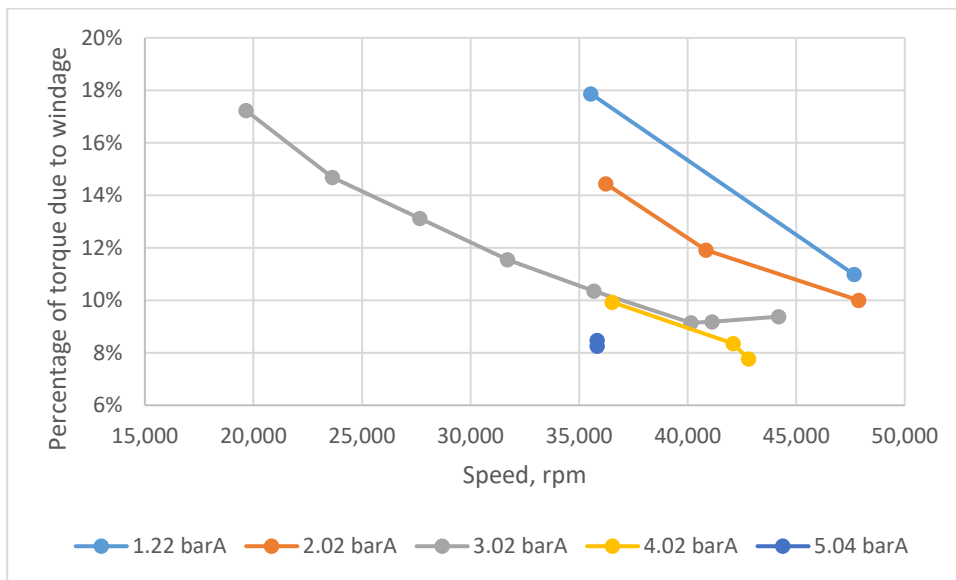


Figure 162: Windage variance with speed and pressure

The reason for the high windage is the coupling that connect the torque meter to the motor and the testing head. These have a high diameter and are not smooth, see Figure 163.



Figure 163: Magtrol torque coupler used to connect the motor via the torque meter to the compressor (Magtrol)

It is recommended that for future work, new couplings are found that have a smaller diameter and a smoother surface to reduce windage losses. This will improve the accuracy of the efficiency measurements.

Figure 164 shows the efficiency measurements for all compressor blade heights except 250%, inlet pressures and speeds measured during this work. Broadly this shows that as the blade height increases, so does the efficiency. Also, increasing the pressure and speed also increase the efficiency. This shows that the forward swept compressor behaves in the same way as conventional backward swept compressors.

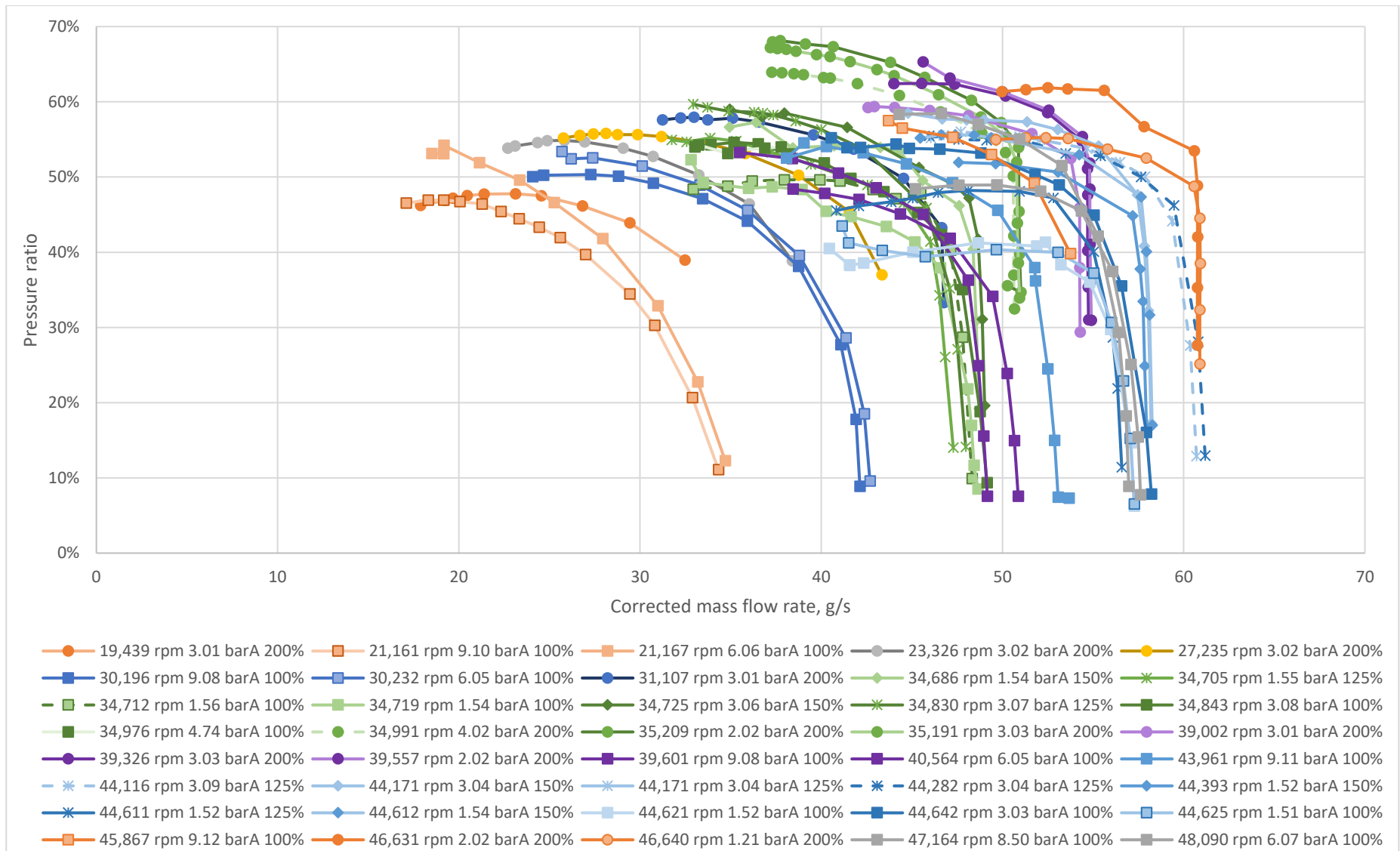


Figure 164: Efficiency vs corrected mass flow rate for all sizes (except 85x250%) and pressures in CO₂

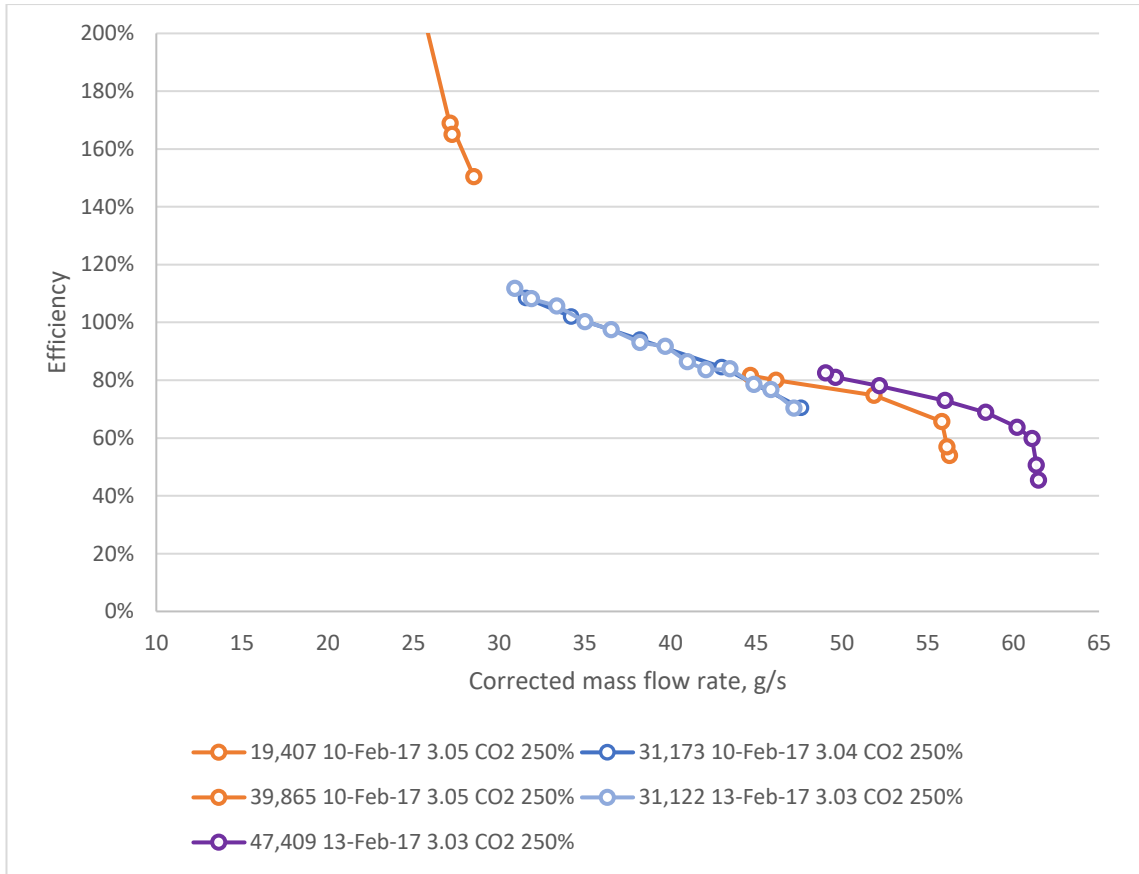


Figure 165: Efficiency data for 85x250% compressor

The data for the 85x250% compressor, Figure 165, shows efficiencies over 100%, upon taking these readings the torque meter was sent back to the manufacturer for calibration. It was discovered that the torque sensing element had become damaged during operation. It is not known when this damage occurred, therefore until all the efficiency data can be repeated with the now repaired torque meter, therefore the accuracy of this data can't be confirmed and will be discounted from all analyses.

Figure 166 shows only the data captured at a corrected speed of approximately 45,000 rpm. Even with the speed variation (44,116 to 47,409 rpm) it is clear the increase in blade height has significantly increased the efficiency – up to 10 percentage points increasing the blade height from 100% to 200% blade height. Also, increases in inlet pressure have also increased the efficiency – up to 15 percentage points for the 85x100% on a pressure increase from 1.5 to 3.0 bara. What is also noticeable is that the data is not always repeatable. The 2 speed lines at 44,600 rpm, inlet pressure of 1.5 bara for the 100% blade height are consistent, however, for the 150% blade height case, the

speed lines at 44,400 and 44,600 rpm with an inlet pressure of 1.5 bara are considerably different, with a difference of 6 percentage points at surge.

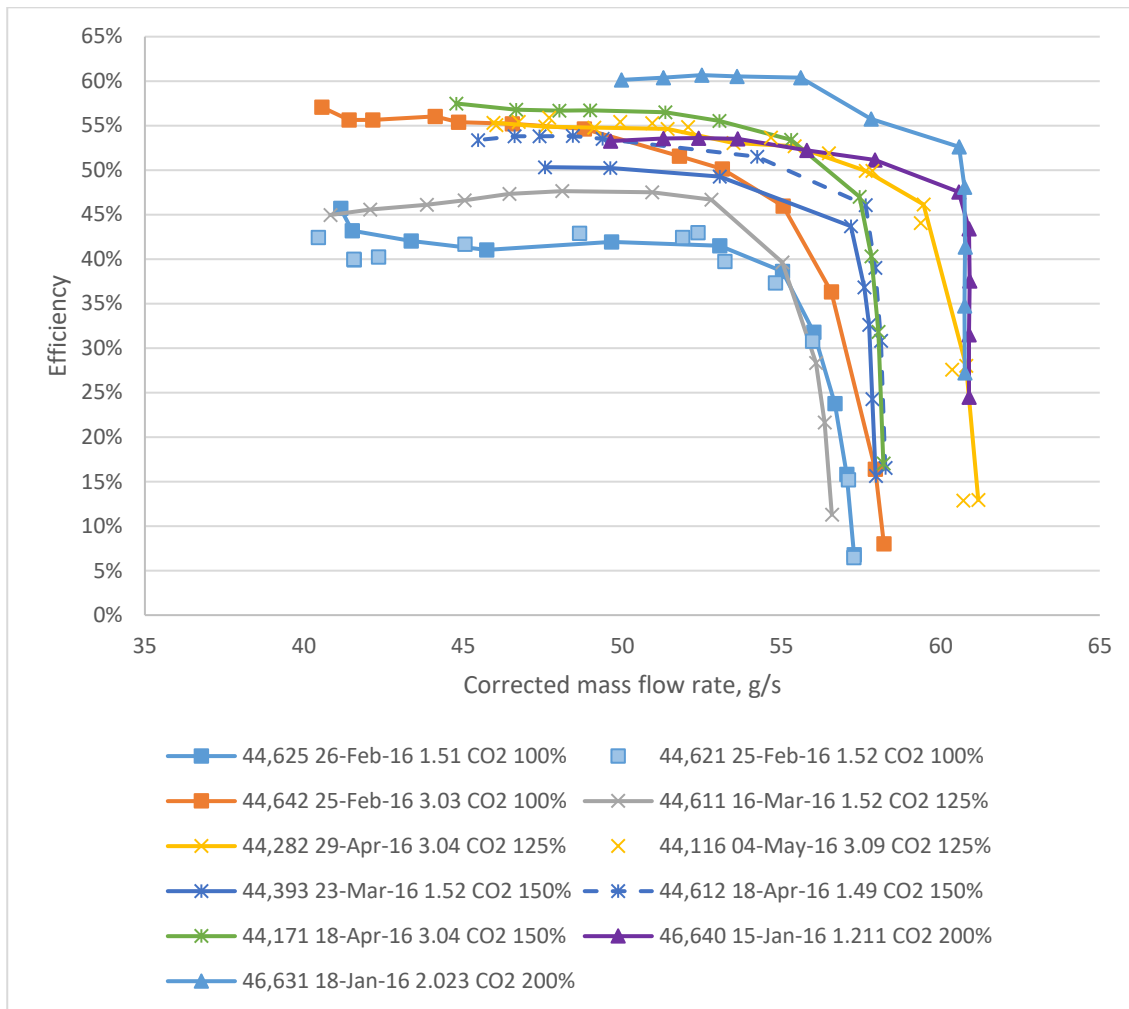


Figure 166: Efficiency results at 45,000 rpm in CO₂

Due to limited time on the test rig, it was not possible to repeat the testing, so no conclusions can be drawn as to the reason for this variation. In future, a redesign of the test rig lowering the windage losses associated with the couplings and including direct measurement of the bearing losses would improve the accuracy of the test results. Figure 168 shows it is unlikely to be an error stemming from inaccurate sensors.

8.6. Error Analysis

Using the sensor errors calculated in Chapter 6, and the methodology developed in Chapter 4 the following graphs show the error in the squarebox measurements. Due to the quantity of data collected, the graphs will only include data on the 85x200% compressor in CO₂ at 3 bara inlet pressure, however the trends hold true for all sizes.

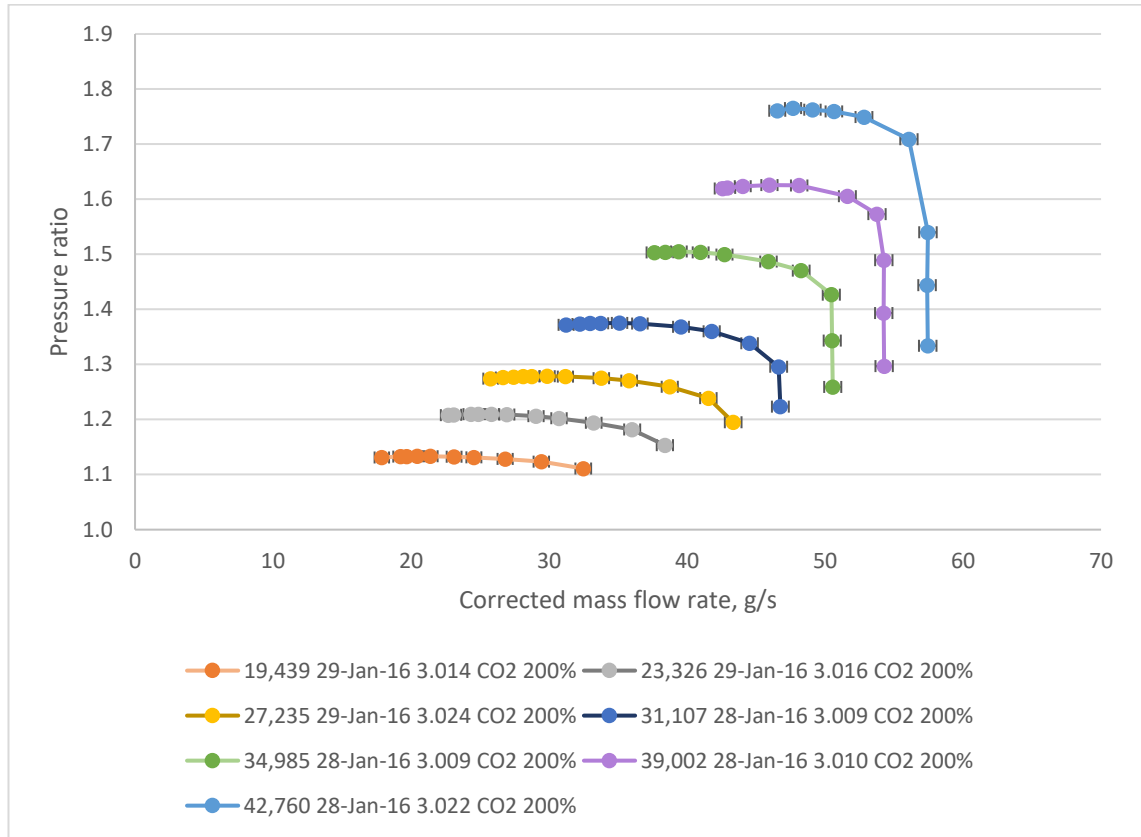


Figure 167: Error in PR and corrected mass flow rate for the pressurised test rig

It can be seen from Figure 167 and Figure 168 that the accuracy of these measurement has improved from the testing completed on the large rig, section 4.4. This was accomplished by directly measuring the sensors signal rather than converting to current or voltage and then measuring that signal, also the quality of the sensors was improved, for example changing from thermocouples to Class A RTD's.

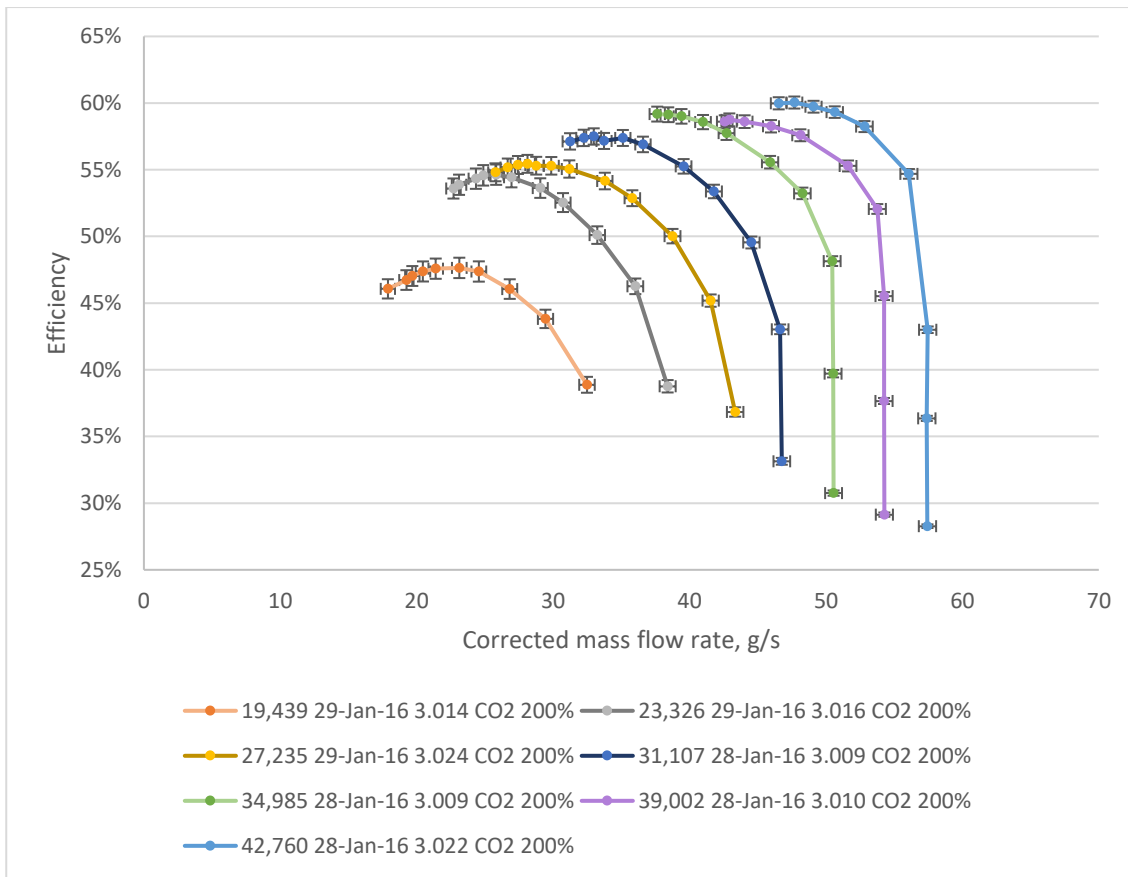


Figure 168: Error in efficiency and corrected mass flow rate for the pressurised test rig

This chapter has presented the results from the pressurised test rig. The methodology for normalising the test data to allow comparison of different inlet conditions and blade heights. A methodology is presented to allow prediction of the performance of the compressor to aid industry in commercialising the technology.

Results from pressure measurements around the impeller have been presented, this has shown that over 30% of the static pressure rise is generated by the impeller at surge disproving the hypothesis that there was no static pressure rise in the impeller.

Finally, the efficiency data has been presented, showing the issues encountered with the torque meter and the difficulty of using large couplings in a pressurised environment.

9. Conclusions

This work began with the aim of furthering the understanding of the highly forward swept compressor, TurboClaw, by directly observing the flow field within the diffuser and developing an empirical model of the compressor performance. In the process two test rigs have been built to understand different phenomena of the compressor.

A special purpose large scale rig was designed and used for both high-speed photography and LDV measurements. The high-speed photography showed the pulsating nature of the flow within the compressor diffuser, confirming hypothesis 1. It also showed the changing profile of the flow within the diffuser passage – from arrow head to perpendicular to the channel.

Laser Doppler Velocimetry, LDV, of the diffuser passage confirmed the pulsing nature of the flow, and also showed that the pulsing nature propagated all the way along the diffuser to the exit. It also revealed the large variation in velocity, both speed (from 22.5 m/s to 73.4 m/s) and direction (-27.7 degrees to 33.3 degrees relative to the tangential), in the vaneless space as the impeller rotated past.

The LDV confirmed what was observed in the high-speed photography, that the flow gravitated towards the outside of the diffuser as it bends. However, the LDV showed no sign of separation, discounting hypothesis 2, unlike the high-speed photography. The LDV measurements were only taken for a single operating point.

Both the LDV and high-speed photography showed a reduction in velocity along the length of the diffuser, consistent with the diffusers roll of converting kinetic energy into pressure.

A 1D analysis of the compressor gas angles did not tally with the LDV measurements. The most likely explanation was the assumption that the impeller generated no static pressure rise. Measurements from the second, smaller, test rig showed that at surge for the 85x100% impeller between 33% and 37% of the compressor pressure static pressure rise is generated within the impeller, disproving hypothesis 3. The measurements also show that the static pressure rise within the impeller is dependent on the blade height of the impeller. The 85x100% impeller generated a pressure ratio of 1.25 whereas the 85x250% impeller only managed 1.19 at 48,090 rpm and 47,409 rpm respectively. This

while the whole compressor pressure ratio was 1.72 and 1.96. More work is required to find how this relationship behaves across all blade heights. Understanding why the 85x100% impeller is generating a higher pressure ratio could lead to improvements on all size improving the maximum pressure ratio achievable.

On the second test rig data was collected for a number of blade height configurations from 85x100% up to 85x250%. A method of scaling the mass flow rate and the speed was developed to allow direct comparison of all the data on a single chart. This data along with historical data provided by DBS was used to create a map predictor tool. By optimising a generic equation to the data, the performance of any compressor can be predicted with only the diameter and blade height of the compressor, along with the inlet conditions specified. As more data is gathered in the future, the model can be updated improving the accuracy and the range of the prediction. As this is a model based upon optimisation of test data, it is only valid within the bounds of the data collected thus far.

Efficiency data was collected for the second test rig using an inline torque meter and the calculation methodology shown in section 7.3. A large percentage of the torque measured, up to 17.9%, was due to windage losses of the couplings, test head shaft and bearings but results were corrected. Also, measurements from across the front face show that there will be significant variation in bearing losses due to axial loading depending on the speed and operating point (surge, choke or somewhere in between). Due to the difficulty in accounting for these losses, there is low confidence in the efficiency results. However, the results show trends which are likely valid. There is an increase in efficiency with the blade height increase, up to 10 percentage points as the blade height increases from 100% to 200% showing earlier tests at DBS were not correct. Also, as the inlet pressure increases so does the efficiency, 15 percentage points on the 85x100% when the pressure increases from 1.5 bara to 3.0 bara. However, the efficiency data does not appear to be repeatable for the testing completed thus far.

10.Future work

A number of areas have been identified that work in the future should focus on. If the optical test rig could be redesigned such that the maximum speed could be increased in the Perspex configuration, and a source of seeding can be found that would allow higher mass flow rate operation. This would allow the flow to be imaged at higher operating speeds and at operating points close to surge and choke. If the source of the instability that leads to surge could be found, modifications could be made to the design that would extend the operating range of the compressor.

Imaging of the diffuser at the bend, exit and in the vaneless space was not satisfactory. These tests should be repeated using multiple light sources to enable the passage to be suitably lit eliminating shadows from the images.

As with the high-speed photography, future work should include repeating the LDV measurements at higher operating speeds and at surge and choke conditions. The testing would also benefit from simultaneous measurements in all 3 directions. This work has not considered out of flow out of plane due to lack of equipment, but should be a focus on any future testing.

Pressure tappings could be included in the wall of the diffuser to allow static pressure measurements which would allow direct measurement of the pressure profile along the passage. Combining this data with the LDV data would allow areas of low efficiency to be identified within the diffuser leading to an improved design.

All the optical investigations in this work have been focused on the stationary diffuser. However, the test rig has the functionality to allow optical measurement of the impeller. This would provide the other half of the jigsaw that is TurboClaw. The variation in the flow within the vaneless space is almost certainly affecting the flow within the impeller, especially around the trailing edge. Being able to visualise both sides of the flow would aid understanding and allow computational fluid dynamics a better chance of success.

For the pressurised test rig, future work must include a full repeat of all the data along with a redesign of the test rig to reduce the losses due to windage and better account for the bearing losses. Once the efficiency data is validated, a model similar to the one developed for pressure ratio can be developed for efficiency.

11. Appendix: Additional LDV images

11.1. Diffuser Bend Individual Images

Figure 169 shows the diffuser bend flow field, the colour of the arrows has been scaled to enhance the speed variation.

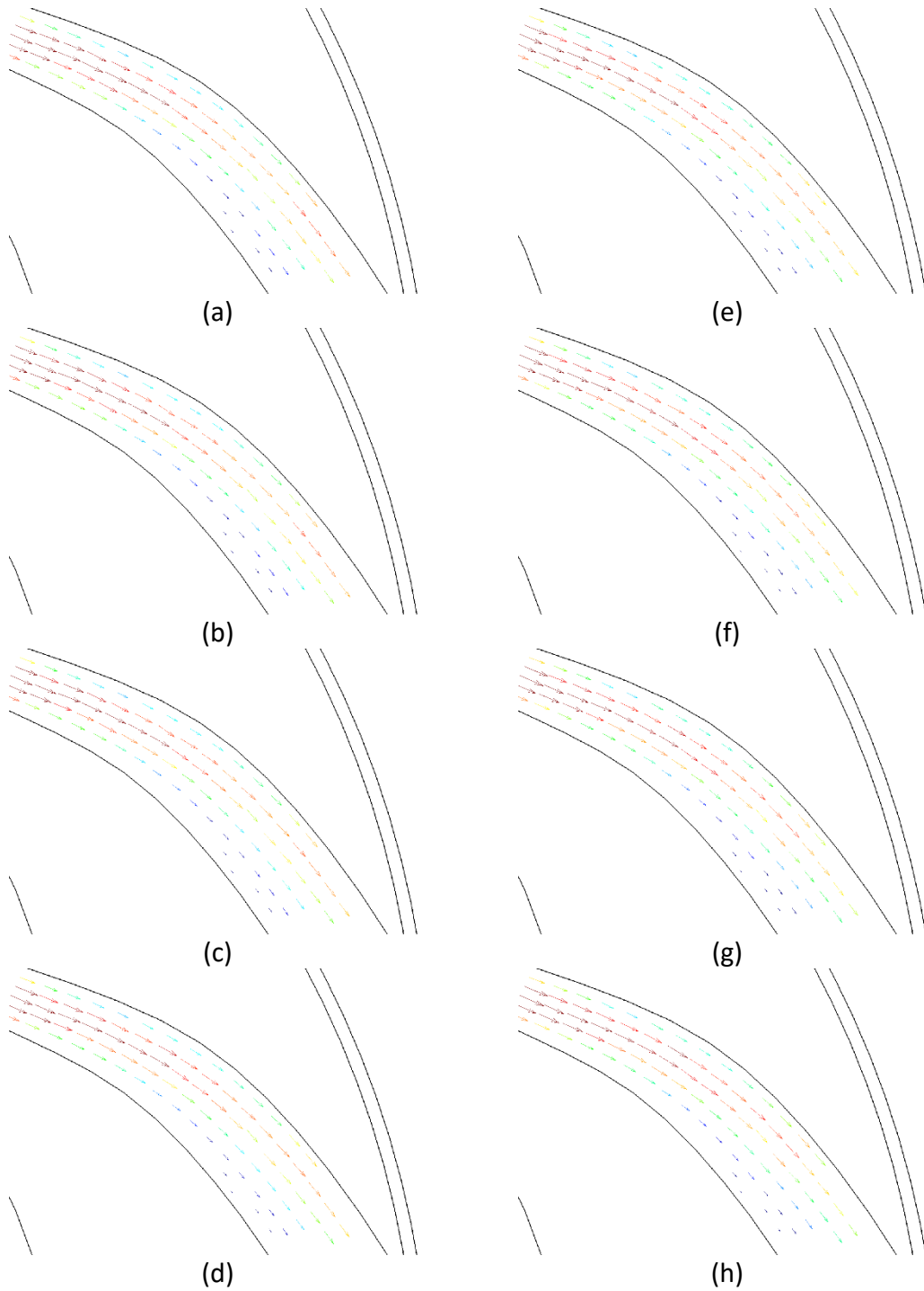


Figure 169 (a-d): Mean velocities at diffuser throat, 1 degree increment impeller rotation

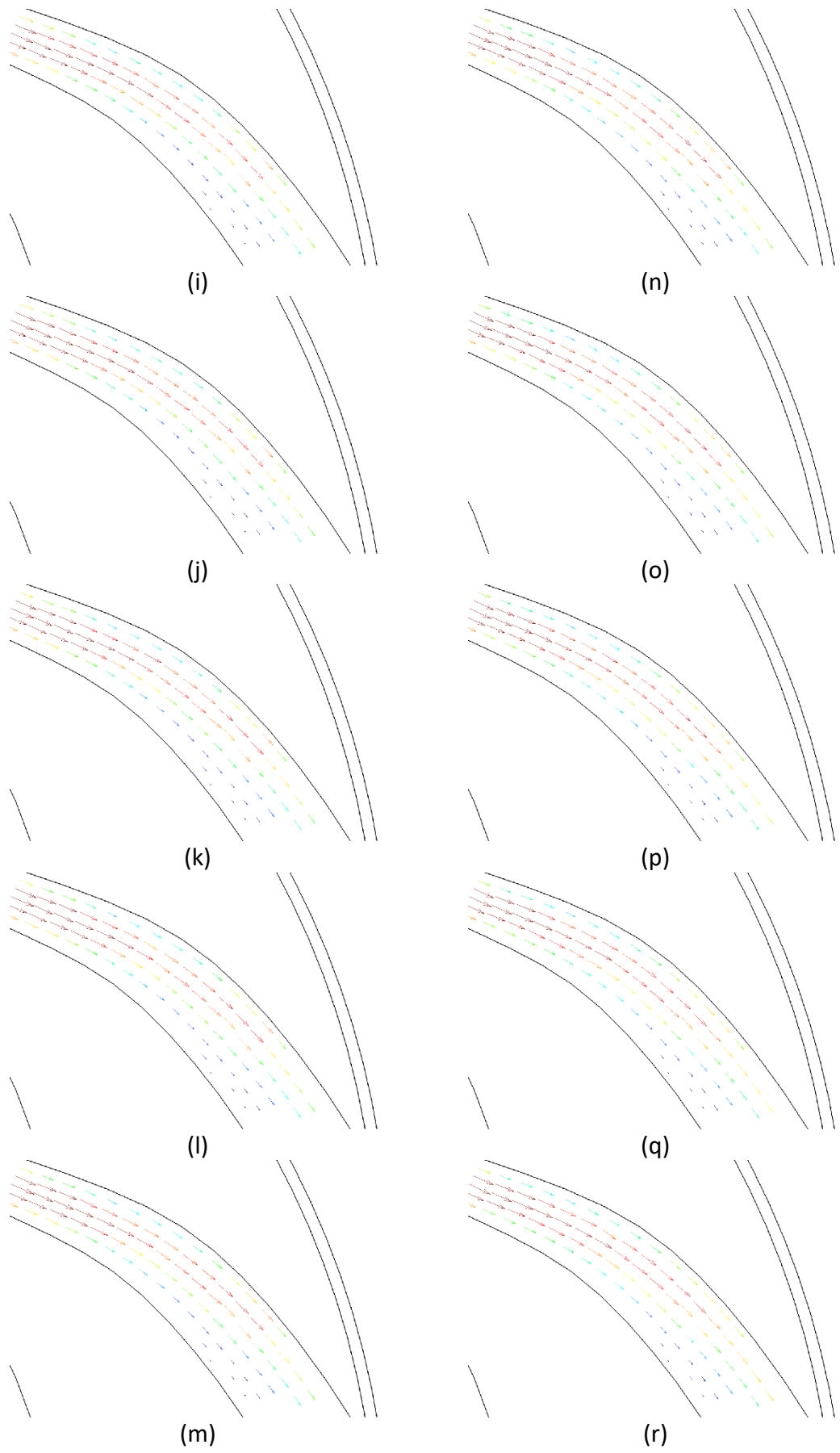


Figure 169 cont.

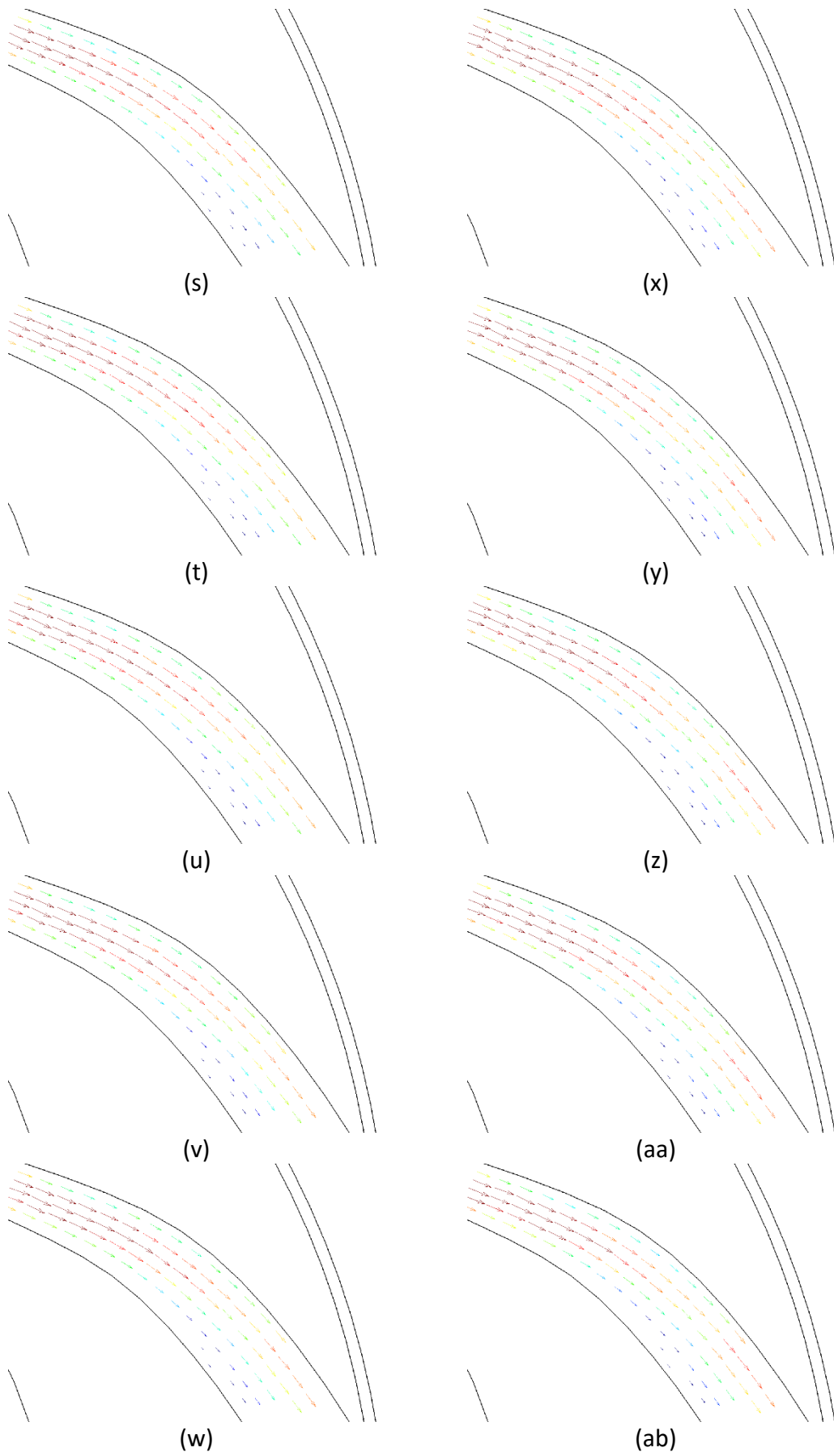


Figure 169 cont.

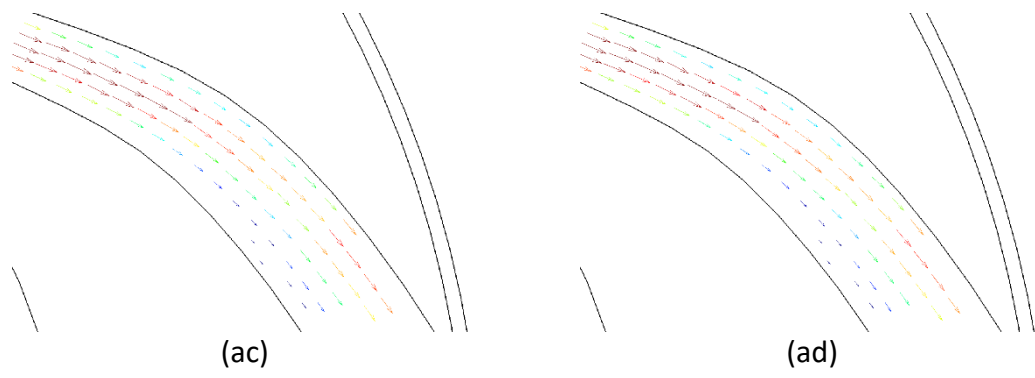


Figure 169 cont.

11.2. Diffuser Bend Individual Images

Figure 170 shows the diffuser exit flow field.

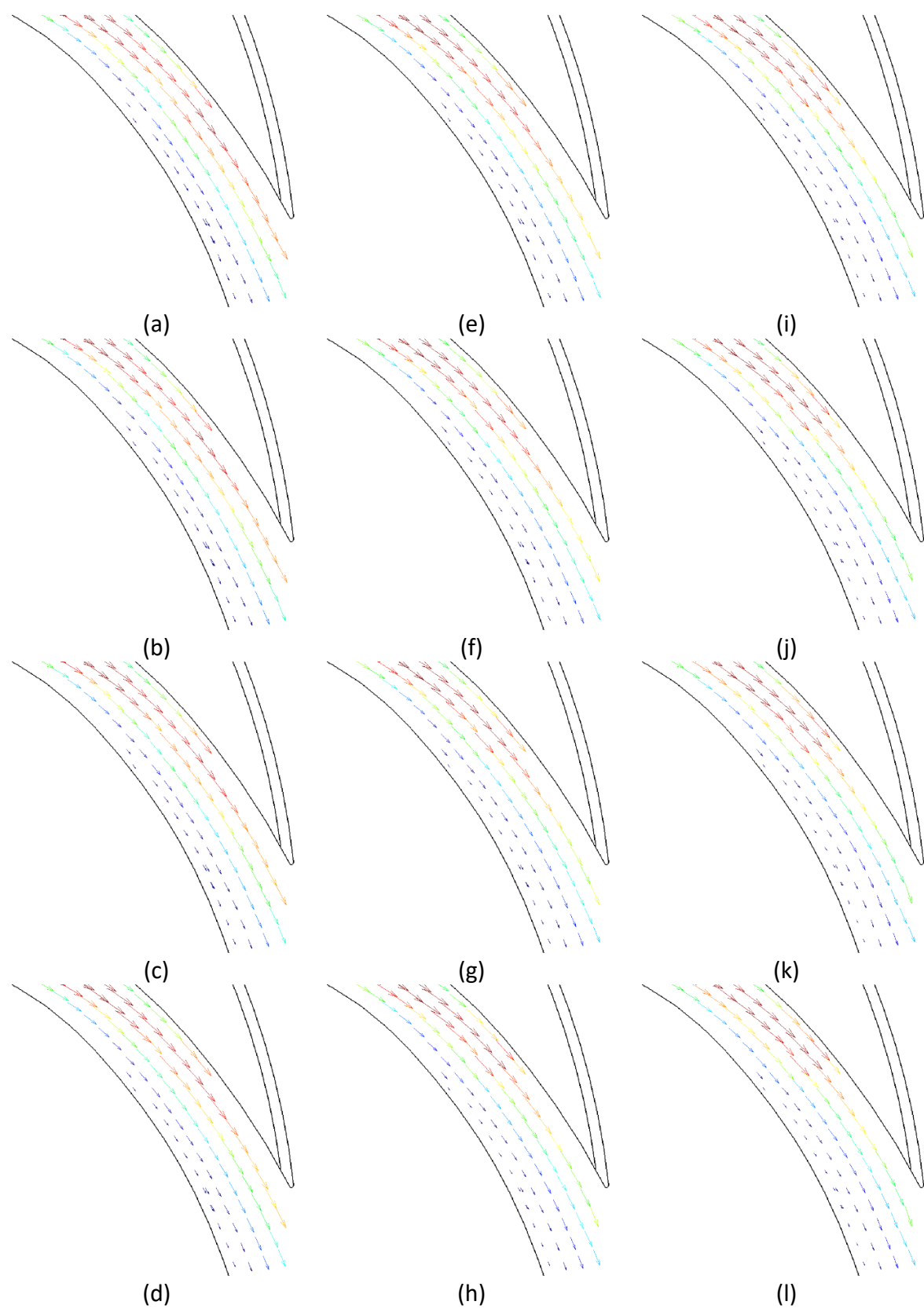


Figure 170 (a-ad): Mean velocities at diffuser throat, 1 degree increment impeller rotation

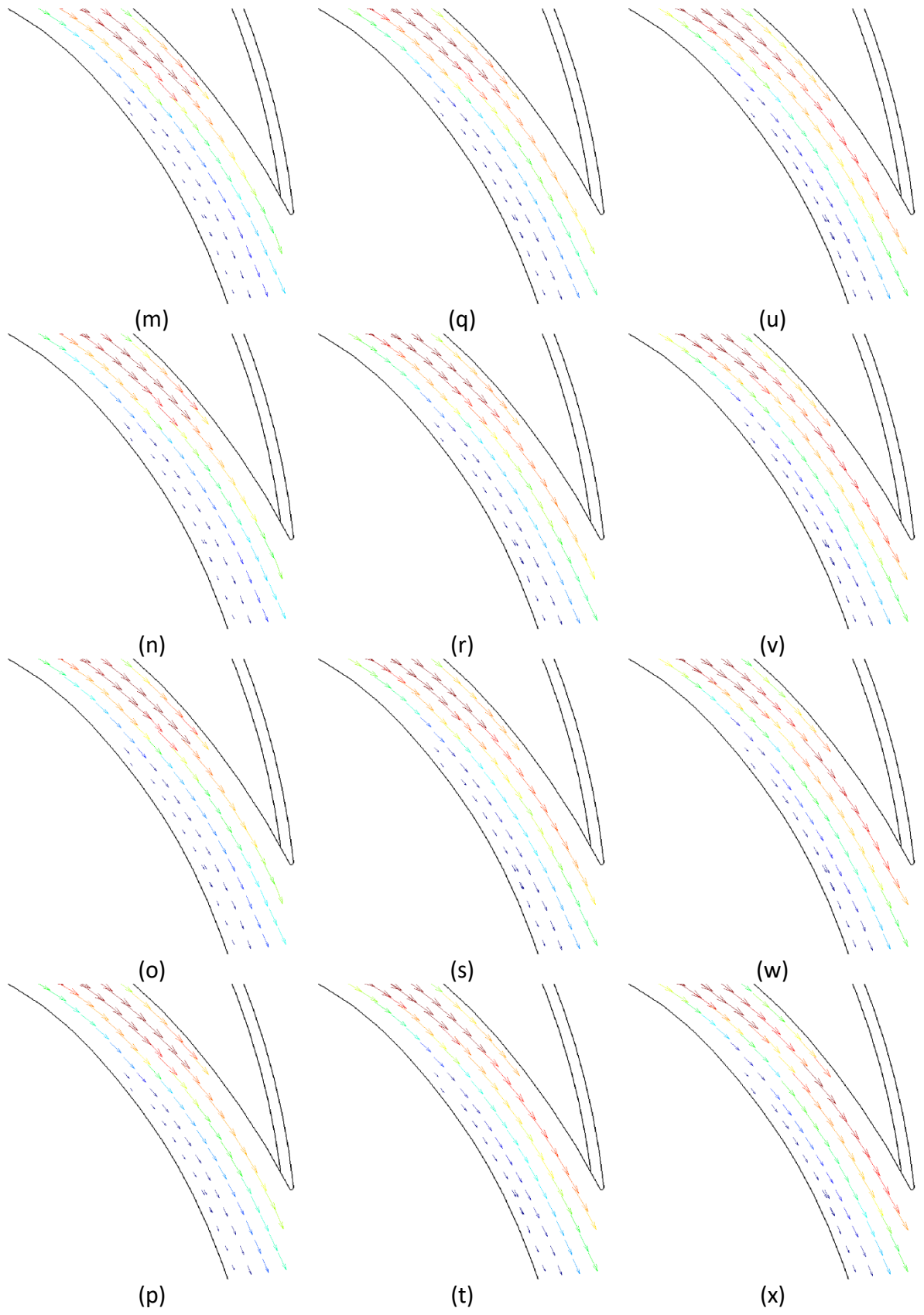


Figure 170 cont.

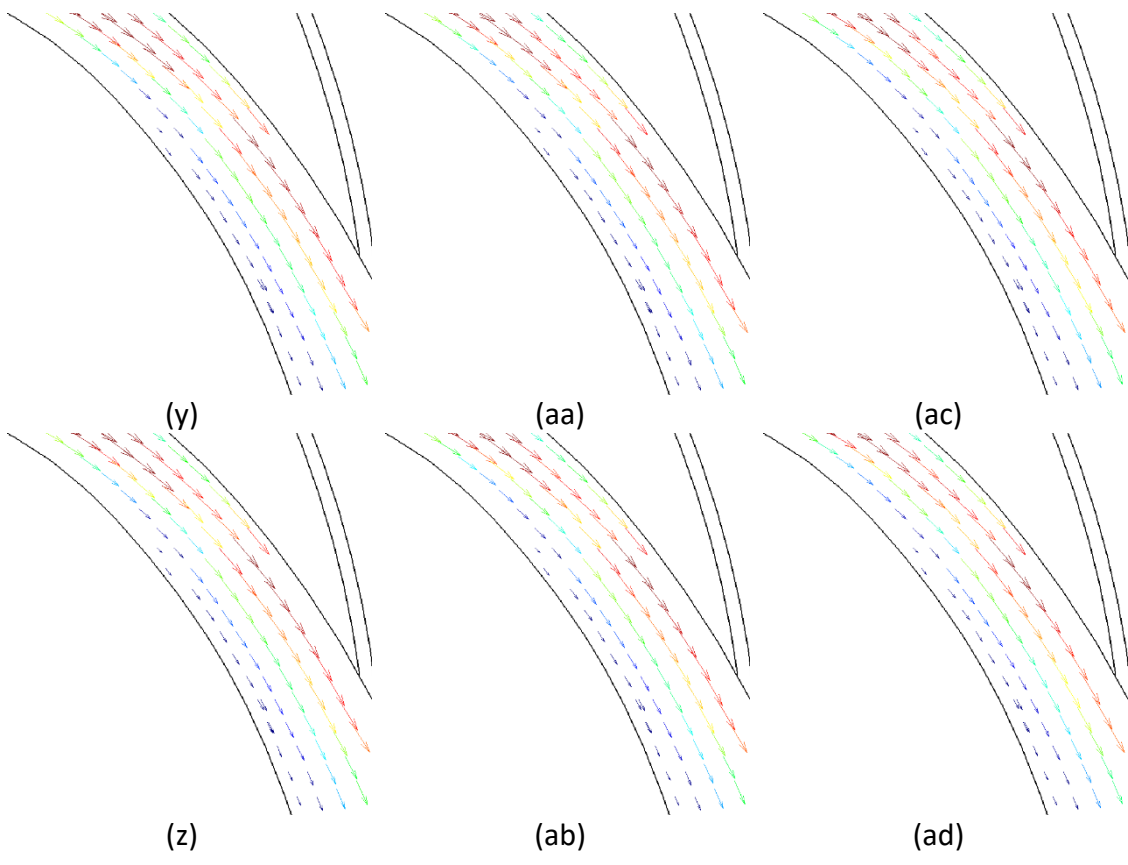


Figure 170 cont.

12.Appendix: Matlab programmes

12.1. Create Mean Image

```
function pathOut = fun_get_mean_image_rc(meanPath,
meanFirst, meanNOF, meanEXT, type)

%%%%-----
%%%%
% meanPath -> file path + image name minus file number and
extension in ''
% meanFirst -> integer number of meanFirst file to be read
i.e. if meanFirst file is ...0005 meanFirst = 5
% meanNOF -> number of files used to calculate the mean
% meanEXT -> image file extension e.g. .tif, .jpg, .png
% type -> 0=mean, 1=standard deviation, 2=both
%%%%-----
%%%%

imgNo = meanFirst + (meanNOF-1);
nTotal=0;

%%%%--opening data images-----
%%%%
for i=meanFirst:imgNo

    path1 = char([meanPath,num2str(i, '%06d'),meanEXT]);
    data=double(imread(path1));

    if (i==meanFirst)
        meanImg=zeros(size(data));
        stdImg=zeros(size(data));
    end

    meanImg=meanImg + data;
    stdImg=stdImg+data.^2;
    nTotal=nTotal+1;

end

%%%%-----
%%%%

%%%%--process the mean image-----
%%%%
if type == 1 || type == 3
    meanImg=meanImg/nTotal;

path2=char([double(meanPath), 'mean', num2str(meanFirst), '-
', num2str(imgNo), meanEXT]);
```



```

    data = uint8(meanImg);
    imwrite(data, path2);

%     figure(1)
%     imshow(data)
end
%%%-
%%%-

%%%--process standard deviation-----
%%%-
if type == 2 || type == 3
    stdImg0=stdImg/nTotal;
    stdImg0=stdImg0-meanImg.^2;
    stdImg=stdImg0.^0.5;

path3=char([double(meanPath), 'std', num2str(meanFirst), '-
', num2str(imgNo), meanEXT]);

    data = uint8(stdImg);
    imwrite(data, path3);

%     figure(2)
%     imshow(data)
end
%%%-
%%%-

pathOut = path2;
disp('Image processing done!')

```

12.2. Background Image Removal

```

function [pathOut, fileOut] = fun_bkgrnd_removal(meanPath,
imPath, imFile, first, nof, step, ext)

%%%-
%%%-
% meanPath -> full file path and file name in ''
% imPath -> image file path in ''
% imFile -> first image name minus file number and
extension in ''
% first -> integer number of first file to be read i.e. if
first file is 000005 first = 5
% nof -> number of files to process
% step -> integer increment in file number i.e. if every
other file to be used then step = 2
% ext -> image file extension e.g. .tif, .jpg, .png in ''

```

```

%%%%-----
%%%%

imgNo = first + (nof-1)*step;
nTotal=0;
meanData=imread(meanPath);

% make folder for contour images
newPath = char([imPath,'foreground\']);
fileExist = exist(newPath, 'dir');
if fileExist == 0
    mkdir(newPath);
end

%%%%--opening data images-----
%%%%
for i=first:step:imgNo

    path1 = char([imPath, imFile,num2str(i, '%06d'),ext]);
    imageData=imread(path1);

    finalIm=imageData - meanData;

    path2 = char([newPath,imFile,'_smoke_',num2str(i,
'%06d'),ext]);
    imwrite(finalIm, path2);
    nTotal=nTotal+1;

end
%%%%-----
%%%%

pathOut = newPath;
fileOut = char([imFile,'_smoke_',num2str(first,
'%06d'),ext]);

```

12.3. Image Intensity Adjustment

```

function fun_im_int_adjust_rc(imPath, imFile, first, nof,
step, ext, noAreas, sizeArea)

%%%%-----
%%%%
% fun_im_intensity_rc(imPath, noAreas, sizeArea)
%
% imPath -> 'file path'
% imFile -> 'file name of image to sample, usually the mean
background image'
% ext -> file extension of image file
% noAreas -> number of areas to sample

```

```

% sizeArea -> size in pixels of square to be sampled
%
% intArray -> output array [xPos yPos averageInt]
"intArray = "
%%%%-----
%%%%
imgNo = first + (nof-1)*step;
nTotal=0;

for i = first:step:imgNo

    path1 = char([imPath,'\',imFile,num2str(i,
'%06d'),ext]);
    data = imread(path1);
    imSize = (size(data));

    if i == 1;
        %%%%--increase intensity of image for selections---
-----%%%%%%%%

        maxInt = max(max(data));
        meanInt = mean(mean(data));
        disp('maxInt = '), disp(maxInt)
        disp('meanInt = '), disp(meanInt)
        mult = input('Enter multiplication value -> ');

        for m = 1:imSize(1)
            for j = 1:imSize(2)
                dataInt(m,j) = data(m,j)*mult; % increase
intensity to max in image
                if dataInt(m,j) > 255
                    dataInt(m,j) = 255;
                end
            end
        end
    end

    %%%%-----
-----%%%%%%%%

    figure(1)
    imshow(dataInt)
%    intensity=zeros(noAreas,16);
    intens=zeros(noAreas:1);

    %%%%--select intensity region-----
-----%%%%%%%%

    for a = 1:noAreas

        impixelinfo
        if a == 1

```

```

        disp(' Set a the top left corner of the
square region')
    end
    impixelinfo
    [x1, y1]=ginput(1);

    %%%--check box fully inside image-----%%
    if x1>=imSize(2)
        x1 = imSize(2)-sizeArea;
    end

    if y1>=imSize(1)
        y1 = imSize(1)-sizeArea;
    end

    if x1<=0
        x1 = 1;
    end

    if y1<=0
        y1 = 1;
    end

    %%%-----%%

    x2 = x1 + (sizeArea-1);
    y2 = y1 + (sizeArea-1);

    z = int16([x1, y1; x2, y2]);
    %    disp(z)

    %%%-----
-----%%

    %%%--plots squares on image-----%%
    x11 = x1 - 1;
    x21 = x2 + 1;
    y11 = y1 - 1;
    y21 = y2 + 1;

    if x1 == 1
        x11 = 1;
    end

    if y1 ==1
        y11 = 1;
    end

    for m = x11:x21
        dataInt(int16(y11),int16(m)) = 255;
    end

```

```

        dataInt(int16(y21),int16(m)) = 255;
    end

    for j = y11:y21
        dataInt(int16(j),int16(x11)) = 255;
        dataInt(int16(j),int16(x21)) = 255;
    end

    figure(1)
    imshow(dataInt)

    xPos(a) = x1;
    yPos(a) = y1;

    path2 =
char([imPath,'\',imFile,'_int_areas',ext]);
    imwrite(dataInt,path2);

    end
end

%     xPos = [290, 500];
%     yPos = [130, 160];
%     noAreas = 2;
%     sizeArea = 4;

    %%%--Get intensity for each pixel in square-----
    %%%%
    for b = 1:noAreas
        x1 = xPos(b);
        x2 = x1 + (sizeArea-1);
        y1 = yPos(b);
        y2 = y1 + (sizeArea-1);

        k = 1;
    %     intensity = zeros(sizeArea*sizeArea,1);
        for m = x1:x2
            for j = y1:y2
                intensity(k) = data(int16(j),int16(m));
                k = k + 1;
            end
        end

        %%%--Calculate average intensity in square-----
    ---%%%%
        intens(b,i) = mean(intensity);

    path5 = char([imPath,'\','_intens.xlsx']);
    xlswrite(path5, intens, 'Sheet1');
end

```

```

end
disp('end loop 1')
imNo = first;
for i = 2:step:imgNo
    intensVector = intens(:,i) - intens(:,1);
    meanIm(i) = round(mean(intensVector));
end
disp('end loop 2')
for i = first:step:imgNo
    path1 = char([imPath, '\', imFile, num2str(i,
'%06d'), ext]);
    data = imread(path1);

    newData = data + meanIm(i);
    path6 = char([imPath, '\', imFile, '_int_', num2str(i,
'%06d'), ext]);
    imwrite(newData, path6);

    imNo = imNo + 1;
end
disp('end loop 3')
xlswrite(path5, meanIm, 'Sheet2');
% intVect = [noAreas, sizeArea, nof];
% path3 = char([imPath, '\', '_intArray.xlsx']);
% xlswrite(path3, intVect, 'Sheet1', 'A1');
% headings = char(['x', 'y', 'I']);
% intArray = [rot90(xPos), rot90(yPos), intens];
% xlswrite(path3, headings, 'Sheet1', 'A2');
% xlswrite(path3, intArray, 'Sheet1', 'A3');

```

12.4. Colour an Image Black or White Depending on Threshold Value

```

function fun_im_threshold(imPath, imFile, first, nof, step,
ext)

imgNo = first + (nof-1)*step;
nTotal=0;

% v = 0:25:255;
% cropPos = [84, 178, 1035, 328];
oldPath = char([imPath, 'foreground\']);

% make folder for images
newPath = char([imPath, 'thold\']);
fileExist = exist(newPath, 'dir');
if fileExist == 0
    mkdir(newPath);
end

fileInt = char([imPath, 'thresholdValues.txt']);

```

```

fileIntExist = exist(fileInt, 'file');
if fileIntExist == 0
%     imMax = 0;
    error('myApp:argChk', 'No input file')
else
    fid = fopen(fileInt, 'r');
    C = textscan(fid, '%d %d');
    imLow = C{1};
%     imHigh = C{2};
end

%%%--opening data images-----
%%%
for i=first:step:imgNo

    path1 = char([oldPath,imFile,num2str(i, '%06d'),ext]);
    data=imread(path1);
    imSize = size(data);
    x = imSize(1);
    y = imSize(2);
    for j = 1:x;
        for k = 1:y;
            if data(j,k)>=imLow;
                data(j,k) = 255;
            else
                data(j,k) = 0;
            end
        end
    end

    imshow(data)
    path2 = char([newPath,imFile,num2str(i, '%06d'),ext]);
    imwrite(data, path2);

    path3 = char([newPath,imFile,'mean-',num2str(first),'-
',num2str(nof),'-',num2str(imLow), ext]);

    if i == first;
        data2 = data;
        imwrite(data2, path3);
    else
        data2 = imread(path3);
        for j = 1:x;
            for k = 1:y;
                if data(j,k) > data2(j,k);
                    data2(j,k) = data(j,k);
                end
            end
        end

        imwrite(data2, path3)
    end
end

```

```

        end
        fclose all;

end
close(figure(1));
fclose all;

```

12.5. Crop Image to Size

```

function fun_im_crop_pos_rc(imPath, imFile, first, nof,
step, xmin, ymin, width, height)

```

```

%%%%-----
%%%%
% Function crops specified area from an image
% basepath -> 'file path + first image name - 0001.tif'
% first -> integer number of first file to be read i.e. if
first file is
% ...0005 first = 5
% nof -> number of files used to calculate the mean
% step -> integer increment in file number i.e. if every
other file to be
% used then step = 2
% ext -> image file extension e.g. .tif, .jpg, .png
%%%%-----
%%%%

imgNo = first + (nof-1)*step;

cropPos = [xmin, ymin, width, height];

%%%%--opening data images-----
%%%%
for i=first:step:imgNo

    path1 = char([imPath,imFile,num2str(i,
'%03d'),' .tif']); % deg
    data=imread(path1);

    useableData = data(:, :, :);

    %%%--crop images-----
    %%%%
    imCrop = imcrop(useableData, cropPos);
    % disp(imshow(imCrop))
    %%%-----
    %%%%

    path2 = char([imPath,imFile,'crop_',num2str(i,
'%02d'),' deg.tif']);
    imwrite(imCrop, path2);

```



```

end
%%%-----
%%%

```

12.6. Average LDV Results by Impeller Position

```

function averageAngleBragg_2018(address, flowsizerFile,
noFiles, segmentSize, individual)%, numBlades)

%-----
% address -> address of flowsizerfile and \
% flowsizerFile -> location of results file. don't include
extension or file number
% noFiles -> number of files to be processed
% segmentSize -> angle for each mean value i.e. 3 (3deg), 5
(5deg)...
% individual -> output individual averaged files y/n
% numBlades -> number of blades in rotor
%-----

arraySizeNew = 30/segmentSize;

stdevFile = char([address, flowsizerFile, '_stdev_',
num2str(segmentSize,'%2.2f'),' .csv']);
meanVelocityFile = char([address,flowsizerFile,
'_velocity_', num2str(segmentSize,'%2.2f'), ' .csv']);
countFile = char([address,flowsizerFile, '_count_',
num2str(segmentSize,'%2.2f'), ' .csv']);
velstdevFile = char([address,flowsizerFile, '_vel_stdev_',
num2str(segmentSize,'%2.2f'), ' .csv']);
gateFile = char([address,flowsizerFile, '_gate_time_',
num2str(segmentSize,'%2.2f'), ' .csv']);

fid4 = fopen(stdevFile, 'w');
fid5 = fopen(meanVelocityFile, 'w');
fid6 = fopen(countFile, 'w');
fid7 = fopen(velstdevFile, 'w');
fid8 = fopen(gateFile, 'w');

stdevFlowArray = zeros(noFiles, arraySizeNew);
meanVelocityArray = zeros(noFiles, arraySizeNew);
countArray = zeros(noFiles, arraySizeNew);
velstdevArray = zeros(noFiles, arraySizeNew);
gateArray = zeros(noFiles, arraySizeNew);

for y=1:noFiles; %file number

    % initialise arrays

```

```

count = zeros(arraySizeNew);

dataHolder = zeros(arraySizeNew, 1000);
for i=1:arraySizeNew
    dataHolder(i,4) = 1000;
end

averageArray = zeros(arraySizeNew, 7); % angle, average
velocity, max vel, min vel, velocity stdev, no samples,
gate time
for i=1:arraySizeNew
    averageArray(i,1) = i*segmentSize;
    averageArray(i,4) = 1000;
end

% read in data from Flowsizer .csv file
fileData = char([address, flowsizerFile, ' ',
num2str(y, '%02d'), '.csv'])
dataRaw = csvread(fileData,2,0);
arraySizeOld = size(dataRaw);

invalidCount = zeros(noFiles);

for j=1:arraySizeNew % segment to average over

    % define bounds of segments
    angleMax = averageArray(j,1);
    if j==1
        angleMin = 0;
    else
        angleMin = averageArray((j-1),1);
    end

    % sort data
    for i=1:arraySizeOld(1) % sorting through all data
        % RMR within segment and within tolerance
        if (rem(dataRaw(i,4),30)>angleMin &&
rem(dataRaw(i,4),30)<=angleMax && dataRaw(i,5)==0);
            averageArray(j,2) =
averageArray(j,2)+dataRaw(i,3); % velocity
            averageArray(j,7) =
averageArray(j,7)+dataRaw(i,7); % gate time
            count(j) = count(j)+1;
            dataHolder(j,count(j)) = dataRaw(i,2);
        %
        % elseif dataRaw(i,5)==1
        %
        %             % sum RMR out of tolerance
        %             invalidCount(y) = invalidCount(y) + 1;
        end
    end
end

```

```

        averageArray(j,2) = averageArray(j,2)/count(j); %
average velocity
        averageArray(j,7) = averageArray(j,7)/count(j); %
average gate time

        counter = 0;
        for k=1:1000 % remove empty cells from array
            counter = counter + 1;
            if dataHolder(j,k)==0.0000000
                break
            end
            dataHolderNoZeros(k) = dataHolder(j,k);
%           dataHolderNoZerosVelocity(k) =
(lambda*(dataHolder(j,k)-
(gratingSpeed(y)*convFact))*1e6)/(2*sinTheta_2);
            end

        averageArray(j,3) = max(dataHolderNoZeros); % max
velocity
        averageArray(j,4) = min(dataHolderNoZeros); % min
velocity
        averageArray(j,5) = std(dataHolderNoZeros); %
standard deviation velocity
        averageArray(j,6) = count(j); % no of valid samples

    end

    invalidCount(y) = sum(dataRaw(:,5));
    disp(char(['file number ', num2str(y, '%02d'), ':
number of invalid data points ', num2str(invalidCount(y),
'%12d')]));

    if individual == 'y';
        fileAverage = char([address, flowsizerFile,
num2str(y,'%3.0f'), '_averaged_',
num2str(segmentSize,'%2.2f'), '.csv']);

        fid2 = fopen(fileAverage, 'w');
        headings = ['angle' ',' 'average vel' ',' 'max vel'
',' 'min vel' ',' 'velocity stdev' ',' 'no. samples' ','
'gate time'];
        fprintf(fid2, '%s\n', headings);
        for z=1:arraySizeNew
            fprintf(fid2, '%0.2f, %0.3f, %0.3f, %0.3f,
%0.3f, %0.0f, %0.3f\n', averageArray(z,:));
        end
    end

end

%   meanFreqArray(y,:) = averageArray(:,2);
stdevFlowArray(y,:) = averageArray(:,5);
countArray(y,:) = averageArray(:,6);

```

```

meanVelocityArray(y,:) = averageArray(:,2);
velstdevArray(y,:) = averageArray(:,5);
gateArray(y,:) = averageArray(:,7);

%     csvwrite(meanFreqFile, meanFreqArray);
csvwrite(stdevFile, stdevFlowArray);
csvwrite(countFile, countArray);
csvwrite(meanVelocityFile, meanVelocityArray);
csvwrite(velstdevFile, velstdevArray);
csvwrite(gateFile, gateArray);

end

fclose('all');

```

12.7. Plot Vector Image from LDV Results

```

function aviobj = LDVvector_2018(address, horizontalFile,
verticalFile, bkgrndImFile)

horizFile = char([address, horizontalFile, '.csv']); %
opening details of test
horizData = csvread(horizFile,0,0);

vertFile = char([address, verticalFile, '.csv']); % opening
details of test
vertData = csvread(vertFile,0,0);

scaledFile = char([address, 'scaledXY.csv']); % opening
details of test

segmentSize = 1; % number of degrees to average over
arraySizeNew = 30/segmentSize;

horizDataSize = size(horizData);
absData = repmat(40, [horizDataSize(1) (horizDataSize(2)-
1)]);

for x = 1:horizDataSize(1);
    for y = 3:(horizDataSize(2)-1);
        absData(x, (y-2)) =
sqrt((horizData(x,y)^2)+(vertData(x,y)^2));
    end
end

maxVel = max(max(absData(:,3:end)))
minVel = min(min(absData(:,3:end)))
disp('-----')

```

```

colourScale = csvread('C:\PhD test programme\Rig\Test
results\LDV\matlab processing\colourScale.csv');
absDatasize = size(absData);
colourData = zeros(absDatasize(1), absDatasize(2), 3);
for x = 1:horizDataSize(1);
    for y = 3:(horizDataSize(2)-1);
        index = round(((absData(x, (y-2))*4.349)-51.10)*3);
% final multiple effects colour scale %2.5 for bend, 3 for
exit
        if index<1;
            index = 1;
        end
        if index>256;
            index = 256;
        end
        colourData(x, (y), :) = colourScale(:, index);
    end
end

% disp(colourData(3, 3, :))

c = fix(clock);
c1 = c(1:3);
c2 = c(4:6);
d = c(1:3);
t = c(4:6);
d = num2str(d);
t = num2str(t);
d = regexprep(d, '\s+', '-');
t = regexprep(t, '\s+', '-');
d_t = strcat(d, '_', t);

%aviFile = char([address, d_t, '_vector.avi']);
%aviobj = VideoWriter(aviFile, 'Uncompressed AVI');
%aviobj.FrameRate = 10;
%open(aviobj);

positionScaled(:, 1) =
(((horizData(:, 1)*1.0069)+54.2)*3.4107)+256.1)*2.68291-
1663.65; %2.68291-1663.65 exit %3.50275-2124.9 bend
%2.5272-500.8 throat
positionScaled(:, 2) = (407.6-
((horizData(:, 2)*0.9696)+93.8)*3.3965))*2.68933-484.18;
%2.68933-484.18 exit %3.4382-382.83 bend %2.6881-22.498
throat;

csvwrite(scaledFile, positionScaled(:, 1:2));

for i=3:arraySizeNew+2
    disp(i-2)

```

```

x = positionScaled(:,1);
y = positionScaled(:,2);
ux = horizData(:,i);
vy = -vertData(:,i);
%   sz = sqrt(ux.^2 + vy.^2); % normalised arrows
%   u = (ux./sz)*13;
%   v = (vy./sz)*13;
    u = (ux./0.5); % scaled arrows 1.0 bend, 4 whole, 1.5
throat 0.5 exit
    v = (vy./0.5);

figure(1);
    path1 = char([bkgrndImFile, num2str(mod((i-3),30),
'%02d'),' deg.tif']);
    path1 = char([bkgrndImFile, '.tif']); % select
depending whether to increment background image
    pathlexist = exist(path1, 'file');
    if pathlexist ~= 2
        disp('file doesnt exist')
        disp(path1)
    else
        data = imread(path1);
        dataShow = data(:,:,1);
        imshow(dataShow);
        set(gcf, 'position', [1 1 978 707])
        %set(gcf, 'position', [1 1 1850 1070]);
        set(gca, 'position', [0 0 1 1], 'units', 'normalized')
        hold on
        for j = 1:horizDataSize(1)
            quiver(x(j),y(j),u(j),v(j), 'color',
colourData(j,i,1:3), 'AutoScale', 'off', 'MaxHeadSize',
1.5);
        end

        %F = getframe(figure(1));
        %writeVideo(aviobj,F);

        path2 = char(['C:\PhD test programme\Rig\Test
results\LDV\30 degree averaging\imageFiles - Diff exit - 30
degree\frame_', num2str((i-3), '%03d'), '.tif']);
        saveas(figure(1), path2);

        clf
        clear('x', 'y', 'u', 'v', 'path1', 'data',
'dataShow', 'path2')

    end

end

close(figure(1));

```

```
%close(aviobj);  
  
disp('Done!')  
disp('-----')
```

13. Bibliography

Abramian M. and Howard J. H. G. Experimental Investigation of the Steady and Unsteady Relative Flow in a Model Centrifugal Impeller Passage [Journal] // Journal of Turbomachinery. - [s.l.] : ASME, 1994. - Vol. 116. - pp. 269-279.

Anderson Jr John D Fundamentals of Aerodynamics [Book]. - [s.l.] : McGraw-Hill Higher Education, 2001. - 3rd.

Arcoumanis C [et al.] Performance and Exit Flow Characteristics of Mixed-Flow Turbines [Journal]. - [s.l.] : International Journal of Rotating Machinery, 1997. - 4 : Vol. 3.

Arjeneh M, Pullen K.R and Etemad S Experimental Study of Radial Low Specific Speed Turbocompressor Running in Reverse as Turboexpander [Conference] // Institute of Mechanical Engineers - 8th International Conference on Compressors and Their Systems. - London, United Kingdom : Woodhead Publishing Limited, 2013.

Australia IPS ipsaus.com [Online]. - 2014. - <http://ipsaus.com.au/rotating-equipment/new-equipment-sales/ge-oil-and-gas/roots-single-stage-oib-api-617-centrifugal-compressor/>.

Barske U. M. and Ing Development of Some Unconventional Centrifugal Pumps [Journal]. - [s.l.] : Proc Instn Mech Engrs, 1960. - 11 : Vol. 174.

Bell R.M and Fottner L Investigations of shock/boundary-layer interaction in a highly loaded compressor cascade [Conference] // Proceedings of the International Gas Turbine and Aeroengine Congress and Exposition. - [s.l.] : ASME, 1995.

Budynas R.G and Nisbett J.K Shigley's Mechanical Engineering Design [Book]. - [s.l.] : McGrawHill, 2006. - ISBN: 0-390-76487-6.

Cascade Machinery & Electric Inc cascade-machinery.com [Online]. - 2014. - <http://www.cascade-machinery.com/38251/441307/Reciprocating-Compressors/CA-Series-Air-Compressor-Pump.html>.

Casey M.V., Dalbert P and Schurter E Radial Compressor Stages for Low Flow Coefficients [Journal]. - [s.l.] : IMechE, 1990. - C403/004.

Choi Young-Do, Kurokawa Junichi and Matsui Jun Performance and Internal Flow Characteristics of a Very Low Specific Speed Centrifugal Pump [Journal] // Journal of Fluid Engineering. - [s.l.] : ASME, 2006. - Vol. 128. - pp. 341-349.

Cukurel B, Lawless P.B and Fleeter S Particle image velocity investigation of a high speed centrifugal compressor diffuser: Spanwise and loading variations [Journal]. - [s.l.] : Journal of Turbomachinery, 2010. - Vol. 132.

Cukurel B, Lawless P.B and Fleeter S PIV investigation of a high-speed centrifugal compressor diffuser: Mid-span loading effects [Conference] // 44th AIAA/ASME/SAE/ASEE Joint Propulsion Conference and Exhibit. - [s.l.] : American Institute of Aeronautics and Astronautics Inc., 2008.

Cumpsty N.A Compressor Aerodynamics [Book]. - Malabar, Florida : Kreiger Publishing Company, 2004. - ISBN 1-57524-247-8.

DBS TSB Project 720298 - Modular multi-stage compressor for energy recovery [Report]. - 2014.

Drain L. E The Laser Doppler Technique [Book]. - [s.l.] : Wiley, 1980.

ESDU ESDU 07004: Flow in Rotating Components [Report]. - [s.l.] : IHS, 2007.

GARRETT MOTION INC. GARRETT® G25-550 [Online]. - 2019. - <https://www.garrettmotion.com/racing-and-performance/performance-catalog/turbo/g-series-g25-550/>.

Griffini D. [et al.] On the Development of an Efficient Regenerative Compressor [Journal] // Energy Procedia. - [s.l.] : Elsevier, 2015. - Vol. 82. - pp. 252-257.

Heckaman B.A Design of optical access for the application of laser doppler velocimetry in a low specific speed centrifugal compressor [Book]. - 2014.

Ibaraki S., Higashimori, H., Mikogami, T. Flow investigation of a centrifugal compressor for automotive turbochargers [Conference] // 1998 SAE International Congress and Exposition. - [s.l.] : SAE International, 1998.

Ibaraki S., Sumida, K., Suita, T. Design and off-design flow fields of a transonic centrifugal compressor impeller [Conference] // Proceedings of the ASME Turbo Expo

2009: Power for Land, Sea and Air. - [s.l.] : American Society of Mechanical Engineers (ASME), 2009. - Vol. 7.

INC SDI Summit Dynamics Regenerative Blowers [Online] // SDI Summit Dynamics INC. - 2018. - 2018. - http://www.sdiohio.com/Pages/blowers_and_air_knives.htm.

Insinna M. [et al.] One-Dimensional Prediction and Three-Dimensional CFD Simulation of the Fluid Dynamics of Regenerative Pumps [Conference] // Proceedings of ASME Turbo Expo 2018. - 2018.

Jensen K.D. Flow Measurements [Conference] // ENCIT2004 –10th Brazilian Congress of Thermal Sciences and Engineering. - Rio de Janeiro : J. of the Braz. Soc. of Mech. Sci. & Eng, 2004. - Vol. XXVI No. 4.

Kobayashi Hiromi 9-506 Tsukubahouse, Nishida Hideo and Miura Haruo Multistage centrifugal compressor [Patent] : EP 0359514 A2 : Application. - 21 Mar 1990.

Kundu A.K, Price M.A and Riordan D Theory and Practice of Aircraft Performance [Book]. - [s.l.] : John Wiley & Sons, 2016.

Lemmon E.W [et al.] Thermodynamic Properties of Air and Mixtures of Nitrogen, Argon and Oxygen from 60 to 2000 K at Pressures to 2000 MPa [Journal]. - [s.l.] : J. Phys. Chem. Ref. Data, 2000. - 3 : Vol. 29.

Magtrol Couplings for TM series Torque Transducers [Online]. - 2018. - http://www.magtrol.com/torque/tm_couplings.html.

Magtrol Torque transducers [Online] // Magtrol. - 2018. - 2018. - http://www.magtrol.com/torque/torquemeter_transducers.html.

Magtrol Torque transducers [Online] // Magtrol. - 2019. - <https://www.magtrol.com/product/torque-transducers/>.

Martin P.B, Pugliese G.J and Leishman J.G Laser Doppler Velocimetry Uncertainty Analysis for Rotor Blade Tip Vortex Measurements [Conference]. - [s.l.] : American Institute of Aeronautics and Astronautics, 2000.

Matweb Aluminium 7075-T6; 70775-T651 [Report]. - [s.l.] : www.matweb.com, 2018.

Melling A Tracer particles and seeding for particle image velocimetry [Journal]. - [s.l.] : Measurement Science and Technology, 1997. - 1406-1416 : Vol. 8.

Nejadrajabali J., Riasi A. and Nourbakhsh S.A. Flow Pattern Analysis and Performance Improvement of Regenerative Flow Pump Using Blade Geometry Modification [Journal] // International Journal of Rotating Machinery. - [s.l.] : Hindawi Publishing Corporation, 2016. - Vol. 2016.

NI CompactDAQ [Online] // National Instruments. - 2018. - 2018. - <http://www.ni.com/data-acquisition/compactdaq/>.

NI The CompactRIO Platform [Online] // National Instruments. - 2018. - 2018. - <http://www.ni.com/compactrio/>.

Nuclear Power for Everybody Pump Theory – Eulers Turbomachine Equations [Online] // Nuclear Power. - 2019. - <https://www.nuclear-power.net/nuclear-engineering/fluid-dynamics/centrifugal-pumps/eulers-turbomachine-equations/>.

Pampreen R. C. Small Turbomachinery Compressor and Fan Aerodynamics [Journal]. - [s.l.] : Journal of Engineering Power, 1973. - pp. 251-256.

Parra J [et al.] Performance Measurements of a Low Specific Speed TurboClaw Compressor [Conference] // 9th International Conference on Compressors and Their Systems. - London, United Kingdom : Institute of Physics Publishing, 2015. - Vol. 1.

Parra J.C The Effect of Reynolds Number on the Efficiency of a Forward Swept Low Specific Speed Turbocompressor [Report]. - [s.l.] : City University London, 2013.

Pullen K [et al.] The TurboClaw compressor for engine downsizing by twin-charging [Conference]. - [s.l.] : 7th International Conference on Compressors and their Systems, 2011.

Pullen K.R [et al.] Electrically Driven Supercharger using the TurboClaw Compressor for Engine Downsizing [Conference] // Institute of Mechanical Engineers - 10th International Conference on Turbochargers and Turbocharging. - [s.l.] : Woodhead Publishing Limited, 2012.

Pullen K.R [et al.] The TurboClaw Compressor for Engine Downsizing by Twin-Charging [Conference] // 7th International Conference on Compressors and Their Systems. - London, United Kingdom : Woodhead Publishing Limited, 2011.

Pullen K.R [et al.] TurboClaw - A Low Cost Turbocompressor Solution for Fuel Cells and Other Applications [Conference] // International Conference on Compressors and Their Systems. - London, United Kingdom : Chandos Publishing, 2009.

Pullen K.R, Etemad S and Cattell R Experimental Investigation of the TurboClaw Low Specific Speed Turbocompressor [Conference] // ASME Turbo Expo 2012: Turbine Technical Conference and Exposition. - Copenhagen, Denmark : American Society of Mechanical Engineers (ASME), 2012. - Vol. 5.

Pumps Vertical [verticalpumps.co.uk](http://www.verticalpumps.co.uk) [Online]. - 2014. - <http://www.verticalpumps.co.uk/#!/pump-specific-speeds/cd81>.

Quail F.J., Strickland M. and Scanlon T. Numerical and Experimental Design Study of a Regenerative Pump [Conference] // Current Themes in Engineering Science. - [s.l.] : American Institute of Physics, 2009. - pp. 165-180.

Rogers C. Experiments With a Low-Specific Speed Partial Emission Centrifugal Compressor [Journal] // Transactions of the ASME. - 1990. - Vol. 112. - pp. 30-37.

Rusak V. Development and Performance of the Wedge Type Low Specific Speed Compressor Wheel [Journal]. - [s.l.] : ASME, 1982. - Vol. 27th International Gas Turbine Conference and Exhibition.

Saito M [et al.] Flow measurement of high specific centrifugal compressors [Conference] // Fluid Control and Measurement. - 1985. - Vol. 1.

Schnitzler J.P [et al.] Experimental determination of a four stage axial compressor map operating in wet compression [Conference] // ASME Turbo Expo 2014: Turbine Technical Conference and Exposition. - [s.l.] : American Society of Mechanical Engineers (ASME), 2014. - Vol. 2A.

Sixsmith H. and Altmann H. A Regenerative Compressor [Journal]. - [s.l.] : Journal of Engineering for Industry, August 1977. - pp. 637-647.

SKF General Catalogue [Book]. - [s.l.] : SKF, 2005.

SKF Super Precision Catalogue [Book]. - 2013.

Song J.W., Raheel M. and Engeda A. A Compressible Flow Theory for Regenerative Compressors with Aerofoil Blades [Journal] // J. Mechanical Engineering Science. - [s.l.] : IMEChE, 2003. - Part C : Vol. 217. - pp. 1241-1257.

Stahlecker D and Gyarmathy G Investigations of turbulent flow in a centrifugal compressor vaned diffuser by 3-component laser velocimetry [Conference] // Proceedings of the 1998 International Gas Turbine & Aeroengine Congress & Exhibition. - [s.l.] : ASME, 1998.

Tanaka M., Kobayashi H. and Nishida H. Development of Wedge Type Impellers for Low Specific Speed Centrifugal Compressors [Journal] // Proceedings of IMECE2008. - 2008. - pp. 1-10.

Taylor John R An Introduction to Error Analysis [Book]. - [s.l.] : University Science Books, 1997. - 2nd.

Technology Power power-technology.com [Online]. - 2018. - <http://www.power-technology.com/contractors/cogeneration/mayekawa/>.

Thornton W A Low Specific Speed, Multistage, Turbocompressor for Microturbine Fuelling [Book]. - [s.l.] : Imperial College London, 2005.

Thornton W Diffuser for a forward-swept tangential flow compressor [Patent] : GB2519503A. - GB, 19 08 2013.

Thornton W.E TurboClaw Software Documentation [Book]. - [s.l.] : Dynamic Boosting Systems Ltd, 2011.

Tricountypools tricountypools.com [Online]. - 2014. - <http://www.tricountypools.com/heaters/item/heaters/titanium-heat-pumps.html>.

TSI PLIF Systems [Online]. - 2018. - 2018. - <http://www.tsi.com/PLIF-Systems/>.

Turbomachinery International International Turbomachinery [Online]. - 2014. - <http://www.turbomachinerymag.com/blog/content/man-supplies-compressor-technology-chinese-synfuels-project>.

Ubaldi M, Zunino P and Ghiglione A Detailed flow measurements within the impeller and the vaneless diffuser of a centrifugal turbomachine [Journal]. - [s.l.] : Experimental Thermal and Fluid Science, 1998. - 147-155 : Vol. 17.

Ubaldi M, Zunino P and Ghiglione A Detailed flow measurements within the impeller and vaneless diffuser of a centrifugal turbomachine [Journal]. - [s.l.] : Experimental Thermal and Fluid Science, 1997. - Vol. 17.

USA Casco Positive displacement compressors [Online]. - Imagebox, 2017. - 01 April 2017. - <http://cascousa.com/compressed-air-101/types-of-compressors/positive-displacement-compressors/>.

Verdonk G Vaned diffuser inlet flow conditions for a high pressure ratio centrifugal compressor [Conference] // ASME 1978 International Gas Turbine Conference and Products Show. - [s.l.] : American Society of Mechanical Engineers (ASME), 1978. - Vol. 1A.

Vine A The Aerodynamic Design and Evaluation of a Low Specific Speed Turbo Compressor [Book]. - 2005.

Vine A.J [et al.] Low Specific Speed Turbocompressors [Conference] // IMechE, Fluid Machinery Group - International Conference on Compressors and Their Systems. - [s.l.] : John Wiley and Sons Inc., 2005.

Vine A.J and Pullen K.R Radial compressor impeller [Patent] : EP1682779B1. - GB, 09 09 2003.

Wernet M.P Digital PIV measurements in the diffuser of a high speed centrifugal compressor [Conference] // 20th AIAA Advanced Measurement and Ground Testing Technology Conference. - [s.l.] : American Institute of Aeronautics and Astronautics Inc, AIAA, 1998.

Yeh Y and Cummins H.Z Localized fluid flow measurements with an He-Ne laser spectrometer [Journal]. - [s.l.] : Applied Physics Letters, 1964. - Vol. 4.